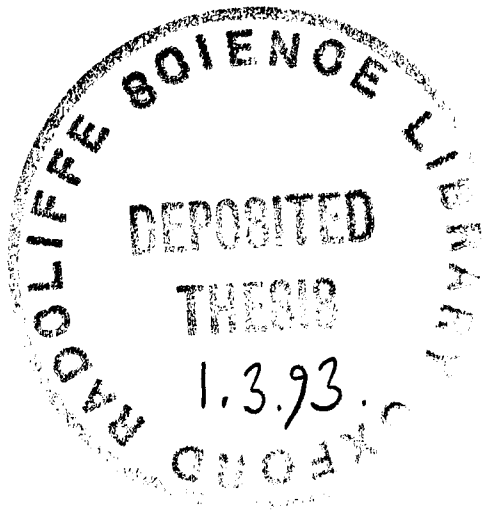
Structure and Dynamics of Metal Clusters

James I. Penman

St John's College
Oxford



A thesis submitted in partial fulfilment of the requirements
for the degree of Doctor of Philosophy
of the University of Oxford

Michaelmas Term 1992

Structure and Dynamics of Metal Clusters

James I. Penman

St John's College
Oxford

A thesis submitted in partial fulfilment of the requirements
for the degree of Doctor of Philosophy
of the University of Oxford

Michaelmas Term 1992

Abstract

This thesis is concerned with the development of *ab-initio* molecular dynamics (AIMD) using density functional theory, and its application to simple diatomics and small sodium clusters. The approach follows Car and Parrinello and the local spin density (LSD) approximation is taken as a starting point for the description of the electronic states in these systems. An improvement to LSD by correcting for the spurious self-interaction terms (SIC), as proposed by Perdew and Zunger, and the way in which this can be implemented is considered. The SIC corrected LSD is tested on simple diatomic molecules, and is shown, especially for the case of H_2, to significantly improve on the LSD description of the potential energy curve and the spin pairing/unpairing transition. LSD and SIC are then compared for small sodium clusters, for which the geometries, binding energies, and polarizabilities are determined, as well as vibrational frequencies for two clusters. Conclusions are hampered by the lack of experimental data, and uncertainties due to the pseudopotential. However SIC gives a more accurate description of the binding energies, and the unique SIC orbitals allow a description of the bonding which accurately predicts the relative stabilities of the clusters and rationalises their geometries.

The problems of breakdown of the Car-Parrinello (CP) method due to "non-adiabatic" effects is considered and it is shown that the problems arising during bond formation and bond breaking, as illustrated by the case of Na_2, can largely be overcome by applying an external thermostat to the fake degrees of freedom. This method is then tested using the dynamics of small sodium clusters. In particular the dynamics of the pseudorotation of Na_3 is studied and it is shown that the mechanism and information about the kinetics can be determined.

Finally other methods for improving upon LSD are considered. It is shown that gradient corrections using a plane wave basis set have inherent problems in implementation. Implementation of the exact Hartree-Fock exchange is considered, and this in conjunction with a form of self-interaction correction on the correlation is shown give very accurate results for simple diatomics which are cheaper than using full configuration interaction methods.

It seems to have become a tradition to dedicate ones thesis, and in the absence of any clear or good reason as to who or why, to dedicate it to ones parents. I do not agree with and so do not follow this meaningless habit.

To my parents

Acknowledgements

As is only natural over the course of three years I have received much help and support from those around me. First and foremost I thank Dr Paul Madden for his excellent supervision ("on the fly"). I would also like to thank Dr Ettore Fois, who for the first year of my research provided much encouragement, enthusiastic discussion, and excellent teaching. Of the many fellow "Maddenites" I would like to mention Matt for, well being Matt really, and Ian for three years of *always* knowing the right buzz-word, or gratuitous insult, and his wide knowledge of CBT. Life (?!) of course would not be the same without the "Loganites", in particular Mike, not least for his support in a particularly "hairy" period. Mention must also be made of Marjorie, without whose tea I don't think I would have survived. Thanks as well to Paul Hodgkinson for help with converting figures from one type of encapsulated postscript to another.

Outside the lab. many friends and acquaintances, old, new, half forgotten, or otherwise, have made life what it has been over the last three years. Especially I thank Jane for being there, Glenn for providing (most of) the entertainment, and Keith for occasionally getting in touch. Thanks too to the "I's" (Infrequents), particularly last year for such a successful season, for never quite killing me in the warm up (thanks Paul!), and for always giving me something to do (defense? what defense?).

If for nothing else, though rarely present, for always being there the very least I can do is to thank my parents.

Finally, Anne ...

If you can keep your head when all about you
Are losing theirs and blaming it on you,
If you can trust yourself when all men doubt you,
But make allowance for their doubting too;
If you can wait and not be tired of waiting,
Or being lied about, don't deal in lies,
Or being hated don't give way to hating,
And yet don't look too good, nor talk too wise:

If you can dream – and not make dreams your master;
If you can think – and not make thoughts your aim;
If you can meet with Triumph and Disaster
And treat these two imposters just the same;
If you can bear to hear the truth you've spoken
Twisted by knaves to make a trap for fools,
Or watch the things you gave your life to, broken
And stop to build 'em up with warn out tools:

If you can make a heap of all your winnings
And risk it on one turn of pitch and toss,
And lose, and start again at your beginnings
And never breath a word about your loss;
If you can force your heart and nerve and sinew
To serve your turn long after they are gone,
And so hold on when there is nothing in you
Except the Will which says to them: 'Hold on!'

If you can talk with crowds and keep your virtue
Or walk with Kings – nor lose the common touch,
If neither foes nor loving friends can hurt you,
If all men count with you but none too much;
If you can fill the unforgiving minute
With sixty seconds worth of distance run,
Yours is the Earth and everything that's in it,
And – what is more – you'll be a Man, my son!

Rudyard Kipling

The Road goes ever on and on
Down for the door where it began.
Now far ahead the Road had gone,
And I must follow if I can,
Pursuing it with eager feet,
Until it joins some larger way
Where many paths and errands meet.
And whither then? I cannot say.

J.R.R. Tolkien

Es irrt der Mensch, so lang er strebt.
Man will err while yet he strives.

von Goethe

Tout passe, tout casse, tout lasse.

Contents

1 Introduction **1**

2 Background Theoretical Considerations **5**
2.1 Density Functional Theory 5
2.1.1 The Kohn-Sham Equations 7
2.1.2 The Exchange-Correlation Energy 10
2.1.3 Spin Density Functional Theory 10
2.2 *Ab-Initio* Molecular Dynamics 14
2.2.1 Classical Molecular Dynamics 14
2.2.2 Car-Parrinello Method 15
2.3 Minimisation of the Energy Functional - The Conjugate Gradient Method 19
2.4 Implementation 23
2.4.1 The Basis Set 24
2.4.2 The External Energy $V_{ext}(\mathbf{r})$ 25
2.4.3 Coulomb Interaction Terms 25
2.4.4 Energy Gradients 26

3 The Self-Interaction Correction **28**
3.1 Brief Critique of the LSD Approximation 28
3.2 The Self-Interaction Correction 30
3.3 LSD vs SIC for Simple Diatomic Systems 33
3.3.1 H_2 35
3.3.2 Na_2 39
3.3.3 Cs_2 41
3.3.4 NaH 41
3.3.5 Conclusions 45

4 Structure and Properties of Small Sodium Clusters **46**
4.1 Geometries and Binding Energies 46
4.2 Electronic Structure 55
4.3 Static Electric Polarizabilities 72
4.4 Vibrational Frequencies 79

4.4.1 Na_3 80
4.4.2 Na_4 80
4.4.3 Conclusions 81

5 Control of the Adiabatic Electronic State in the CP Method 82
5.1 Breakdown of the CP Method 82
5.1.1 Non-Adiabatic Events in the Dynamics of Na_2 85
5.2 Thermostated Equations of Motion 88
5.2.1 Constant Temperature MD - The Nosé-Hoover Thermostat 91
5.2.2 Application of the Nosé-Hoover Thermostat to The CP Equations of Motion 93
5.3 Optimisation of the Nosé-Hoover Thermostat Parameters . . . 98
5.4 Examples of Nosé-Hoover Thermostated CP MD 99
5.4.1 The Pseudorotation of Na_3 99
5.4.2 The Pseudorotation of Na_4 115
5.4.3 Inversion of the Na_6 Pentagonal Pyramid 120

6 Beyond the Local Density Approximation 123
6.1 The Stoll, Pavlidou, and Preuß Correction to the Correlation Energy 123
6.2 The Generalised Gradient Approximation for the Exchange Energy 124
6.3 Implementation of the Perdew and Wang GGA Exchange Functional in Self Consistent Calculations 127
6.3.1 Partially Converged Na_2 Calculations 142
6.4 The Hartree-Fock-Kohn-Sham Method 144
6.4.1 Implementation 145
6.5 Comparison of LSD, SIC, SPP, HFKS, and HFKS-SPP for Simple Diatomic Systems 145
6.5.1 H_2 146
6.5.2 Na_2 149
6.5.3 Cs_2 151
6.5.4 NaH 151
6.5.5 Conclusions 153
6.6 The Use of HFKS and HFKS-SPP To Study Small Sodium Clusters 155
6.6.1 Geometries and Binding Energies 155
6.6.2 Polarizabilities 156
6.6.3 Conclusions 157

A The Derivation of the Orthonormality Constraint Algorithms for CP Dynamics 158

B Pseudopotentials 161

C Derivation of the Exchange Potential for Perdew's Exchange Energy Functional 164

D Useful Conversion Factors 167

List of Tables

2.1 The parameters for the Perdew and Zunger parameterisation of the correlation energy 13

3.1 Cutoff and Box Length Parameters 33
3.2 Rate of convergence of H-atom calculations with increasing cutoff. Box length = 20a.u. 34
3.3 Rate of convergence of Na_8 calculations with increasing cutoff. Boxlen = 36.0a.u. 34
3.4 Comparison of the H_2 binding energies and bond lengths from LSD and SIC Calculations with Experiment. 36
3.5 Comparison of the Na_2 binding energies and bond lengths from LSD and SIC calculations with experiment. 41
3.6 Comparison of the Cs_2 binding energies and bond lengths from LSD and SIC calculations with experiment. 44
3.7 Comparison of the NaH binding energies and bond lengths from LSD and SIC calculations. 44

4.1 Na_2 bond lengths in a.u. 48
4.2 Na_3 bond lengths in a.u. for the acute geometry. 48
4.3 Na_3 bond lengths in a.u. for the obtuse geometry. 50
4.4 Na_4 bond lengths in a.u. for the regular rhombic geometry. . . 50
4.5 Na_4 bond lengths in a.u. for the irregular rhombic geometry. . 50
4.6 Na_5 bond lengths in a.u. 51
4.7 Na_6 bond lengths in a.u. for the D_{3h} geometry. 51
4.8 Na_6 bond lengths in a.u. for the $C_{5\nu}$ geometry. 51
4.9 Na_7 bond lengths in a.u. for the D_{5h} geometry. 52
4.10 Na_7 bond lengths in a.u. for the D_{2h} geometry. 52
4.11 Na_8 bond lengths in a.u. for the D_{2d} geometry. 52
4.12 Na_8 bond lengths in a.u. for the T_d geometry. 52
4.13 Binding energies per atom in eV for stable geometries of sodium clusters. 54
4.14 Binding energies per atom in eV for the most stable geometries of sodium clusters. The first two columns marked LSD and SIC are from this work. 54

4.15 Variation of α_{xx} ($=\bar{\alpha}$) in a.u. with field for the sodium atom in LSD and SIC, calculated assuming linear response. 75
4.16 Diagonal components of the polarizability tensor and the spherically averaged polarizability $\bar{\alpha} = \frac{1}{3}(\alpha_{xx}+\alpha_{yy}+\alpha_{zz})$ in $\mathring{A}^3$ using LSD. 76
4.17 Diagonal components of the polarizability tensor and the spherically averaged polarizability $\bar{\alpha} = \frac{1}{3}(\alpha_{xx}+\alpha_{yy}+\alpha_{zz})$ in $\mathring{A}^3$ using SIC. 76
4.18 Diagonal components of the polarizability tensor and the spherically averaged polarizability $\bar{\alpha} = \frac{1}{3}(\alpha_{xx}+\alpha_{yy}+\alpha_{zz})$ in $\mathring{A}^3$ due to Moullet *et al.* [69] 77
4.19 Experimental static electric polarizabilities due to Knight *et al.* [42] 77
4.20 Vibrational frequencies of Na_3. 81
4.21 Vibrational frequencies of Na_4. 81

6.1 Hydrogen atom exchange energies using LSD and HF densities in the LSD and GGA exchange functionals. Results are in a.u. 128
6.2 Convergence tests using GGA exchange with unmodified F. All data is in a.u. 132
6.3 Convergence tests using GGA exchange with modified F. All data is in a.u. 132
6.4 Unduallled convergence tests using GGA exchange with unmodified F. All data is in a.u. 132
6.5 Unduallled convergence tests using GGA exchange with modified F. All data is in a.u. 132
6.6 Comparison of the H_2 binding energies and bond lengths from various calculations with experiment. 146
6.7 Comparison of the Na_2 binding energies and bond lengths from various calculations with experiment. 149
6.8 Comparison of the Cs_2 binding energies and bond lengths from various calculations with experiment. 151
6.9 Comparison of the NaH binding energies and bond lengths from various calculations. 153
6.10 Binding energies and bond lengths for Na_3 using HFKS, and HFKS-SPP. 156
6.11 Binding energies and bond lengths for Na_4 using HFKS, and HFKS-SPP. 156
6.12 Diagonal components of the polarizability tensor and the spherically averaged polarizability $\bar{\alpha}$ in $\mathring{A}^3$ for Na_4 using HFKS, and HFKS-SPP. 157

List of Figures

2.1 Comparison of the Stich *et al.* implementation of the CG method (b) and the variation of the CG method used in this work (a). 22

3.1 The potential energy curves for H_2 using LSD and SIC. The "exact" potential energy curve due to Kolos and Wolniewicz [45] is also shown. 37
3.2 The local moment curves for H_2 using LSD and SIC. 37
3.3 The local moment (L_0) as a function of $U/4t$ for a one dimensional Hubbard model, where U is the on-site Coulomb interaction, and t is the hopping integral. These results are from reference [105] 38
3.4 The potential energy curves for Na_2 using LDA,LSD and SIC. Also shown is the experimental curve due to Verma *et al.* [116] . 40
3.5 The local moment curves for Na_2 using LSD and SIC. 40
3.6 The potential energy curves for Cs_2 using LSD and SIC. The experimental potential energy curve due to Weickenmeier *et al.* [121] is also shown. 42
3.7 The local moment curves for Cs_2 using LSD and SIC. 42
3.8 The potential energy curves for NaH using LSD and SIC. . . . 43
3.9 The local moment curves for NaH using LSD and SIC. 43
3.10 The dipole moment curves for NaH using LSD and SIC. . . . 45

4.1 The stable geometries found for sodium clusters with between 2, and 8 atoms. Working from left to right and down the page these are: Na_2, Na_3 (obtuse), Na_3 (acute), Na_4 (regular rhombus), Na_4 (irregular rhombus), Na_5, Na_6 (D_{3h}), Na_6 (C_{5v}), Na_7 (D_{2h}), Na_7 (D_{5h}) Na_8 (D_{2d}), Na_8 (T_d). 49
4.2 The binding energies per atom, $\Delta E/n$ versus nuclearity, n, for the ground state geometries using LSD, SIC, CI [20] , PI [31] , and LDA [93] 53
4.3 The splitting of the p-levels in a jellium model with (a) an oblate distortion, and (b) a prolate distortion. 57

4.4 The valence electron density maps for Na_2. The left hand map was calculated in LSD, the right in SIC. 58
4.5 The valence electron density maps for the obtuse Na_3 geometry. The left hand map was calculated in LSD, the right in SIC. 59
4.6 The valence electron density maps for the acute Na_3 geometry. The left hand map was calculated in LSD, the right in SIC. . . 59
4.7 The valence electron density maps for the regular rhombic Na_4 geometry. The left hand map was calculated in LSD, the right in SIC. 60
4.8 The valence electron density maps for the Na_5. The left hand map was calculated in LSD, the right in SIC. 60
4.9 The valence electron density maps for the triangular Na_6 geometry. The left hand map was calculated in LSD, the right in SIC. 61
4.10 The valence electron density maps for the pentagonal pyramidal Na_6 geometry. The left hand map was calculated in LSD, the right in SIC. 61
4.11 The valence electron density maps for the planar hexagonal Na_7 geometry. The left hand map was calculated in LSD, the right in SIC. 62
4.12 The valence electron density maps for the pentagonal bipyramidal Na_7 geometry. The left hand map was calculated in LSD, the right in SIC. 62
4.13 Na_2 valence electron densities for decreasing separation of the ions. The separations are (i) 11.0 a.u., (ii) 9.87 a.u., (iii) 8.85 a.u., (iv) 6.05 a.u. 63
4.14 The valence electron density (i) and the orbital density maps (ii-iii) for the triangular Na_4 geometry. The orbital density maps are all for the same spin. The opposite spins give identical densities. (a) is using LSD, and (b) is using SIC. 65
4.15 The valence electron density (a) and the orbital density maps (b-e) for square Na_4, using SIC. The density maps (b), and (c) have the same spin, and (d), and (e) have the opposite spin. 67
4.16 The valence electron density (i) and the orbital density maps (ii-iv) for the triangular Na_6 geometry. (a) is using LSD, and (b) is using SIC. 68
4.17 The valence electron density (i) and the orbital density maps (ii-iv) for the pentagonal pyramidal Na_6 geometry. (a) is using LSD, and (b) is using SIC. 69
4.18 The valence electron density (i) and the orbital density maps (ii-iv) for the obtuse Na_3 geometry. (ii) and (iii) are for the same spin. (a) is using LSD, and (b) is using SIC. 70

4.19 The valence electron density (i) and the orbital density maps (ii-iv) for the acute Na_3 geometry. (ii) and (iii) are for the same spin. (a) is using LSD, and (b) is using SIC. 71
4.20 Induced dipole moment, $p_{ind,x}$, versus applied field in x-direction, F_x, for Na_4 using LSD. 74
4.21 Spherically averaged polarizabilities $\bar{\alpha} = \frac{1}{3}(\alpha_{xx} + \alpha_{yy} + \alpha_{zz})$. The experimental data is due to Knight *et al.* [42] 75

5.1 The ion potential energy for a dynamics run for Na_2, using conventional CP algorithm. 86
5.2 The fake kinetic energy for a dynamics run for Na_2, using conventional CP algorithm. 86
5.3 The ion potential energy for a dynamics run for Na_2, using conventional CP algorithm starting from a separation of 4.2 a.u. 89
5.4 The fake kinetic energy for a dynamics run for Na_2, using conventional CP algorithm starting from a separation of 4.2 a.u. 89
5.5 The ion potential energy for a dynamics run for Na_2, using conventional CP algorithm and LSD. 90
5.6 The fake kinetic energy for a dynamics run for Na_2, using conventional CP algorithm and LSD. 90
5.7 The ion potential energy for a dynamics run for Na_2, using a single Nosé-Hoover thermostat. 95
5.8 The fake kinetic energy for a dynamics run for Na_2, using a single Nosé-Hoover thermostat. 95
5.9 The ion potential energy for a dynamics run for Na_2, using two Nosé-Hoover thermostats. 96
5.10 The fake kinetic energy for a dynamics run for Na_2, using two Nosé-Hoover thermostats. 96
5.11 The ion potential energy for a dynamics run for Na_2, using the Nosé-Hoover thermostat using the parameters: μ=400, ζ=0.5, f=0.025, δt=6.4. 100
5.12 The ion potential energy for a dynamics run for Na_2, using the Nosé-Hoover thermostat using the parameters: μ=400, ζ=2.0, f=0.025, δt=6.4. 100
5.13 The ion potential energy for a dynamics run for Na_2, using the Nosé-Hoover thermostat using the parameters: μ=400, ζ=1.0, f=0.0125, δt=6.4. 101
5.14 The ion potential energy for a dynamics run for Na_2, using the Nosé-Hoover thermostat using the parameters: μ=400, ζ=1.0, f=0.05, δt=6.4. 101

5.15 The ion potential energy for a dynamics run for Na_2, using the Nosé-Hoover thermostat using the parameters: μ=400, ζ=0.333, f=0.0125, δt=6.4. 102
5.16 The ion potential energy for a dynamics run for Na_2, using the Nosé-Hoover thermostat using the parameters: μ=400, ζ=1.0, f=0.025, δt=6.4. 102
5.17 The ion potential energy versus step for a dynamics run for Na_2, using the Nosé-Hoover thermostat using the parameters: μ=400, ζ=1.0, f=0.025, δt=6.4. 103
5.18 The fake kinetic energy for a dynamics run for Na_2, using the Nosé-Hoover thermostat using the parameters: μ=400, ζ=1.0, f=0.025, δt=6.4. 103
5.19 The net forces for a dynamics run for Na_2, using the Nosé-Hoover thermostat using the parameters: μ=400, ζ=1.0, f=0.025, δt=6.4. 104
5.20 The total energy for a dynamics run for Na_2, using the Nosé-Hoover thermostat using the parameters: μ=400, ζ=1.0, f=0.025, δt=6.4. 104
5.21 The thermostat parameter ξ for a dynamics run for Na_2, using the Nosé-Hoover thermostat using the parameters: μ=400, ζ=1.0, f=0.025, δt=6.4. 105
5.22 The energy flux through the thermostat for a dynamics run for Na_2, using the Nosé-Hoover thermostat using the parameters: μ=400, ζ=1.0, f=0.025, δt=6.4. 105
5.23 The ion potential energy for a dynamics run for Na_2, using the Nosé-Hoover thermostat using the optimum parameters: μ=200, ζ=0.5, f=0.025, δt=6.4. 106
5.24 The ion potential energy versus step for a dynamics run for Na_2, using the Nosé-Hoover thermostat using the parameters: μ=200, ζ=0.5, f=0.025, δt=6.4. 106
5.25 The total energy for a dynamics run for Na_2, using the Nosé-Hoover thermostat using the parameters: μ=200, ζ=0.5, f=0.025, δt=6.4. 107
5.26 The fake kinetic energy for a dynamics run for Na_2, using the Nosé-Hoover thermostat using the parameters: μ=200, ζ=0.5, f=0.025, δt=6.4. 107
5.27 The thermostat parameter ξ for a dynamics run for Na_2, using the Nosé-Hoover thermostat using the parameters: μ=200, ζ=0.5, f=0.025, δt=6.4. 108
5.28 The net forces for a dynamics run for Na_2, using the Nosé-Hoover thermostat using the parameters: μ=200, ζ=0.5, f=0.025, δt=6.4. 108

5.29 The energy flux through the thermostat for a dynamics run for Na_2, using the Nosé-Hoover thermostat using the parameters: μ=200, ζ=0.5, f=0.025, δt=6.4. 109
5.30 The ion kinetic energy for a typical 20000 step dynamics run for Na_3, using the Nosé-Hoover thermostat. 111
5.31 The fake kinetic energy for a typical 20000 step dynamics run for Na_3, using the Nosé-Hoover thermostat. 111
5.32 The total energy flux for a typical 20000 step dynamics run for Na_3, using the Nosé-Hoover thermostat. 112
5.33 The variation in the bond lengths for a typical 20000 step dynamics run for Na_3, using the Nosé-Hoover thermostat. . . 112
5.34 The ion potential energy for a typical 20000 step dynamics run for Na_3, using the Nosé-Hoover thermostat. 113
5.35 The mechanism for pseudorotation of Na_3. 114
5.36 The isomerisation parameter, d(t), versus number of steps for Na_3 dynamics. 115
5.37 Initial velocities given toNa_4 cluster to attempt to "fire" it into the equivalent pseudorotated geometry. 116
5.38 The potential energy for dynamics on Na_4 using SIC and starting from the rhombic geometry. 117
5.39 The fake kinetic energy for dynamics on Na_4 using SIC and starting from the rhombic geometry. 117
5.40 The potential energy for dynamics on Na_4 using SIC and starting from rest in the square planar geometry. 118
5.41 The fake kinetic energy for dynamics on Na_4 using SIC and starting from rest in the square planar geometry. 118
5.42 Na_4. valence electron densities after (a) 0, (b) 1400, (c) 2000, and (d) 2300 steps. 119
5.43 The potential energy for dynamics run on pentagonal pyramidal Na_6 using SIC and firing the apical atom through the pentagon. 121
5.44 The fake kinetic energy for dynamics run on pentagonal pyramidal Na_6 using SIC and firing the apical atom through the pentagon. 121

6.1 The modified functional $F(s)$ versus s for various values of the parameter μ. 130
6.2 $\rho(x)$ (a.u.) for varying amplitudes of applied sinusoidal potential. 133
6.3 $|\nabla\rho(x)|$ (a.u.) for varying amplitudes of applied sinusoidal potential. 134
6.4 $\nabla^2\rho(x)$ (a.u.) for varying amplitudes of applied sinusoidal potential. 135

6.5 $V_x(x)$ (a.u.) for varying amplitudes of applied sinusoidal potential. 136
6.6 $s(x)$ (a.u.) for varying amplitudes of applied sinusoidal potential. 137
6.7 $F(s) - 1$ for varying amplitudes of applied sinusoidal potential. 138
6.8 $s^{-1}\frac{dF}{ds}$ for varying amplitudes of applied sinusoidal potential. . 139
6.9 $s^{-1}\frac{d}{ds}\left(s^{-1}\frac{dF}{ds}\right)$ for varying amplitudes of applied sinusoidal potential. 140
6.10 The potential energy curves for Na_2. The experimental potential energy curve is due to Verma *et al.* [116] 143
6.11 The potential energy curves for H_2 using HFKS, HFKS-SPP, SPP, LSD and SIC. The "exact" potential energy curve due to Kolos and Wolniewicz [45] is also shown. 147
6.12 The local moment curves for H_2 using HFKS, HFKS-SPP, SPP, LSD and SIC. 147
6.13 The potential energy curves for triplet H_2 using HFKS, HFKS-SPP, SPP, LSD and SIC. The potential energy curve due to Kolos and Wolniewicz [44] is also shown. 148
6.14 The potential energy curves for Na_2 using HFKS, HFKS-SPP, SPP, LSD and SIC. The experimental potential energy curve due to Verma *et al.* [116] is also shown. 150
6.15 The local moment curves for Na_2 using HFKS, HFKS-SPP, SPP, LSD and SIC. 150
6.16 The potential energy curves for Cs_2 using HFKS, HFKS-SPP, SPP, LSD and SIC. The experimental potential energy curve due to Weickenmeier *et al.* [121] is also shown. 152
6.17 The local moment curves for Cs_2 using HFKS, HFKS-SPP, SPP, LSD and SIC. 152
6.18 The potential energy curves for NaH using HFKS, HFKS-SPP, SPP, LSD and SIC. 154
6.19 The local moment curves for NaH using HFKS, HFKS-SPP, SPP, LSD and SIC. 154
6.20 The dipole moment curves for NaH using HFKS, HFKS-SPP, SPP, LSD and SIC. 155

Chapter 1

Introduction

Molecular dynamics [1] is now a well established tool for studying a wide range of materials and molecules. The understanding of the mechanisms of many dynamical phenomena has been greatly enhanced by the way this method enables the atomic and molecular motions to be seen. This method essentially entails using finite difference methods to propagate the Newtonian equations of motion for the set of atoms under study. To do this some form of the potential energy surface needs to be assumed in order to determine the forces on each atom. Until recently the only method used was to assume that the system could be described by a sum of pairwise or N-body interactions. The problem then reduced itself to designing effective N-body interaction potentials. However this approach suffers the serious handicaps that in general these potentials are not transferable from one system to another, and whenever valence electrons are itinerant, such as in bond formation or bond breaking, the method breaks down.

In 1985 Car and Parrinello [13] demonstrated that *ab-initio* molecular dynamics (AIMD) could be carried out using a computationally tractable algorithm. In this method the electronic degrees of freedom of the system are described explicitly and included in an extended Lagrangian, which ensures that as the equations of motion of the ions are propagated the electrons remain on or close to the Born-Oppenheimer (BO) surface, so that reliable forces can be calculated. As well as being used for molecular dynamics this method could also be used to find the minimum of the energy functionals and hence the ground state of the system. Almost as a by-product then this method allows both static and dynamic studies of the ground state properties of a given system. Note though that systems where electronic excitations occur are still excluded, as use is still made of the BO approximation to separate the ionic and electronic motion. It is this approach then that forms the basis and starting point for this thesis.

In a certain sense the problem with "classical" molecular dynamics (MD) is that in trying to describe a system in terms simply of the ionic coordinates

it underdetermines the problem. The success of Car-Parrinello (CP) molecular dynamics is that it introduces the extra degrees of freedom necessary to describe the system. The clever part of the algorithm though is the way in which the ion coordinate dynamics and the "dynamics" of the "fake" system are coupled so that the extra degrees of freedom are updated at each step in such a way that no expensive re-optimisations are required.

The approach of Car and Parrinello turns out to be quite general, and can be used to improve "classical" MD even when full AIMD would not be practical. For example Sprik and Klein [102, 101] have used a CP based approach to describe liquid water. In this extra degrees of freedom are added to describe polarization effects. These extra degrees of freedom are the magnitudes of charges placed at fixed positions in the molecular framework. Similarly Löwen *et al.* [58] have used the Fourier components of the counter ion density as extra variables to describe colloids accurately. The results are in better agreement with experiment in both cases than obtained by previous methods.

In Car and Parrinello's original work, and in this thesis, the intention is to develop a truly *ab-initio* MD method. Thus the electrons must be described using one of the various quantum mechanical methods available. The CP method is not restricted in principle to any particular approach. For molecular systems then it would be quite reasonable to use Hartree-Fock theory and a localised basis set; the extra degrees of freedom being the wavefunctions or coefficients of their expansion in the basis set. Some attempts have been made at implementing CP in this approach [33, 23]. However a localised, atom-centred, basis set does present extra problems due to spurious Pulay forces [86, 87]. Car and Parrinello instead used density functional theory and a plane wave basis set. This was probably initially motivated by the fact that they were simulating condensed matter, using the standard method of periodic boundary conditions. Plane waves do have a distinct advantage though as they allow straightforward use of fast Fourier transform methods in the calculation that greatly enhance the speed of calculation.

As the program on which this thesis was based was also intended for condensed matter simulations it too was written using density functional theory and a plane wave basis set with periodic boundary conditions. Now in principle for density functional theory one only needs the total electron density $\rho(\mathbf{r})$ to describe the electronic system. Thus the extra degrees of freedom would be the coefficients of (in this case) the plane wave expansion of the density. Recently attempts have been made to implement this in CP dynamics (eg. Zérah *et al.* [122], Meroni *et al.* [65]), but problems persist in finding a sufficiently accurate functional for the kinetic energy. Instead in this, and most other density functional work, the Kohn-Sham method is employed, whereby orbitals are reintroduced in order to accurately describe the electronic kinetic energy. The extra degrees of freedom then are the

coefficients of the plane wave expansion of these orbitals.

In the Kohn-Sham method although the problem of the kinetic energy is resolved, there remains the difficulty of finding a sufficiently accurate form of the exchange and correlation energies. The most commonly used solution is to assume that the results for the homogenous electron gas can be applied locally. Depending on whether this is done for the total density or the spin densities individually this is known as the local density (LDA), or local spin density (LSD) approximation.

There are shortcomings with this approach though. Firstly LSD is inadequate in a large number of situations. For example LSD does not accurately describe spin pairing/unpairing or metal insulator transitions. There is thus a need to investigate improvements to the local density functional theories that take account of these problems. Secondly, there are problems inherent in the CP method that ensure that for certain systems breakdown will always occur. These are systems with no band gap, ie. metals, and systems where energy bands cross, such as occurs during bond formation and bond breaking. One further problem also exists. As already stated the method separates the electronic and ionic degrees of freedom using the BO approximation. This will break down if electronic excitations occur. These systems though will be specifically excluded from consideration in this thesis. Coker [100] has carried out work in overcoming this problem.

The aim of this thesis then is to consider ways of overcoming the first two problems. The initial motivation was (and is) to enable the accurate and reliable simulation of liquid metals, in particular liquid sodium near the metal-insulator transition. To help elucidate the sources of difficulty though this system was not considered, instead smaller and simpler systems were studied.

Firstly chapter 2 will set out the basic theoretical background. Density functional theory is briefly discussed in the first section, followed by a discussion of classical and CP molecular dynamics. Although simulated annealing using CP could be used to find the ground state for a given configuration of atoms it is found that conjugate gradient methods are far more efficient. This then is discussed in the third section. Finally there is brief discussion of how these methods were implemented.

Chapter 3 discusses the self-interaction correction (SIC) method due to Perdew and Zunger [84] which improves the LSD method by explicitly subtracting the spurious self terms. LSD and SIC are then compared for simple diatomics. Chapter 4 discusses the application of LSD and SIC to small sodium clusters, whose geometries are optimised using a CP based steepest descent method. The density functional calculations are also compared to other methods such as configuration interaction and path integral calculations. In chapter 5 the use of thermostats on the "fake" degrees of freedom to prevent breakdown of the CP method is discussed, with particular refer-

ence to bond formation and bond breaking. Finally chapter 6 discusses the difficulties in implementing gradient corrections to LSD, and the use of the exact Hartree-Fock exchange functional, as well as a form of self-interaction for the correlation energy. The latter two are compared to LSD and SIC for simple diatomic molecules.

Chapter 2

Background Theoretical Considerations

In this chapter I will consider the necessary background to the rest of this thesis. The first section deals with density functional theory [72] and how it is developed from the initial work of Hohenberg and Kohn [36]. I will then consider the problem of carrying out molecular dynamics from first principles, and the method proposed by Car and Parrinello [13]. Although nearly all implementations to date have used density functional theory for the electronic part of the problem I have deliberately kept the arguments general to show that this is not a necessary restriction. The next section deals with the minimisation of energy functionals and the chapter finishes with a summary of how the methods considered in the chapter have been implemented.

2.1 Density Functional Theory

The foundations of density functional theory (DFT) are two theorems by Hohenberg and Kohn [36]:

1. A given electron density $\rho(\mathbf{r})$ determines the external potential $V_{\mathbf{ext}}(\mathbf{r})$ to within a trivial additive constant. Thus the density $\rho(\mathbf{r})$ determines the ground state and all its properties, and the energy is a functional of the density.

2. The energy is a minimum at the ground state and the density that minimises the energy is the ground-state density distribution.

The proofs are quite straightforward, although I will follow the simpler and more general proofs given by Jones and Gunarsson [39]. Consider N electrons

moving in an external potential $V_{\text{ext}}(\mathbf{r})$ giving us the Hamiltonian,

$$H = T + V_{\text{ee}} + \sum_{i=1}^{N} V_{\text{ext}}(\mathbf{r}_i), \tag{2.1}$$

where T is the kinetic energy and V_{ee} the electron electron interaction operators. For all N-representable densities $\rho(\mathbf{r})$, ie. all those for which $\rho(\mathbf{r})$ obeys the following:

$$\rho(\mathbf{r}) \geq 0; \int \rho(\mathbf{r})d\mathbf{r} = N; \int |\rho(\mathbf{r})|^2 d\mathbf{r} < \infty, \tag{2.2}$$

it can be shown that this density can be obtained from an anti-symmetric wavefunction $\Psi(\mathbf{r}_1, \mathbf{r}_2, \ldots, \mathbf{r}_N)$ and we can define the functional,

$$F[\rho] = \min_{\Psi \to \rho} \langle \Psi | T + V_{\text{ee}} | \Psi \rangle, \tag{2.3}$$

where the minimum is taken over all Ψ that give ρ. In the sense that it refers to neither a specific system nor external potential $V_{\text{ext}}(\mathbf{r})$, $F[\rho]$ is universal. Writing the ground state energy, wave function, and density as E_{GS},Ψ_{GS}, and $\rho_{\text{GS}}(\mathbf{r})$ then the two basic theorems of DFT are:

$$E[\rho] \equiv \int d\mathbf{r} V_{\text{ext}}(\mathbf{r})\rho(\mathbf{r}) + F[\rho] \geq E_{\text{GS}}, \tag{2.4}$$

for all N-representable $\rho(\mathbf{r})$, and

$$\int d\mathbf{r} V_{\text{ext}}(\mathbf{r})\rho_{\text{GS}}(\mathbf{r}) + F[\rho_{\text{GS}}] = E_{\text{GS}}. \tag{2.5}$$

Thus to prove equation 2.4 let $\Psi^{\rho}_{\text{min}}(\mathbf{r})$ be a wavefunction that minimises 2.3, so that,

$$F[\rho] = \langle \Psi^{\rho}_{\text{min}} | T + V_{\text{ee}} | \Psi^{\rho}_{\text{min}} \rangle. \tag{2.6}$$

Writing $V = \sum_i V_{\text{ext}}(\mathbf{r}_i)$ we have,

$$\begin{aligned} \int d\mathbf{r} V_{\text{ext}}(\mathbf{r})\rho_{\text{GS}}(\mathbf{r}) + F[\rho_{\text{GS}}] &= \langle \Psi^{\rho}_{\text{min}} | V + T + V_{\text{ee}} | \Psi^{\rho}_{\text{min}} \rangle \\ &\geq E_{\text{GS}}, \end{aligned} \tag{2.7}$$

according to the minimum property of the ground state, hence proving equation 2.4.

Using the minimum property again,

$$\begin{aligned} E_{\text{GS}} &= \langle \Psi^{\rho}_{\text{GS}} | V + T + V_{\text{ee}} | \Psi^{\rho}_{\text{GS}} \rangle \\ &\leq \langle \Psi^{\rho_{\text{GS}}}_{\text{min}} | V + T + V_{\text{ee}} | \Psi^{\rho_{\text{GS}}}_{\text{min}} \rangle. \end{aligned} \tag{2.8}$$

Subtracting the interaction with the external potential we obtain,

$$\langle \Psi_{\rm GS}|T+V_{\rm ee}|\Psi_{\rm GS}\rangle \leq \langle \Psi^{\rho_{\rm GS}}_{\rm min}|T+V_{\rm ee}|\Psi^{\rho_{\rm GS}}_{\rm min}\rangle\,. \tag{2.9}$$

On the other hand, the definition of $\Psi^{\rho}_{\rm min}$ yields the reverse relation between the two sides of equation 2.9. This is only possible if,

$$\langle \Psi_{\rm GS}|T+V_{\rm ee}|\Psi_{\rm GS}\rangle = \langle \Psi^{\rho_{\rm GS}}_{\rm min}|T+V_{\rm ee}|\Psi^{\rho_{\rm GS}}_{\rm min}\rangle\,. \tag{2.10}$$

Thus we have,

$$\begin{aligned} E_{\rm GS} &= \int d\mathbf{r} V_{\rm ext}(\mathbf{r})\rho_{\rm GS}(\mathbf{r}) + \langle \Psi_{\rm GS}|T+V_{\rm ee}|\Psi_{\rm GS}\rangle \\ &= \int d\mathbf{r} V_{\rm ext}(\mathbf{r})\rho_{\rm GS}(\mathbf{r}) + \langle \Psi^{\rho_{\rm GS}}_{\rm min}|T+V_{\rm ee}|\Psi^{\rho_{\rm GS}}_{\rm min}\rangle \\ &= \int d\mathbf{r} V_{\rm ext}(\mathbf{r})\rho_{\rm GS}(\mathbf{r}) + F[\rho_{\rm GS}]. \end{aligned} \tag{2.11}$$

2.1.1 The Kohn-Sham Equations

From the preceeding section we can write the total energy of the system purely as a function of the electron density, for all reasonable electron densities, ie.

$$E[\rho] = \int \rho(\mathbf{r}) V_{\rm ext}(\mathbf{r}) d\mathbf{r} + F[\rho], \tag{2.12}$$

where $F[\rho] = T[\rho] + V_{\rm ee}[\rho]$.

The problem now remains to find the form of the functionals in this expression. An initial guess might be to approximate $V_{\rm ee}$ by solely its classical part, the Coulomb potential energy $J[\rho]$,

$$J[\rho] = \frac{1}{2}\int\int \frac{\rho(\mathbf{r}_1)\rho(\mathbf{r}_2)}{|\mathbf{r}_2-\mathbf{r}_1|} d\mathbf{r}_1 d\mathbf{r}_2, \tag{2.13}$$

and take $T[\rho]$ from the theory of the non-interacting uniform electron gas, ie.

$$T[\rho] = C_{\rm F}\int d\mathbf{r}\rho^{\frac{5}{3}}(\mathbf{r})\;;\; C_{\rm F} = \frac{3}{10}\left(3\pi^2\right)^{\frac{2}{3}}. \tag{2.14}$$

This gives the Thomas-Fermi model [22, 107]. This however has serious problems, not least that it does not lead to chemical bonds.

Another approach was followed by Kohn and Sham [46] who suggested introducing orbitals to facilitate the accurate calculation of the kinetic energy, leaving a small residual correction. Their approach was to introduce a non-interacting reference system with the Hamiltonian,

$$\hat{\mathcal{H}}_s = \sum_i^N \left(-\frac{1}{2}\nabla_i^2\right) + \sum_i^N v_s(\mathbf{r}), \tag{2.15}$$

and for which the ground state electron density is exactly ρ. This system has an exact determinantal ground state wavefunction,

$$\Psi_s = \frac{1}{\sqrt{N!}} \det\left[\psi_1, \psi_2, \ldots, \psi_N\right], \tag{2.16}$$

where ψ_i are the N lowest eigenstates of the one electron hamiltonian $\hat{h}_s$,

$$\hat{h}_s \psi_i = \left[-\frac{1}{2}\nabla^2 + v_s(\mathbf{r})\right] \psi_i = \varepsilon_i \psi_i. \tag{2.17}$$

The kinetic energy is then given by,

$$\begin{aligned} T_s[\rho] &= \left\langle \Psi_s \left| \sum_i -\frac{1}{2}\nabla_i^2 \right| \Psi_s \right\rangle \\ &= \sum_{i=1}^{N} \left\langle \psi_i \left| -\frac{1}{2}\nabla^2 \right| \psi_i \right\rangle. \end{aligned} \tag{2.18}$$

However this is unnecessarily restrictive and it requires that the density is non-interacting v-representable, where we define the density to be v-representable if it is the density associated with the antisymmetric ground state wave function of the Hamiltonian of the form,

$$\hat{\mathcal{H}} = \sum_{i=1}^{N} \left(-\frac{1}{2}\nabla_i^2\right) + \sum_{i=1}^{N} v(r_i) + \sum_{i<j}^{N} \frac{1}{\mathbf{r}_{ij}}, \tag{2.19}$$

with *some* external potential $v(\mathbf{r}_i)$. To avoid this we may define $T_s[\rho]$ as a universal functional analogous to $F[\rho]$, ie.

$$\begin{aligned} T_s[\rho] &= \min_{\Psi_D \to \rho} \left\langle \Psi_D \left| \hat{T} \right| \Psi_D \right\rangle \\ &= \min_{\sum |\psi_i|^2 = \rho} \left[\sum_{i=1}^{N} \int \psi_i^*(\mathbf{x}) \left(-\frac{1}{2}\nabla^2\right) \psi_i(\mathbf{x}) d(\mathbf{x}) \right]. \end{aligned} \tag{2.20}$$

This is applicable for all N-representable densities.

We now need to separate $T_s[\rho]$ out of the kinetic energy functional. For this we rewrite $F[\rho]$ as,

$$F[\rho] = T_s[\rho] + J[\rho] + E_{\mathrm{xc}}[\rho], \tag{2.21}$$

where,

$$E_{\mathrm{xc}} \equiv T[\rho] - T_s[\rho] + V_{\mathrm{ee}}[\rho] - J[\rho]. \tag{2.22}$$

This now defines the quantity E_{xc}, the exchange-correlation energy. It contains the difference between T and T_s and the non-classical part of $V_{\mathrm{ee}}[\rho]$.

The ground state electron density is that which minimises $E[\rho]$ and hence satisfies the Euler equation,

$$\mu = v_{\text{eff}}(\mathbf{r}) + \frac{\delta T_s[\rho]}{\delta \rho}, \tag{2.23}$$

where,

$$\begin{aligned} v_{\text{eff}}(\mathbf{r}) &= V_{\text{ext}}(\mathbf{r}) + \frac{\delta J[\rho]}{\delta \rho(\mathbf{r})} + \frac{\delta E_{\text{xc}}[\rho]}{\delta \rho(\mathbf{r})} \\ &= V_{\text{ext}}(\mathbf{r}) + \int \frac{\rho(\mathbf{r}')}{|\mathbf{r} - \mathbf{r}'|} d\mathbf{r}' + v_{\text{xc}}(\mathbf{r}). \end{aligned} \tag{2.24}$$

In summary then,

$$\begin{aligned} E[\rho] &= T_s[\rho] + J[\rho] + E_{\text{xc}}[\rho] + \int V_{\text{ext}}(\mathbf{r})\rho(\mathbf{r})d\mathbf{r} \\ &= \sum_i^N \sum_s \int \psi_i^*(\mathbf{r}) \left(-\frac{1}{2}\nabla^2\right) \psi_i(\mathbf{r}) d\mathbf{r} + J[\rho] + E_{\text{xc}}[\rho] \\ &+ \int V_{\text{ext}}(\mathbf{r})\rho(\mathbf{r})d\mathbf{r}, \end{aligned} \tag{2.25}$$

with,

$$\rho(\mathbf{r}) = \sum_i^N \sum_s |\psi_i(\mathbf{r}, s)|^2. \tag{2.26}$$

We also require the orbitals to be orthonormal, ie.

$$\int \psi_i^*(\mathbf{x})\psi_j(\mathbf{x})d\mathbf{x} = \delta_{ij}. \tag{2.27}$$

We can satisfy this constraint using the method of Lagrange multipliers. Thus define,

$$\Omega[\{\psi_i\}] = E[\rho] - \sum_i^N \sum_j^N \varepsilon_{ij} \int \psi_i^*(\mathbf{x})\psi_j(\mathbf{x})d\mathbf{x}, \tag{2.28}$$

where ε_{ij} are the Lagrange multipliers. For $E[\rho]$ to be a minimum

$$\delta\Omega[\{\psi_i\}] = 0. \tag{2.29}$$

This leads to,

$$\begin{aligned} \hat{h}_{\text{eff}}\psi_i &= \left[-\frac{1}{2}\nabla^2 + v_{\text{eff}}\right] \psi_i = \sum_j^N \varepsilon_{ij}\psi_j, \\ v_{\text{eff}}(\mathbf{r}) &= V_{\text{ext}}(\mathbf{r}) + \int V_{\text{ext}}(\mathbf{r})\rho(\mathbf{r})d\mathbf{r} + v_{\text{xc}}(\mathbf{r}). \end{aligned} \tag{2.30}$$

These are the Kohn-Sham equations.

2.1.2 The Exchange-Correlation Energy

The most common approach to the exchange-correlation energy is to assume that the results from the uniform electron gas theory can be applied locally leading to the local density approximation (LDA).

$$E_{\mathbf{xc}}^{LDA}[\rho] = \int \rho(\mathbf{r})\varepsilon_{\mathbf{xc}}[\rho]d\mathbf{r} \tag{2.31}$$

where $\varepsilon_{\mathbf{xc}}[\rho]$ indicates the exchange-correlation energy per particle of a uniform electron gas of density ρ.

$\varepsilon_{\mathbf{xc}}$ may be divided into exchange and correlation components,

$$\varepsilon_{\mathbf{xc}}[\rho] = \varepsilon_{\mathbf{x}}[\rho] + \varepsilon_{\mathbf{c}}[\rho]. \tag{2.32}$$

From the theory of the uniform electron gas

$$\varepsilon_{\mathbf{x}}[\rho] = -C_{\mathbf{x}}\rho^{\frac{1}{3}}(\mathbf{r}); C_{\mathbf{x}} = \frac{3}{4}\left(\frac{3}{\pi}\right)^{\frac{1}{3}}. \tag{2.33}$$

Unfortunately there is no available closed form for the correlation energy for the uniform electron gas. However a commonly used correlation functional is that based on the Green function Monte-Carlo results of Ceperley and Alder [16]. These will be given in the next section as they explicitly depend on spin polarization. Suffice at present to say that the simple LDA approximation uses the spin unpolarized result.

2.1.3 Spin Density Functional Theory

So far the density functional theory discussed is restricted to systems with only scalar external potentials. Should we wish to deal with a more general potential, such as a magnetic field, we need more than just the total density to describe the system. Instead we need the α- and β- electron densities, $\rho^{\alpha}(\mathbf{r})$, and $\rho^{\beta}(\mathbf{r})$. Equivalently we may use the electron spin polarization $\zeta(\mathbf{r}) = (\rho^{\alpha}(\mathbf{r}) - \rho^{\beta}(\mathbf{r}))/\rho(\mathbf{r})$. The theory then becomes a spin density functional theory.

Spin density functional theories actually have more use than simply allowing the description of systems with vector potentials. With the extra information of the spin polarization we can build better functionals for the exchange and correlation energy.

The formalism is entirely analogous. Instead of $F[\rho]$ defined in equation 2.3 we define the universal functional

$$F[\rho^{\alpha}, \rho^{\beta}] = \min_{\Psi \to \rho^{\alpha}, \rho^{\beta}} \left\langle \Psi \left| \hat{T} + \hat{V}_{\mathbf{ee}} \right| \Psi \right\rangle. \tag{2.34}$$

Then we have,

$$E[\rho^\alpha, \rho^\beta] = \int V_{\text{ext}}(\mathbf{r})\rho(\mathbf{r})d\mathbf{r} + F[\rho^\alpha, \rho^\beta]. \tag{2.35}$$

For the Kohn-Sham method we define,

$$T_s[\rho^\alpha, \rho^\beta] = \min_{\phi_{i\sigma}\to\rho^\alpha,\rho^\beta} \sum_{i\sigma} n_{i\sigma} \int d\mathbf{r}\ \phi^*_{i\sigma}(\mathbf{r}) \left(-\frac{1}{2}\nabla^2\right) \phi_{i\sigma}(\mathbf{r}). \tag{2.36}$$

Here the minimisation is over the set $N_{i\sigma}$ and $\phi_{i\sigma}$ with the constraints

$$\sum_i n_{i\sigma} \left|\phi_{i\sigma}(\mathbf{r})\right|^2 = \rho^\sigma(\mathbf{r}). \tag{2.37}$$

(NB. we now only need the spatial part of the spin orbital, $\phi_{i\sigma}(\mathbf{r})$, where, $\psi_i(\mathbf{r}, s) = \phi_{i\sigma}(\mathbf{r})\sigma(s)$) Thus we arrive at,

$$\begin{aligned} F[\rho^\alpha, \rho^\beta] &= \sum_{i\sigma} n_{i\sigma} \int d\mathbf{r}\ \phi^*_{i\sigma}(\mathbf{r}) \left(-\frac{1}{2}\nabla^2\right) \phi_{i\sigma}(\mathbf{r}) + J[\rho] \\ &+ E_{\text{xc}}[\rho^\alpha, \rho^\beta] + \int V_{\text{ext}}(\mathbf{r})\rho(\mathbf{r})d\mathbf{r}. \end{aligned} \tag{2.38}$$

The corresponding Kohn-Sham equations are then found by minimising equation 2.38 with respect to $\phi_{i\sigma}$ assuming fixed $n_{i\sigma}$ and with the appropriate orthonormality constraints. This leads to the Euler equation,

$$\frac{\delta}{\delta\phi_{i\sigma}} \left(E - \sum_{j\sigma'} \varepsilon_{i\sigma'} n_{j\sigma'} \int d\mathbf{r} \phi^*_{j\sigma'}(\mathbf{r}) \left(-\frac{1}{2}\nabla^2\right) \phi_{j\sigma'}(\mathbf{r}) \right) = 0, \tag{2.39}$$

and to the Kohn-Sham equations,

$$\begin{aligned} \hat{h}^\sigma_{\text{eff}}\phi_{i\sigma}(\mathbf{r}) &= \left[-\frac{1}{2}\nabla^2 + v_{\text{eff}}(\mathbf{r})\right] \phi_{i\sigma}(\mathbf{r}) \\ &= \varepsilon_{i\sigma}\phi_{i\sigma}(\mathbf{r}) \quad ;\ i = 1, 2, \ldots, N^\sigma. \end{aligned} \tag{2.40}$$

N^σ = No. electrons of spin $\sigma = \int d\mathbf{r}\rho^\sigma(\mathbf{r})$ with,

$$\begin{aligned} v^\sigma_{\text{eff}}(\mathbf{r}) &= V_{\text{ext}}(\mathbf{r}) + \int \frac{\rho(\mathbf{r}')}{|\mathbf{r} - \mathbf{r}'|} d\mathbf{r}' \\ &+ \frac{\delta E_{\text{xc}}[\rho^\alpha, \rho^\beta]}{\delta\rho^\sigma(\mathbf{r})}. \end{aligned} \tag{2.41}$$

The eigenvalues have the significance that,

$$\frac{\delta E}{\delta n_{i\sigma}} = \int d\mathbf{r}\ \phi^*_{i\sigma}(\mathbf{r})\hat{h}^\sigma_{\text{eff}}\phi_{i\sigma}(\mathbf{r}) = \varepsilon_{i\sigma}. \tag{2.42}$$

Equation 2.38 must now be minimised with respect to $n_{i\sigma}$ subject to the constraint $\sum_{i\sigma} n_{i\sigma} = N$, the total number of electrons. This leads to,

$$\delta(E - \mu N) = \sum_{i\sigma} (\varepsilon_{i\sigma} - \mu)\, \delta n_{i\sigma} \geq 0, \tag{2.43}$$

where μ = chemical potential.

From equation 2.43 an aufbau principle obviously follows, ie. $n_{i\sigma} = 1$ if $\varepsilon_{i\sigma} < \mu$ and $n_{i\sigma} = 0$ if $\varepsilon_{i\sigma} > \mu$.

Once again we are left with the term E_{xc}. This can be split into separate exchange and correlation terms as before, ie.

$$E_{\mathrm{xc}}[\rho^{\alpha}, \rho^{\beta}] = E_{\mathrm{x}}[\rho^{\alpha}, \rho^{\beta}] + E_{\mathrm{c}}[\rho^{\alpha}, \rho^{\beta}]. \tag{2.44}$$

From density matrix theory the exchange part is

$$E_{\mathrm{x}}[\rho^{\alpha}, \rho^{\beta}] = -\frac{1}{2} \int\int \frac{1}{r_{12}} \left(|\rho_1^{\alpha\alpha}(\mathbf{r}_1, \mathbf{r}_2)|^2 + |\rho_1^{\beta\beta}(\mathbf{r}_1, \mathbf{r}_2)|^2 \right) d\mathbf{r}_1 d\mathbf{r}_2, \tag{2.45}$$

with

$$\rho_1^{\sigma\sigma}(\mathbf{r}_1, \mathbf{r}_2) = \sum_i n_{i\sigma} \phi_{i\sigma}(\mathbf{r}_1) \phi_{i\sigma}^*(\mathbf{r}_2). \tag{2.46}$$

Once more we may apply the result for the homogenous electron gas local leading to the local spin density approximation (LSD).

$$E_{\mathrm{x}}[\rho^{\alpha}, \rho^{\beta}] = 2^{\frac{1}{3}} C_{\mathrm{x}} \int \left[(\rho^{\alpha})^{\frac{4}{3}} + \left(\rho^{\beta}\right)^{\frac{4}{3}} \right] d\mathbf{r}. \tag{2.47}$$

This may then be written in terms of ζ and ρ as follows:
$\rho^{\alpha} = \frac{1}{2}(1 + \zeta)\rho$ and $\rho^{\beta} = \frac{1}{2}(1 - \zeta)\rho$ thus,

$$\begin{aligned} E_{\mathrm{x}}^{LSD}[\rho^{\alpha}, \rho^{\beta}] &= \frac{1}{2} C_{\mathrm{x}} \int \rho^{\frac{4}{3}} \left[(1+\zeta)^{\frac{4}{3}} + (1-\zeta)^{\frac{4}{3}} \right] d\mathbf{r} \\ &= \int \rho \varepsilon(\rho, \zeta) d\mathbf{r}, \end{aligned} \tag{2.48}$$

where,

$$\varepsilon_{\mathrm{x}}(\rho, \zeta) = \varepsilon_{\mathrm{x}}^0(\rho, \zeta) + \left[\varepsilon_{\mathrm{x}}^1(\rho) - \varepsilon_{\mathrm{x}}^0(\rho) \right] f(\zeta), \tag{2.49}$$

with the exchange density for the spin compensated ("paramagnetic") homogenous electron gas given by,

$$\varepsilon_{\mathrm{x}}^0(\rho) = \varepsilon_{\mathrm{x}}(\rho, 0) = C_{\mathrm{x}} \rho^{\frac{1}{3}} \tag{2.50}$$

and the spin completely polarized ("ferromagnetic") case by

$$\varepsilon_{\mathrm{x}}^1(\rho) = \varepsilon_{\mathrm{x}}(\rho, 1) = 2^{\frac{1}{3}} C_{\mathrm{x}} \rho^{\frac{1}{3}}, \tag{2.51}$$

Parameter	0	1
γ	-0.1423	-0.0843
β_1	1.0529	1.3981
β_2	0.3334	0.2611
C	0.0020	0.0007
D	-0.0116	-0.0048
A	0.0311	0.01555
B	-0.048	-0.0269

Table 2.1: The parameters for the Perdew and Zunger parameterisation of the correlation energy

and,

$$f(\zeta) = \frac{1}{2}\left(2^{\frac{1}{3}} - 1\right)^{-1}\left[(1+\zeta)^{\frac{4}{3}} + (1-\zeta)^{\frac{4}{3}} - 2\right]. \tag{2.52}$$

This is the form E_x^{LSD} used in this work.

For the correlation energy the Perdew and Zunger [84] parameterization of the Ceperley and Alder [16] results are as follows,

$$E_c^{LSD}[\rho^\alpha, \rho^\beta] = \int \rho\varepsilon_c(\rho,\zeta)d\mathbf{r}, \tag{2.53}$$

$$\varepsilon_c(\rho,\zeta) = \varepsilon_c^0(\rho,\zeta) + \left[\varepsilon_c^1(\rho) - \varepsilon_c^0(\rho)\right] f(\zeta), \tag{2.54}$$

where $f(\zeta)$ is as for the exchange and 1="ferromagnetic", and 0 = "paramagnetic", and $\rho = (\frac{4}{3}\pi r_s^3)^{-1}$.

For $r_s \geq 1$;

$$\varepsilon_c^i = \gamma_i / \left(1 + \beta_1^i\sqrt{r_s} + \beta_2^i r_s\right) \quad ; \; i = 1, 0 \; , \tag{2.55}$$

and for $r_s < 1$;

$$\varepsilon_c^i = A_i \ln r_s + B_i + C_i r_s \ln r_s + D_i r_s \; , \tag{2.56}$$

where the parameters are given in table 2.1.

An important result of using the LSD approximation rather than the LDA is that the former permits spin polarized systems while the latter forces the system to be spin paired. The situation is analogous to the relation between unrestricted and restricted Hartree-Fock theory [106]. It must be remembered though that this is due to the nature of the LDA and LSD approximations. The Hohenberg-Kohn theorems tell us that, in principle we can construct functionals purely of the electron density to handle exactly cases where a *scalar* potential $V_{ext}(\mathbf{r})$ leads to spin unpairing.

2.2 *Ab-Initio* Molecular Dynamics

2.2.1 Classical Molecular Dynamics

Classically for a system of particles with kinetic energy $\mathcal{T}$ and potential energy $\mathcal{V}$ we may define a Lagrangian $\mathcal{L}$ as [28]

$$\mathcal{L} = \mathcal{T} - \mathcal{V} \tag{2.57}$$

For a generalised set of coordinates q_i and their time derivatives $\dot{q}_i$ this then is used to define the Lagrangian equations of motion

$$\frac{d}{dt}\left(\frac{\partial \mathcal{L}}{\partial \dot{q}_i}\right) - \left(\frac{\partial \mathcal{L}}{\partial q_i}\right) = 0. \tag{2.58}$$

If we now consider a system of atoms with masses m_j and Cartesian coordinates $\mathbf{r}_j$, equations 2.58 then becomes the familiar Newtonian equations of motion;

$$m_j \ddot{\mathbf{r}}_j = \mathbf{f}_j, \tag{2.59}$$

where,

$$\mathbf{f}_j = \nabla_{\mathbf{r}_j} \mathcal{L} = -\nabla_{\mathbf{r}_j} \mathcal{V}, \tag{2.60}$$

is the force on atom j.

Now the point in introducing a generalised set of coordinates $\{q_i\}$ is that we can, for conservative systems, select these coordinates so that they are independent of each other, eg. normal modes of vibration. Sometimes however it is more convenient to apply an external constraint rather than find the independent set of coordinates. If these constraints are such that we can write them as,

$$f(q_1, q_2, q_3, \ldots, q_n, t) = 0, \tag{2.61}$$

then they are described as *holonomic*. This is important because holonomic constraints are non-dissipative, ie. the constrained system conserves energy, which is *not* the case for non-holonomic constraints.

We now need a computational scheme for solving the equations of motion. If $\mathbf{r}(t)$, $\mathbf{v}(t)$, $\mathbf{a}(t)$ are the particle positions, velocities, and accelerations respectively at time t then expanding $\mathbf{r}(t)$ as a Taylor series we have

$$\begin{aligned} \mathbf{r}(t+\delta t) &= \mathbf{r}(t) + \delta t\, \mathbf{v}(t) + \frac{1}{2}\delta t^2 \mathbf{a}(t) + \ldots \\ \mathbf{r}(t-\delta t) &= \mathbf{r}(t) - \delta t\, \mathbf{v}(t) + \frac{1}{2}\delta t^2 \mathbf{a}(t) + \ldots \end{aligned} \tag{2.62}$$

Eliminating $\mathbf{v}(t)$ gives,

$$\mathbf{r}(t+\delta t) = 2\mathbf{r}(t) - \mathbf{r}(t-\delta t) + \delta t^2 \mathbf{a}(t). \tag{2.63}$$

This is the well known Verlet equation [1]. The velocities if required are given by,

$$\mathbf{v}(t) = \frac{\mathbf{r}(t+\delta t) - \mathbf{r}(t-\delta t)}{2\delta t}. \tag{2.64}$$

A variant of this is the leap-frog algorithm,

$$\begin{aligned} \mathbf{r}(t+\delta t) &= \mathbf{r}(t) + \delta t\ \mathbf{v}(t+\frac{1}{2}\delta t), \\ \mathbf{v}(t+\frac{1}{2}\delta t) &= \mathbf{v}(t-\frac{1}{2}\delta t) + \delta t\ \mathbf{a}(t). \end{aligned} \tag{2.65}$$

In all these $\mathbf{a}(t)$ is given by

$$\mathbf{a}(t) = \frac{\dot{\mathbf{p}}_i}{m_i} = -\frac{1}{m_i}\nabla_{\mathbf{r}_i}\mathcal{V}(t) = \frac{\mathbf{f}_i(t)}{m_i}. \tag{2.66}$$

Thus a knowledge of $\mathcal{V}(t)$ yields a full knowledge of the dynamics of the system. In classical MD $\mathcal{V}$ is usually assumed to be derivable from the sum of pairwise interactions of atoms. Sometimes three body interactions have to be considered but essentially the method is to reduce the problem to a sum of N-body (where N is small and usually 2) interactions which can be calculated separately and put in analytical form or tabulated.

This method works very well for many systems. However it suffers the great disadvantage that these N-body potentials are not transferable between systems with different chemical environments. They also break down in any calculation where the bonding pattern shifts significantly. In general wherever valence electrons are itinerant the method of pair or many body potentials breaks down.

2.2.2 Car-Parrinello Method

From the previous section it is clear that the problem of itinerant electrons and non-transferability would be solved in a simulation scheme where the adiabatic electronic ground state for each ionic configuration is found and from this the internuclear forces calculated "on the fly". Note that here and throughout we restrict ourselves to the adiabatic ground state, thus any systems involving electronic transitions are explicitly excluded. We can now envisage the following scheme:

1. Start with atomic coordinates and velocities.
2. Solve the electronic problem, to obtain adiabatic ground state.
3. Use the electronic structure and the Hellman-Feynman theorem to calculate forces on atoms.

4. Carry out classical MD step.

5. Take new coordinates and return to step 2.

However it is found that this scheme requires a prohibitively accurate calculation in step 2 for the forces in step 3 to be sufficiently accurate for energy conserving dynamics. To proceed then Car and Parrinello [13, 92] introduced the following scheme.

Central to the CP method is the definition of an extended Lagrangian,

$$\mathcal{L} = (T_{\text{FKE}} + T_{\text{IKE}}) - E[\{\psi_{i\sigma}\}\mathbf{R}_I] + C, \tag{2.67}$$

where,

$$\begin{aligned} T_{\text{FKE}} &= \sum_{\sigma}\sum_{i}^{\text{occ}} \int d\mathbf{r}\, \frac{\mu_i}{2} \left|\dot{\psi}_{i\sigma}(\mathbf{r})\right|^2, \\ T_{\text{IKE}} &= \frac{1}{2}\sum_I M_I \dot{\mathbf{R}}_I^2, \\ E[\{\psi_{i\sigma}\}, \mathbf{R}_I] &= E_{\text{ion}} + E_{\text{elec}}, \\ C &= \text{orthonormality constraints}, \\ &= \sum_{ij}\sum_{\sigma} \lambda_{ij} \left(\int d\mathbf{r}\, \psi^*_{i\sigma}(\mathbf{r})\psi_{j\sigma}(\mathbf{r}) - \delta_{ij} \right). \end{aligned} \tag{2.68}$$

$\mathbf{R}_I$ are the ionic coordinates and $\{\psi_{i\sigma}(\mathbf{r})\}$ the ground state orbitals corresponding to this configuration, although here they enter as parameters for the potential energy surface $E[\{\psi_{i\sigma}(\mathbf{r})\}, \mathbf{R}_I]$. The term T_{FKE} is the kinetic energy of the parameters $\{\psi_{i\sigma}\}$ required for them to keep up with the ionic system. Equation 2.67 thus defines a coupled electronic and ionic system. μ_i are the arbitrary "mass" parameters for the electronic system, which are usually given the same value, μ, while M_I are the physical masses of the ions. The equations of motion associated with this Lagrangian are,

$$\mu\ddot{\psi}_{i\sigma}(\mathbf{r},t) = -\frac{\delta E}{\delta \psi^*_{i\sigma}(\mathbf{r},t)} + \sum \lambda^{\sigma^*}_{ij}\psi_{j\sigma}(\mathbf{r},t), \tag{2.69}$$

$$M_I\ddot{\mathbf{R}}_I = -\frac{\partial E}{\partial \mathbf{R}_I(t)}. \tag{2.70}$$

Analytically the Lagrange multipliers λ^{σ}_{ij} are given by,

$$\lambda^{\sigma}_{ij} = H^{\sigma}_{ij} - \mu \int d\mathbf{r}\dot{\psi}^*_{j\sigma}(\mathbf{r},t)\dot{\psi}_{i\sigma}(\mathbf{r},t), \tag{2.71}$$

where $H^{\sigma}_{ij} = \int d\mathbf{r}\psi^*_{j\sigma}H^{\sigma}\psi_{i\sigma}(\mathbf{r},t)$.

Numerically equations 2.69 and 2.70 may be integrated by the leap-frog or Verlet algorithms. In practice we use the former for the ionic motion and the latter for the electronic degrees of freedom ie

$$\begin{aligned}
\psi_{i\sigma}(\mathbf{r}, t+\delta t) &= -\psi_{i\sigma}(\mathbf{r}, t-\delta t) + 2\psi_{i\sigma}(\mathbf{r}, t) \\
&+ \frac{(\delta t)^2}{\mu}\left(-\frac{\delta E}{\delta \psi^*_{i\sigma}(\mathbf{r}, t)} + \sum_j \lambda^{\sigma^*}_{ij}\psi_{j\sigma}(\mathbf{r}, t)\right), \qquad (2.72)\\
\mathbf{R}_I(t+\delta t) &= \mathbf{R}_I(t) + \delta t\ \mathbf{v}_I(t+\frac{1}{2}\delta t), \qquad (2.73)\\
\mathbf{v}_I(t+\frac{1}{2}\delta t) &= \mathbf{v}_I(t-\frac{1}{2}\delta t) + \frac{\delta t}{M_I}\frac{\partial E}{\partial \mathbf{R}_I(t)}. \qquad (2.74)
\end{aligned}$$

In principle equation 2.71 could be used to determine the Lagrange multipliers λ^{σ}_{ij}. However in practice numerical errors in the constraints rapidly increase causing spurious forces and a breakdown of energy conservation. The following iterative scheme is thus used to avoid this.

The details are given in appendix A, but note we need to satisfy

$$\langle \psi_{i\sigma}(t+\delta t) | \psi_{j\sigma}(t+\delta t)\rangle = \delta_{ij} \qquad (2.75)$$

Substituting for $\psi_{i\sigma}(t+\delta t)$ from equation 2.72, and dropping the spin index, σ, for clarity, we can derive the relation,

$$\begin{aligned}
\lambda^{(n+1)}_{ij} &= -\frac{1}{D}\left(D_{ij} - \delta_{ij}\right) \\
&- \sum_l \lambda^{(n)^*}_{jl}\left[2\Delta S_{il} - \Delta R1_{il} - DL_{il}\right] \\
&- \sum_k \lambda^{(n)}_{ik}\left[2\Delta S_{kj} - \Delta R2_{kj} - DH_{kj}\right] \\
&- D\left(\sum_k\sum_l \lambda^{(n)}_{ik}\lambda^{*(n)}_{jl}S_{kl}\right) - \lambda^{(n)^*}_{ji}, \qquad (2.76)
\end{aligned}$$

where,

$$\begin{aligned}
\mathbf{F}_i &= \frac{\delta E}{\delta \psi^*_i(\mathbf{r}, t)},\\
D &= \frac{(\delta t)^2}{\mu},\\
H_{ij} &= \langle \psi_i(t) | \mathbf{F}_j \rangle,\\
HO_{ij} &= \langle \psi_i(t-\delta t) | \mathbf{F}_j \rangle,\\
L_{ij} &= \langle \mathbf{F}_i | \psi_j(t) \rangle,\\
LO_{ij} &= \langle \mathbf{F}_i | \psi_j(t-\delta t) \rangle,\\
R1_{ij} &= \langle \psi_i(t-\delta t) | \psi_j(t) \rangle,
\end{aligned}$$

$$
\begin{aligned}
R2_{ij} &= \langle \psi_i(t) | \psi_j(t-\delta t) \rangle \,, \\
G_{ij} &= \langle \mathbf{F}_i | \mathbf{F}_j \rangle \,, \\
S_{ij} &= \langle \psi_i(t) | \psi_j(t) \rangle \,, \\
SO_{ij} &= \langle \psi_i(t-\delta t) | \psi_j(t-\delta t) \rangle \,, \\
D_{ij} &= 4S_{ij} - 2R2_{ij} - 2DH_{ij}, \\
&- 2R1_{ij} + SO_{ij} + DHO_{ij}, \\
&- 2DL_{ij} + DLO_{ij} + D^2 G_{ij}, \\
\Delta S_{ij} &= S_{ij} - \delta_{ij}, \\
\Delta RN_{ij} &= RN_{ij} - \delta ij.
\end{aligned} \tag{2.77}
$$

Thus starting from an initial guess,

$$
\lambda_{ij}^{(0)} = H_{ij} - DG_{ij}, \tag{2.78}
$$

we iterate equation 2.76 for each spin until the constraints are satisfied to a given tolerance, thus ensuring that errors in the constraints do not build up.

So we now have a numerical scheme for solving the equation of motion defined by the Lagrangian defined by equation 2.67; where does this get us? Firstly if the ion coordinates are fixed this defines a dynamical optimisation scheme for obtaining the ground state electronic system corresponding to that configuration. However, as we shall see, conjugate gradient methods afford a better route. The trick with equation 2.67 is that with suitable choice of μ, and provided the frequencies of the ionic motion are not resonant with the electronic degrees of freedom, although coupled, the ionic and electronic degrees of freedom do not equilibrate. Thus the electronic degrees of freedom can be maintained at a far lower temperature than the ionic, with T_{FKE} oscillating around the value required for the electronic system to remain on the adiabatic ground state whilst the ions pursue essentially energy conserving dynamics. Indeed it has been argued that it is this oscillation that causes the stability of the CP method [92, 75, 74]. In the naive scheme outlined earlier the electronic motion *always* lags behind the ionic, causing a spurious drag, while with the second order term in the CP approach the electronic degrees of freedom when lagging the ions are accelerated and overshoot the ions. Thus overall errors cancel. It should be pointed out ,though, that Car and Parrinello criticise the details of this argument [14]. It would be fair to say the CP method still lacks a rigorous theoretical framework though Pastore, Smargiassi,and Buda [73] have made an attempt to redress this.

2.3 Minimisation of the Energy Functional - The Conjugate Gradient Method

As already stated the Car-Parrinello method can also be used to obtain the orbitals corresponding to the ground state density associated with a given energy functional via a simulated annealing approach. This turns out to be relatively inefficient and the method we use is based on the conjugate gradient (CG) approach of Štich *et al.* [104].

The CG method [85] is based on expanding the functional $f(X)$ to be minimised about some point P up to the quadratic term ie

$$f(X) \simeq c - \langle b|X\rangle + \frac{1}{2}\langle X|A \mid X\rangle \tag{2.79}$$

where,

$$X \equiv (x_1, x_2, \ldots, x_L) \; ; \; c \equiv f(P) \; ; \; b \equiv -\nabla f|_P \; ; \; A_{ij} \equiv \left.\frac{\partial^2 f}{\partial x_i \partial x_j}\right|_P , \tag{2.80}$$

with **A** a symmetric positive definite Hessian matrix.

We can then define an iterative scheme

$$p^{(n+1)} = p^{(n)} + \lambda^{(n)} h^{(n)} \quad ; \quad n = 0, 1, 2, \ldots , \tag{2.81}$$

with $\lambda^{(n)}$ a scalar and $h^{(n)}$ a vector in multidimensional space. For steepest descent,

$$h^{(n)} = -\nabla f\left(P^{(n)}\right), \tag{2.82}$$

and λ is either fixed or chosen to minimise f along the direction defined by $h^{(n)}$. This however proves to be inefficient as the orthogonality, or near orthogonality, of consecutive steps often causes very slow convergence near the minima. This would improve if we incorporate the information contained in **A**. To do this explicitly is prohibitively expensive, but using the form of equation 2.80, the conjugate gradient method is exact for a functional of quadratic form. Again equation 2.81 is used with $\lambda^{(n)}$ obtained by a 1-D line minimisation along $h^{(n)}$ where now $h^{(n)}$ is defined by,

$$h^{(n)} = \begin{cases} g^{(n)} & , \quad n = 0; \\ g^{(n)} + \gamma^{(n-1)} h^{(n-1)} & , \quad n = 1, 2, \ldots , \end{cases} \tag{2.83}$$

where,

$$g^{(n)} = -\nabla f(P^{(n)}), \tag{2.84}$$

$$\gamma^{(n)} = \frac{\left\langle g^{(n+1)} \middle| g^{(n+1)} \right\rangle}{\left\langle g^{(n)} \middle| g^{(n)} \right\rangle}. \tag{2.85}$$

$h^{(n)}$ can be shown to satisfy the conjugacy condition,

$$\left\langle h^{(n)} \mid A \mid h^{(m)} \right\rangle = 0 \quad \forall\, n \neq m. \tag{2.86}$$

To implement the CG method to minimise the energy functional E with respect to a set of orthonormal orbitals $\{\phi_{i\sigma}\}$ we now need the gradient of this functional with respect to the these orbitals subject to the orthonormality constraint. Note then from the CP equation of motion that the rhs of

$$\begin{aligned} \mu\ddot{\phi}_{i\sigma} &= -\frac{\delta E}{\delta \phi^*_{i\sigma}} - \frac{\delta C}{\delta \phi^*_{i\sigma}} \\ &= H^\sigma \phi_{i\sigma} - \sum_j \lambda^\sigma_{ji} \phi_{j\sigma}, \end{aligned} \tag{2.87}$$

is the force, or gradient directed downhill in the functional E along surface in which the orthogonality is constrained. Further at the solution

$$\ddot{\phi}_{i\sigma} = 0, \tag{2.88}$$

and the $\{\phi_{i\sigma}\}$ are orthogonal, thus

$$\lambda^\sigma_{ij} = \langle \phi_{i\sigma} \mid H^\sigma \mid \phi_{j\sigma} \rangle\,. \tag{2.89}$$

Therefore the gradient term required is,

$$-\frac{\delta(E+C)}{\delta \phi^*_{i\sigma}} = -H^\sigma \phi_{i\sigma} + \sum_j \langle \phi_{j\sigma} \mid H^\sigma \mid \phi_{i\sigma} \rangle\, \phi_{j\sigma}. \tag{2.90}$$

Given the wavefunctions $\{\phi^{(n)}_{i\sigma}\}$ at the n^{th} step of some iteration procedure we wish to use this gradient to generate new orbitals $\{\phi^{(n+1)}_{i\sigma}\}$ which are close to the minimum and orthogonal,

$$\phi^{(n+1)}_{i\sigma} = \phi^{(n)}_{i\sigma} + \xi^{(n)}_{i\sigma} h^{(n)}_{i\sigma}, \tag{2.91}$$

with

$$h^{(n)}_{i\sigma} = G^{(n)}_{i\sigma} + \gamma^{(n-1)} h^{(n-1)}_{i\sigma}, \tag{2.92}$$

$$G^{(n)}_{i\sigma} = -H^{(n)}_{i\sigma} \phi^{(n)}_{i\sigma} + \sum_j \left\langle \phi^{(n)}_{j\sigma} \mid H^{(n)}_{i\sigma} \mid \phi^{(n)}_{i\sigma} \right\rangle \phi^{(n)}_{j\sigma}, \tag{2.93}$$

$$\gamma^{(n)} = \frac{\sum_{i\sigma} \left\langle G^{(n+1)}_{i\sigma} \mid G^{(n+1)}_{i\sigma} \right\rangle}{\sum_{i\sigma} \left\langle G^{(n)}_{i\sigma} \mid G^{(n)}_{i\sigma} \right\rangle}. \tag{2.94}$$

Note that so far this is standard CG, *except* that we use a separate ξ for *each* orbital. In the true CG method ξ is chosen to minimise E along the

direction $h_{i\sigma}^{(n)}$. Instead we use the condition that the gradient actually at the minimum should be zero, ie. we choose $\xi_{i\sigma}^{(n)}$ to satisfy

$$\left| H_\sigma^{(n)} \phi_{i\sigma}^{(n+1)} - \sum_j \left\langle \phi_{j\sigma}^{(n)} \mid H_\sigma^{(n)} \mid \phi_{i\sigma}^{(n)} \right\rangle \phi_{j\sigma}^{(n+1)} \right| = 0. \tag{2.95}$$

Note here for convenience we use $H_\sigma^{(n)}$, not $H_\sigma^{(n+1)}$ as we should, as this would complicate matters more than necessary as $H_\sigma^{(n+1)}$ depends on $\xi_{i\sigma}^{(n)}$. By contrast Štich *et al.* actually carried out the line minimisation of,

$$\tilde{E}(\xi^{(n)}) = \sum_{ij} \left\langle \phi_{i\sigma}^{(n+1)} \mid H_\sigma^{(n)} \mid \phi_{j\sigma}^{(n+1)} \right\rangle S_{ij}^{(n+1)^{-1}}, \tag{2.96}$$

$$S_{ij}^{(n+1)} = \left\langle \phi_{i\sigma}^{(n+1)} \mid \phi_{j\sigma}^{(n+1)} \right\rangle. \tag{2.97}$$

The rates of convergence of these methods are compared in figure 2.1 for the minimisation of the LSD functional for 64 Na atoms in a liquid like configuration. The two calculations converged to the same minimum as checked directly from the orbitals at convergence. Numerous other tests gave similar results. In this implementation the cpu time per step is significantly lower for our method, due to the avoidance of matrix inversion and trial and error location of the line minimum.

To solve equation 2.95 for $\xi_{i\sigma}^{(n)}$ substitute for $\phi_{i\sigma}^{(n+1)}$ using equation 2.91. If we define

$$A_{i\sigma}^{(n)} = H_{i\sigma}^{(n)} h_{i\sigma}^{(n)} - \sum_j \left\langle \phi_{j\sigma}^{(n)} \mid H_{i\sigma}^{(n)} \mid \phi_{i\sigma}^{(n)} \right\rangle h_{j\sigma}^{(n)}, \tag{2.98}$$

$$B_{i\sigma}^{(n)} = H_{i\sigma}^{(n)} \phi_{i\sigma}^{(n)} - \sum_j \left\langle \phi_{j\sigma}^{(n)} \mid H_{i\sigma}^{(n)} \mid \phi_{i\sigma}^{(n)} \right\rangle \phi_{j\sigma}^{(n)}, \tag{2.99}$$

$$\tag{2.100}$$

this gives,

$$\left| A_{i\sigma}^{(n)} \xi_{i\sigma}^{(n)} + B_{i\sigma}^{(n)} \right| = 0, \tag{2.101}$$

or

$$A_{i\sigma}^{(n)^*} A_{i\sigma}^{(n)} \xi_{i\sigma}^{(n)^2} + \left(A_{i\sigma}^{(n)} B_{i\sigma}^{(n)^*} + A_{i\sigma}^{(n)^*} B_{i\sigma}^{(n)} \right) \xi_{i\sigma}^{(n)} + B_{i\sigma}^{(n)^*} B_{i\sigma}^{(n)} = 0. \tag{2.102}$$

ie. a quadratic in $\xi_{i\sigma}^{(n)}$. We find that it does not matter which root is taken. The roots are only equal though when at the minimum due to the approximation in using $H_\sigma^{(n)}$. The approach is roughly like a Newton approximation as $B_{i\sigma}^{(n)} = -G_{i\sigma}^{(n)}$.

The final scheme is then:

1. Start initial guess $\phi_{i\sigma}^{(0)}$.

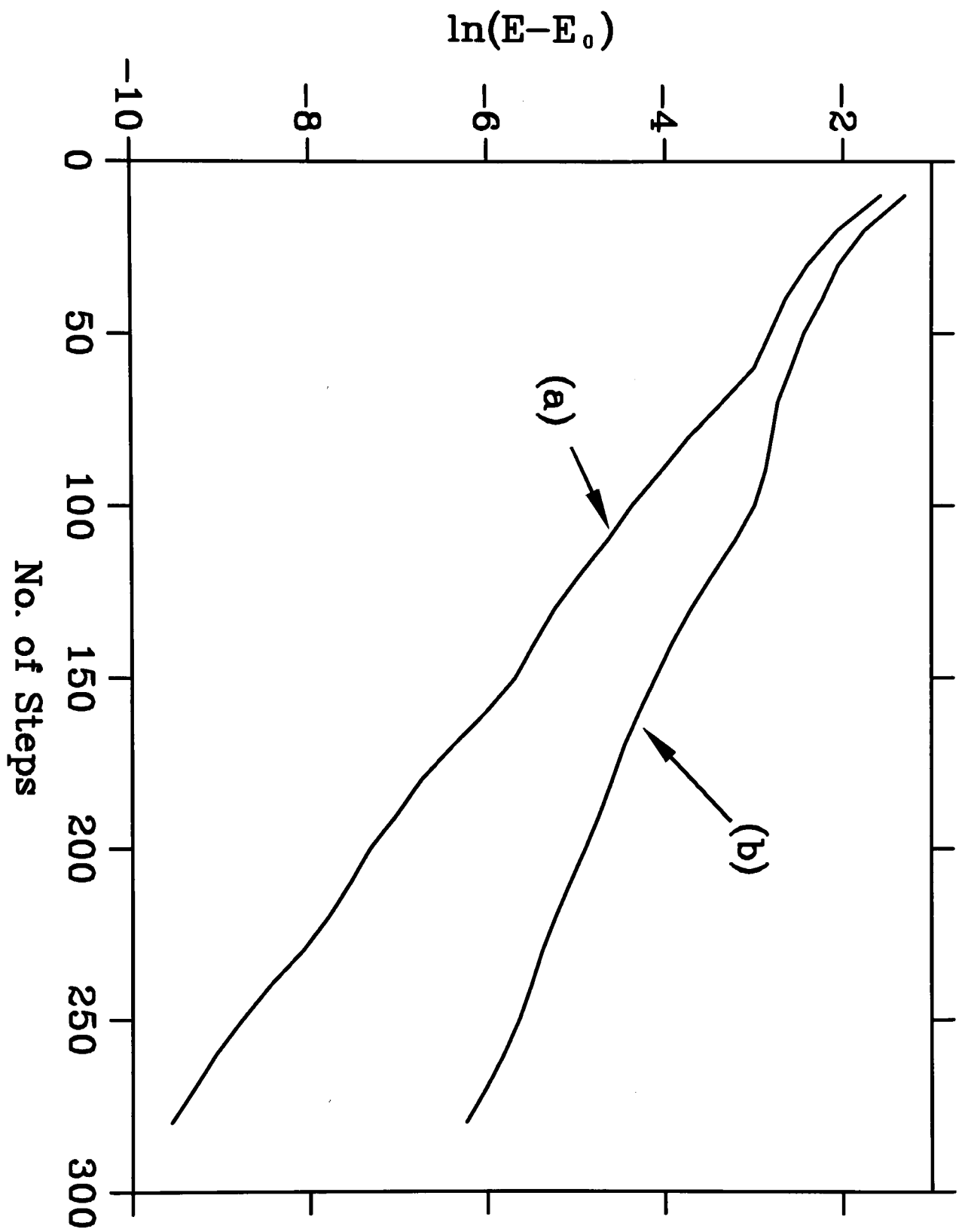


Figure 2.1: Comparison of the Stich *et al.* implementation of the CG method (b) and the variation of the CG method used in this work (a).

2. Set $h_{i\sigma}^{(n)} = 0$ and $h_{i\sigma}^{(1)} = G_{i\sigma}^{(0)}$.

3. Calculate $G_{i\sigma}^{(n)}$ using equation 2.93.

4. Calculate $\gamma_{i\sigma}^{(n+1)}$ using equation 2.94.

5. Calculate $h_{i\sigma}^{(n)}$ using equation 2.92.

6. Calculate $\xi_{i\sigma}^{(n)}$ using equation 2.101.

7. Calculate $\phi_{i\sigma}^{(n+1)}$ using equation 2.91.

8. Call Gram-Schmidt routine to ensure orthonormality.

9. Check tolerance : return to step 3 if not reached.

Note that we still need step 8 as the constraints are only rigidly maintained by the algorithm at the minimum.

Due to its historical origin we still call this a CG method, even though the final result is significantly different, and decline to apologise to nomenclature pedants.

2.4 Implementation

The code used in this thesis was derived from the LDA, CP code developed by Remler. The LSD version of the code was developed by Fois, and the work in developing the SIC code was done in collaboration with Fois, as was the initial development of the Hoover thermostat code used in chapter 6. Details of the implementation in the LDA are given in Remler's thesis [91] and in the review by Remler and Madden [92]. Here I shall outline the essential features.

In a LSD DFT calculation the total energy of the system in a simulation cell Ω is,

$$E = E_{\text{elec}} + E_{\text{II}}, \tag{2.103}$$

where

$$E_{\text{elec}} = E_{\text{eke}} + E_{\text{Hart}} + E_{\text{ext}} + E_{\text{xc}}, \tag{2.104}$$

$$E_{\text{eke}} = -\Omega^{-1} \sum_{i\sigma} \int_{\Omega} d\mathbf{r} \left[\frac{1}{2} \psi_{i\sigma}^{*}(\mathbf{r}) \nabla^2 \psi_{i\sigma}(\mathbf{r}) \right], \tag{2.105}$$

$$E_{\text{Hart}} = \frac{1}{2} \Omega^{-1} \int_{\Omega} d\mathbf{r}_1 \Omega^{-1} \int_{\Omega} d\mathbf{r}_2 \frac{\rho(\mathbf{r}_1)\rho(\mathbf{r}_2)}{|\mathbf{r}_1 - \mathbf{r}_2|}, \tag{2.106}$$

$$E_{\text{ext}} = \Omega^{-1} \int_{\Omega} d\mathbf{r} V_{\text{ext}}(\mathbf{r}) \rho(\mathbf{r}), \tag{2.107}$$

$$E_{\mathrm{xc}} = E_{\mathrm{x}} + E\mathrm{c} = \Omega^{-1} \int_{\Omega} \varepsilon_{\mathrm{xc}}\left(\rho(\mathbf{r}), \zeta(\mathbf{r})\right) \rho(\mathbf{r}) d\mathbf{r}, \tag{2.108}$$

$$E_{\mathrm{II}} = \sum_{I} \sum_{J} \frac{Z_I Z_J}{|\mathbf{R}_I - \mathbf{R}_J|}. \tag{2.109}$$

E_{eke} is the electron kinetic energy, E_{Hart} is the classical coulomb energy, E_{ext} the external and E_{xc} the exchange-correlation energies. E_{II} is the ion coulomb term where I,J label the ions and Z_I, Z_J are the corresponding charges.

2.4.1 The Basis Set

As the program has been developed for condensed matter simulations it has been written with cubic periodic boundary conditions. For such a periodic system the density must also be periodic and so can be written as a Fourier series,

$$\rho(\mathbf{r}) = \sum_{\mathbf{g}} \rho(\mathbf{g}) e^{-i\mathbf{g}\cdot\mathbf{r}}. \tag{2.110}$$

However from Bloch's theorem [3], the one electron wavefunction has to take the form,

$$\psi_{i\sigma}(\mathbf{r}) = e^{-i\mathbf{k}\cdot\mathbf{r}} \sum_{\mathbf{g}} c_{\mathbf{g}}^{i\sigma,\mathbf{k}} e^{-i\mathbf{g}\cdot\mathbf{r}}. \tag{2.111}$$

If we wrote the energy functional purely as a function of ρ this would not matter as,

$$\rho(\mathbf{r}) = \sum_{i\sigma} \psi_{i\sigma}^{*}(\mathbf{r}) \psi_{i\sigma}(\mathbf{r}) = \sum_{i\sigma} \sum_{\mathbf{g}} \sum_{\mathbf{g}'} c_{\mathbf{g}}^{i\sigma,\mathbf{k}} c_{\mathbf{g}'}^{i\sigma,\mathbf{k}} e^{i(\mathbf{g}-\mathbf{g}')\cdot\mathbf{r}}, \tag{2.112}$$

which does not explicitly depend on $\mathbf{k}$. However the term E_{eke} *does* depend on $\psi_{i\sigma}$ in the KS approach.

The effect of $\mathbf{k}$ is to allow longer wavelength in the expansion of $\psi_{i\sigma}(\mathbf{r})$ than the length of the simulation cell. However for systems with localised wavefunctions the terms with $\mathbf{k} = (0,0,0)$, or the Γ point, dominate and we need only consider these terms. As all the calculations in this work are for atomic or molecular/cluster systems which must have localised $\psi_{i\sigma}(\mathbf{r})$ I used only Γ-point calculations, ie. for this work I use a plane wave basis set for $\psi_{i\sigma}(\mathbf{r})$ given by,

$$\psi_{i\sigma}(\mathbf{r}) = \sum_{\mathbf{g}} c_{\mathbf{g}}^{i\sigma} e^{i\mathbf{g}\cdot\mathbf{r}}. \tag{2.113}$$

In principle we need an infinite number of terms but in practice the series may be truncated. The expansion is truncated spherically so that,

$$\frac{1}{2} |\mathbf{g}|^2 \leq E_{\mathrm{max}}. \tag{2.114}$$

Thus for a cell of dimension $L \times L \times L$, with g of the form $(2\pi/L)(i,j,k)$ then $i^2 + j^2 + k^2 \leq g^2_{\max}$ where,

$$\frac{1}{2}\frac{4\pi^2}{L^2} g^2_{\max} = E_{\max}. \tag{2.115}$$

One further point to note is that being the square of the wave function $\rho(\mathbf{r})$ can vary twice as rapidly. Therefore the cutoff for the expansion of the density *should* be twice that for the wavefunction. However if a basis set for $\psi_{i\sigma}(\mathbf{r})$ is used that is more than adequate the same basis set can be used for the density. Although great care is needed this provides considerable cpu and memory savings. This method is known as dualling.

2.4.2 The External Energy $V_{\text{ext}}(\mathbf{r})$

One could consider all electrons in the system and thus $V_{\text{ext}}(\mathbf{r})$ is then just the coulomb potential due to the bare nuclei. However the core electrons are rarely of interest and greatly add to the expense of a calculation both by increasing the number of electrons considered and the basis set size needed due the rapid oscillations of the core wavefunctions. However it is possible to find a pseudopotential that describes the collective effect of the core electrons and the nuclei on the valence electrons [35]. These may be non-local but for some elements (eg. sodium) a local form can be found that is reliable, ie.

$$V_{\text{ext}}(\mathbf{r}) = \sum_I V^{\text{loc}}(|\mathbf{r} - \mathbf{R}_I|), \tag{2.116}$$

where the sum I is over the ions

2.4.3 Coulomb Interaction Terms

For infinite periodic systems we may write,

$$E_{\text{Hart}} = \sum_{\mathbf{g}} \rho(\mathbf{g})\rho(-\mathbf{g})\frac{4\pi}{g^2}, \tag{2.117}$$

where,

$$\rho(\mathbf{g}) = \Omega^{-1} \int_\Omega d\mathbf{r}\ \rho(\mathbf{r}) e^{-i\mathbf{g}\cdot\mathbf{r}}. \tag{2.118}$$

E_{II} may be calculated using an Ewald series expansion for non-neutral systems due to Tosi [114].

$$\begin{aligned} E_{\text{II}} &= \sum_I \sum_J \frac{Z_I Z_J}{|\mathbf{R}_I - \mathbf{R}_J|} \\ &= \frac{1}{2}\sum_I \sum_J Z_I Z_J \sum_{\mathbf{g}} \frac{4\pi}{g^2\Omega} \cos\left[\mathbf{g}\cdot(\mathbf{R}_I - \mathbf{R}_J)\right] \exp\left(\frac{-g^2}{4\eta^2}\right) \end{aligned}$$

$$+ \quad \frac{1}{2}\sum_I \sum_J Z_I Z_J \sum_{\mathbf{L}} \left[\frac{\operatorname{erfc}(\eta x)}{x}\right]_{\mathbf{x}=\mathbf{L}+\mathbf{R}_I+\mathbf{R}_J}$$
$$+ \quad \frac{1}{2}\sum_I \sum_J Z_I Z_J \frac{-\pi}{\eta^2 \Omega} + \frac{1}{2}\sum_I \sum_J Z_I Z_J \sum_{\mathbf{L}} \frac{-2\eta}{\pi^{\frac{1}{2}}}, \tag{2.119}$$

and for a local pseudopotential,

$$\begin{aligned} E_{\text{ext}} &= \sum_{\mathbf{g}} V_{\text{ext}}(\mathbf{g})\rho(-\mathbf{g}) \\ &= \sum_{\mathbf{g}} \rho(-\mathbf{g}) V^{\text{loc}}(\mathbf{g}) S(\mathbf{g}), \end{aligned} \tag{2.120}$$

where,

$$S(\mathbf{g}) = \frac{1}{N}\sum_I e^{-i\mathbf{g}\cdot\mathbf{R}_I}, \tag{2.121}$$

$$\begin{aligned} V^{\text{loc}}(\mathbf{g}) &= \Omega_{\text{at}}^{-1} \int_{\infty} d\mathbf{r} V^{\text{loc}}(\mathbf{r}) e^{-i\mathbf{g}\cdot\mathbf{r}}, \\ &= \frac{4\pi}{\Omega_{\text{at}} g} \int_0^{\infty} dr r \sin(gr) V^{\text{loc}}(\mathbf{r}), \end{aligned} \tag{2.122}$$

and Ω_{at} = volume per atom, N = number of ions in cell.

Note though that all these contain a $\mathbf{g} = (0,0,0)$ term that is infinite. However the $\mathbf{g} = (0,0,0)$ term in E_{ext} should exactly cancel the positive infinite terms in E_{Hart} and E_{II} for overall neutral systems. Thus to eliminate the problem the sums over $\mathbf{g}$ are simply done excluding the $\mathbf{g} = (0,0,0)$ term.

2.4.4 Energy Gradients

Finally we need the terms $\frac{\delta E_{\text{elec}}}{\delta \psi_{i\sigma}^*}$, $\frac{\partial E_{\text{II}}}{\partial \mathbf{R}_I}$, $\frac{\partial E_{\text{ext}}}{\partial \mathbf{R}_I}$ in order to apply the Hellman-Feynman theorem. From the discussion of the KS equation it is clear that

$$\frac{\delta E_{\text{elec}}}{\delta \psi_{i\sigma}^*} = h_{\text{eff}}^{\sigma} \psi_{i\sigma}(\mathbf{r}) = \left[-\frac{1}{2}\nabla^2 + v_{\text{eff}}^{\sigma}(\mathbf{r})\right] \psi_{i\sigma}(\mathbf{r}). \tag{2.123}$$

The terms $\frac{\partial E_{\text{II}}}{\partial \mathbf{R}_I}$, $\frac{\partial E_{\text{ext}}}{\partial \mathbf{R}_I}$ are needed for the force on the ions $\mathbf{F}_I$ ie.

$$\mathbf{F}_I = -\frac{\partial E_{\text{II}}}{\partial \mathbf{R}_I} - \frac{\partial E_{\text{ext}}}{\partial \mathbf{R}_I}. \tag{2.124}$$

The forces due to the ion-ion interactions are,

$$\begin{aligned} -\frac{\partial E_{\text{II}}}{\partial \mathbf{R}_I} &= \frac{1}{2}\sum_{I\neq J} Z_I Z_J \sum_{\mathbf{g}} \frac{4\pi}{g^2 \Omega} \sin\left[\mathbf{g}\cdot(\mathbf{R}_I - \mathbf{R}_J)\right] \exp\left(\frac{-\mathbf{g}^2}{4\eta^2}\right) \mathbf{g} \\ &+ \frac{1}{2}\sum_{J\neq I} Z_I Z_J \sum_{\mathbf{L}}{}' \left[\frac{\mathbf{x}\,\operatorname{erfc}(\eta x)}{x^3}\right]_{\mathbf{x}=\mathbf{L}+\mathbf{R}_I+\mathbf{R}_J}. \end{aligned} \tag{2.125}$$

The forces due to the ion-electron interactions are,

$$-\frac{\partial E_{\text{ext}}}{\partial \mathbf{R_I}} = i\sum_{\mathbf{g}}{}' \mathbf{g}\rho^*(\mathbf{g})V^{\text{loc}}(\mathbf{g})e^{-i\mathbf{g}\cdot\mathbf{R}_I}, \tag{2.126}$$

where the prime indicates that the sum excludes the $\mathbf{g} = (0,0,0)$ term.

Chapter 3

The Self-Interaction Correction

In the last chapter I outlined the use of the LSD approximation. This approximation has been highly successful. However there are a number of areas in which it fails. In this chapter I will briefly outline these areas before discussing the self-interaction correction (SIC) method due to Perdew and Zunger [84], for improving the LSD approximation. The third section will discuss the implementation of this method within the CP and CG schemes described in the previous chapter. The final section will discuss calculations on various simple systems to illustrate the effect of the SIC method.

3.1 Brief Critique of the LSD Approximation

The following is an illustrative and not exhaustive list of problems with LSD calculations [84].

1. The coulomb term contains a spurious self-interaction term. This is most clearly seen in the one-electron case where,

$$U[\rho] = \frac{1}{2}\int d\mathbf{r}_1 \int d\mathbf{r}_2 \frac{\rho(\mathbf{r}_1)\rho(\mathbf{r}_2)}{|\mathbf{r}_1 - \mathbf{r}_2|}, \tag{3.1}$$

   clearly does not vanish. This self term should be exactly cancelled by a self term in the exchange-correlation energy. However this cancellation is only exact in LSD for a homogenous electron gas or when the KS orbitals are completely delocalised.

2. The LSD total energy for metal surfaces is too low compared with the exact value, while that for atoms is too high.

3. The magnitude of the exchange for the atoms is consistently underestimated by as much as 10-15% in LSD while the correlation energy is overestimated by as much as 100-200%.

4. LSD calculations predict that certain negative ions eg. H^-, O^-, F^-, are unstable, contrary to experiment.

5. Self consistent LSD band structure calculations systematically underestimate the one electron energy gaps of insulators by up to 40% . More generally the LSD single electron energy eigenvalues are not close to the physical removal energies for bound states, ie. there is no direct equivalent to Koopmans theorem.

6. At long range the single electron LSD potential for ions of charge q is not the electronically correct $-(q+1)/r$, but $-q/r$. Amongst other things this leads to erroneous descriptions of charged point defect states in solids, ionisation energies, and outer regions of wavefunctions.

7. The spin splitting of energy bands in ferromagnetic metals, eg. Ni, calculated with LSD is often larger than the experimental value.

8. LSD total energies unduly favour the $d^{n-1}s^1$ configuration over the $d^{n-2}s^2$ configuration in the 3d transition atoms.

The above list was cited by Perdew and Zunger [84] in their paper on the self-interaction correction. In this work they show that explicit subtraction of the self-interaction terms either improves or completely removes these deficiencies, eg. their version of the SIC has the correct long range potential. Perdew [80] has further argued that any approximation to the true functionals in DFT should satisfy three principles.

1. *Separability* - if two or more objects are separated by a large distance of empty space the total energy should be the sum of the energies of the individual objects.

2. *Extensivety* - if the bulk unit cell of a solid is free of electric monopole and dipole moments, the total energy is $E = fV + \sigma A$, V and A being the volume and the surface area of the solid respectively. Atoms will then cluster together if there is a unit cell which minimises the bulk energy f; the clusters will tend to have compact, surface minimising shapes if the surface energy σ is positive.

3. *Integer Preference* - for a collection of separated objects there is a preference for an integer number of electrons to be located on each object.

Local density approximations clearly satisfy the first two principles but fail to show integer preference. Further LSD is not exact in the one electron limit, which is that for a single electron separated from all others the total energy should just be the eigenvalue of the one electron Schrödinger equation with potential $V_{\mathbf{ext}}(\mathbf{r})$. A "self-interaction correction" then is a procedure to correct a density functional that is not exact in the one electron limit.

3.2 The Self-Interaction Correction

For one electron the potential energy function for the electron-electron interaction must be zero, ie.

$$V_{\mathbf{ee}}\left[|\phi_{\alpha\sigma}|^2\right] = 0, \tag{3.2}$$

which is not the case in the LSD approximation.

Various attempts have been made to remove this spurious self term. For example Fermi and Amaldi [72] tried to correct the $V_{\mathbf{ee}}$ term in Thomas-Fermi theory using,

$$V_{\mathbf{ee}}^{\mathbf{FA}}[\rho] = \frac{N-1}{2N}\int\int \frac{\rho(\mathbf{r}_1)\rho(\mathbf{r}_2)}{|\mathbf{r}_1-\mathbf{r}_2|}d\mathbf{r}_1 d\mathbf{r}_2. \tag{3.3}$$

However we shall follow the approach due to Perdew and Zunger. They proposed that the self term for each electron should be explicitly subtracted. Thus one can define the energy of the electron system as,

$$E^{\mathrm{SIC}} = E^{\mathrm{LSD}} - \sum_{\alpha\sigma}\epsilon_{\alpha\sigma}, \tag{3.4}$$

where,

$$E^{\mathrm{LSD}} = \sum_{\alpha\sigma}\left\langle \phi_{\alpha\sigma}\left|-\frac{1}{2}\nabla^2\right|\phi_{\alpha\sigma}\right\rangle + U[\rho] + E_{\mathbf{xc}}[\rho_\uparrow,\rho_\downarrow] + \int d\mathbf{r}V_{\mathbf{ext}}(\mathbf{r})\rho(\mathbf{r}), \tag{3.5}$$

just as previously, and

$$\epsilon_{\alpha\sigma} = U[\rho_{\alpha\sigma}] + E_{\mathbf{xc}}[\rho_{\alpha\sigma},0], \tag{3.6}$$

$$\rho_{\alpha\sigma}(\mathbf{r}) = |\phi_{\alpha\sigma}(\mathbf{r})|^2. \tag{3.7}$$

We can then proceed as previously to define the Kohn-Sham equations,

$$\hat{h}_{\alpha\sigma}^{\mathrm{SIC}}\phi_{\alpha\sigma}(\mathbf{r}) = \lambda_{\alpha\sigma}^{\mathrm{SIC}}\phi_{\alpha\sigma}(\mathbf{r}), \tag{3.8}$$

where,

$$\hat{h}_{\alpha\sigma}^{\mathrm{SIC}} = \frac{\delta E^{\mathrm{SIC}}}{\delta\phi_{\alpha\sigma}^*}$$

$$
\begin{aligned}
&= -\frac{1}{2}\nabla^2 + V_{\text{ext}}(\mathbf{r}) + \int \frac{\rho(\mathbf{r}')}{|\mathbf{r}-\mathbf{r}'|} d\mathbf{r}' \\
&+ v_{\text{xc}}(\mathbf{r}) - V_{\alpha\sigma}^{\text{SIC}}(\mathbf{r}) \\
&= \hat{h}_{\sigma}^{\text{LSD}} - V_{\alpha\sigma}^{\text{SIC}}(\mathbf{r}), \qquad (3.9)
\end{aligned}
$$

$$
V_{\alpha\sigma}^{\text{SIC}}(\mathbf{r}) = \int \frac{\rho_{\alpha\sigma}(\mathbf{r}')}{|\mathbf{r}-\mathbf{r}'|} d\mathbf{r}' + v_{\text{xc}}[\rho_{\alpha\sigma}, 0]. \qquad (3.10)
$$

There is an important difference between the LSD and the SIC Hamiltonian in that the latter is orbitally dependent. As a result the energy functional in equation 3.4 is *not* independent of the orbitals as is the case for LSD, ie. a unitary transformation of the orbitals in SIC *does* alter the energy. Furthermore the orbitals are not orthogonal, and as a result the Lagrange multiplier matrix is not diagonal. The eigenvalues though are still taken to be the diagonal elements of this matrix. As argued by Pederson [77, 76], we must apply the additional constraint that the orbitals must maximise the self-interaction. Inspection of equation 3.4 shows that due to the minus sign this minimises the energy. It is also clear that the SIC orbitals as a result of this will be localised, as the the spurious self terms removed by the SIC are positive.

Pederson's constraint is obtained by considering the unitary transformation $\mathrm{U}_{\alpha\beta}^{\sigma}$ that maximises the self-interaction correction, ie. such that,

$$
\frac{\delta \sum_{\alpha\sigma} \epsilon_{\alpha\sigma}}{\delta \mathrm{U}_{\alpha\beta}^{\sigma}} = 0. \qquad (3.11)
$$

The result is that,

$$
\left\langle \phi_{\alpha\sigma} \left| V_{\alpha\sigma}^{\text{SIC}} - V_{\beta\sigma}^{\text{SIC}} \right| \phi_{\beta\sigma} \right\rangle = 0. \qquad (3.12)
$$

In principle the orbitals resulting from the SIC are not orthogonal, thus we should not apply an orthogonality constraint. However Perdew and Zunger performed a comparison of results both with and without orthogonality constraints and found that there was in practice no significant difference between their results. Further when we attempt to minimise the energy functional the system "bosonises", ie. all the electrons attempt to enter the same lowest energy orbital. Thus within our scheme orthogonality is not just desirable from the point of view of computational simplicity, but is a necessity.

The final scheme then for minimising the SIC energy functional is:

1. Perform the standard conjugate gradient step as defined in chapter 2.
2. Perform a Gram-Schmidt orthogonalisation.
3. Find the unitary transformation $\mathbf{U}$ such that,

$$
\left\langle \sum_k \mathrm{U}_{kj}^{\sigma} \phi_{k\sigma} \left| V_{j\sigma}^{\text{SIC}} - V_{i\sigma}^{\text{SIC}} \right| \sum_l \mathrm{U}_{li}^{\sigma} \phi_{l\sigma} \right\rangle = 0. \qquad (3.13)
$$

To see how to carry out step 3 consider $\{\chi_{\alpha\sigma}\}$ such that,

$$\left\langle \chi_{\alpha\sigma} \left| V_{\alpha\sigma}^{\mathrm{SIC}} - V_{\beta\sigma}^{\mathrm{SIC}} \right| \chi_{\beta\sigma} \right\rangle = 0, \tag{3.14}$$

ie.

$$\chi_{j\sigma} = \sum_k U_{kj}^{\sigma} \phi_{k\sigma}. \tag{3.15}$$

Now writing,

$$U_{ij}^{\sigma} = \delta_{ij}^{\sigma} + \tau_{ij}^{\sigma}, \tag{3.16}$$

and dropping the spin indices for convenience,

$$\begin{aligned} \chi_j &= \sum_k (\delta_{kj} + \tau_{kj})\, \phi_k \\ &= \phi_j + \sum_k \tau_{kj} \phi_k. \end{aligned} \tag{3.17}$$

Substituting in equation 3.14 we have,

$$\left\langle \phi_j + \sum_k \tau_{kj} \phi_k \left| V_j^{\mathrm{SIC}} - V_i^{\mathrm{SIC}} \right| \phi_i + \sum_l \tau_{li} \phi_l \right\rangle = 0. \tag{3.18}$$

Expanding this becomes,

$$\begin{aligned} 0 &= < j|j-i|i > \\ &+ \sum_k \tau_{kj} < k|j-i|i > \\ &+ \sum_l \tau_{li} < j|j-i|l > \\ &+ \sum_l \sum_k \tau_{li}\tau_{kj} < k|j-i|l >, \end{aligned} \tag{3.19}$$

where,

$$< k|j-i|l > \equiv \left\langle \phi_{k\sigma} \left| V_{j\sigma}^{\mathrm{SIC}} - V_{i\sigma}^{\mathrm{SIC}} \right| \phi_{l\sigma} \right\rangle. \tag{3.20}$$

Hence,

$$\begin{aligned} \tau_{ji} &= \tau_{ji}^0 \\ &+ \frac{1}{2} \Bigg\{ \sum_k \tau_{kj} \left(< k|j-i|i > - \delta_{ki} \right) \\ &\quad + \sum_l \tau_{li} \left(< j|j-i|l > - \delta_{lj} \right) \\ &\quad + \sum_l \sum_k \tau_{li}\tau_{kj} < k|j-i|l > \Bigg\}. \end{aligned} \tag{3.21}$$

This uses the fact that $\tau_{ji} = -\tau_{ij}$ and defines,

$$\tau_{ji}^0 = \frac{1}{2} < j|j-i|i >, \tag{3.22}$$

Atom in Simulation	Box Length (a.u.)	No. of Plane Waves	Cutoff (Ryd.)
H	20.0	10189	28.424
Na	36.0	6999	6.823
Cs	36.0	6999	6.823

Table 3.1: Cutoff and Box Length Parameters

as the 0^{th} order solution.

In practice a simplified version of the iterative scheme defined by equation 3.21 is used where the SIC potentials are frozen at their initial values. This is often a sufficiently good approximation as the orbitals immediately after the CG step are close to the localised ones we seek. However in cases where large rotations are required, as can occur at the start of an optimisation run, it may be desirable to apply the procedure several times between each CG step, ie. the SIC potentials are redetermined with the rotated orbitals and the iterative scheme is repeated. In most simulations in this thesis though this was not necessary.

The **U**'s calculated so far do not guarantee unitarity, so the transformed orbitals could deviate from orthonormality. Rather than re-apply the Gram-Schmidt routine to the orbitals it is more convenient to apply this procedure to the **U**'s themselves and then transform the orbitals,

$$\phi'_{i\sigma} = \sum U^{\sigma}_{ji}\phi_{j\sigma}. \tag{3.23}$$

3.3 LSD vs SIC for Simple Diatomic Systems

In this section I will compare the results of calculations using the CG schemes described previously to calculate the potential energy curves and other properties of the H_2, Na_2, and Cs_2 dimers. In this and subsequent work the parameters in table 3.1 were used.

The degree of convergence of calculations is shown for the H-atom in table 3.2 and for Na_8 in table 3.3. It is clear from these tables that full convergence with respect to the plane wave expansion has not been reached but this is not required [29]. Provided that we only compare data with the same cutoff these values prove quite sufficient for accurate comparison. This is particularly important for the hydrogen atom calculations because these cannot fully converge even in principle due to the inability to properly describe the cusp. It should be pointed out though, that the choice of cutoff is partly historic. The box length has to be chosen so as to ensure that the

maxq	Cutoff (Ryd.)	Ionic Potential Energy (a.u.) LSD	SIC
7	6.2178	-0.42163053	-0.36905991
8	7.8956	-0.43249669	-0.38077456
9	9.7709	-0.44181066	-0.39079931
10	11.4835	-0.44661756	-0.39586951
11	14.1135	-0.45373783	-0.40352925
12	16.5809	-0.45644677	-0.40636629
13	19.2457	-0.46022219	-0.41038361
14	22.1079	-0.46332809	-0.41366327
16	28.4244	-0.46759657	-0.41814641

Table 3.2: Rate of convergence of H-atom calculations with increasing cutoff. Box length = 20a.u.

maxq	Cutoff (Ryd.)	Ionic PE (a.u.) (LSD)
14	6.823	-1.6849992
16	8.773	-1.6850705
17	9.839	-1.6851227
18	10.966	-1.6851522
19	12.154	-1.6851636
20	13.403	-1.6851657
21	14.713	-1.6851661

Table 3.3: Rate of convergence of Na_8 calculations with increasing cutoff. Boxlen = 36.0a.u.

dimers (or later, clusters) in adjacent boxes do not interact. Having chosen this parameter the cutoff was chosen as the largest permitted at the time by the memory of the computer (initially a Convex C1). The cutoff in the sodium calculations had already been tested on solid sodium where it was found to accurately reproduce the phonon spectrum.

For all hydrogen calculations the bare coulomb potential was used ie.

$$V^{\mathrm{loc}}(\mathrm{g}) = -\frac{4\pi}{g^2}. \tag{3.24}$$

For sodium calculations the Topp and Hopfield pseudopotential [111] was used whilst for caesium a "home grown" pseudopotential due to Fois was used. The details of these pseudopotentials are given in appendix B.

3.3.1 H_2

The potential energy curve for the dissociation of the H_2 molecule is a paradigm for the competition between correlation and delocalisation effects. The conventional valence description of the H_2 molecule [64] is that two electrons occupy the σ_g molecular orbital with paired spin,

$$\psi_B(1,2) = A[\sigma_g^{\alpha}(1)\sigma_g^{\beta}(2)], \tag{3.25}$$

ie. the electrons are spin paired throughout space and occupy extended orbitals. As the bond is extended the electron-electron repulsion tends to outweigh the tendency of the electrons to delocalise themselves in extended orbitals. The wavefunction may be regarded as made up of configurations in which they occupy separate regions of space which are spin polarized. In the fully dissociated limit the wavefunction is,

$$\psi_D(1,2) = A[a^{\alpha}(1)b^{\beta}(2)] - A[a^{\beta}(1)b^{\alpha}(2)], \tag{3.26}$$

where a, and b are the individual atomic orbitals. A wavefunction which allows for these correlations effects is,

$$\psi(1,2) = \frac{\psi_B(1,2) + \lambda A[\sigma_u^{\alpha}(1)\sigma_u^{\beta}(2)]}{(1+\lambda^2)^{\frac{1}{2}}}, \tag{3.27}$$

where σ_u is the anti-bonding molecular orbital, and λ is a variational parameter which goes from zero at the equilibrium separation to -1 in the atomic limit. λ is thus a measure of the correlation driven local spin unpairing in the configurations which make up the ground state wavefunction. It is known to make a rather sharp transition between the two limits [64]

In figure 3.1 is shown a comparison of the potential energy curves for H_2 using LSD and SIC and the "exact" calculation due to Kolos and Wolniewicz

Method	Binding Energy/Atom (a.u.)	Bond Length (a.u.)
Expt. [103]	0.08309	1.40
LSD	0.08533	1.54
SIC	0.08602	1.45

Table 3.4: Comparison of the H_2 binding energies and bond lengths from LSD and SIC Calculations with Experiment.

[45]. The LSD and SIC potentials were calculated at a series of points using the CG method and the curve fitted via a spline fit using UNIRAS 6.2. The minima were found by a series of calculations that bracketed the minima into smaller and smaller region until the separation at the minima was determined to two decimal places. This method was used because it was decided that dynamics on the H_2 system might prove unreliable due to too few grid points in real space, causing insufficient accuracy in the forces to locate the minima reliably. Note that with maxq=16 we have 2maxq + 1 + ipad = 36 points along each edge of the simulation cell, ie. grid points are separated by more than 0.5 a.u. This is large compared to rate of variation of the H_2 potential energy. Thus although dynamics could be performed it was decided that it would not provide sufficient reliability for this system.

Table 3.4 compares the binding energies and bond lengths. Both methods overestimate the binding energies; SIC is in fact worse than LSD. However the SIC bond length is in far better agreement with experiment than the LSD bond length.

Comparing the shapes of the P.E. curves, although the depth of the LSD curve is quite accurate, apart from the repulsive wall and near dissociation it is a poor match for the exact curve. The SIC curve by comparison is a far better match particularly near the minimum. However it too is not a perfect match as it rises too quickly to the dissociation limit. As we will see later this is the spin pairing/unpairing region. However it should be noted that compared to some unrestricted Hartree-Fock and CI calculations given by Szabo and Ostlund [106] both the LSD and SIC curves are quite accurate descriptions of the true P.E. curve.

The degree of spin unpairing as a function of the internuclear separation can be examined by calculating the "local moment" given by [105]

$$L = \int d\mathbf{r} \left(\frac{3}{4}\right) [n_\alpha(\mathbf{r}) + n_\beta(\mathbf{r}) - 2n_\alpha(\mathbf{r})n_\beta(\mathbf{r})] \tag{3.28}$$

where $n_\sigma(\mathbf{r}) = \rho_\sigma(\mathbf{r})/\rho(\mathbf{r})$

L varies between values of $\frac{3}{8}$ for a perfectly spin paired state and $\frac{3}{4}$ for a state which is perfectly spin unpaired. Figure 3.2 shows a comparison of L

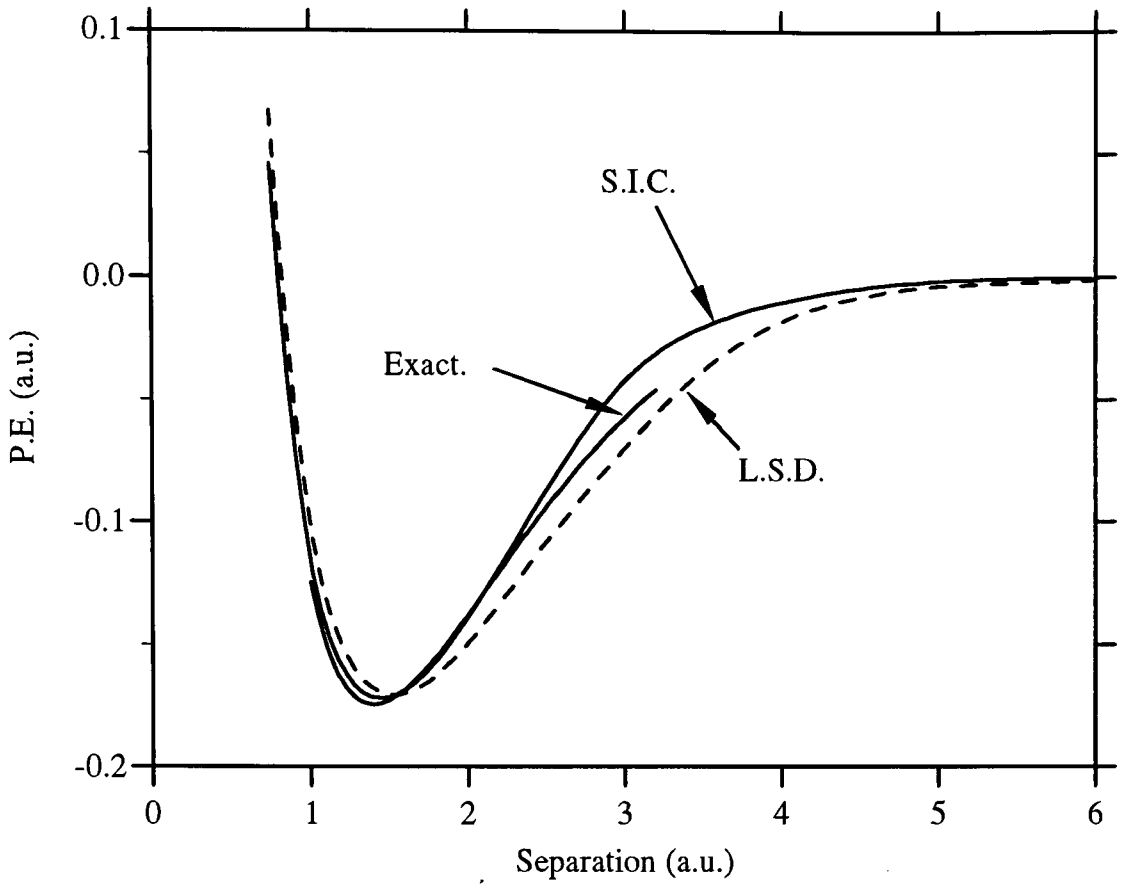


Figure 3.1: The potential energy curves for H_2 using LSD and SIC. The "exact" potential energy curve due to Kolos and Wolniewicz [45] is also shown.

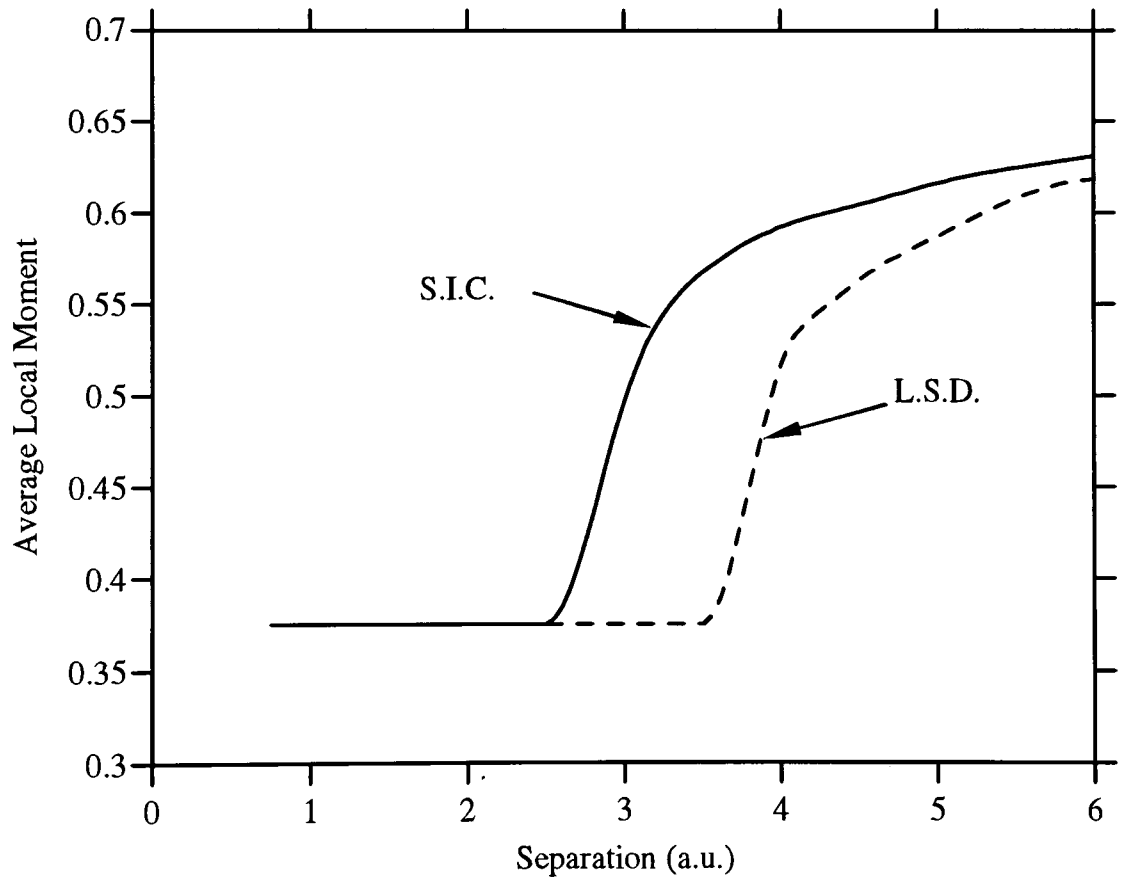


Figure 3.2: The local moment curves for H_2 using LSD and SIC.

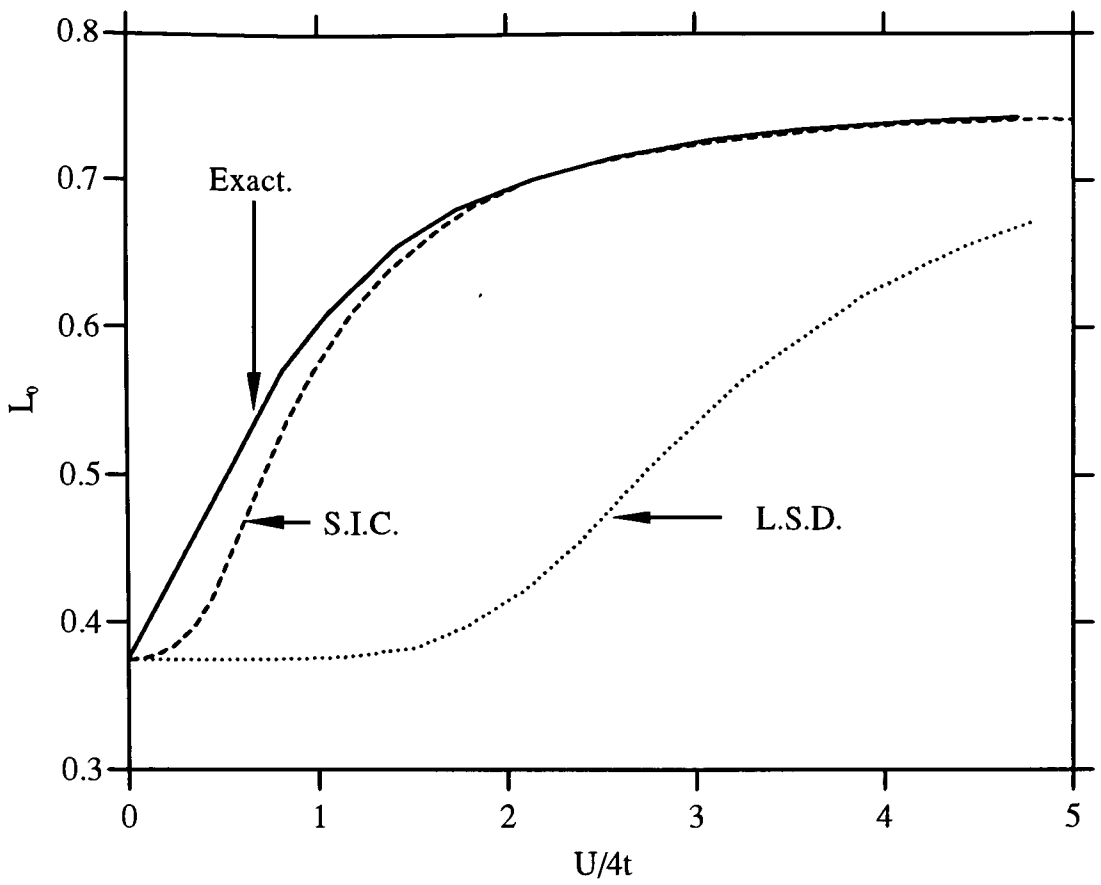


Figure 3.3: The local moment (L_0) as a function of $U/4t$ for a one dimensional Hubbard model, where U is the on-site Coulomb interaction, and t is the hopping integral. These results are from reference [105].

for LSD and SIC. Note that although the lower limit is indeed $\frac{3}{8}$, the upper is not $\frac{3}{4}$. This merely reflects the fact that although at large separations we have a spin up electron localised on one atom and a spin down on the other, there must be some point at which the two localised orbitals touch and that although the density is essentially zero, at that point the system is calculated as spin paired, giving $L = \frac{3}{8}$ for that point. The important point is that the SIC calculation becomes spin unpaired more readily than the LSD, ie. correlation effects are more pronounced in the SIC calculation. In fact we should anticipate this result as in SIC we are maximising the magnitude of the electron-electron self-interaction term, thus favouring localised over delocalised orbitals. Clearly then we would expect the system to change to the localised atomic ones from the delocalised molecular orbitals more readily and rapidly in SIC calculations than in LSD. This is what is shown in figure 3.2. In other words SIC facilitates the localisation of electrons under the influence of the electron-electron interaction.

It is worth noting that Svane and Gunarsson [105] have found similar behaviour for extended systems. Figure 3.3 is reproduced from their paper on localisation in the SIC DFT formalism. As a model system they used the 1-D Hubbard model for which there is an exact solution. Clearly the SIC calculation agrees well with the exact calculation throughout the parameter

range while the LSD calculation is in poor agreement.

3.3.2 Na_2

The binding in Na_2 is determined by the same factors as H_2, as the core electrons take no part in bonding, as we implicitly accept when we use a pseudopotential to allow us to concentrate on the valence electrons. Thus effectively the only difference between the two systems is the nature of the "external" potential and the mass of the nuclei, the latter not affecting bonding.

Figure 3.4 shows a comparison of LSD, SIC, and LDA P.E. curves with the experimental one due to Verma *et al* [116]. Table 3.5 compares LSD, SIC and LDA binding energies and bond lengths. The P.E. curves were generated in the same way as the H_2 P.E. curves. The minima however were determined both by the same method as for H_2 and by a steepest descent procedure within the CP method, where the ion velocities in the leap-frog algorithm were set to zero and a "mass" of $40m_e$ (m_e = mass of electron, which is 1a.u. of mass) and a "time step" of 6.4 a.u. were used to give the largest possible steps that allowed the wavefunctions to stay on the Born-Oppenheimer surface. A fake mass, μ, of 400 a.u. was used. The two methods gave exact agreement for the bond length, and essentially identical potential energies.

The first point to note from figure 3.4 and table 3.5 is that the LDA and LSD calculations are in exact agreement at short distances. This is simply because for spin paired systems the LSD approximation reduces to the LDA. However the LDA is totally inadequate at the dissociation limit. This is because it allows for dissociation into Na^+ and Na^- and 2Na with equal probability, as it forces the system to remain spin paired. As mentioned in chapter 2, the LDA is analogous to the HF approximation whilst LSD is analogous to the unrestricted HF approximation.

There is little to choose between the shape of the LSD curve and the SIC as compared to the experimental one and again the SIC gives a worse binding energy; this time under estimating it by about twice the error in the LSD calculation. Note, this disagrees with the point made by others (eg. [84, 20]) that LSD calculations systematically overestimate binding energies. The SIC bond length is again shorter than the LSD and is closer to the experimental value. It should be pointed out that the pseudopotential is also an important factor in determining these parameters. Work by Moullet *et al.* [69] also using LSD gives bond lengths of 5.47 a.u., and 5.78 a.u., for different pseudopotentials.

Figure 3.5 shows the local moment curves for Na_2. Again we see that in the SIC calculation the system spin unpairs more readily than in the LSD calculation. The arguments for this are identical to those for H_2.

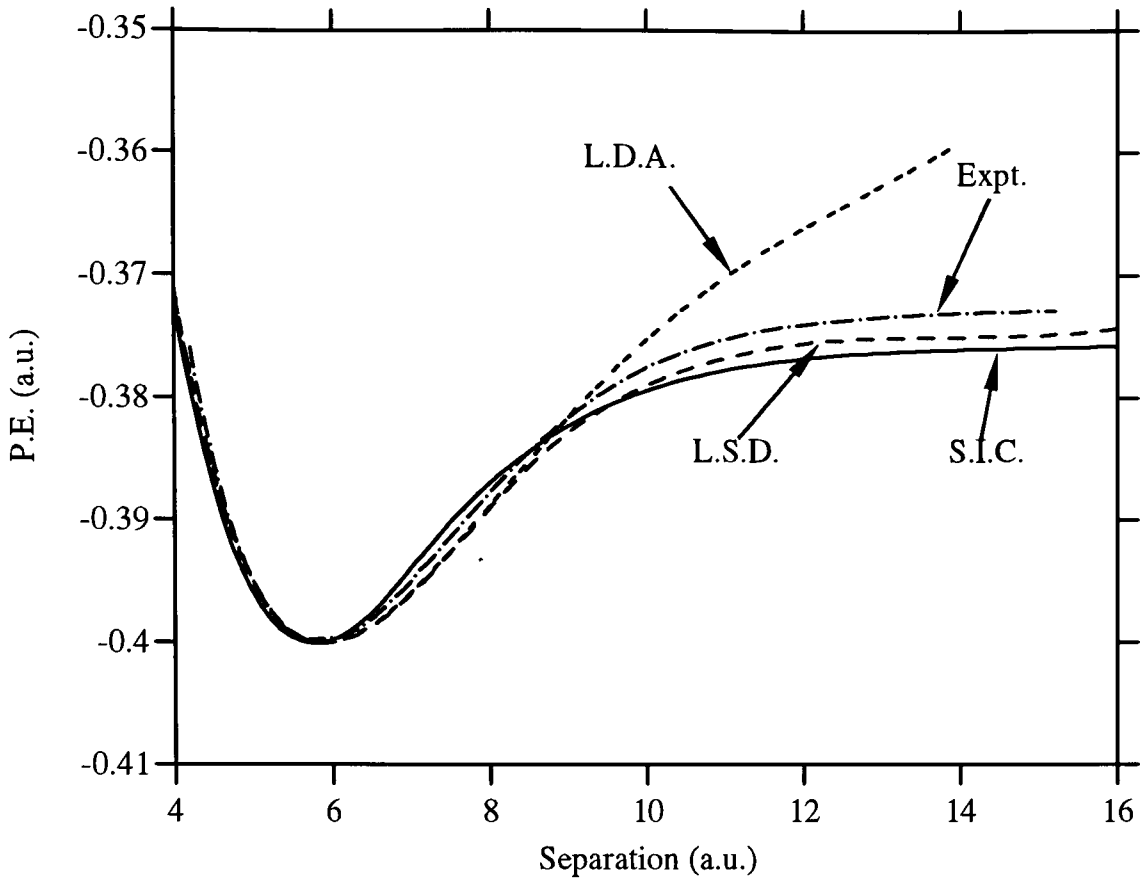


Figure 3.4: The potential energy curves for Na_2 using LDA,LSD and SIC. Also shown is the experimental curve due to Verma *et al.* [116].

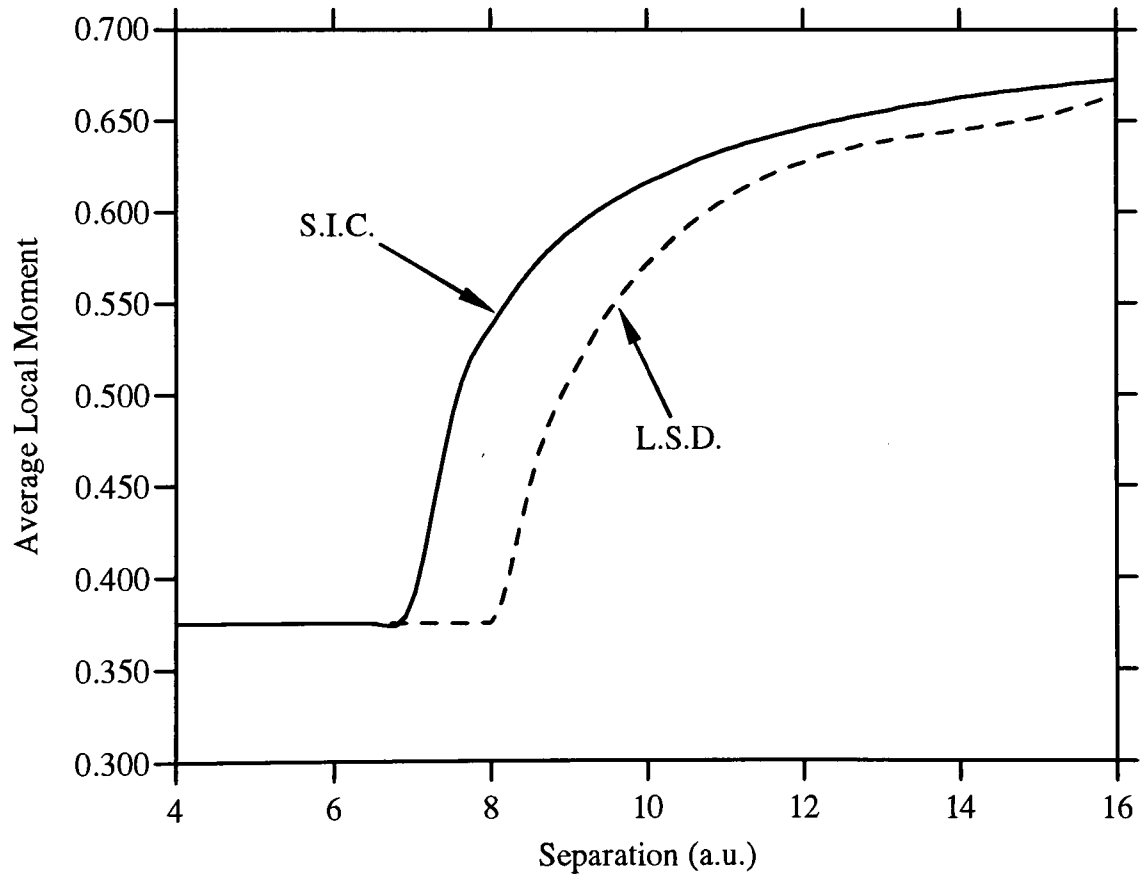


Figure 3.5: The local moment curves for Na_2 using LSD and SIC.

Method	Binding Energy/Atom (cm^{-1})	Bond Length (a.u.)
LDA		5.89
LSD	2863	5.89
SIC	2677	5.76
Expt.(ref.[116])	3012 ± 3	5.818
Expt.(ref.[17])	2945 ± 35	5.818
Expt.(ref.[49])	2994 ± 10	5.818

Table 3.5: Comparison of the Na_2 binding energies and bond lengths from LSD and SIC calculations with experiment.

3.3.3 Cs_2

The P.E. curve for LSD and SIC are compared with the experimental one due to Weickenmeier *et al.* [121] in figure 3.6. Binding energies and bond lengths are compared for the same work in table 3.6 along with the recent two electron configuration interaction (CI) [106] calculations of Foucrault *et al.* [24], some older CI calculations and other experimental data. The details of the calculations are as for Na_2

The first thing to notice is that we are markedly out in the calculation of the bond length. However we take no account of core-polarization effects in our calculations. This is something that Foucrault *et al.* [24] have done in their work and they attribute their accuracy to this. If we compare our results with the older CI calculations that omit the core polarization effects we can see that in fact we do slightly better relative to experiment.

Again the SIC gives a shorter bond length than LSD and this time the SIC binding energy is in better agreement with experiment; again both methods under estimating the binding energy.

Figure 3.7 shows the local moment curves for Cs_2. Again LSD is more reluctant to spin polarize but this time the effect is less marked. This we would expect as the self-interaction of an electron on the larger Cs_2 atom will be less. Thus the driving force for the difference is reduced.

3.3.4 NaH

With the previous calculations, as the dimers are homonuclear, there is no charge transfer between atoms. In a crude model however, NaH is expected to be represented by $Na^+ \ldots H^-$, for small separations, but as $Na \ldots H$ for long separations.

Table 3.7 shows the bond lengths and binding energies found using LSD and SIC. The difference in bond lengths is small compared to the differences

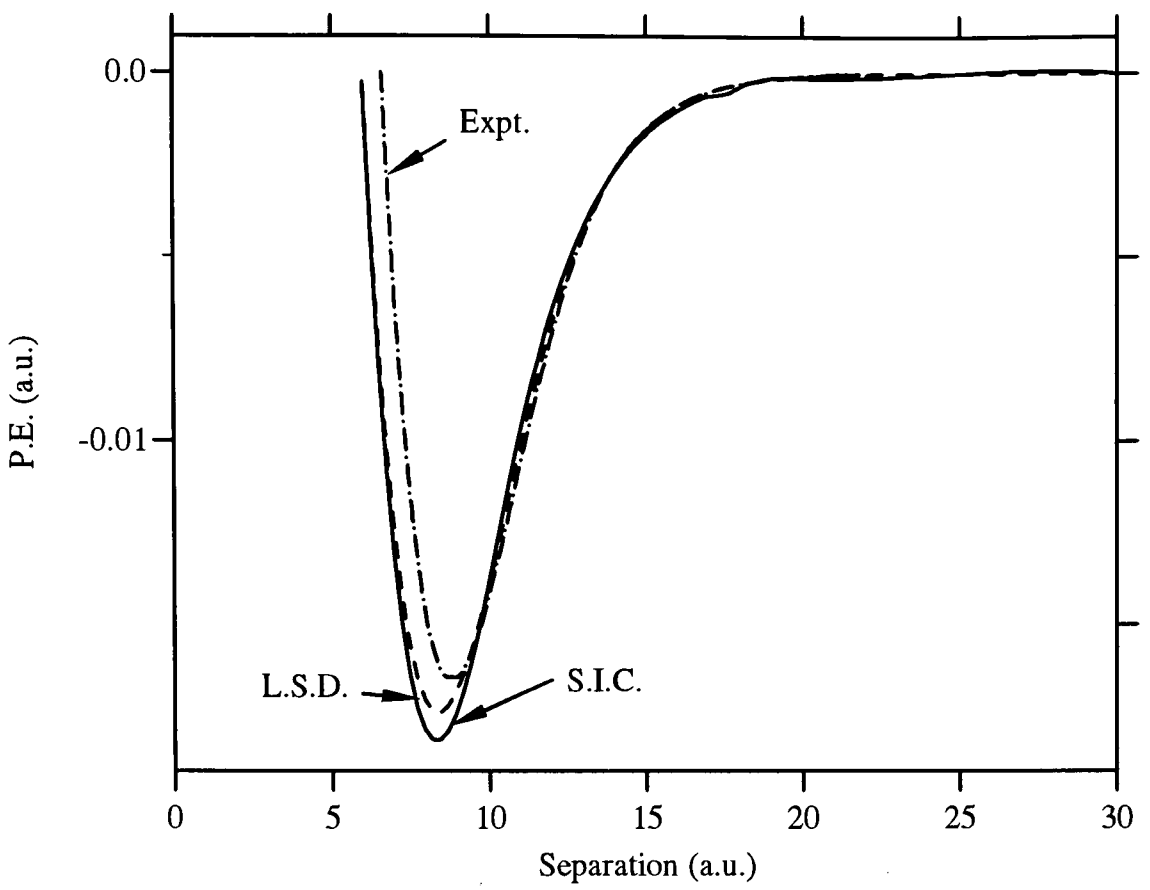


Figure 3.6: The potential energy curves for Cs_2 using LSD and SIC. The experimental potential energy curve due to Weickenmeier *et al.* [121] is also shown.

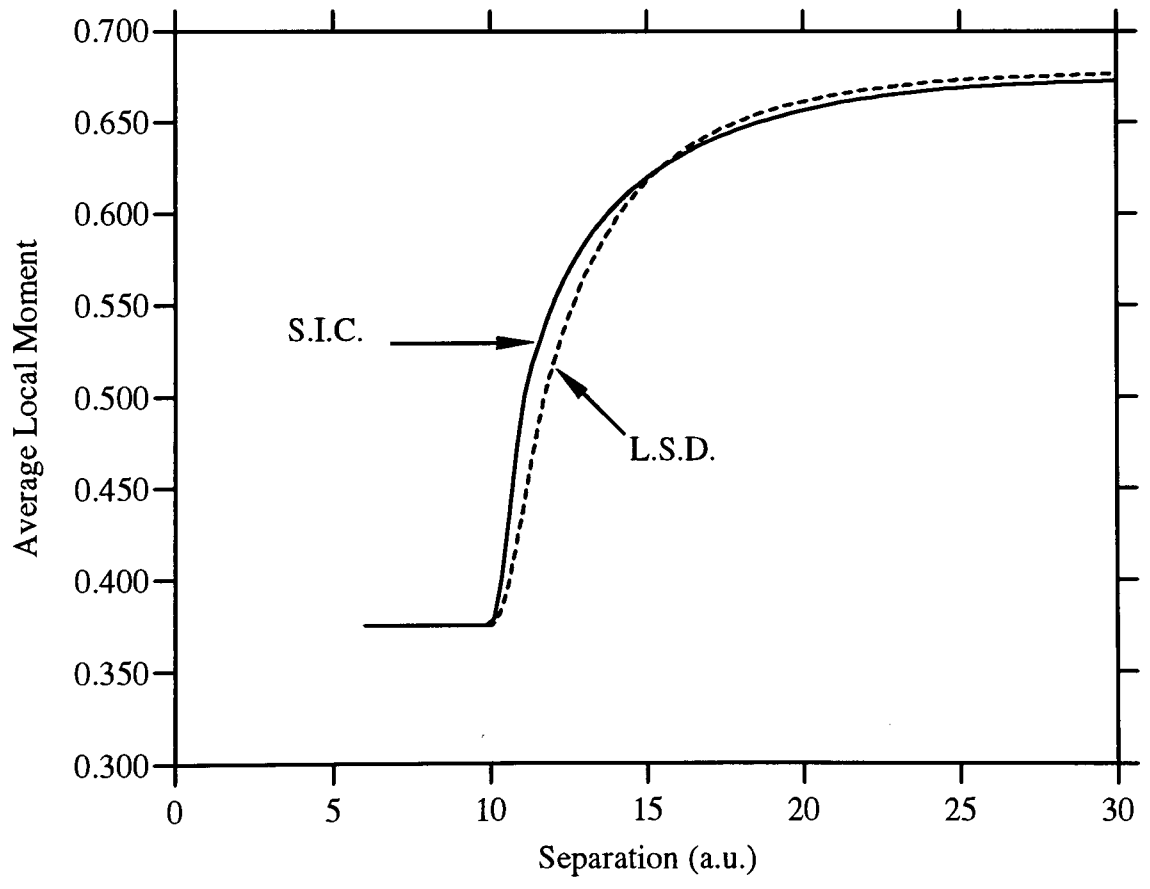


Figure 3.7: The local moment curves for Cs_2 using LSD and SIC.

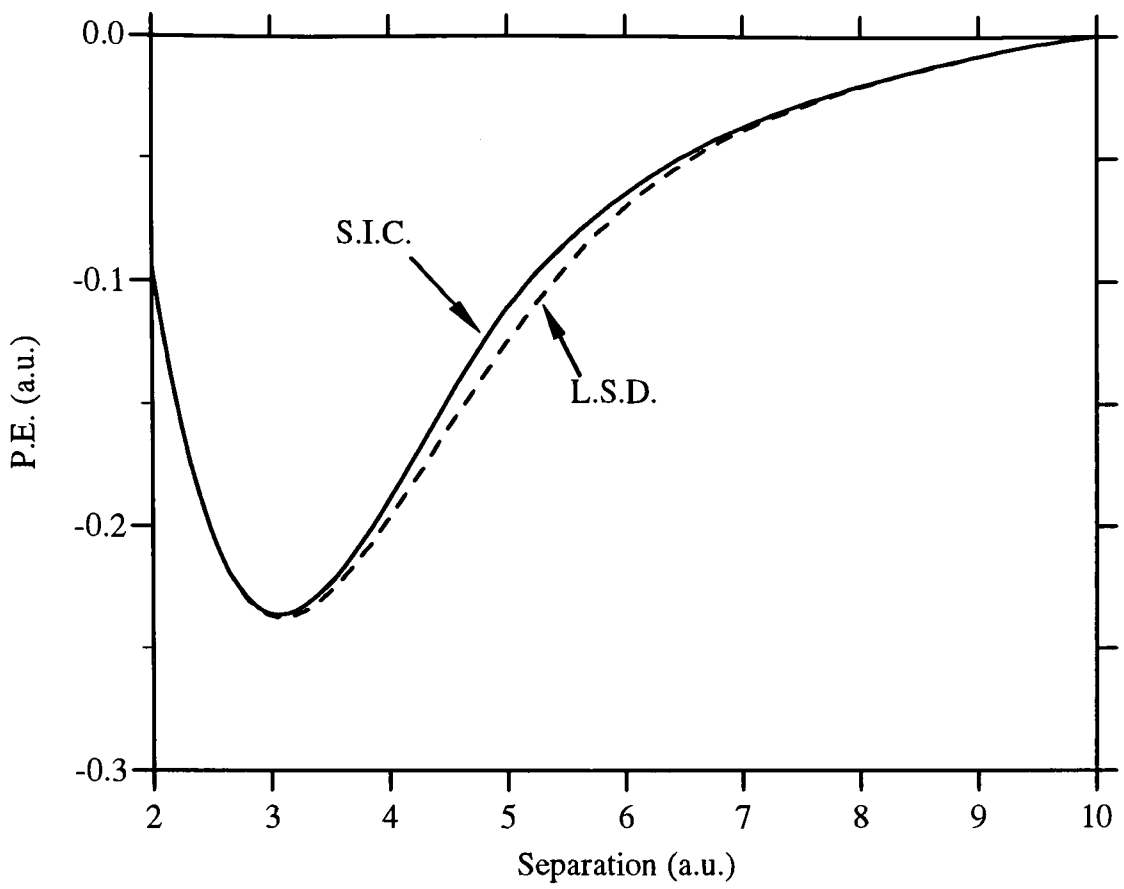


Figure 3.8: The potential energy curves for NaH using LSD and SIC.

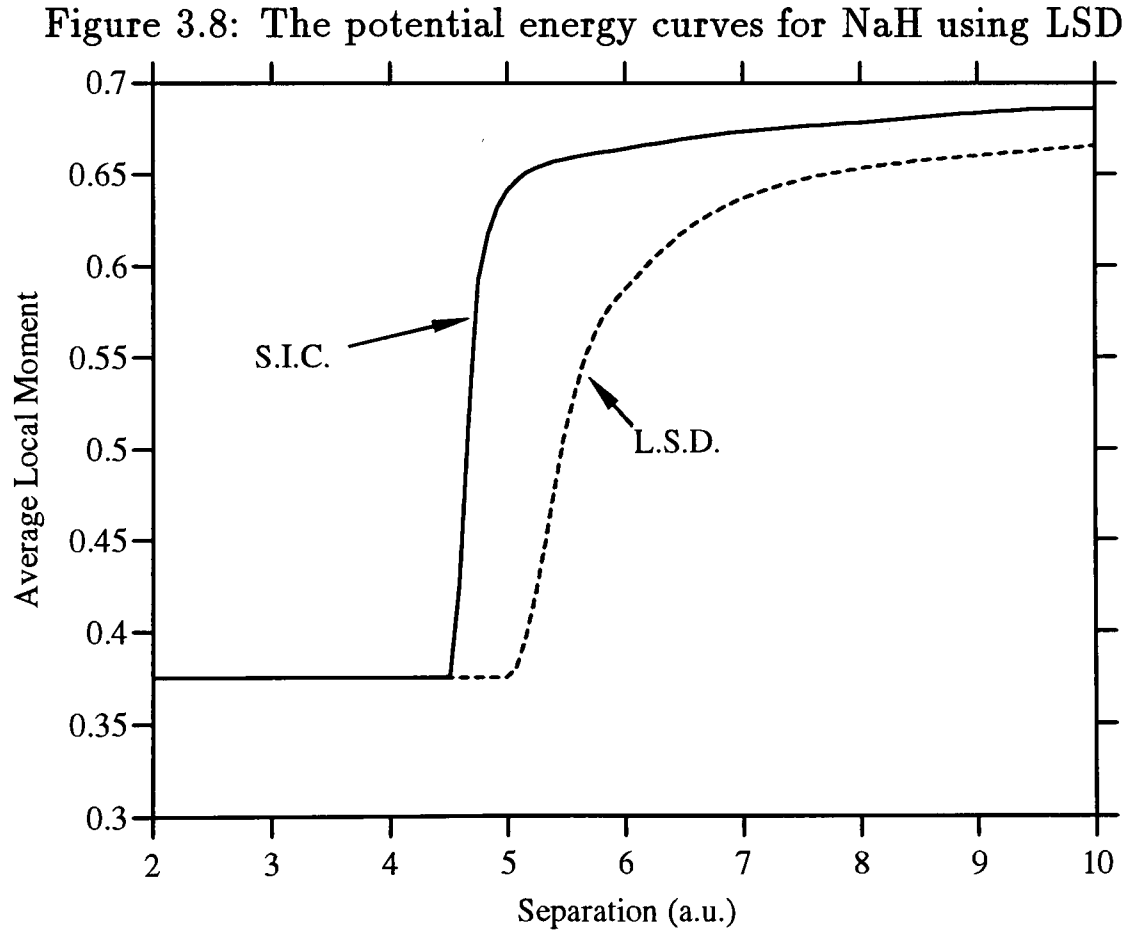


Figure 3.9: The local moment curves for NaH using LSD and SIC.

Method	Binding Energy/Atom (cm^{-1})	Bond Length (a.u.)
LDA		8.35
LSD	1653	8.35
SIC	1734	8.30
Expt.(ref.[121])	1824.8 ± 0.4	8.79
Expt.(ref.[37, 88])	1824 ± 8	8.78
CI (2e) (ref.[24])	1824	8.66
CI (2e) (ref.[24])	1873	8.66
CI (2e) (ref.[117])	1714	8.71
CI (2e) (ref.[54])	1663	9.45

Table 3.6: Comparison of the Cs_2 binding energies and bond lengths from LSD and SIC calculations with experiment.

Method	Binding Energy/Atom (a.u.)	Bond Length (a.u.)
LSD	0.346	3.09
SIC	0.343	3.05

Table 3.7: Comparison of the NaH binding energies and bond lengths from LSD and SIC calculations.

for H_2 and Na_2. The binding energies are considerably larger than for the homonuclear diatomics, SIC having the smaller binding energy.

Figure 3.8 shows the potential energy curves using LSD and SIC. For convenience the zero of energy was taken to be the PE at a separation of 10 a.u. For large, and small separations, the two approximations are in close agreement. As expected though there is a significant discrepancy between the two methods in the spin pairing/unpairing region.

Figure 3.9 shows the local moment curves for NaH. Once more it is clear that SIC spin unpairs far more readily and rapidly than is the case for LSD. Figure 3.10 compares the dipole moments. From this it can be seen that in the spin paired region SIC more closely approaches the "ideal" of total charge transfer from Na to H, though the increase in dipole moment with separation is notably non-linear. This may partly be due to size effects, ie even if the actual position was one of $Na^+ \ldots H^-$ both these ions have a finite size and would be expected to overlap. It is also clear that the change from spin paired to spin unpaired, where ignoring polarization the dipole moment is expected to be zero, is far more rapid for SIC than LSD.

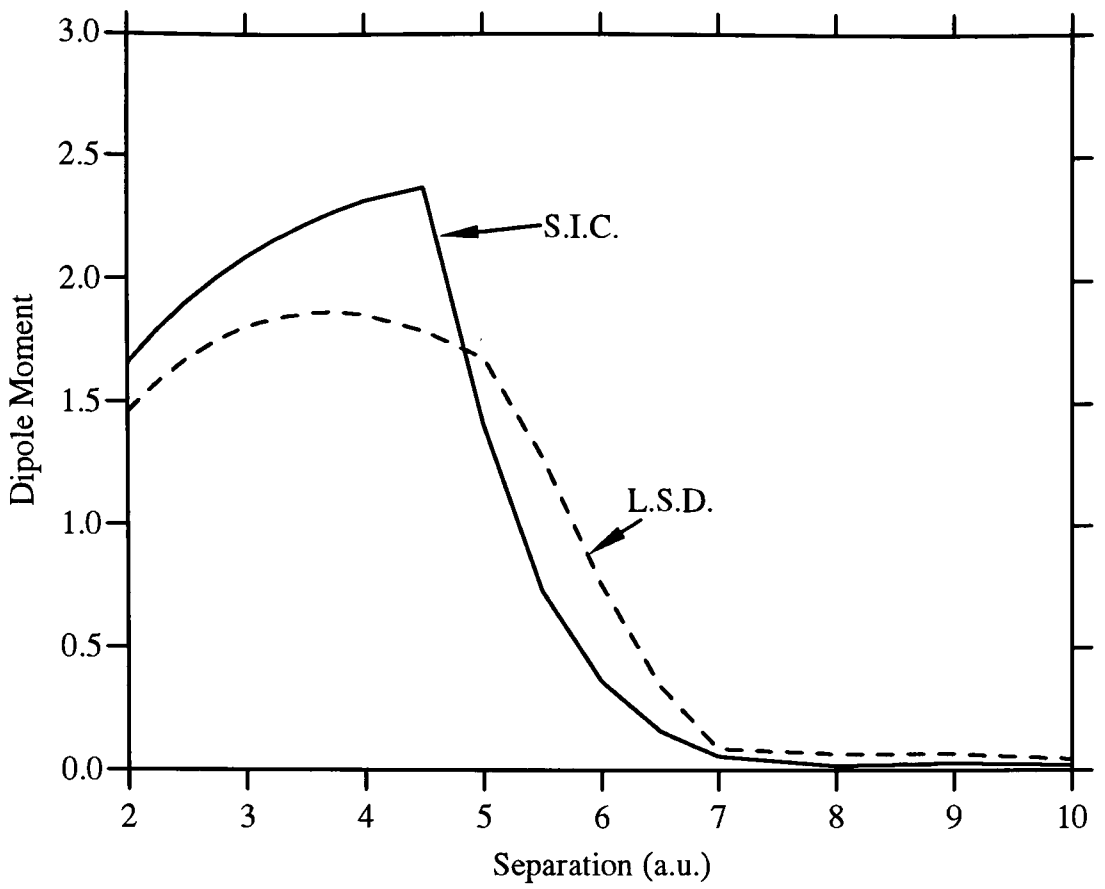


Figure 3.10: The dipole moment curves for NaH using LSD and SIC.

3.3.5 Conclusions

From the above calculations we can make the following observations. Firstly as expected SIC spin polarization occurs more readily than LSD. Consistent with the argument that this is due to the influence of electron-electron self-interaction is the fact that the effect diminishes with the size of atom. The next point to note is that consistently the SIC gives a shorter bond length than LSD. This is due to the fact that the SIC orbitals will be more localised than the LSD orbitals to maximise the self-interaction. Finally there is no obvious trend in the binding energies.

Again it should be emphasised though that if we are interested in the exact values then we should optimise the pseudopotentials for each method [71]. However this would obscure the role of the functional which is our primary interest.

Chapter 4

Structure and Properties of Small Sodium Clusters

Metal clusters [21] form a bridge between atomic/molecular properties, and the properties of the bulk material. As such they demonstrate an interesting compromise in their behaviour. Previous studies have treated metal clusters either as small fragments of the bulk material, the jellium model [34], or as molecules using quantum chemical methods. Amongst the methods used are configuration interaction (CI) (eg. [20]), generalised valence bond (GVB) (eg. [62]), and path integral (PI) (eg. [31]). There have also been several studies using density functional theory, eg. the work of Röthlisberger and Andreoni [93]. All previous DFT studies, not using the jellium model, however have been carried out using LDA or LSD. This chapter then will discuss the results of using SIC as well as LSD to study clusters of sodium atoms with between two and eight atoms.

4.1 Geometries and Binding Energies

A widely used method to describe metal clusters is the spherical jellium model [34]. This ignores the geometry of the ions completely and treats the cluster as a set of electrons confined in a spherically symmetric potential with a uniform background neutralising charge. This is analogous to the free electron model for bulk metals in ignoring the details of the ion electron interaction. With the documented successes of the spherical jellium model [34], this might lead one to consider alkali metal clusters as small droplets of the bulk material. However, it is quite clear from previous work (see for example the review by Koutecký and Fantucci [21]) that the geometries of such clusters are not simply those of bulk phase fragments. Conversely they are not what one might immediately expect from simple molecular structure models. This section will consider the various geometries, and their stabil-

ities, predicted by LSD and SIC, and compare them to the results of other models.

In order to find the geometries that are local minima in the potential energy surface for a particular cluster, the following procedure was used. Firstly a guess at a local minimum was made. For the LSD calculations this was based on the results published in other work, except for one of the Na_4 geometries (the distorted rhombus), which was started from a tetrahedral geometry, and the Na_8 calculation which was started from a cubic geometry. All the SIC calculations were started from the optimised LSD geometries. A CG minimisation was performed to obtain the electronic structure at this initial geometry. A steepest descent algorithm within the CP method was then employed. Here the ion velocities in the leap-frog algorithm were set to zero at each step, and a "mass" of $40m_e$ was used (m_e = mass of electron, which is the atom unit of mass), and a "time step" of 6.4 a.u. was used. This gave the largest steps that reliably allowed the wavefunction to stay on the Born-Oppenheimer surface. A fake mass, μ, of 400 a.u. was used.

Clearly one cannot continue optimising the geometry until the net forces are exactly zero. Thus the criterion for stopping an optimisation was that the forces on each ion were less than 10^{-6}a.u. To ensure that the calculation was sufficiently converged for forces to be correct to this accuracy, a CG minimisation was performed at this final geometry. It was never found necessary to continue the geometry optimisation after this point however.

In principle the absolute minimum could be found by a simulated annealing method. For this ion dynamics would be performed, at initially high temperature, and kinetic energy removed every few hundred, or even thousand, steps. In this way the system would sample most of the potential energy surface, and with care, and perhaps occasional reheating of the system, avoid being trapped in a local minimum. However this is clearly expensive, and we are also interested in the local minima, to compare with other work, and with the absolute minimum energy geometry. Clearly then with a sufficiently good initial guess the steepest descent method is considerably cheaper, as the cpu time per step is identical in both cases.

For Na_3 both acute and obtuse isosceles triangular structures were found. A regular and an irregular rhombic geometry were found for Na_4 . Na_5 has a planar trapezoidal geometry. For Na_6 a planar triangular and pentagonal pyramidal geometry were obtained. Na_7 also gave two structures, a planar centred hexagon and a bicapped pentagonal pyramid. Na_8 gave a tetracapped tetrahedron in LSD which is distorted to give the D_{2d} geometry found by Moullet *et al.* [69], while SIC gave a regular tetracapped tetrahedron . Note though that this was *not* an exhaustive search.

The results of these calculations using both LSD and SIC are shown in figure 4.1 and tables 4.1-4.12 along with the data for equivalent geometries found by other workers. All the methods find similar geometries. The SIC

Method	a
LSD	5.89
SIC	5.76
LDA	5.89
LSD [69]	5.47
LSD [69]	5.47
Expt. [116]	5.818

Table 4.1: Na_2 bond lengths in a.u.

Method	a	b
LSD	7.20	5.92
SIC	7.18	5.80
LSD [69]	6.35	5.45
LSD [69]	6.86	5.80

Table 4.2: Na_3 bond lengths in a.u. for the acute geometry.

calculations give shorter bond lengths, in general, than the LSD, while the LSD calculations of Moullet *et al.* [69] tend to give shorter bond lengths. This is consistent with the results for the dimer presented in the last chapter. The omission of data for a particular method and cluster indicates that no results in the work were published. This is probably due to the workers not looking for that geometry. For example in the case of the irregular rhombic Na_4 geometry if a simulation is started from a regular rhombus then the symmetry of the forces is such that the irregular geometry cannot be produced. However, this probably is not the case for the acute Na_3 geometry. It is noticeable that this is found only in the LSD and SIC calculations. The difference in energy between this and the obtuse geometry in SIC is found to be very close to the activation barrier for the pseudorotation of the cluster (see chapter 5). Thus it is likely that the acute geometry is actually the transition state for the pseudorotation, and not a minimum but a saddle point.

Hall [31], using a finite temperature path integral Monte Carlo method, found several asymmetric minima for Na_5, and Na_6, as well as Na_4, and that the potential energy surface for these clusters is very flat. It was found, by observing the rate at which the geometries optimised, and from CP dynamics (see chapter 5) that the potential energy surfaces for all the LSD and SIC calculations were relatively flat, supporting Hall's findings. Röthlisberger

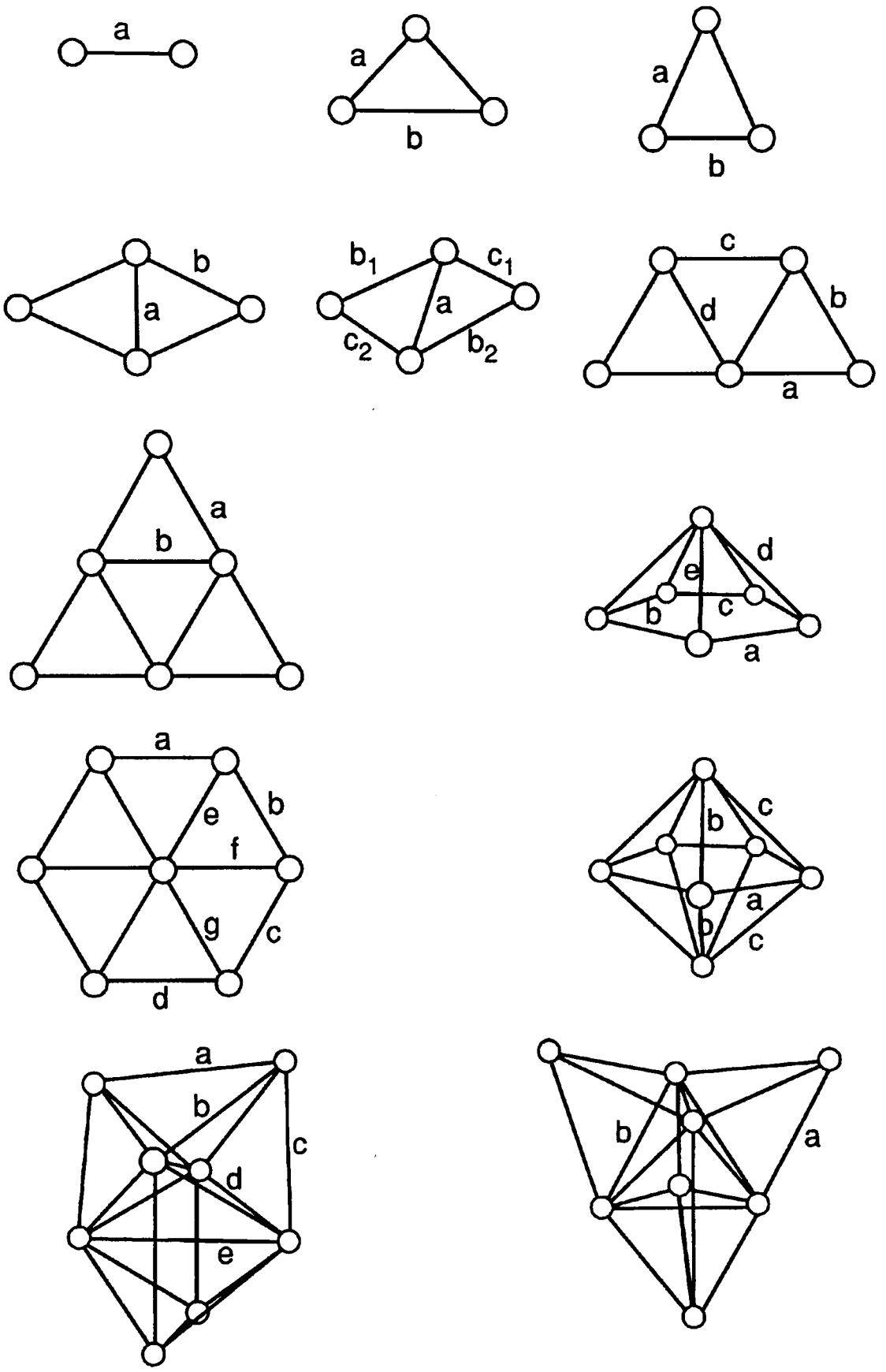


Figure 4.1: The stable geometries found for sodium clusters with between 2, and 8 atoms. Working from left to right and down the page these are: Na_2, Na_3 (obtuse), Na_3 (acute), Na_4 (regular rhombus), Na_4 (irregular rhombus), Na_5, Na_6 (D_{3h}), Na_6 (C_{5v}), Na_7 (D_{2h}), Na_7 (D_{5h}) Na_8 (D_{2d}), Na_8 (T_d).

Method	a	b
LSD	6.24	8.61
SIC	6.15	8.50
LSD [69]	5.68	7.15
LSD [69]	6.05	8.02
PI [90]	6.05	8.02
MBPT [90]	7.01	10.62

Table 4.3: Na_3 bond lengths in a.u. for the obtuse geometry.

Method	a	b
LSD	5.96	6.79
SIC	5.88	6.71
LDA	5.96	6.79
LSD [69]	5.42	6.18
LSD [69]	5.80	6.57
PI [90]	5.86	6.83
MBPT [90]		6.97
CI [9]	6.06	6.95

Table 4.4: Na_4 bond lengths in a.u. for the regular rhombic geometry.

Method	a	b_1	b_2	c_1	c_2
LSD	5.98	7.05	7.05	6.58	6.58
SIC	6.03	7.41	7.41	6.23	6.23
LDA	5.98	7.05	7.05	6.58	6.58
PI [90]	5.86	7.22	7.36	6.39	6.33

Table 4.5: Na_4 bond lengths in a.u. for the irregular rhombic geometry.

Method	a	b	c	d
LSD	6.58	6.56	6.80	6.82
SIC	6.54	6.54	6.70	6.68
LSD [69]	6.03	6.04	6.36	6.01
LSD [69]	6.39	6.37	6.55	6.42
PI [90]	6.93	6.65	6.93	6.50
PI [90]	6.82	6.82	6.82	6.50
CI [10]	6.52	6.48	6.64	6.69

Table 4.6: Na_5 bond lengths in a.u.

Method	a	b
LSD	6.54	6.97
SIC	6.50	6.87
LSD [69]	6.02	6.27
LSD [69]	6.34	6.67
PI [90]	6.73	6.73
CI [10]	6.46	6.86

Table 4.7: Na_6 bond lengths in a.u. for the D_{3h} geometry.

Method	a	b	c	d	e
LSD	6.91	6.91	6.91	6.50	6.50
SIC	6.85	6.88	6.91	6.46	6.45
LSD (planar)	7.33	7.33	7.33	6.23	6.23
LSD [69]	6.27	6.27	6.27	5.89	5.89
LSD [69]	6.62	6.62	6.62	6.30	6.30
CI [10]	6.85	6.85	6.85	6.32	6.32

Table 4.8: Na_6 bond lengths in a.u. for the $C_{5\nu}$ geometry.

Method	a	b	c
LSD	6.76	6.85	6.85
SIC	6.78	6.97	6.68
LSD [69]	6.10	6.02	6.02
LSD [69]	6.50	6.55	6.55
CI [10]	6.65	6.70	6.70

Table 4.9: Na_7 bond lengths in a.u. for the D_{5h} geometry.

Method	a	b	c	d	e	f	g
LSD	6.58	6.62	6.62	6.58	6.65	6.91	6.65
SIC	6.53	6.66	7.42	6.13	6.73	6.92	6.76
LSD [69]	5.94	6.25	6.25	5.94	6.03	6.25	6.03
LSD [69]	6.30	6.63	6.63	6.30	6.39	6.77	6.39

Table 4.10: Na_7 bond lengths in a.u. for the D_{2h} geometry.

Method	a	b	c	d	e
LSD	9.16	6.87	6.43	6.81	10.27
LSD [69]	6.76	6.55	6.27	5.51	7.80
LSD [69]	7.23	6.87	6.43	6.81	8.35

Table 4.11: Na_8 bond lengths in a.u. for the D_{2d} geometry.

Method	a	b
SIC	6.77	6.82
LSD [69]	6.07	6.11
LSD [69]	6.49	6.54

Table 4.12: Na_8 bond lengths in a.u. for the T_d geometry.

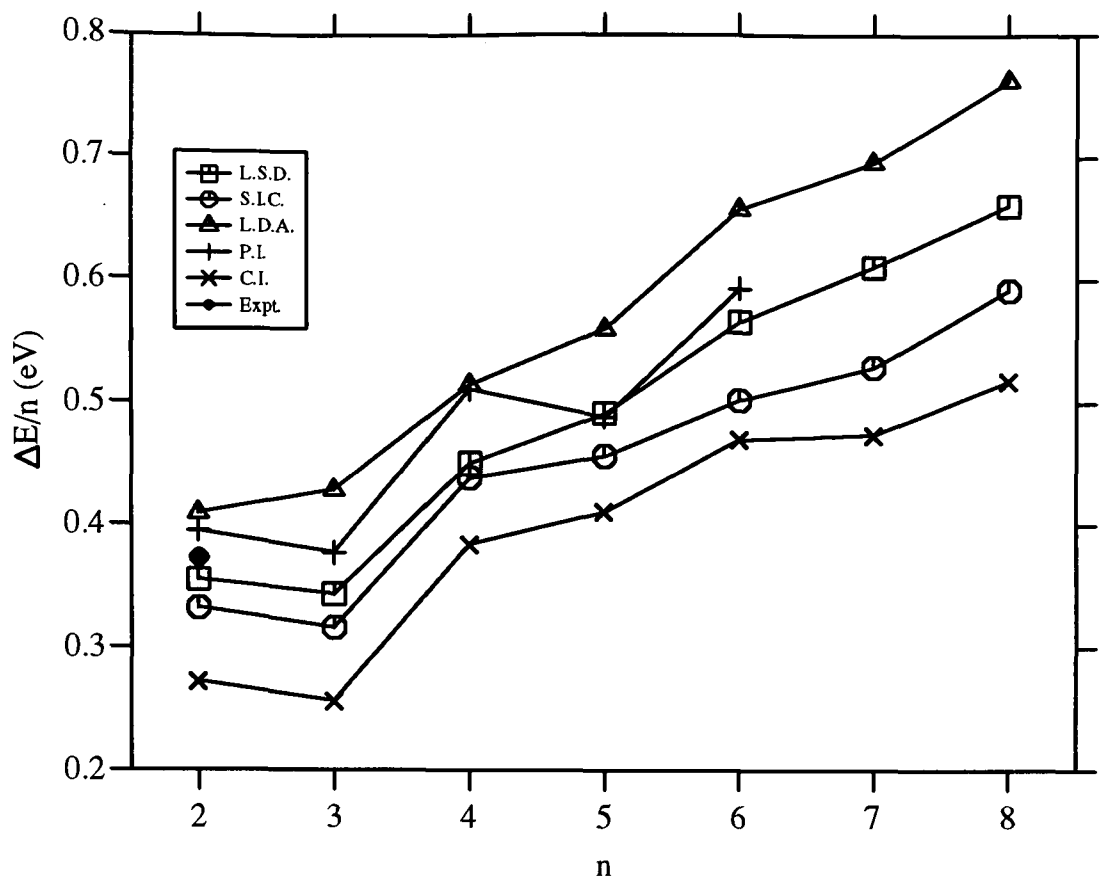


Figure 4.2: The binding energies per atom, $\Delta E/n$ versus nuclearity, n, for the ground state geometries using LSD, SIC, CI [20], PI [31], and LDA [93].

and Andreoni [93] found similar results using CP dynamics and LDA. The conclusion then is that the potential energy surfaces of the clusters of nuclearity studied here (ie. less than 8) are very flat and except for Na_2 and Na_3 probably have many shallow minima. The geometries found, and shown here, are probably the most stable. However, as noted by Röthlisberger and Andreoni, with such flat potential energy surfaces finite temperature effects are likely to be quite significant.

The most noticeable feature of these geometries is the preference for planar geometries for clusters up to a nuclearity of around 6. Similar results have been obtained for lithium clusters [21, 20, 112, 113]. It is also noticeable that these clusters can be thought of as being made up of triangles of atoms. I will return to these points in the next section on electronic structure.

Table 4.13 shows the binding energies per atom ($\Delta E_n/n$) of the clusters found using LSD and SIC, whilst table 4.14 and figure 4.2 compare the binding energies per atom of the most stable geometry for each cluster nuclearity found by various methods. Figure 4.2 shows that the binding energies generally increase with increasing nuclearity, but superimposed on this there are oscillations in stability of odd and even clusters, the even clusters being relatively more stable.

It is clear from this data that the SIC binding energies are systematically lower than the LSD ones, though the energy difference is not large. This

	LSD	SIC
Na_2	0.355	0.332
Na_3 (obtuse)	0.343	0.316
Na_3 (acute)	0.329	0.305
Na_4 (regular)	0.450	0.438
Na_4 (irregular)	0.450	0.438
Na_5	0.491	0.456
Na_6 ($C_{5\nu}$)	0.566	0.526
Na_6 (D_{3h})	0.559	0.498
Na_7 (D_{5h})	0.611	0.529
Na_7 (D_{2h})	0.540	0.486
Na_8	0.661	0.592

Table 4.13: Binding energies per atom in eV for stable geometries of sodium clusters.

	LSD	SIC	PI[31]	LSD[61]	CI[20]	LDA[93]	MBPT[90]
Na_2	0.355	0.332	0.395	0.45	0.272	0.409	0.274
Na_3	0.343	0.316	0.377	0.43	0.256	0.428	0.189
Na_4	0.450	0.438	0.510	0.61	0.384	0.514	0.351
Na_5	0.491	0.456	0.488	0.64	0.411	0.560	0.287
Na_6	0.566	0.526	0.593	0.73	0.470	0.658	0.456
Na_7	0.611	0.529		0.82	0.474	0.696	0.441
Na_8	0.661	0.592		0.86	0.518	0.763	

Table 4.14: Binding energies per atom in eV for the most stable geometries of sodium clusters. The first two columns marked LSD and SIC are from this work.

finding is what one would expect, as the self-interaction, erroneously included in the LSD will raise the energy of localised effective one particle states relative to extended ones. In the clusters one expects that the one particle states extend over the full cluster, so that the self-interaction is lower than in the atom. Correcting for the self-interaction therefore stabilises the atom relative to the cluster and reduces the dissociation energy.

The CI data due to Fantucci *et al.* [20] shown in figure 4.2 are from all electron calculations, and it should be noted that the geometries were not optimised at the full CI level. The relative energies in these calculations and the SIC match each other quite well, but again there is a systematic displacement with the CI binding energies lower than the SIC. It should be noted that this may be due to the use of a pseudopotential in the SIC, rather than differences between CI and SIC. The differences are of the same order or larger than the differences between LSD and SIC. It should also be noted that as the LSD and SIC result for Na_2 underestimates the binding energy this figure would tend to indicate that both the LSD and SIC calculations are in better agreement with experiment than the CI calculations. Unfortunately no other experimental binding energies have been found.

The LDA results due to Röthlisberger and Andreoni [93] show a similar pattern to the LSD and SIC, this time though displaced to higher energies, and they overestimate the experimental Na_2 binding energy. The PI calculations of Hall [31] show the same trends but greatly exaggerate the odd/even oscillation compared to the other data.

The relative stabilities of the clusters of the same nuclearity, for the LSD calculations are in agreement with the LSD work of Moullet *et al.* [69]. However the SIC results do not always give the same geometry as the most stable as the LSD. In particular using LSD the pentagonal pyramidal geometry , for Na_6 is most stable whilst for SIC the triangular geometry is the most stable. I will discuss this point fully in the next section. It can also be seen that SIC gives a different geometry for Na_8. As the SIC calculation was started from the LSD geometry, the D_{2d} geometry would appear not to be stable in SIC. This agrees with the conclusion from polarizability data (*vide infra*), that the T_d geometry is the geometry found experimentally.

4.2 Electronic Structure

One of the most significant findings of molecular beam studies on alkali metals was the discovery by Knight *et al.* [43] that the mass spectra of the clusters produced in a supersonic expansion with argon carrier gas show pronounced peaks analogous to the magic numbers observed in nuclei. Experimentally these peaks have been observed at N=2, 8, 20, 40, 58, 198±2, 263±5, 341±5, 443±5, and 557±5, where N is the number of atoms in the cluster. This ob-

servation can be explained by the jellium model [34]. Here the positive ions of the cluster are smeared out into a uniform background spherical shape with equal density to the bulk. Using this model one obtains electronic energy levels in the order, 1s, 1p, 1d, 2s, 1f, 2p, 1g,... One then expects relatively stable clusters when a particular angular momentum level is completely filled. Such stable clusters would be expected to predominate in the beam experiments, so from this model one predicts the "magic numbers", N=2, 8, 20, 40, 58, 92, 138, 196, 254, 338, 440, and 562 for neutral clusters. As can be seen this is in excellent agreement with experiment. Note though that the agreement is less good when we include all the magic numbers predicted by this approach eg. N=18.

At first sight the jellium model, despite its success in accounting for the observed abundances of clusters, might appear to offer little insight into the geometries of the clusters. Indeed we are initially lead to expect the clusters to take on as near spherical geometries as possible, and apart from Na_8 (and Na_2 which has no alternatives) from the the last section this is clearly not the case. However Mingos *et al.* [118, 66] have given convincing arguments that this can be explained within the jellium model. In a spherical environment the three p-levels are degenerate. However if the potential is distorted in either an oblate, or prolate manner, then the degeneracy is lifted. An oblate distortion of a sphere results in a discus shape, and a prolate distortion a rugby ball shape. This splitting of the p-levels is illustrated in figure 4.3. One can see that for a prolate distortion the p_0 level is lowered in energy and the $p_{\pm 1}$ levels are raised. Using Na_4 as an example, the closest to spherical geometry would be a tetrahedron. However this would have two electrons in a 1p state which could be stabilised by distortion. From figure 4.3 a prolate distortion will give the greater stabilisation. Another possible geometry for Na_4 is square planar, but this still has a degeneracy in the p-levels. thus to obtain maximum stabilisation a further prolate distortion is required to give the rhombic geometry found by the calculations. Thus even the distortion from a three dimensional to a 2 dimensional geometry can be rationalised within a jellium model. Again taking Na_3 as an example, we have one electron in the 1p state and clearly this is stabilised by distorting the nearest to spherical symmetry, equilateral, geometry in a prolate manner, to give an obtuse isosceles geometry. This is exactly what is found in other calculations. Of course in the language of quantum chemistry what we have is a Jahn-Teller distortion that lifts the degeneracy of a partially filled state and stabilises the system. It is clear why Na_8 has a pseudo spherical geometry; the 1p level is completely filled and so no stabilisation by this mechanism can be obtained.

One should not overemphasise the extent of these splittings though. If they were too large then the basis of the arguments for the magic numbers would break down. In fact Magaud *et al.* [59] make the point that the accurate prediction of magic numbers by the jellium model for small clusters

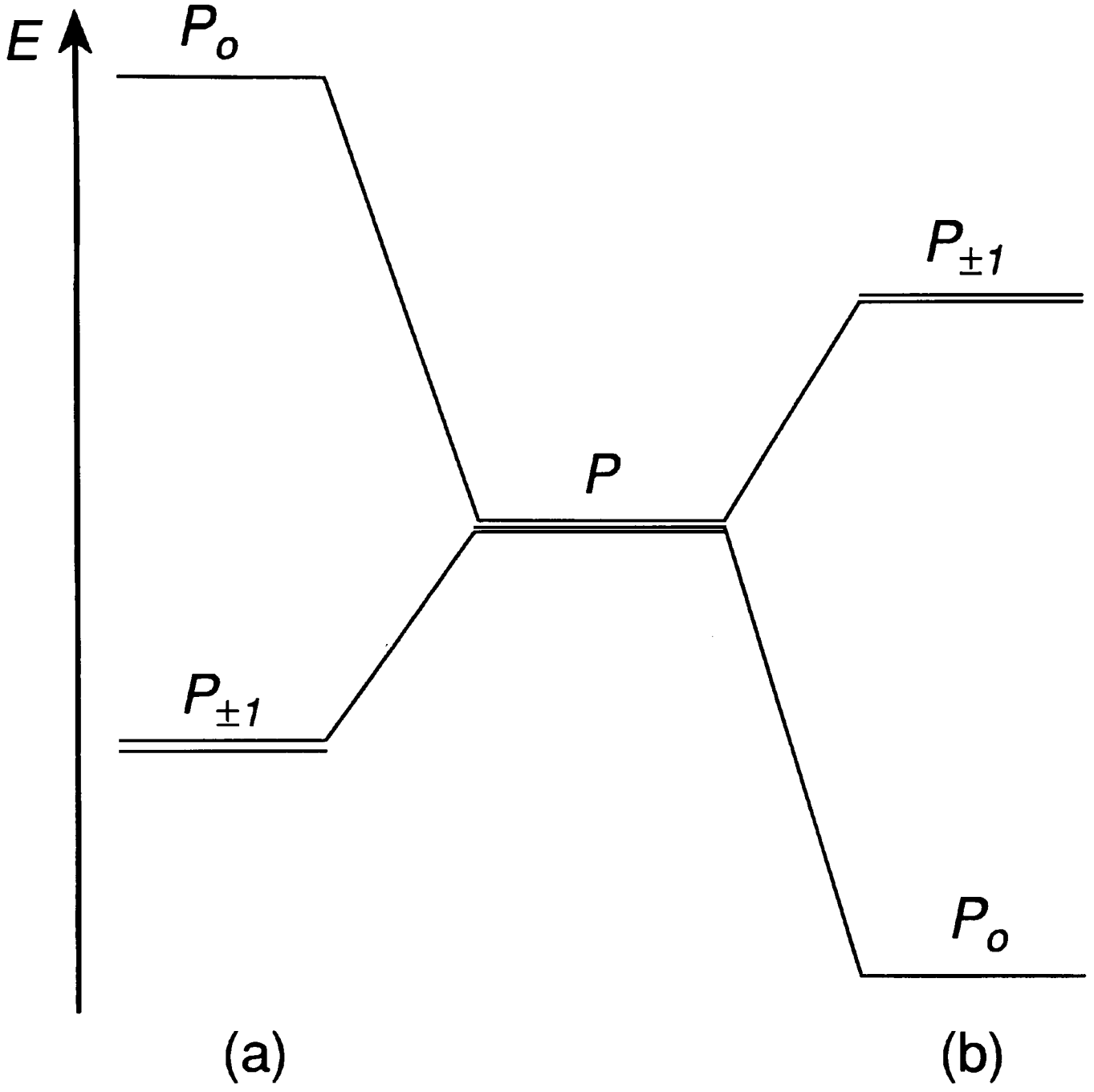


Figure 4.3: The splitting of the p-levels in a jellium model with (a) an oblate distortion, and (b) a prolate distortion.

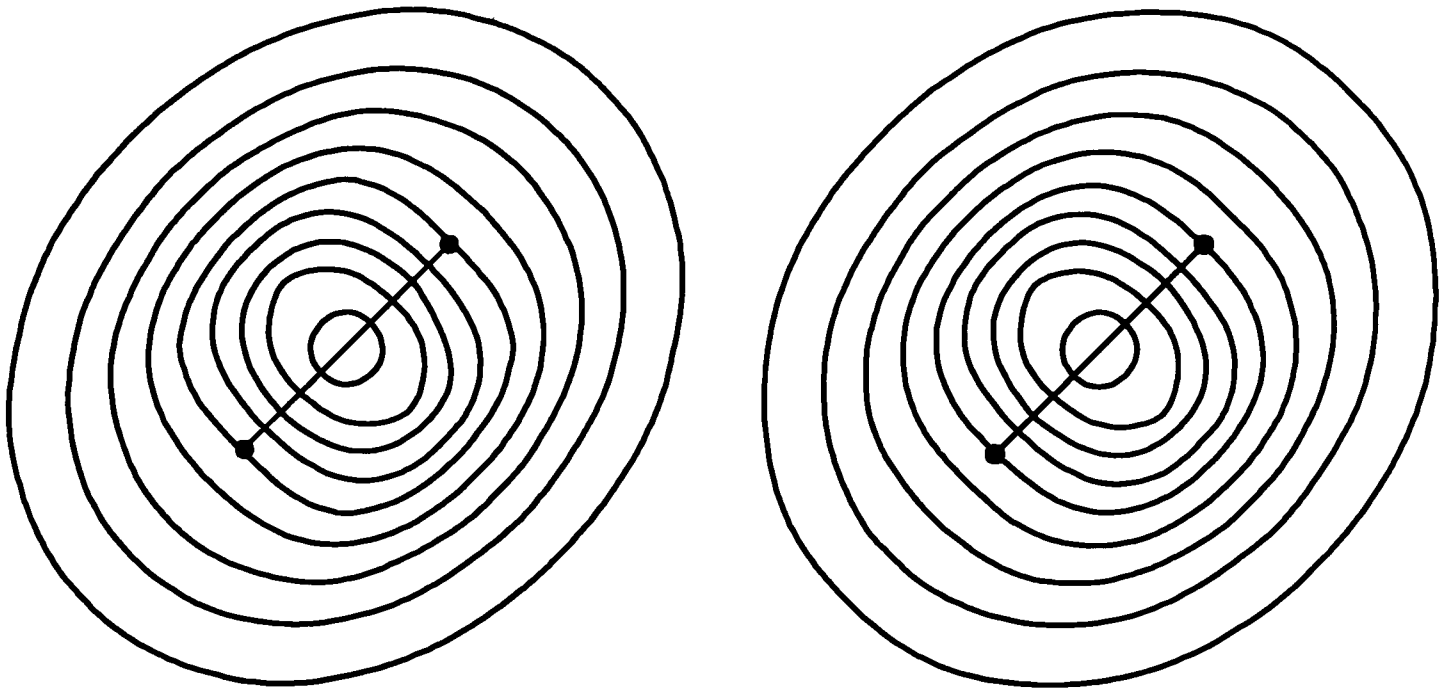


Figure 4.4: The valence electron density maps for Na_2. The left hand map was calculated in LSD, the right in SIC.

is precisely *because* this splitting is small relative to the gaps between angular momentum states.

Is it possible to rationalise the bonding in the geometries obtained by LSD and SIC within these approximations? Figure 4.4-4.12 shows the valence electron density maps in the cluster plane for Na_2-Na_7. In the cases of the non-planar Na_6 and Na_7 clusters the plane shown is that of the pentagon of five atoms. These were obtained by calculating the valence density from the wavefunction generated by the CG method, on a 40 by 40 grid and plotting the resulting contours using UNIMAP.

Qualitatively the density maps for LSD and SIC are similar. The maps for Na_4 agrees with that found by Hall [31], and the Na_5 map agrees with that found by Moullet *et al.* [69]. The first thing to notice is that the maxima are *not* at the nuclei as one might expect. Non-nuclear sites of electron density maxima have been called non-nuclear attractors or pseudo-atoms. The concepts and how they arise in the topological theory of atoms in molecules are discussed in a review by Bader *et al.* [4]. We can see these pseudoatoms appearing in figure 4.13, which shows the valence electron density for the dimer at different separations, using SIC. The density maxima are on the atoms at large separations, as expected for essentially isolated atoms. As the separation is decreased though the maxima can be seen to displace from the atoms but still appear as two distinct maxima. Finally near the equilibrium bond length the density has coalesced into a single maximum. LSD showed qualitatively the same result. Similar non-nuclear attractors have been found for the lithium dimer [27].

For clusters other than the dimer and the trimers these pseudoatoms lie

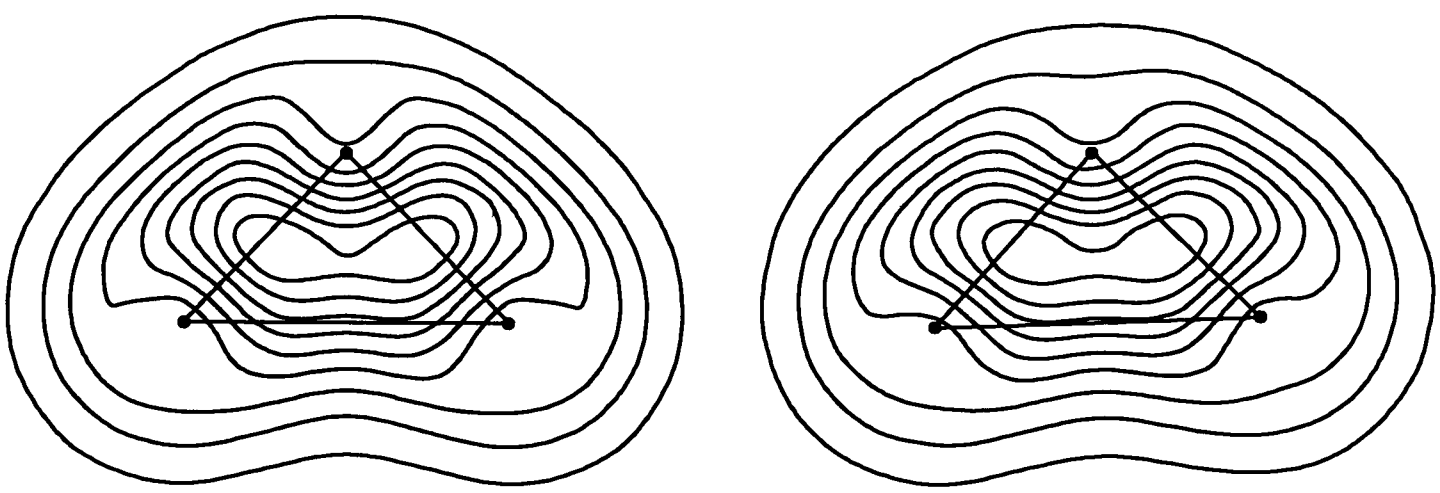


Figure 4.5: The valence electron density maps for the obtuse Na_3 geometry. The left hand map was calculated in LSD, the right in SIC.

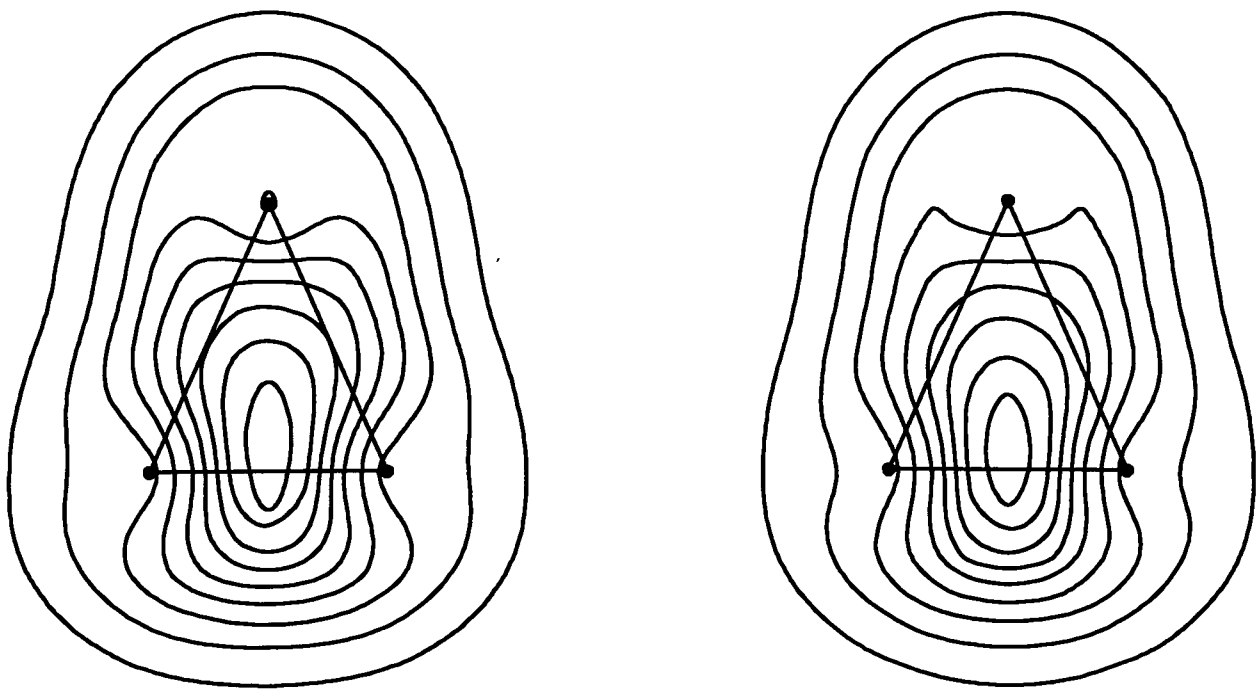


Figure 4.6: The valence electron density maps for the acute Na_3 geometry. The left hand map was calculated in LSD, the right in SIC.

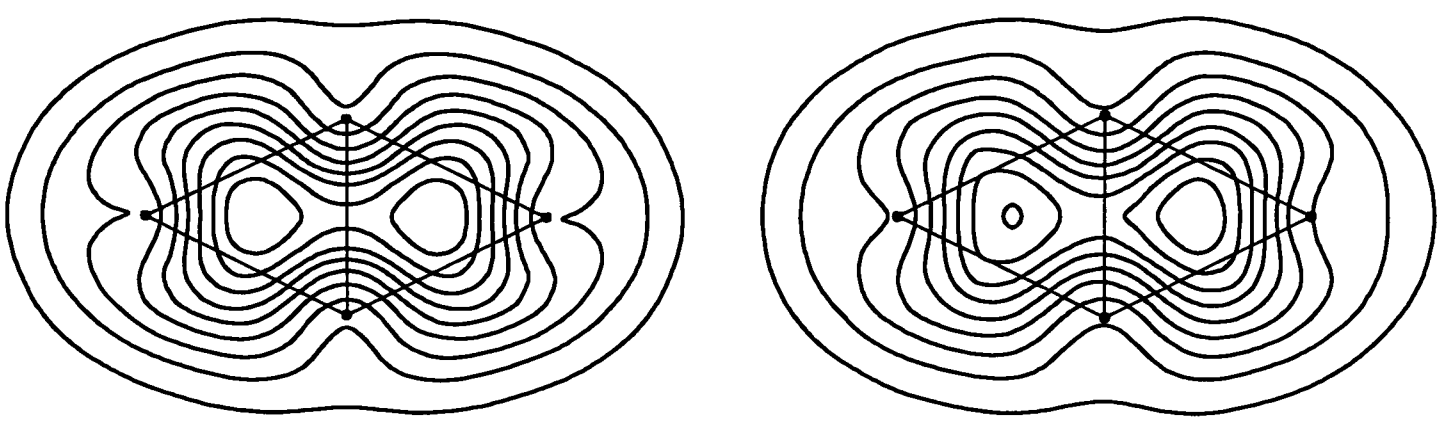


Figure 4.7: The valence electron density maps for the regular rhombic Na_4 geometry. The left hand map was calculated in LSD, the right in SIC.

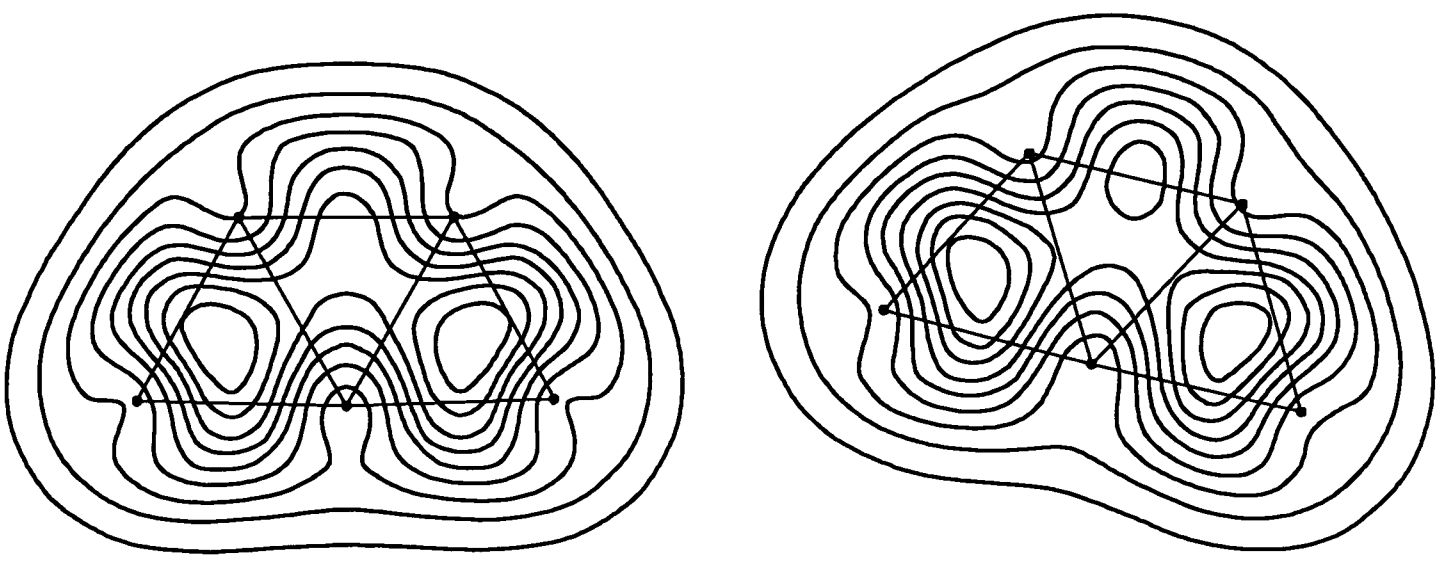


Figure 4.8: The valence electron density maps for the Na_5. The left hand map was calculated in LSD, the right in SIC.

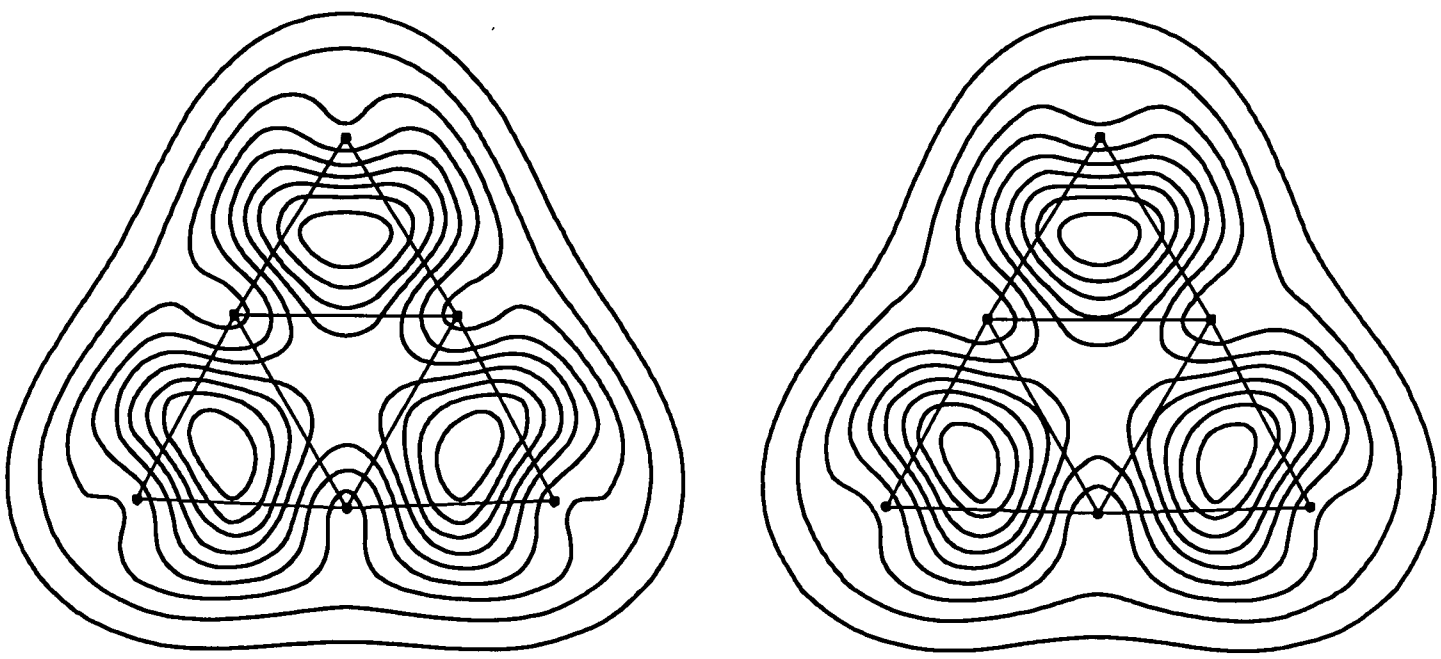


Figure 4.9: The valence electron density maps for the triangular Na_6 geometry. The left hand map was calculated in LSD, the right in SIC.

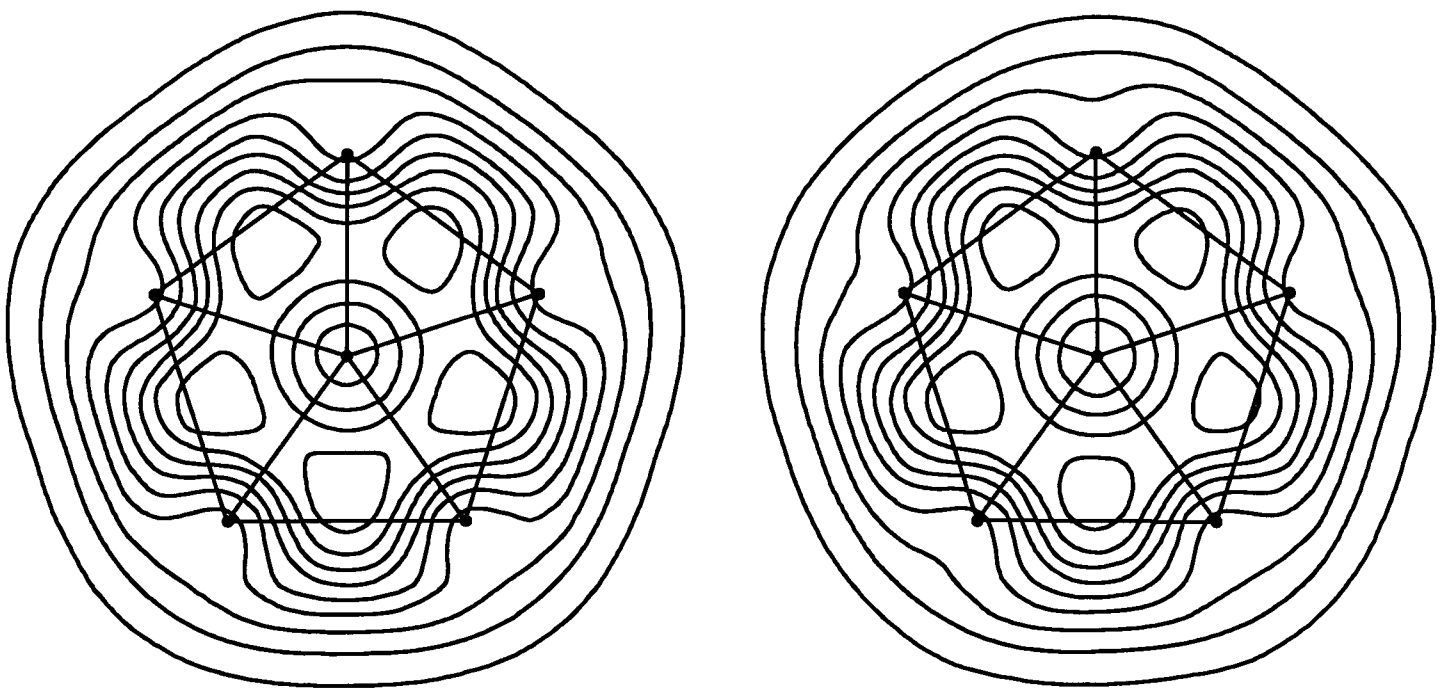


Figure 4.10: The valence electron density maps for the pentagonal pyramidal Na_6 geometry. The left hand map was calculated in LSD, the right in SIC.

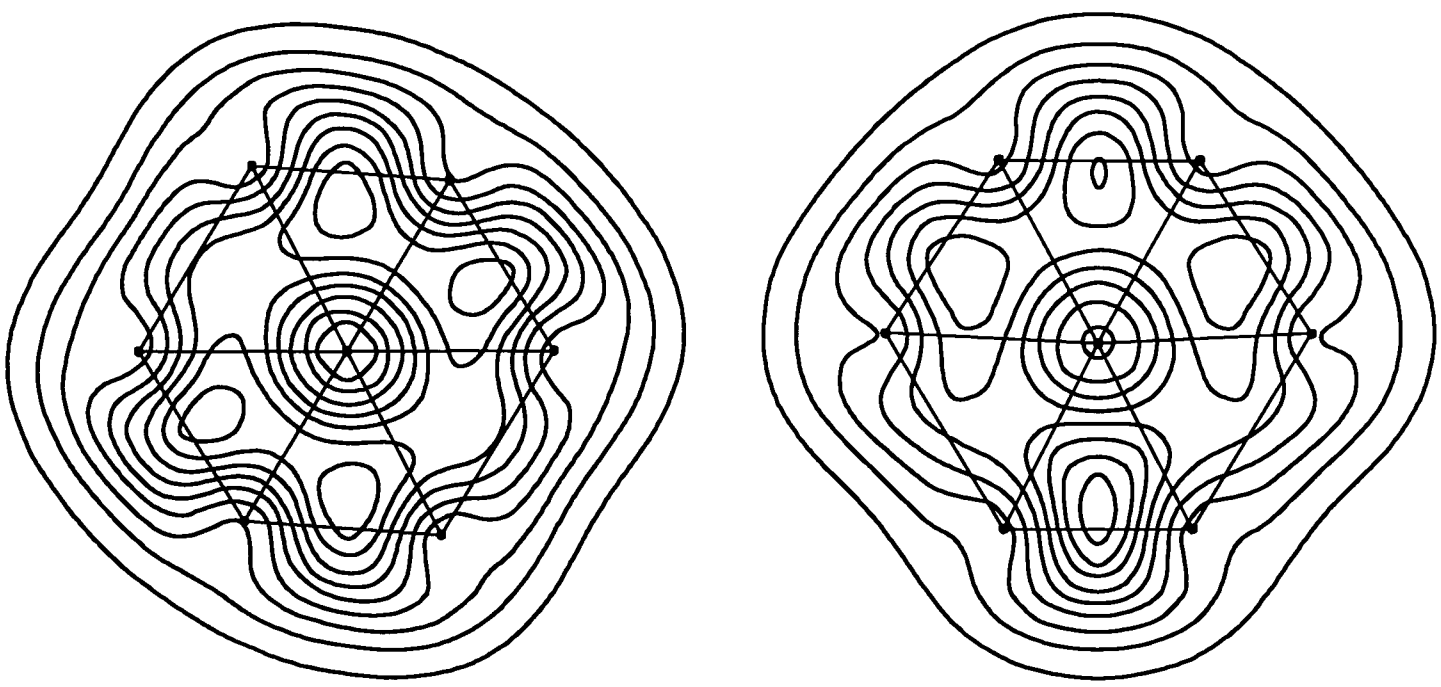


Figure 4.11: The valence electron density maps for the planar hexagonal Na_7 geometry. The left hand map was calculated in LSD, the right in SIC.

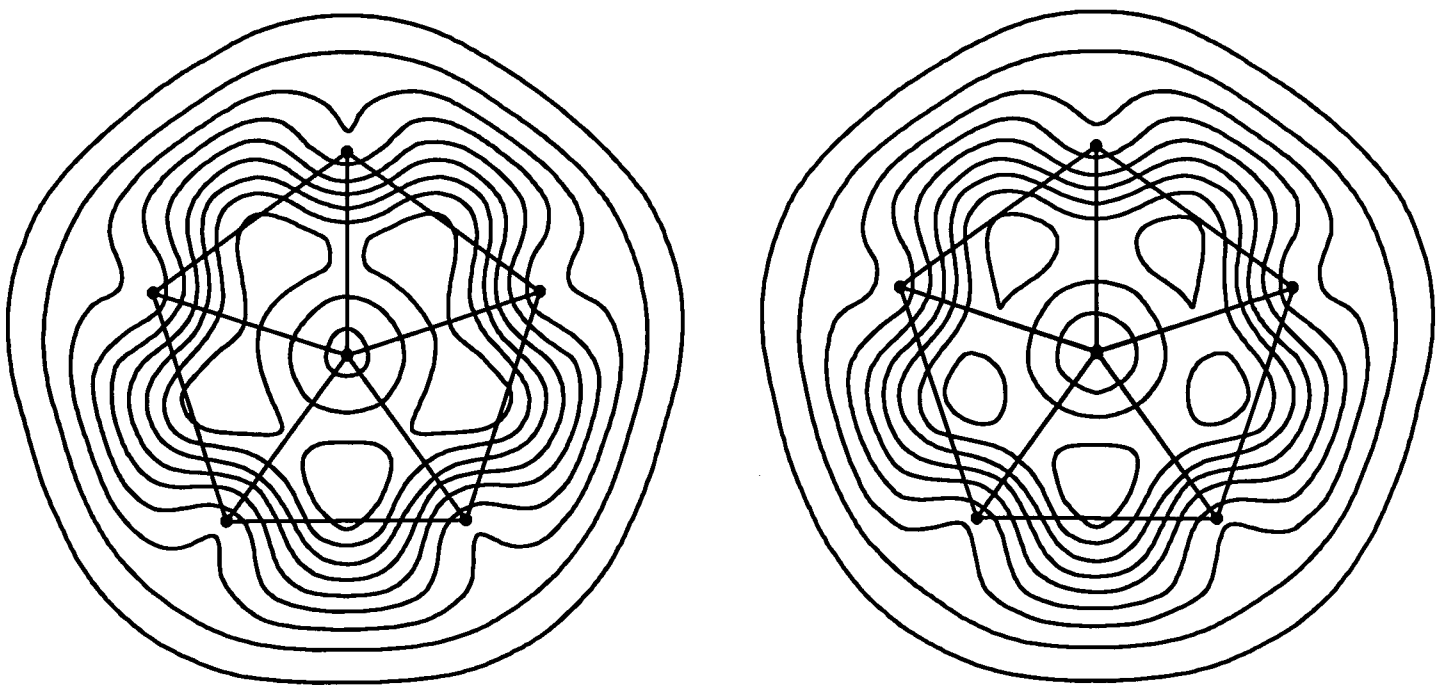


Figure 4.12: The valence electron density maps for the pentagonal bipyramidal Na_7 geometry. The left hand map was calculated in LSD, the right in SIC.

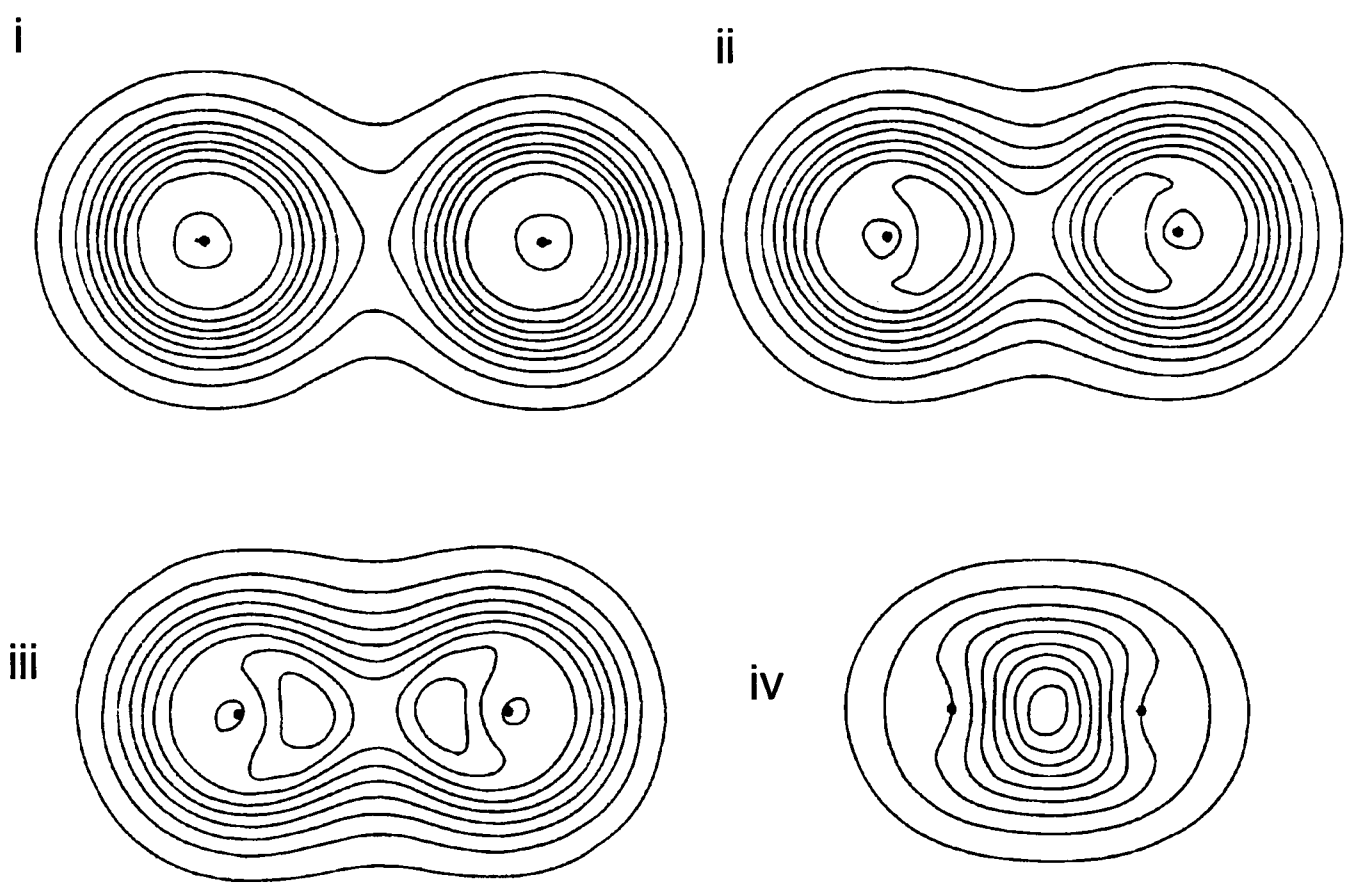


Figure 4.13: Na_2 valence electron densities for decreasing separation of the ions. The separations are (i) 11.0 a.u., (ii) 9.87 a.u., (iii) 8.85 a.u., (iv) 6.05 a.u.

within triangles of sodium atoms. This can be rationalised by suggesting that there is a tendency towards two electron, three centre bonding. Similar observations were made by McAdon and Goddard using generalised valence bond theory (GVB) for lithium clusters [62]. From their findings they deduced the following rules for three dimensional metallic clusters:

1. Orbitals (each with one electron) are localised in different tetrahedral holes where possible.

2. If necessary, two orbitals may be placed in one tetrahedron (localised on opposite faces or edges), but they must be spin paired.

3. No more than 3 electrons may be distributed between a pair of *edge-shared* tetrahedra.

4. No more than 2 electrons may be distributed between a pair of *face-shared* tetrahedra, and these must be spin paired.

5. Additional electrons must be in surface orbitals at edge or face sites that do not share edges with occupied tetrahedra.

6. It is unfavourable to occupy more than four tetrahedra (or pairs of tetrahedra) sharing one central atom.

These rules may be rationalised by the tendency of electrons to spin pair, and for spin pairs to maximise their separation. Applying these considerations to the sodium clusters found in this work it can be seen that three dimensional structures would have unfavourable interactions of electrons with the same spin that would be forced too close to each other. To see this more clearly I shall consider the specific cases of Na_4, and Na_6.

For Na_4 use of pair-additive potentials would suggest that the tetrahedral geometry as this maximises the number of bonds. However McAdon and Goddard [62] have pointed out that this would lead to four orbitals localised on each face of the tetrahedron, thus forcing orbitals of the same spin into close proximity. A distortion to the planar rhombic geometry then maximises both spin pairing and separation between spin pairs. The result is a pair of three centre, two electron bonds, the electron pairs appearing as the maxima in the valence electron densities. How then does this fit with the orbitals produced by LSD and SIC? Figure 4.14 shows the total valence and valence orbital densities for Na_4 using LSD and SIC. In LSD the choice of orbitals is arbitrary to within a unitary transformation, the ones shown are the Kohn-Sham orbitals, ie. those that diagonalise the Hamiltonian matrix. It can be seen that although the total valence density agrees with the McAdon and Goddard picture, the valence orbitals are better described as s-like and p-like, ie. more akin to the jellium model. This adds support to the jellium

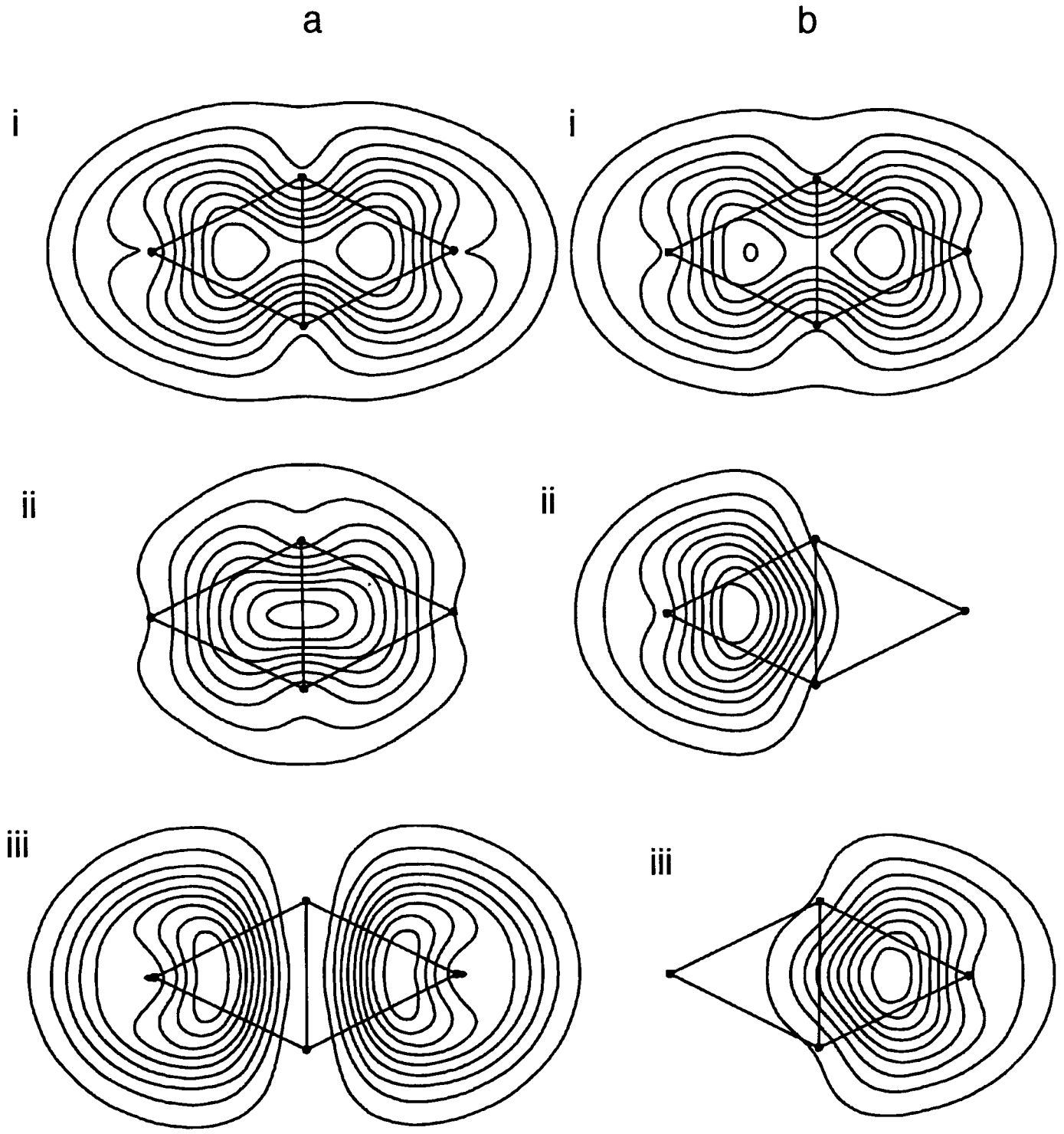


Figure 4.14: The valence electron density (i) and the orbital density maps (ii-iii) for the triangular Na_4 geometry. The orbital density maps are all for the same spin. The opposite spins give identical densities. (a) is using LSD, and (b) is using SIC.

model and shows that the two approaches are equivalent, and can be viewed as the most delocalised description. The SIC orbitals however are unique and localised, and it can be seen that the most natural description is of two localised spin pairs involved in three centre, two electron bonding, ie. in direct agreement with the McAdon and Goddard picture. In principle, as the total valence densities are almost identical, the LSD orbitals could be transformed into the equivalent set to the SIC. However in the SIC this localised set fall out quite naturally.

It is also instructive to look at the situation for square Na_4. This is not a minimum because a Jahn-Teller distortion (to the rhombus) will lower the energy. The total valence density using SIC is shown in figure 4.15. It can be seen that the system is almost completely spin unpaired. The single electron orbitals are arranged between pairs of atoms with the spin alternating round the square in an "antiferromagnetic" fashion. Again this is in accord with the principles of maximising the overlap between orbitals of opposite spin and minimising it between orbitals of the same spin. A similar pattern has been found for larger rings of other metal atoms [63] in GVB calculations.

For Na_6 there are two geometries found. The total valence and orbital densities for both, using LSD and SIC are shown in figure 4.16, and figure 4.17. For LSD, as for Na_4, the Kohn-Sham orbitals are shown. These, in both cases, can be described as an s-type and two p-type orbitals; this character being especially pronounced for the pentagonal pyramidal structure, which is not surprising as it is more "spherical" than the triangular geometry. Again this connects with the jellium picture. In SIC though the picture is quite different. The single particle orbitals for the triangular geometry are localised in triangles of atoms, with no two triangles adjacent, ie. optimal from the arguments described above. For the other geometry though the spin up and spin down orbitals are no longer identical, and although the total valence density has maxima located in triangles of atoms, the orbitals follow no real pattern. The reason is that in this geometry it is impossible to place a spin pair in a triangle of atoms without having two adjacent spin pairs. It is worth noting that with SIC it is the triangular geometry that is the *more* stable as predicted by these arguments, while it is *less* stable using LSD. Clearly then SIC orbitals provide a natural basis for predicting the likely stability of clusters. Care should be taken though as it can be seen from the binding energies in table 4.14 that the energy differences involved are small and other factors may become important. GVB calculations without the "perfect-pairing" assumption used by McAdon and Goddard have recently confirmed the instability of the pentagonal structure with respect to the triangular one [89]

Na_3 does not exhibit this three centre, two electron bonding, simply because it is not geometrically possible. In fact the bonding for both Na_3 isomers is a compromise that is actually closer to the "classical" two centre

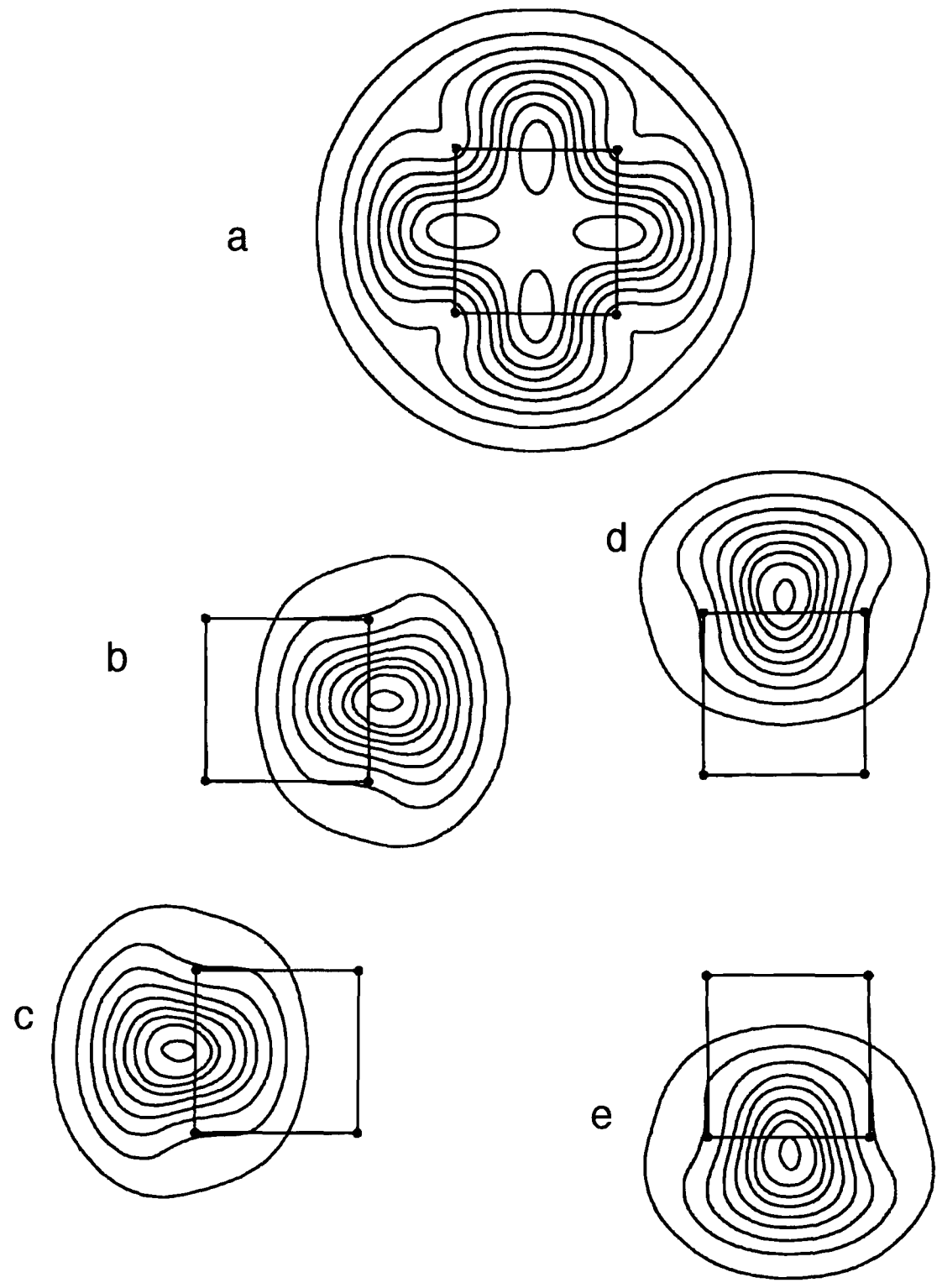


Figure 4.15: The valence electron density (a) and the orbital density maps (b-e) for square Na_4, using SIC. The density maps (b), and (c) have the same spin, and (d), and (e) have the opposite spin.

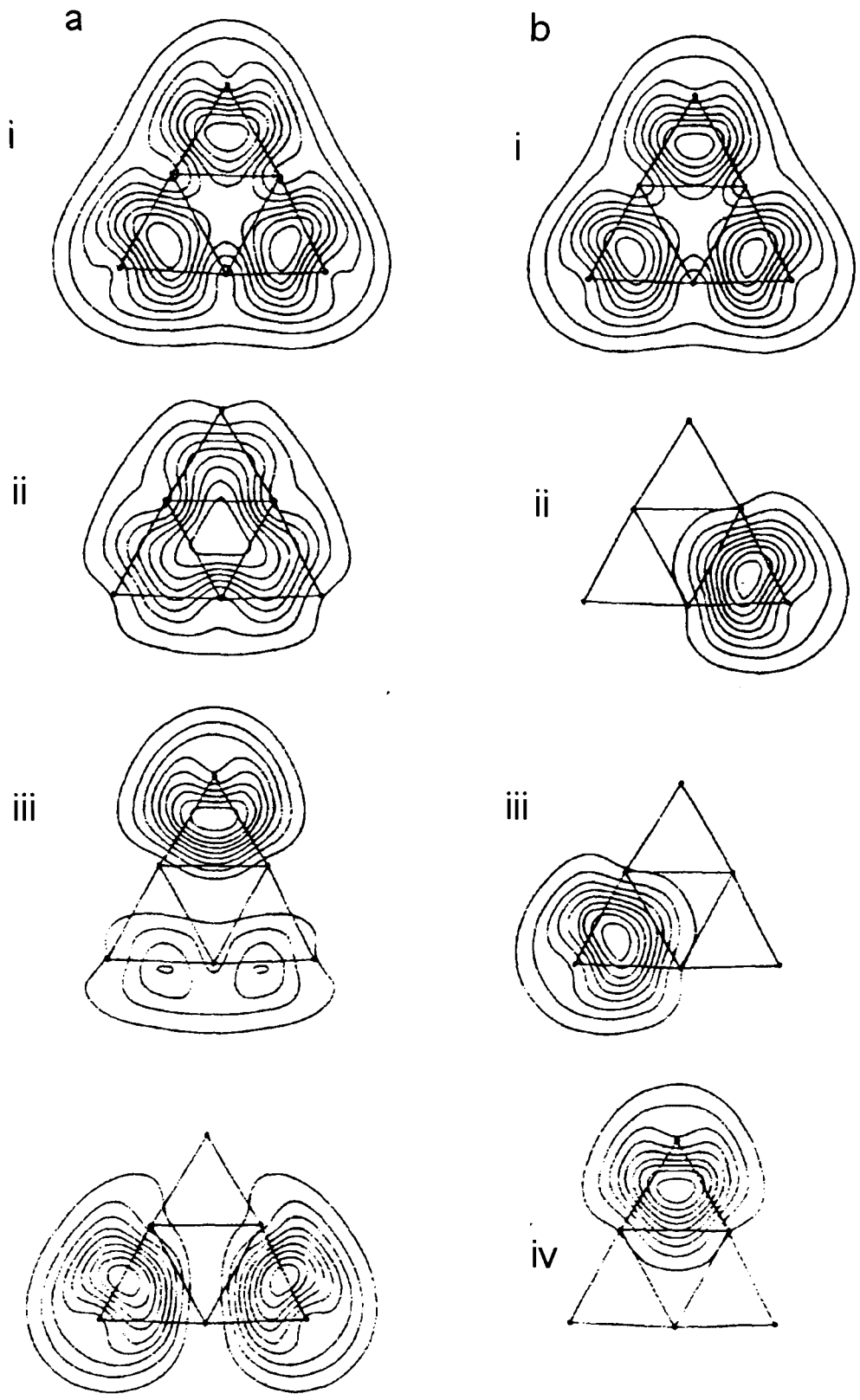


Figure 4.16: The valence electron density (i) and the orbital density maps (ii-iv) for the triangular Na_6 geometry. (a) is using LSD, and (b) is using SIC.

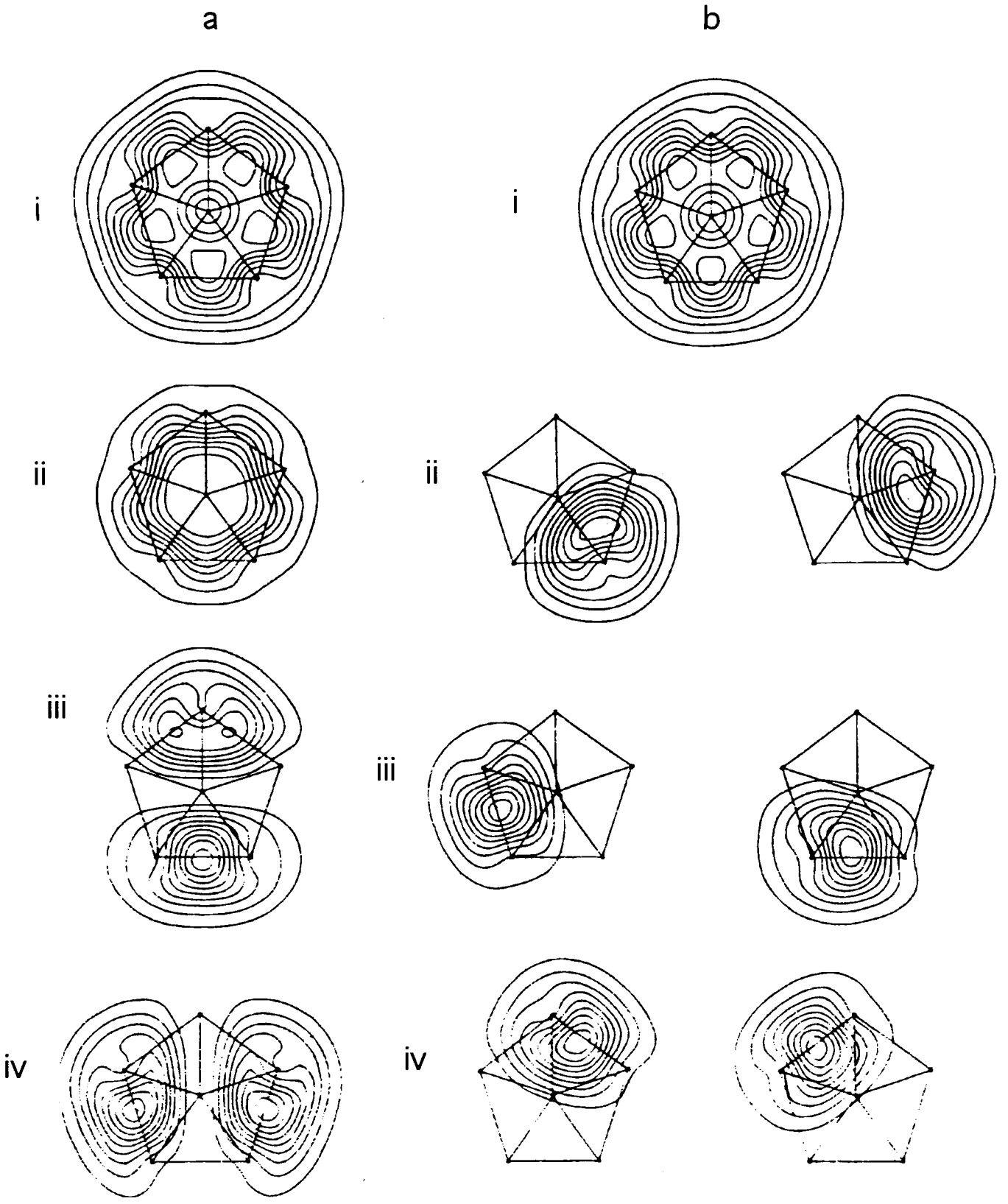


Figure 4.17: The valence electron density (i) and the orbital density maps (ii-iv) for the pentagonal pyramidal Na_6 geometry. (a) is using LSD, and (b) is using SIC.

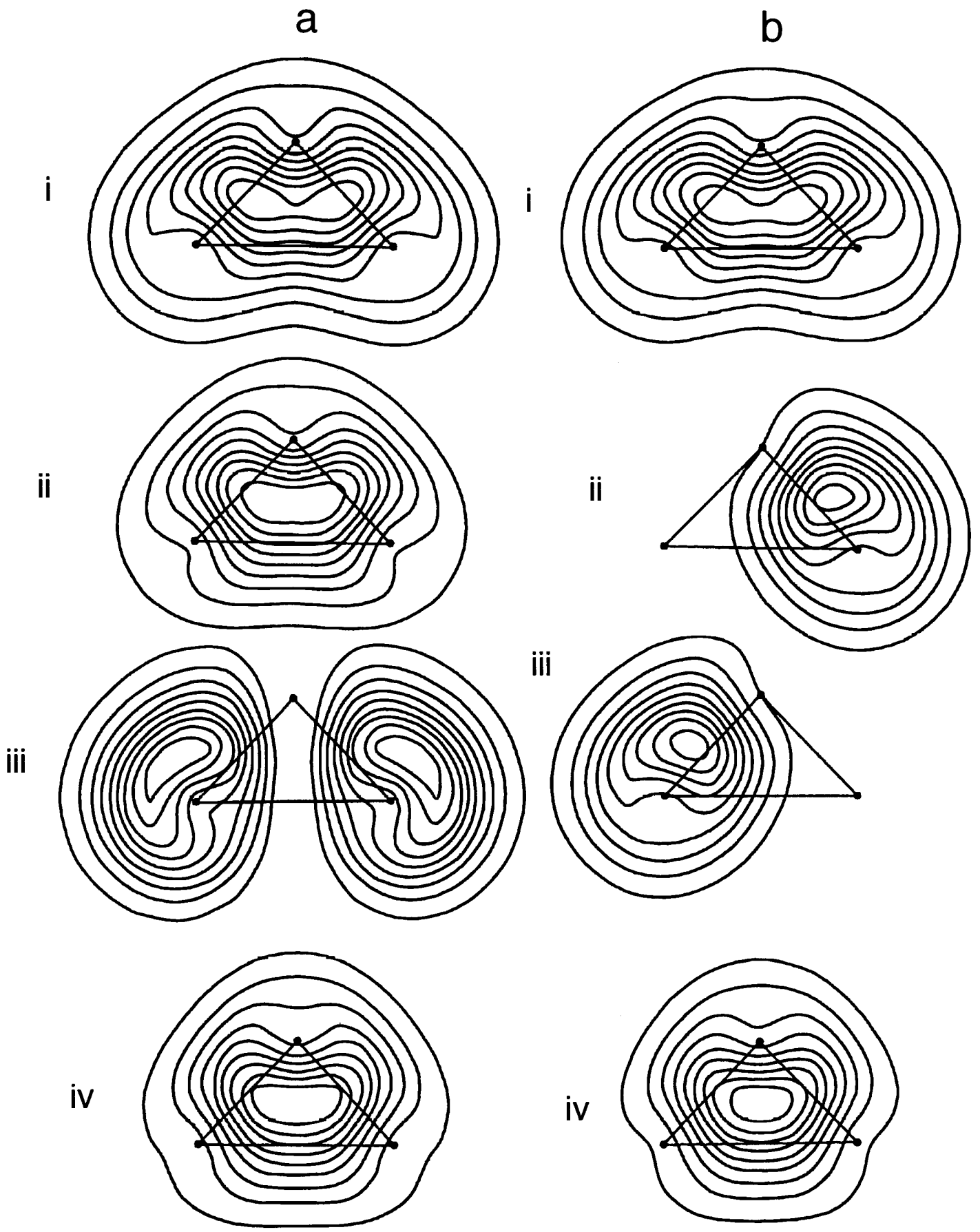


Figure 4.18: The valence electron density (i) and the orbital density maps (ii-iv) for the obtuse Na_3 geometry. (ii) and (iii) are for the same spin. (a) is using LSD, and (b) is using SIC.

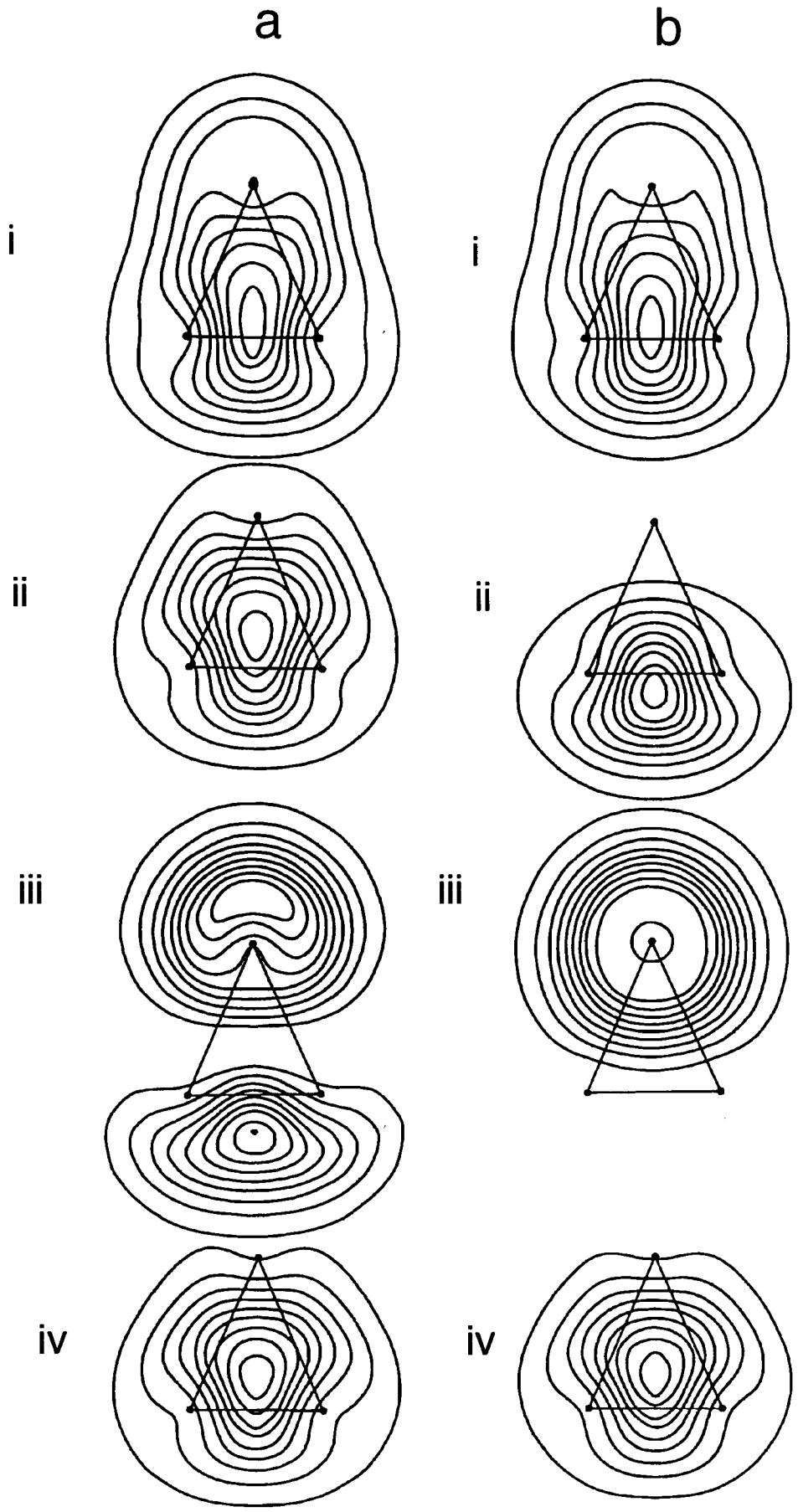


Figure 4.19: The valence electron density (i) and the orbital density maps (ii-iv) for the acute Na_3 geometry. (ii) and (iii) are for the same spin. (a) is using LSD, and (b) is using SIC.

two electron picture. Figure 4.18 shows the total valence electron and orbital densities for the obtuse geometry, and figure 4.19 the equivalent densities for the acute geometry. From the total valence density it can be seen that for the obtuse geometry there are two minima located at the mid-points of the two short "bonds". This tends to imply that there is a compromise between forming two two centre bonds and a three centre bond. Looking at the orbital densities once more the LSD Kohn-Sham orbitals appear as a doubly occupied p-type orbital reminiscent of the jellium picture. For SIC though two orbitals of the same spin are localised on the midpoints of the two short "bonds", whilst the electron of opposite spin is localised in the centre of the triangle. Clearly this electron is trying to form a bond with the other two electrons, resulting in what could be loosely described as two "two centre, $1\frac{1}{2}$ electron" bonding.

The case for the acute geometry though is quite different. The total valence density maps have a single maximum in the centre of the short "bond", implying a single actual bond. The LSD orbitals are once more s-, and p-like in nature. However the SIC orbitals show that essentially there is an electron pair indeed localised on the short bond length whilst the remaining electron is localised on the apical atom. Here the picture then is of an Na_2 dimer with a loosely bound sodium atom.

As already mentioned the acute isomer is probably not stable at all, but the transition state for the pseudorotation of Na_3. Clearly then for this pseudorotation to occur one of the semi-bonds in the obtuse geometry must break leading the the weakly bound $Na \cdots Na_2$ cluster, followed by reformation of the bond. Note that the LSD Kohn-Sham orbitals give little insight into this process, being virtually unchanged throughout. However once more the localised SIC orbitals have a useful interpretive value.

4.3 Static Electric Polarizabilities

One of the difficulties in discussing cluster geometries is that there is no structural data for the free cluster. Indeed the only direct structural data available is from electron spin resonance results for the trimer and heptamer in a rare gas matrix [56]. However indirect support for a particular structure over another may be obtained by comparing properties calculated for the different isomers with experiment. Good agreement clearly would support the reliability of a particular isomer. This section then will consider the calculation of the static electric polarizabilities of the clusters discussed in the previous sections, in LSD and SIC, and compare these results with experiment.

To determine the static electric polarizability the external potential was modified to include the interaction of the electron density with an applied

static electric field, this extra term being $\mathbf{F} \cdot \mathbf{r}$. This is equivalent to adding an extra term E_{int} to the total energy to account for the interaction, where,

$$E_{\text{int}} = -\int \rho(\mathbf{r})\mathbf{F} \cdot \mathbf{r}\, d\mathbf{r}. \tag{4.1}$$

The ions were kept static and electronic minimisations using the CG method were performed using an electric field equivalent to a potential increasing linearly across the cell.

As the clusters studied are neutral their dipole moments $\boldsymbol{\mu}$ can be calculated as the sum of the ionic and electric contributions,

$$\boldsymbol{\mu} = \boldsymbol{\mu}^{\text{ion}} + \boldsymbol{\mu}^{\text{el}} = \sum_j Z_j \mathbf{R}_j - \int \mathbf{r}\rho(\mathbf{r})d\mathbf{r}, \tag{4.2}$$

where Z_j and $\mathbf{R}_j$ are the charge and position of the j^{th} core. Some of the clusters have permanent dipole moments $\boldsymbol{\mu}_0$ in the absence of an applied external field.

The symmetric polarizability tensor α is related to the induced dipole $\mathbf{p}_{\text{ind}}$ via,

$$\mathbf{p}_{\text{ind}}(\mathbf{F}) = \boldsymbol{\mu}(\mathbf{F}) - \boldsymbol{\mu}_0 = \alpha \cdot \mathbf{F} + O(\mathbf{F}^2). \tag{4.3}$$

In other words, α is the derivative of the induced dipole with respect to the field $\mathbf{F}$, provided the field is small enough for the linear response approximation to hold. By applying then in different directions, a field along the x,y,z axes of the cell being chosen, it is simple to solve for α. The solution is made even simpler by the fact that the principle axes of the symmetric polarizability tensor are uniquely determined by the symmetry of the cluster. Thus the principle elements of the polarizability tensor, which are all we need to determine the spherically averaged polarizability, $\bar{\alpha}$, which is the result of experiments, are obtained by arranging that the applied field coincides with the principle axes, so that the off diagonal elements are zero, and,

$$\alpha_{ii} = \frac{\mathrm{p}_{\text{ind,i}}}{F_i}, \tag{4.4}$$

where i indicates x,y, or z. Should this be inconvenient the matrix of $\mathbf{p}_{\text{ind}}$ for the three different applied fields can simply be diagonalised to yield α_{xx}, α_{yy}, and α_{zz}.

The remaining consideration then is what magnitude of applied field should be used. For accuracy larger fields are preferred so as to reduce problems from purely numerical effects. However the field must be small enough that the system is still within the linear response régime. Table 4.15 shows the variation in α_{xx} $(=\bar{\alpha})$, with field strength for the sodium atom calculated in the above way, assuming linear response. Clearly from this a field of 5×10^{-4}a.u. is safely in the linear response régime, so this field was

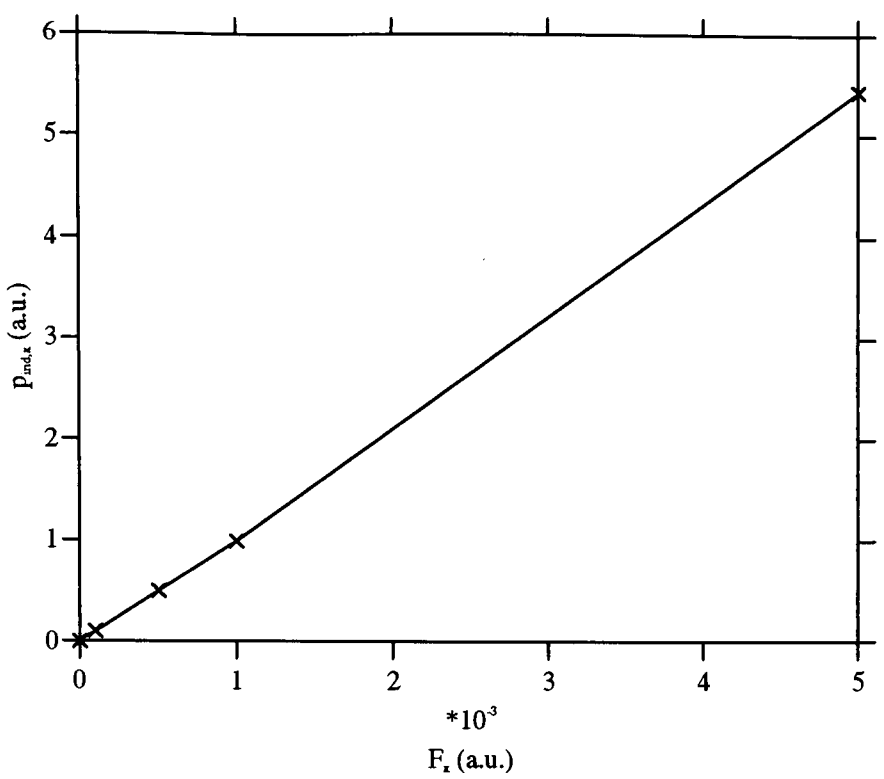


Figure 4.20: Induced dipole moment, $p_{ind,x}$, versus applied field in x-direction, F_x, for Na_4 using LSD.

used in all further calculations. Figure 4.20 shows the variation in $p_{ind,x}$ for Na_4 using LSD. This again shows that a field of 5×10^{-4} a.u. is a suitable field strength.

As the ions are not allowed to relax, a reasonable approximation for sodium [69], then the static polarizability can also be calculated from the energy difference,

$$\begin{aligned} \Delta E &= E_{\rm tot}(\mathbf{F}) - E_{\rm tot}(0) \\ &= -\boldsymbol{\mu_0} \cdot \mathbf{F} - \frac{1}{2}\mathbf{F} \cdot \alpha \cdot \mathbf{F} + O(\mathbf{F}^3). \end{aligned} \tag{4.5}$$

This provides a check on self consistency, and for the calculations checked ΔE was consistent with α from equation 4.4.

The results of these calculations using LSD and SIC are shown in tables 4.16, and 4.17, whilst table 4.18 shows the results due to Moullet *et al.* [69] and table 4.19 shows the experimental results due to Knight *et al.* [42]. The spherically averaged polarizabilities $\bar{\alpha} = \frac{1}{3}(\alpha_{xx} + \alpha_{yy} + \alpha_{zz})$ are compared in figure 4.21 along with the experimental results due to Knight *et al.* [42]. Where more than one isomer has been found, the polarizability for the most stable is plotted.

From figure 4.21 it can be seen that both the SIC and LSD results are in good agreement with experiment. The SIC polarizabilities are smaller

	α_{xx}	
Field (a.u.)	LSD	SIC
1×10^{-4}	158.1	159.7
2×10^{-4}	158.1	159.7
3×10^{-4}	158.1	159.7
4×10^{-4}	158.1	159.7
5×10^{-4}	158.1	159.7
6×10^{-4}	158.1	159.7
7×10^{-4}	158.2	159.7
8×10^{-4}	158.2	159.8
9×10^{-4}	158.2	159.8
1×10^{-3}	158.3	159.8
2×10^{-3}	159.3	160.5
3×10^{-3}	160.9	161.6
4×10^{-3}	163.6	163.2
5×10^{-3}	167.7	165.8

Table 4.15: Variation of α_{xx} $(=\bar{\alpha})$ in a.u. with field for the sodium atom in LSD and SIC, calculated assuming linear response.

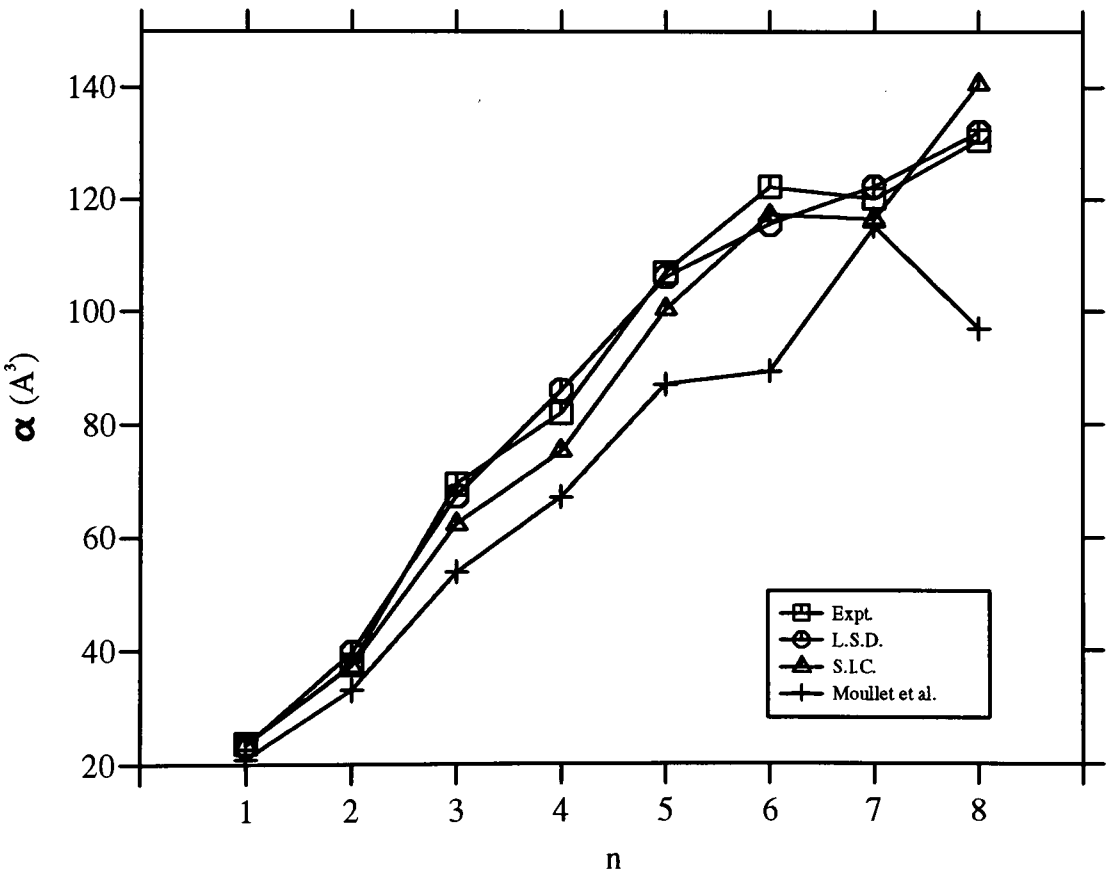


Figure 4.21: Spherically averaged polarizabilities $\bar{\alpha} = \frac{1}{3}(\alpha_{xx} + \alpha_{yy} + \alpha_{zz})$. The experimental data is due to Knight *et al.* [42].

	α_{xx}	α_{yy}	α_{zz}	$\bar{\alpha}$
Na	23.4	23.4	2346	23.4
Na_2	55.4	31.7	31.7	39.6
Na_3 (acute)	65.0	92.0	42.6	66.5
Na_3 (obtuse)	103.3	56.2	42.4	67.3
Na_4 (regular)	145.4	63.4	49.1	86.0
Na_5	158.9	103.1	56.2	106.1
Na_6 (D_{3h})	155.7	154.5	63.2	124.5
Na_6 (C_{5v})	140.7	140.7	65.2	115.5
Na_7 (D_{2h})	189.8	182.2	70.2	147.4
Na_7 (D_{5h})	134.4	134.7	97.7	122.3
Na_8	124.9	124.8	146.2	132.0

Table 4.16: Diagonal components of the polarizability tensor and the spherically averaged polarizability $\bar{\alpha} = \frac{1}{3}(\alpha_{xx} + \alpha_{yy} + \alpha_{zz})$ in $Å^3$ using LSD.

	α_{xx}	α_{yy}	α_{zz}	$\bar{\alpha}$
Na	23.6	23.6	23.6	23.6
Na_2	50.1	30.9	30.9	37.3
Na_3 (acute)	57.5	81.4	41.7	60.2
Na_3 (obtuse)	91.6	54.1	41.3	62.3
Na_4 (regular)	118.0	60.3	47.4	75.2
Na_5	145.0	101.7	54.5	100.4
Na_6 (D_{3h})	145.5	144.4	61.8	117.2
Na_6 (C_{5v})	189.2	158.3	64.1	137.2
Na_7 (D_{2h})	213.2	222.5	79.1	171.6
Na_7 (D_{5h})	127.1	126.5	96.0	116.5
Na_8	140.6	140.6	140.6	140.6

Table 4.17: Diagonal components of the polarizability tensor and the spherically averaged polarizability $\bar{\alpha} = \frac{1}{3}(\alpha_{xx} + \alpha_{yy} + \alpha_{zz})$ in $Å^3$ using SIC.

	α_{xx}	α_{yy}	α_{zz}	$\bar{\alpha}$
Na	21.0	21.0	21.0	21.0
Na_2	47.2	26.1	26.1	33.1
Na_3 (acute)	74.3	50.6	42.6	53.0
Na_3 (obtuse)	78.8	46.6	42.4	53.8
Na_4 (regular)	104.8	49.9	46.6	67.1
Na_5	118.3	81.9	60.9	87.0
Na_6 (D_{3h})	117.4	115.1	67.5	100.0
Na_6 ($C_{5\nu}$)	105.1	105.2	57.9	89.4
Na_7 (D_{2h})	99.7	100.1	75.4	91.7
Na_7 (D_{5h})	144.5	129.8	71.1	115.1
Na_8	93.2	92.6	105.3	97.0

Table 4.18: Diagonal components of the polarizability tensor and the spherically averaged polarizability $\bar{\alpha} = \frac{1}{3}(\alpha_{xx} + \alpha_{yy} + \alpha_{zz})$ in $Å^3$ due to Moullet *et al.* [69].

	$\bar{\alpha}$
Na	23.6
Na_2	37.5
Na_3	69.4
Na_4	81.9
Na_5	106.9
Na_6	122.2
Na_7	120.1
Na_8	130.6

Table 4.19: Experimental static electric polarizabilities due to Knight *et al.* [42].

than the LSD as might be expected due to the more localised nature of the states in SIC. It is clear from the figure that while LSD produces numerically reasonably accurate results, the SIC reproduces better the trends shown in the experimental data. However, the assertion by Moullet *et al.* [69] that the discrepancy between their data is due to the shortcomings of LSD is only partially justified. Certainly the value obtained for the sodium atom in SIC is in excellent agreement with experiment. The error in the LSD though is not significant, and for the clusters the errors in both are of similar magnitude. As pointed out above though the errors in SIC are more systematic. It should be noted though that no account has been taken of core polarization effects, although these may be included to some extent in the pseudopotential. An error is thus *expected* which is proportional to the cluster nuclearity. In other words one might expect to have to add a term like $n\bar{\alpha}_{\text{ion}}$ where n is the number of atoms in the cluster and $\bar{\alpha}_{\text{ion}}$ the polarizability of the ion core, which for sodium is about 1 a.u.

Is it possible though to deduce the experimental geometry from such data? For Na_3 the answer is unequivocal. Both LSD and SIC give best agreement for the obtuse geometry, which both had found to be the most stable. The case of Na_6 is more interesting. Both LSD and SIC give best agreement for the triangular geometry, even though this is *not* the ground state in LSD. This appears to back the arguments given in the last section. For Na_7 agreement is again obtained, this time for the bicapped pentagonal pyramid predicted by both methods to be the ground state. Thus on face value the spherically averaged polarizability does seem to be a useful guide to the true geometries of the clusters, and where disagreement occurs this seems to back the conclusions of SIC. However care should be taken, especially when the differences in polarizabilities is small, as the error bars for the experimental data are not insignificant, and particularly for large clusters core polarization effects may be significant.

The experimental polarizabilities have the drawback that information about the anisotropy of the polarizability tensor is lost. However some of this detail is preserved in the total absorption cross sections of alkali metal clusters [98, 120, 11]. Kresin [48] has fitted these results to a collective resonance model. This relates the resonance frequency, ω_i, to the principle values of the static polarizability tensor, α_{ii},

$$\omega_i^2 = \frac{ne^2}{m_e \alpha_{ii}}, \tag{4.6}$$

where n is the number of valence electrons. This result assumes that all the valence electron oscillator strength goes into the Mie resonance. This is clearly a crude approximation but it appears to give moderately reliable results. At a purely qualitative level then this leads us to predict that the spectra will show either one, two, or three major peaks. In particular for

Na_8 LSD predicts that two peaks should be present, one at 478 nm and the other at 442 nm, whilst SIC predicts a single peak at 490 nm. This would appear to support the T_d structure found using SIC. However the width of the experimental resonance is about 70 nm and this may in fact contain two peaks that actually merge, thus the evidence is not entirely conclusive. It is clear that a more detailed line shape analysis is required for definitive conclusions. Also, as can be seen for Na_7 the experimental spectra are not yet fully consistent [119]. In their comparison with previous experiments, Wang *et al.* show a single resonance peak, whilst Selby *et al.* [97] show two peaks. Finally it should be noted that the experiments are carried out at finite temperature and so more than one isomer may be present. Indeed bearing in mind the flatness of the potential energy surfaces mentioned earlier, the cluster at finite temperatures may be vibrating between many isomers.

In conclusion then SIC appears to be more accurate than LSD for determining polarizabilities, and, just as important, accurately reproduces the experimental trends. Accurate determination of the static electric polarizability does provide indirect structural evidence. However this should be used with care. Simple models for the absorption cross section of clusters do not appear to be sufficiently reliable to definitively determine the experimental geometry. It should also be noted that the experimental results for the polarizability and the cross sections have large error bars, and may not be sufficiently accurate for reliable comparison.

4.4 Vibrational Frequencies

Another potential method for helping in structure determination is the calculation of vibrational frequencies. At present the only experimental data available is for Na_3 [12] so currently its use is somewhat restricted. However this section will describe how such calculations can be made using LSD and SIC and compare the results from these two approximations.

The method used is based on the harmonic approximation relating the forces on the atoms to their displacement,

$$\mathbf{F} = -\mathbf{G}\boldsymbol{\delta}, \tag{4.7}$$

where $\mathbf{F}$ is the 3N vector describing the forces on the atoms and $\boldsymbol{\delta} = \mathbf{R} - \mathbf{R_0}$, where $\mathbf{R_0}$ represents the 3N cartesian coordinates of the initial geometry, and $\mathbf{R}$ those of the displaced geometry. N is the number of atoms in the cluster. $\mathbf{G}$ is the force constant matrix, the ij^{th} element of which is the second derivative of the potential with respect to the i^{th} and j^{th} Cartesian coordinates. The square roots of the eigenvalues ε_i of $\mathbf{G}$ are the vibrational frequencies of the cluster as,

$$\varepsilon_i = m_e \omega_i^2, \tag{4.8}$$

and $m_e = 1$ in atomic units.

Thus to determine the vibrational frequencies each atom in turn was displaced a small distance along one of the Cartesian axes, and the forces on each atom determined by a conjugate gradient minimisation. Repeating this for all three Cartesian axes for all the atoms yields 3N force vectors $\mathbf{F}_i$, and 3N displacement vectors. These can be written in matrix form to give,

$$(\mathbf{F}_1, \cdots, \mathbf{F}_i, \cdots \mathbf{F}_{3N}) = -\mathbf{G}\,(\boldsymbol{\delta}_1, \cdots, \boldsymbol{\delta}_i, \cdots, \boldsymbol{\delta}_{3N})\,. \tag{4.9}$$

In practice as the forces at the equilibrium geometry are not exactly zero, these residual forces were subtracted from the forces after displacement to give $\boldsymbol{\Delta}\mathbf{F}$. Thus equation 4.9 can be written as,

$$\boldsymbol{\Delta}\mathbf{F} = -\mathbf{G}\boldsymbol{\delta}, \tag{4.10}$$

where it should be noted that $\boldsymbol{\Delta}\mathbf{F}$ and $\boldsymbol{\delta}$ now represent the force and displacement matrices. $\mathbf{G}$ is easily found by matrix methods and the eigenvalues, and hence the vibrational frequencies, ω_i, can be determined. Note though that of the 3N eigenvalues generated using this method only 3N-6 (3N-5 for linear molecules) correspond to vibrations. The six (or five) rotational and translational modes are easily spotted as they give negative eigenvalues and hence imaginary frequencies. The internal coordinates for the motion can easily be found as they are given by the eigenvectors of $\mathbf{G}$. Seeley and Keyes [96] have applied this harmonic normal mode analysis to Lennard-Jones liquids.

4.4.1 Na_3

The results for Na_3 are shown in table 4.20 along with the LSD results due to Moullet *et al.* [69], and Martins *et al.* [61], along with anharmonically corrected results of Martins *et al.* [108], and the experimental results due to Broyer *et al.* [12]. The SIC frequencies are lower than the LSD results, and for the two lower frequencies are in far better agreement with experiment. It should be noted though that when Thompson *et al.* [108], using the data of Martins *et al.*, took into account anharmonicity effects, the agreement with experiment was greatly improved. The LSD results from this work however are markedly different from both the Moullet *et al.*, and the Martins *et al.* results. It is not clear then how much consideration of anharmonicity effects would alter the LSD and SIC results.

4.4.2 Na_4

The vibrational frequencies for Na_4 are given in table 4.21. In contrast to the case for Na_3, the SIC frequencies are higher than the LSD. It should be noted that the very low frequencies found for LSD correspond to very

	$\omega(\mathrm{cm}^{-1})$					
Vibration	LSD	SIC	LSD [69]	LSD [61]	LSD [108]	Expt. [12]
ω_1	146.5	130.4	154	148	142	139
ω_2	126.9	91.6	109	68	94	87
ω_3	90.0	40.5	64	63	58	48

Table 4.20: Vibrational frequencies of Na_3.

	$\omega(\mathrm{cm}^{-1})$	
Vibration	LSD	SIC
ω_1	146.1	154.4
ω_2	126.9	140.1
ω_3	90.0	99.5
ω_4	68.5	79.1
ω_5	38.5	71.5
ω_6	16.2	41.6

Table 4.21: Vibrational frequencies of Na_4.

small force differences and are probably not too reliable. In the absence of experimental data and considering the comment on anharmonicity effects for the Na_3 cluster, it does not seem possible to draw any significant conclusions.

4.4.3 Conclusions

It is clear from the Na_3 data that as the clusters are very "floppy" molecules, anharmonicity effects make a significant contribution to the vibrational frequencies. As the differences between LSD and SIC, and indeed between LSD results using different pseudopotentials, are of the same magnitude as these effects it would appear to be pointless to attempt a meaningful comparison. For a useful analysis it appears clear then that incorporation of anharmonicity effects will be necessary. Also, not surprisingly, the choice of pseudopotential is at least as significant as the self-interaction. However should experimental data become available, conclusion as to the geometry of a particular cluster may still be possible on symmetry grounds.

Chapter 5

Control of the Adiabatic Electronic State in the CP Method

As outlined in section 2.2.2 the CP method is an efficient approach for performing molecular dynamics essentially *ab initio*, subject to the approximations used to find the electronic ground state. In this chapter I will briefly outline the conditions under which the CP algorithm breaks down, then go on to consider how this problem can be alleviated. I will use Na_2 bond formation and bond breaking as a model system with which to refine the procedure.

5.1 Breakdown of the CP Method

The success of the method is that, for many problems, the CP equations of motion automatically update the electronic state as the ions move, at each step. There is no need to re-optimise to find the Born-Oppenheimer electronic ground state. As already shown these equations take the form,

$$\mu\ddot{\psi}_{\alpha\sigma} = -\frac{\delta E_{\rm elec}}{\delta \psi^*_{\alpha\sigma}} + \sum_\beta \lambda^{\sigma *}_{\alpha\beta}\psi_{\beta\sigma}, \tag{5.1}$$

$$M_{\rm I}\ddot{\mathbf{R}}_{\rm I} = -\nabla_{\rm I}(E_{\rm elec} + E_{\rm II}), \tag{5.2}$$

where $\psi_{\alpha\sigma}$ are orbitals, introduced to represent the total density in the Kohn-Sham realisation of DFT [47], which are kept orthonormal by the constraint expressed in the second term on the r.h.s. ($\lambda^\sigma_{\alpha\beta}$ are Lagrange multipliers). $E_{\rm elec}$ is the electronic energy functional and $\mathbf{R}_{\rm I}$ are the ion positions, with $E_{\rm II}$ the direct ion-ion term. These equations are of the same form as the equations of motion of a set of classical, rigid molecules [13, 15, 92]. As

already shown (section 2.2.2) they may be integrated simultaneously with a suitable time step, using normal MD methods [1]. A run is started from an electronic state which corresponds to the ground state for the initial ionic positions.

The wavefunction motion generated by the first equation is often called the "fake" motion and the inertia parameter μ is the "fake mass". As already stated, in "favorable" circumstances, the fictitious motion will carry the orbitals to the new ground state as the ions move. With the electrons in their ground state, the forces on the ions due to the electrons ($-\nabla_{\mathrm{I}} E_{\mathrm{elec}}$) may be calculated from the Hellman-Feynman Theorem, and the ions move along the adiabatic potential surface.

Since the CP equations of motion are derived from a total Lagrangian for the ionic and fake dynamical systems, so long as the electronic state remains sufficiently close to the ground state for the HF theorem to give reliable forces, these equations conserve the total energy given by,

$$E = E_{\mathrm{FKE}} + E_{\mathrm{IKE}} + E_{\mathrm{II}}(\mathbf{R}^N) + E_{\mathrm{BO}}(\mathbf{R}^N), \tag{5.3}$$

where the successive terms are the fake kinetic energy, the ion kinetic energy, and the values for the current ion positions of the inter-ion potential, and of the electronic energy functional on the BO surface. In the "favourable" circumstances, the ions explore their phase space and the value of E_{FKE} is determined by the requirement that the orbitals move (ie. $\dot{\psi}_{\alpha\sigma} \neq 0$) adiabatically to update the electronic state as the ions move. Normal, microcanonical, ion dynamics requires the conservation of E_{REAL}, given by,

$$E_{\mathrm{REAL}} = E_{\mathrm{IKE}} + E_{\mathrm{II}}(\mathbf{R}^N) + E_{\mathrm{BO}}(\mathbf{R}^N), \tag{5.4}$$

Thus for the ions to perform microcanonical dynamics we require that E_{FKE} is kept very small compared to E_{REAL}. This may normally done by choosing a suitably small fake mass (typically 400 a.u.). Provided this condition is satisfied conservation of E effectively ensures the conservation of E_{REAL} and hence microcanonical dynamics.

It is clear from the above then that under "favourable" circumstances the ions move with an average kinetic energy (temperature) that is determined by the thermodynamic state of the system being simulated, whilst the electronic degrees of freedom have a far lower temperature which is determined in the ideal case purely by the motion required to maintain adiabaticity. As a result it is necessary that the system of ions plus electronic degrees of freedom remains in a non-equilibrium, two temperature state for a long period. If however the total system were ergodic, the ionic and electronic degrees of freedom would readily exchange energy and rapidly equilibrate, causing the fake system (on average) to have the same temperature as the ionic; precisely what is not wanted. Thus the success of the CP method is due to the fact

that energy exchange between the two sub-systems is poor, enabling the total system to remain in the two temperature, non-equilibrium, "adiabatic" state for long periods of time compared to the time required for the ions to explore appreciable regions of phase space.

It is clear that the "unfavourable" circumstances correspond to the situation where energy exchange between the two sub-systems is sufficiently good that over a period of time energy is drained from the ionic to the fake system, causing the electronic system to depart from the BO ground state. In other words excitation of the fake degrees of freedom occurs such that there becomes significant orbital motion other than that required for adiabaticity. Under these circumstances the Hellman-Feynman theorem breaks down and so the forces and the ion dynamics become unreliable and the system ceases to be conservative. At this point the electronic state must be re-optimised and the CP trajectory restarted [25]. This is clearly undesirable since only piecewise trajectories are obtained, and because reoptimising and restarting take up a significant amount of computer time. The aim of this chapter is to describe an alternative method for ensuring that the electronic state remains sufficiently close to the ground state for the Hellman-Feynman theorem to be valid, avoiding the need for stopping and restarting.

The conditions for realising the "favourable" circumstances, in which the adiabatic state persists for long times, have been carefully discussed by Pastore *et al.* [73]. The property of remaining in the adiabatic state for long periods is associated with the nature of the real electronic excitation spectrum of the system being simulated. The dynamics of the fake system resembles that of a set of classical oscillators moving about a minimum position which is the electronic ground state. In stable, adiabatic runs, the amplitude of these oscillations remains small. The oscillation frequencies are determined by the real electronic excitation energies ($\Delta\varepsilon_{ij}$) and by the fake inertia, μ; in fact as $(\Delta\varepsilon_{ij}/\mu)^{\frac{1}{2}}$. The ion dynamics is also associated with a set of characteristic frequencies, whose density of states (as in classical MD) is approximately given by the Fourier transform of the velocity autocorrelation function. Energy transfer between the ionic system and the fake dynamical system will be efficient if the range of ionic and fake oscillation frequencies overlap, as then the resonance condition for efficient energy transfer is satisfied. If this is the case adiabaticity will be poor. The "favourable" circumstances therefore (in general) require the existence of a significant energy gap before the appearance of (real) electronic excitations in the system under study, ie. the situation expected to pertain in crystalline semiconductors and stable molecules. If such a gap occurs, the oscillation frequencies of the fake system can always be adjusted to be sufficiently high as to not overlap with the ionic vibrational density of states, by choosing the fake inertia to be small. There is a price to be paid for this though, in that the CP time step must be chosen

to be small enough for the integration algorithm to follow the oscillations of the fake system. Non-adiabaticity must, however, be *expected* in metals and when dealing with situations in which electronic states cross or approach closely, eg. in the normal case when bonds are being formed or broken.

5.1.1 Non-Adiabatic Events in the Dynamics of Na_2

To illustrate the severity of the problem the collision process of two Na atoms using SIC for the electrons will be used. The potential energy curve for this is given in section 3.3.2. To simulate the collision process we set the ions 11 a.u. apart in the simulation cell (cell length=36 a.u., $q_{\max}$=14) along the longest diagonal and the electronic ground state obtained by a CG minimisation. The ions are then allowed to move from rest. They should then accelerate towards each other, pass through the minimum, rebound off the repulsive wall, and return to their initial positions before coming to rest again (and repeating the process if allowed to). This scenario presents several problems for the algorithm if it is to be successfully realised. In the vicinity of the minimum the ions are moving very rapidly (T$\sim$ 5000K), and thus the electronic degrees of freedom will have to move very rapidly simply to keep up with the ions. However a potentially greater problem in view of the above arguments can be predicted by inspecting the local moment curve (figure 3.5). In the region 7 a.u.-9 a.u. the system changes between spin paired and spin unpaired, ie. the spin paired and unpaired curves cross in this region, which is exactly the sort of problem we have argued causes adiabaticity. In this region we must somehow allow the electronic degrees of freedom to move quickly to allow for the rapid change in the nature of the ground state, whilst preventing E_{FKE} continuing to rise and drain energy from the ionic system.

In figures 5.1, and 5.2 are shown the results from a simulation with the SIC energy functional and normal CP algorithm. The fake mass μ was 400 a.u. and the time step 6.4 a.u. Figure 5.1 shows the potential energy,

$$E_{\mathrm{PE}} = E_{\mathrm{II}}(\mathbf{R}^N) + E_{\mathrm{BO}}(\mathbf{R}^N), \tag{5.5}$$

calculated at points along the trajectory. We can see from this that in fact the algorithm copes quite well with bond formation as the two ions come together, and the P.E. is very close to the correct value. In the region of the minimum the P.E. curve does start to diverge from the true curve, but not significantly. The real problems occur when the ions try to dissociate. The P.E. goes into oscillation, initially between the spin paired and spin unpaired values, and then randomly above the spin unpaired curve, and the system ceases to be conservative as indicated by the fact that the ions fail to reach the initial separation.

The behaviour of E_{FKE} for this simulation is shown in figure 5.2. This shows two regions of high fake K.E. The first starts in the spin pairing region

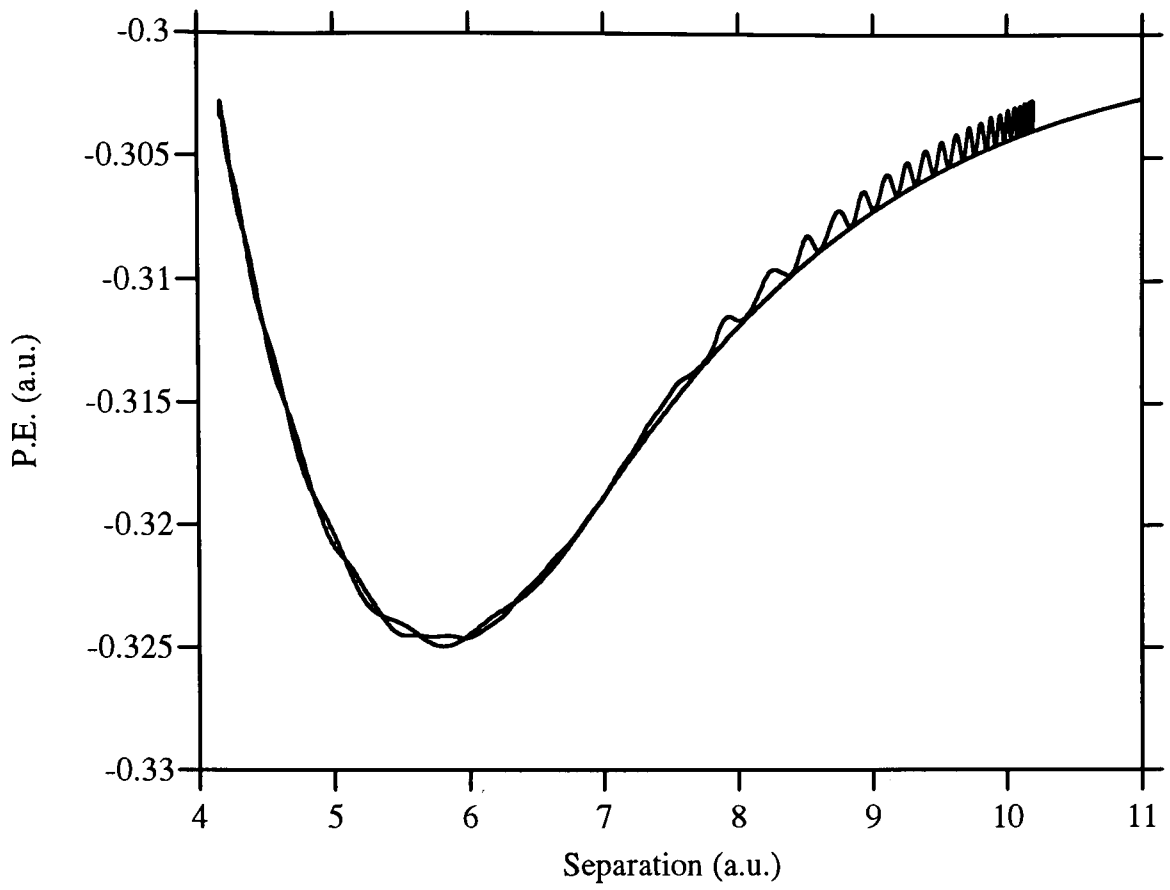


Figure 5.1: The ion potential energy for a dynamics run for Na_2, using conventional CP algorithm.

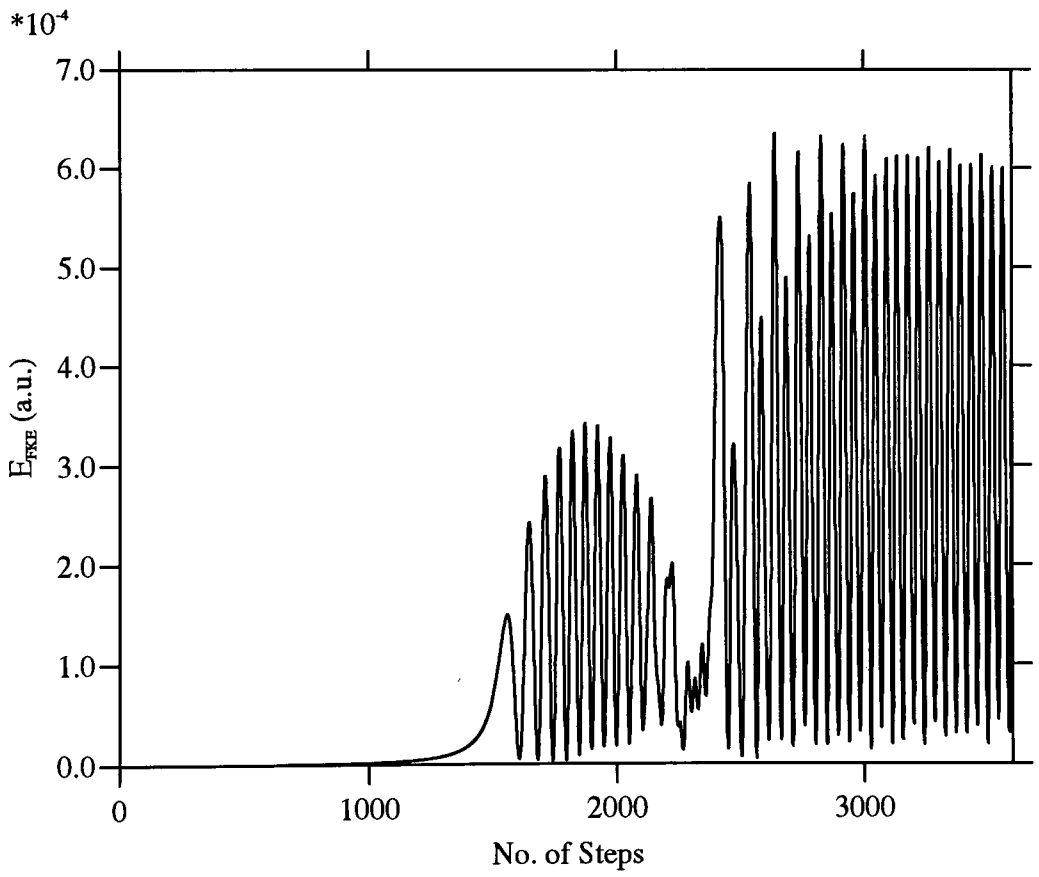


Figure 5.2: The fake kinetic energy for a dynamics run for Na_2, using conventional CP algorithm.

where the wavefunctions change from atomic to molecular. This is expected as the coefficients *have* to change rapidly to cope with this sudden rearrangement. However E_{FKE} continues to rise after this region is traversed. This again is not too surprising due to the high velocity of the ions in the region. E_{FKE} only dies down again after approximately 1900 steps. This corresponds to the rebound region where the ions are moving slowly. As the ions increase speed again, E_{FKE} rises as expected, but this time as the system reaches the region where the electrons should spin unpair the algorithm breaks down terminally, as shown by the undamped oscillations in E_{FKE}. The algorithm is unable to recover from this position.

The reason for this catastrophic failure is that the algorithm is unable to produce the necessary changes in the wavefunction to remain on the ground state. When the ions start to separate from the turning point on the repulsive wall of the potential, the two electrons are in spatially identical orbitals, ie. the molecular orbital. However, to remain on the ground state the electrons must move into spatially distinct orbitals, which become the atomic orbitals in the dissociation limit. There is nothing though in the algorithm to break the symmetry. As the orbitals approach the point at which this change must begin (a separation of roughly 7 a.u.) the forces on the orbitals are identical, apart from purely numerical errors; hence there is no way for the distinct character of the two orbitals to emerge apart from the growth of differences due to these numerical errors. Essentially the electrons wish to separate, because of their mutual repulsion, but they have no way of knowing which way they should move. This problem does not arise on the inward journey since then two spatially distinct orbitals are becoming identical, and there is also a residual spin paired character as mentioned in section 3.3.2

We can show that the rise in E_{FKE} is not due simply to breakdown caused by the ion velocity in the following way. If we start at a separation of 4.2 a.u. ie. high up on the repulsive wall, then let the ions go, they will pass through the minimum before meeting a curve crossing region. Thus any instabilities due purely to ion velocity will be shown. The P.E. and E_{FKE} curves for such a run for are shown in figure 5.3, and 5.4. As the ions pass through the minimum E_{FKE} is at least one order of magnitude smaller than in the run started from a separation of 11 a.u. Interestingly the ions continue to follow the spin paired curve. E_{FKE} shows no problems are encountered until the ions start to return towards the minimum, and the system tries to jump onto the spin unpaired curve. At this point as expected the fake kinetic energy becomes large and the algorithm breaks down. It would appear then that in the previous run there is a residual asymmetry in the orbitals that helps facilitate spin unpairing. This may be due to some "memory" of the initial state, but is more likely due to numerical noise from the earlier partial breakdown. In this run though the system remains close to the BO surface, and seems to pass through the spin unpairing region before it has chance to

perturb the system significantly.

Runs using LSD show similar behaviour. Figures 5.5 and 5.6 shows the P.E. and E_{FKE} curves for the LSD run equivalent to the first SIC run. The point to note is that although the characteristics on the inward trajectory are just like those of the SIC, it seems to have passed the spin unpairing transition without a total breakdown. The P.E. has departed from the BO surface but although energy conservation has been lost we do not have such catastrophic failure. This appears to be due to the fact that the spin unpairing occurs when the ions are travelling more slowly, thus the fake kinetic energy only has to make the spin unpairing transition without having to cope with excessive ion velocities at the same time.

From the above runs we can see the following pattern emerge:

1. Breakdown of the CP method is accompanied by high E_{FKE}, though high E_{FKE} does not always mean breakdown of the CP method as this may be necessary simply to stay on the BO surface.

2. The CP method is robust enough that if the system enters a region away from curve crossing, where the fake kinetic energy needed for adiabaticity is low, it can recover from an unfavourable position.

3. Very high ion velocities does not in itself present a problem, but can accentuate other difficulties.

4. Curve crossing need not be terminal to the CP method. In these runs the curve crossing region is crossed quickly and there seems insufficient time to significantly perturb the system unless there is already a departure from the BO surface. However once oscillations of the system between two curves occurs the situation is not self-correcting.

5. Spin unpairing is the largest problem as it creates problems of symmetry breaking, and once on the wrong curve a jump to the correct one induces non-adiabaticity.

5.2 Thermostated Equations of Motion

It is clear that the departure from the electronic ground state, and hence breakdown of the CP algorithm is associated with the rise in E_{FKE}, ie. a rise in the temperature of the electronic degrees of freedom. An obvious conclusion then is that we should control this heating of the fake motion by connecting it to some kind of thermostat. A similar problem, of imposing an adiabatic condition on a system of classical charges designed to represent polarization effects in water was considered by Sprik [101]. He showed that

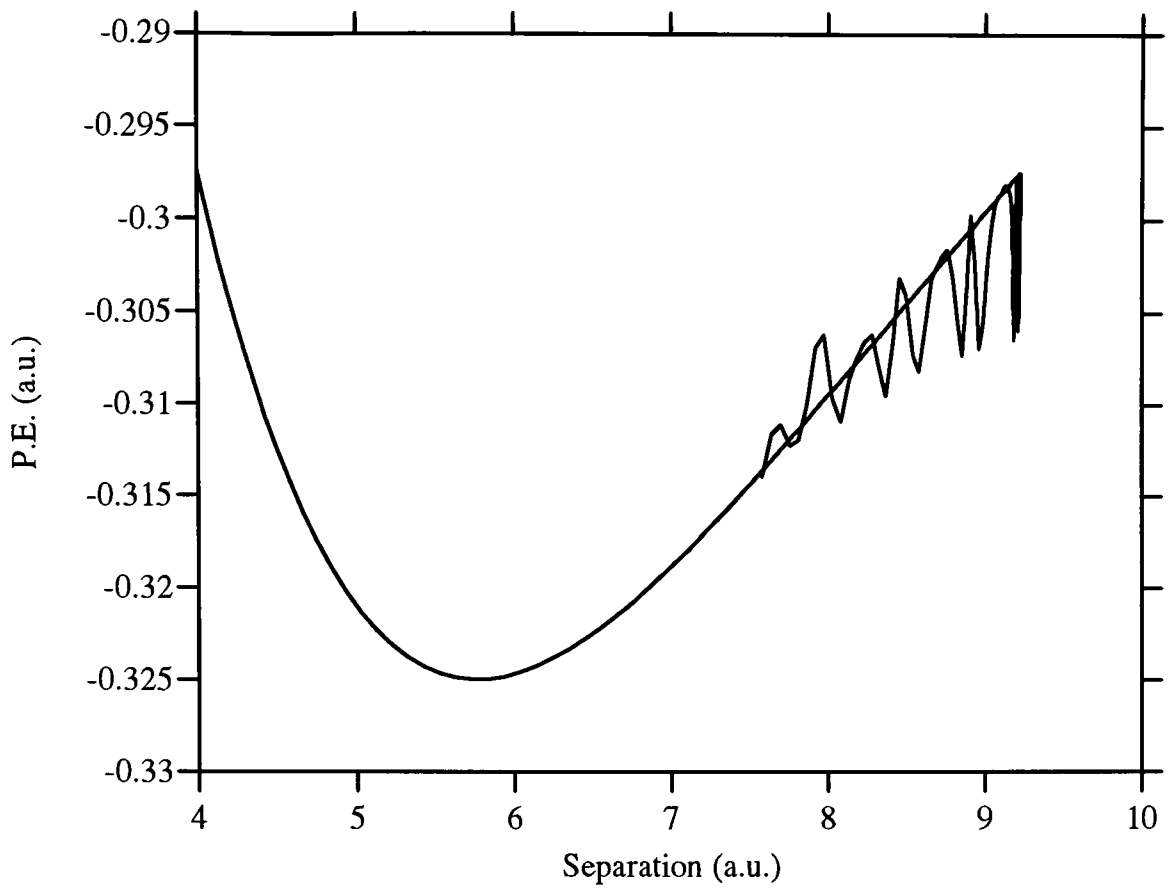


Figure 5.3: The ion potential energy for a dynamics run for Na_2, using conventional CP algorithm starting from a separation of 4.2 a.u.

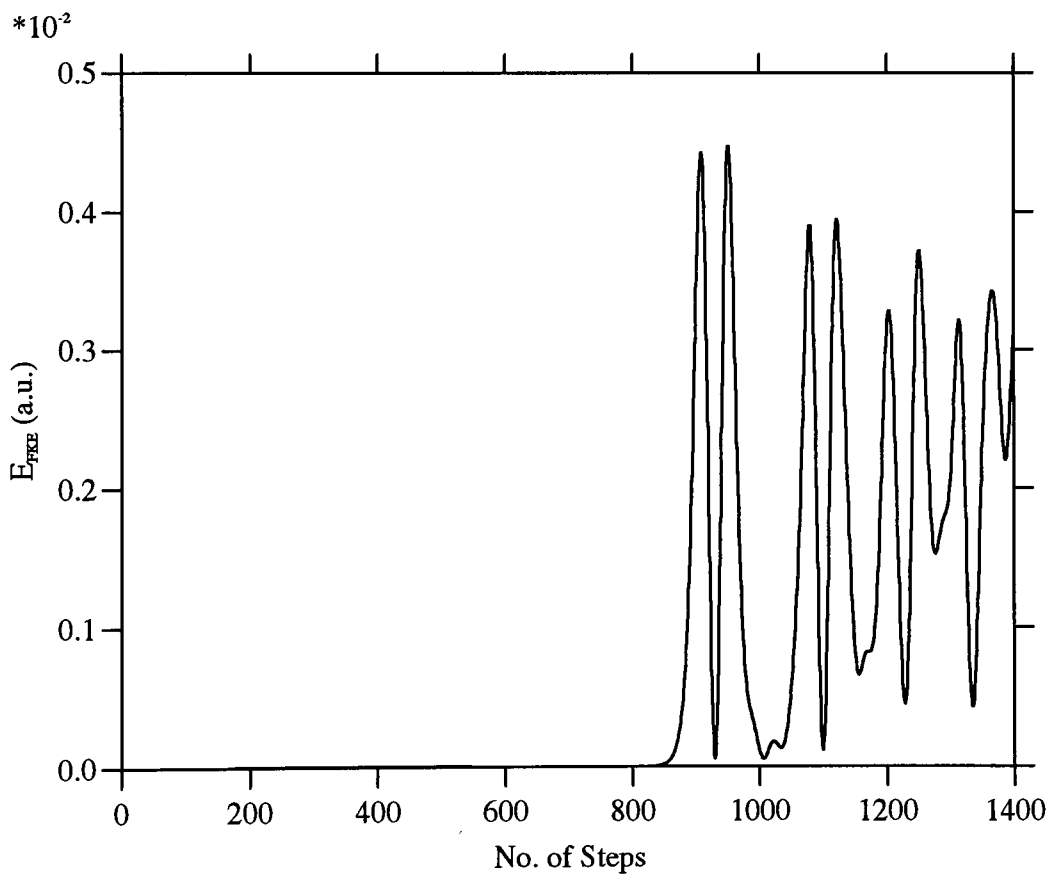


Figure 5.4: The fake kinetic energy for a dynamics run for Na_2, using conventional CP algorithm starting from a separation of 4.2 a.u.

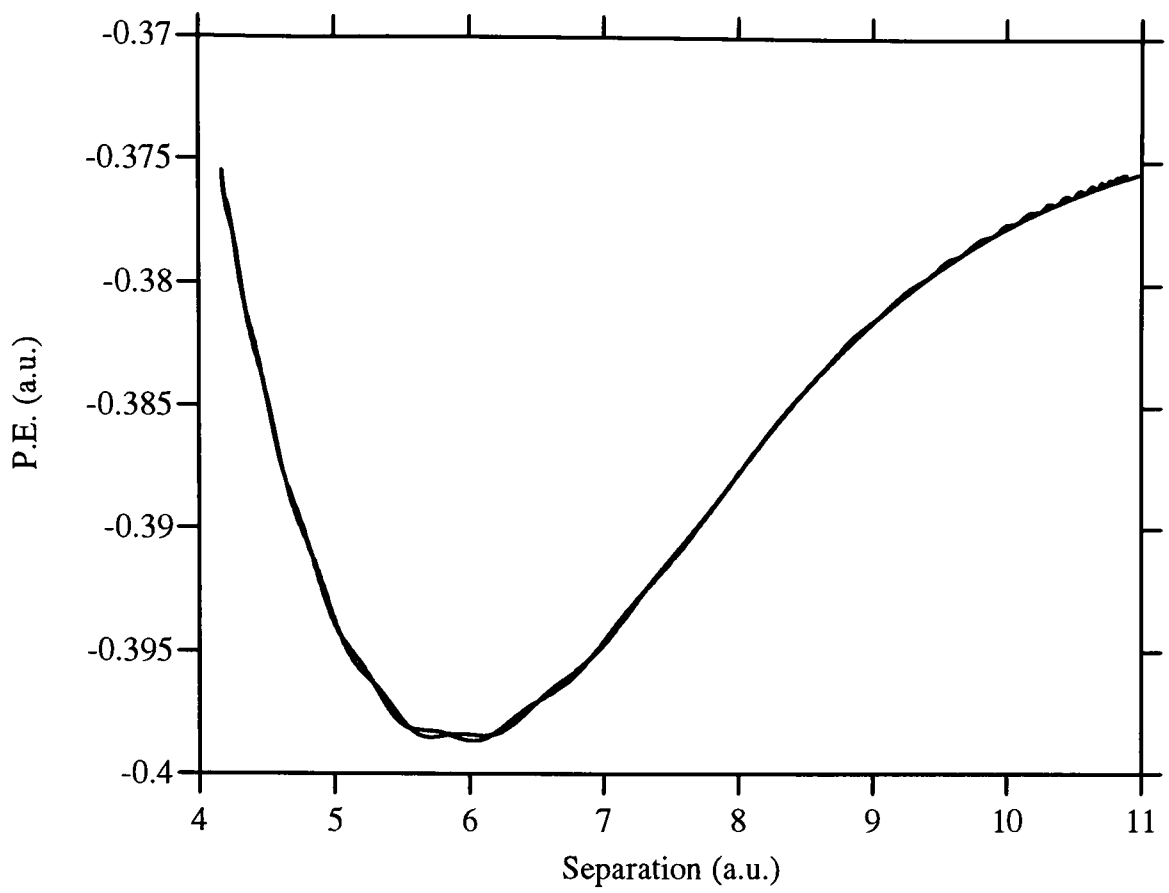


Figure 5.5: The ion potential energy for a dynamics run for Na_2, using conventional CP algorithm and LSD.

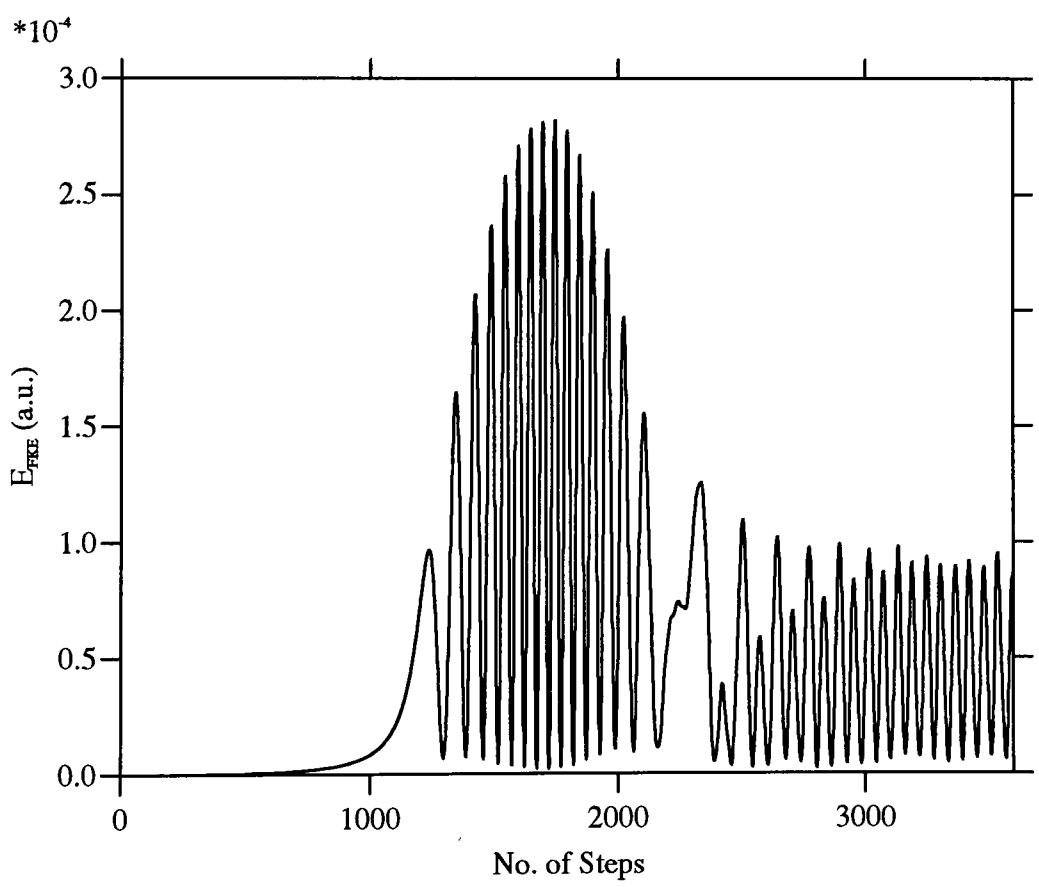


Figure 5.6: The fake kinetic energy for a dynamics run for Na_2, using conventional CP algorithm and LSD.

the two temperature, non-equilibrium state could be maintained by modifying the equations of motion in the way suggested by Hoover [38] in order to implement the Nosé thermostat [70]. In the next section I will outline the Nosé-Hoover thermostat in classical MD, before considering its application to the CP equations of motion.

5.2.1 Constant Temperature MD - The Nosé-Hoover Thermostat

There are several approaches to constant temperature MD, one of which is to include an extra degree of freedom to represent a thermal reservoir. In the Nosé's[70] implementation of this method the real particle velocities are related to the time derivatives of the positions via,

$$\mathbf{v}_i = s\dot{\mathbf{r}}_i = \mathbf{p}_i/ms, \tag{5.6}$$

where s is an extra degree of freedom, with conjugate momentum p_s. This extra degree of freedom has an associated potential energy, $\mathcal{V}_s$, and kinetic energy, $\mathcal{K}_s$, given by,

$$\mathcal{V}_s = (f+1)k_bT\ln s, \tag{5.7}$$

$$\mathcal{K}_s = \frac{1}{2}Q\dot{s}^2 = p_s^2/2Q, \tag{5.8}$$

where f is the number of degrees of freedom (3N-3 if the total momentum is fixed), T is the thermal temperature, and Q is an inertia parameter, which controls the rate of temperature fluctuations.

The Lagrangian for the system is,

$$\mathcal{L}_s = \mathcal{K} + \mathcal{K}_s - \mathcal{V} - \mathcal{V}_s, \tag{5.9}$$

where $\mathcal{K}$, and $\mathcal{V}$ are the kinetic and potential energies of the system other than the reservoir. From this one can obtain the equations of motion,

$$\ddot{\mathbf{r}}_i = \mathbf{F}_i/ms^2 - 2\dot{s}\dot{\mathbf{r}}_i/s, \tag{5.10}$$

$$Q\ddot{s} = \sum_i m\dot{\mathbf{r}}_i^2 s - (f+1)k_BT/s, \tag{5.11}$$

The Hamiltonian of the extended system, $\mathcal{H}_s = \mathcal{K}+\mathcal{K}_s+\mathcal{V}+\mathcal{V}_s$, is a constant of motion.

Hoover [38], however, extended this analysis to eliminate the time scaling parameter s. This leads to the equations of motion,

$$\dot{\mathbf{r}}_i = \mathbf{p}_i/m, \tag{5.12}$$

$$\dot{\mathbf{p}}_i = \mathbf{F}_i - \xi\mathbf{p}_i, \tag{5.13}$$

where the friction parameter ξ is given by,

$$\dot{\xi} = \frac{f}{Q} k_B (T - \tau), \tag{5.14}$$

where T is the instantaneous temperature of the system and τ is the temperature of the thermal reservoir.

The above equations define molecular dynamics with the Nosé-Hoover thermostat. As shown by Hoover [38] they generate states in the canonical ensemble. However Toxvaerd [115] has argued that care has to be taken in the algorithm used to integrate these equations to ensure that the results of the simulation are indeed in a true canonical ensemble, especially when using a Verlet type algorithm rather than a leap-frog algorithm. This need not concern us though for two reasons. Firstly use of a small time step, as already required by the CP method, avoids the problem, and secondly we are only interested in controlling E_{FKE}, not in ensuring that the fake motion has a canonical distribution.

From the Verlet algorithm then we have,

$$\mathbf{r}_i(t + \delta t) = 2\mathbf{r}_i(t) - \mathbf{r}_i(t - \delta t) + (\delta t)^2 \mathbf{a}_i(t), \tag{5.15}$$

$$\mathbf{v}_i(t) = \frac{\mathbf{r}_i(t + \delta t) - \mathbf{r}_i(t - \delta t)}{2\delta t}. \tag{5.16}$$

However from equations 5.14 and 5.13 we can write,

$$\xi(t + \delta t) = \frac{f}{Q} k_B (T - \tau)\delta t + \xi(t), \tag{5.17}$$

$$\mathbf{a}_i = \mathbf{F}_i/m - \xi \mathbf{v}_i(t). \tag{5.18}$$

After a little manipulation we arrive at,

$$\mathbf{r}_i(t + \delta t) = \frac{4\mathbf{r}(t)}{(2 + \xi(t)\delta t)} - \mathbf{r}_i(t - \delta t)\left(\frac{2 - \xi(t)\delta t}{2 + \xi(t)\delta t}\right) + \mathbf{F}_i \frac{(\delta t)^2}{m} \frac{2}{(2 + \xi(t)\delta t)}. \tag{5.19}$$

In the CP method though we use a very small time step thus it is acceptable instead of using equation 5.16 for the velocity to use,

$$\mathbf{v}_i(t) \simeq \mathbf{v}(t - \frac{1}{2}\delta t) = \frac{\mathbf{r}_i(t) - \mathbf{r}_i(t - \delta t)}{\delta t}. \tag{5.20}$$

This leads to,

$$\mathbf{r}_i(t+\delta t) = \mathbf{r}_i(t) - \mathbf{r}_i(t-\delta t) + (\mathbf{r}_i(t) - \mathbf{r}_i(t - \delta t))(1 - \xi(t)\delta t) + \mathbf{F}_i \frac{(\delta t)^2}{m}, \tag{5.21}$$

which along with equation 5.17 constitutes the Verlet type algorithm for integrating the Nosé-Hoover equations of motion.

5.2.2 Application of the Nosé-Hoover Thermostat to The CP Equations of Motion

From the preceding section it is clear that the thermostated electronic CP equations of motion are,

$$\mu\ddot{\psi}_{i\sigma} = -\frac{\delta E}{\delta\psi^*_{i\sigma}} + \sum_j \lambda^{\sigma^*}_{ij}\psi_{j\sigma} - \mu\xi\dot{\psi}_{i\sigma}, \tag{5.22}$$

and these may be integrated using,

$$\xi(t+\delta t) = \frac{f}{Q}k_B(T-\tau)\delta t + \xi(t), \tag{5.23}$$

$$\begin{aligned}\psi_{i\sigma}(t+\delta t) &= \psi_{i\sigma}(t) + (\psi_{i\sigma}(t) - \psi_{i\sigma}(t-\delta t))(1-\chi) \\ &+ \frac{(\delta t)^2}{\mu}\left(-\frac{\delta E}{\delta\psi^*_{i\sigma}} + \sum_j \lambda^{\sigma^*}_{ij}\psi_{j\sigma}(t)\right),\end{aligned} \tag{5.24}$$

where $\chi = \xi(t)\delta t$. λ^{σ}_{ij} are the Lagrange multipliers for the orthonormality constraint. We used a similar iterative scheme to that for the normal CP method (see appendix A). This is derived by substituting equation 5.24 into the constraint,

$$\langle\psi_{i\sigma}(t+\delta t)|\psi_{j\sigma}(t+\delta t)\rangle = \delta_{ij}, \tag{5.25}$$

to give (dropping the spin index σ for clarity),

$$\begin{aligned}\lambda^{(n+1)}_{ij} &= -\frac{1}{D}(D_{ij} - \delta_{ij}) \\ &- \sum_l \lambda^{(n)^*}_{jl}\left((2-\chi)\Delta S_{il} + (\chi-1)\Delta R1_{il} - DL_{il}\right) \\ &- \sum_k \lambda^{(n)}_{jl}\left((2-\chi)\Delta S_{kj} + (\chi-1)\Delta R2_{kj} - DH_{kj}\right) \\ &- D\left(\sum_k\sum_l \lambda^{(n)}_{ik}\lambda^{(n)^*}_{jl}S_{kl}\right) - \lambda^{(n)^*}_{ji},\end{aligned} \tag{5.26}$$

where,

$$\begin{aligned}\mathbf{F}_i &= \frac{\delta E}{\delta\psi^*_i(\mathbf{r},t)}, \\ D &= \frac{(\delta t)^2}{\mu}, \\ H_{ij} &= \langle\psi_i(t)|\mathbf{F}_j\rangle, \\ HO_{ij} &= \langle\psi_i(t-\delta t)|\mathbf{F}_j\rangle,\end{aligned}$$

$$
\begin{aligned}
L_{ij} &= \langle \mathbf{F}_i | \psi_j(t) \rangle \,, \\
LO_{ij} &= \langle \mathbf{F}_i | \psi_j(t-\delta t) \rangle \,, \\
R1_{ij} &= \langle \psi_i(t-\delta t) | \psi_j(t) \rangle \,, \\
R2_{ij} &= \langle \psi_i(t) | \psi_j(t-\delta t) \rangle \,, \\
G_{ij} &= \langle \mathbf{F}_i | \mathbf{F}_j \rangle \,, \\
S_{ij} &= \langle \psi_i(t) | \psi_j(t) \rangle \,, \\
SO_{ij} &= \langle \psi_i(t-\delta t) | \psi_j(t-\delta t) \rangle \,, \\
D_{ij} &= (4 - 4\chi + \chi^2) S_{ij} + (-2 + 3\chi - \chi^2) R2_{ij} + (-2 + \chi) DH_{ij}, \\
&+ (-2 + 3\chi - \chi^2) R1_{ij} + (1 - 2\chi + \chi^2) SO_{ij} + (1 - \chi) DHO_{ij}, \\
&+ (-2 + \chi) DL_{ij} + (1 - \chi) DLO_{ij} + D^2 G_{ij}, \\
\Delta S_{ij} &= S_{ij} - \delta_{ij}, \\
\Delta RN_{ij} &= RN_{ij} - \delta ij.
\end{aligned} \tag{5.27}
$$

Thus if we start from an initial guess,

$$
\lambda_{ij}^{(0)} = H_{ij} - DG_{ij}. \tag{5.28}
$$

we can use equation 5.26 iteratively until convergence is obtained. The ion motion can be propagated as previously by the leap-frog algorithm.

Figure 5.7, and 5.8 shows typical P.E. and E_{FKE} for the Na_2 system described earlier using this thermostat. In this run $f = 2\mathrm{ncoeff}(n_\alpha + n_\beta) - (n_\alpha^2 - n_\beta^2)$, where n_σ is the number of electrons of spin σ; $Q = 10(n_\alpha + n_\beta)$; μ=400 a.u. and the time step is 6.4 a.u. The target temperature is naively set very low (10^{-11}). We can see here that there is a distinct improvement in the quality of the P.E. curve on the inward trajectory. On the outward trajectory there is a slight deviation near the minimum, but again the main problem is where the system tries to spin unpair. The system follows the *wrong* curve for some distance before jumping to the correct curve. The thermostat prevents this being catastrophic as it is in the unthermostated case but this behaviour is undesirable. To help induce this symmetry breaking process we can put separate thermostats on each spin, ie. ξ can be made spin dependant. Such a run is shown in figures 5.9, and 5.10. Here we actually used a value of Q double that in the previous run. As shown later Q does not seem to affect the spin unpairing, merely how quickly the oscillations afterwards are quenched. From this we can see that the two thermostats do indeed help but is not the panacea we require.

A careful analysis shows some flaws in the above scheme. Firstly the temperature of the fake system should *not* always be low, as when the ions move rapidly, then so must the orbitals, to keep on the BO surface. Now suppose the actual adiabatic electronic state could be described as one electron occupying an atomic orbital on each atom, and suppose we were trying to

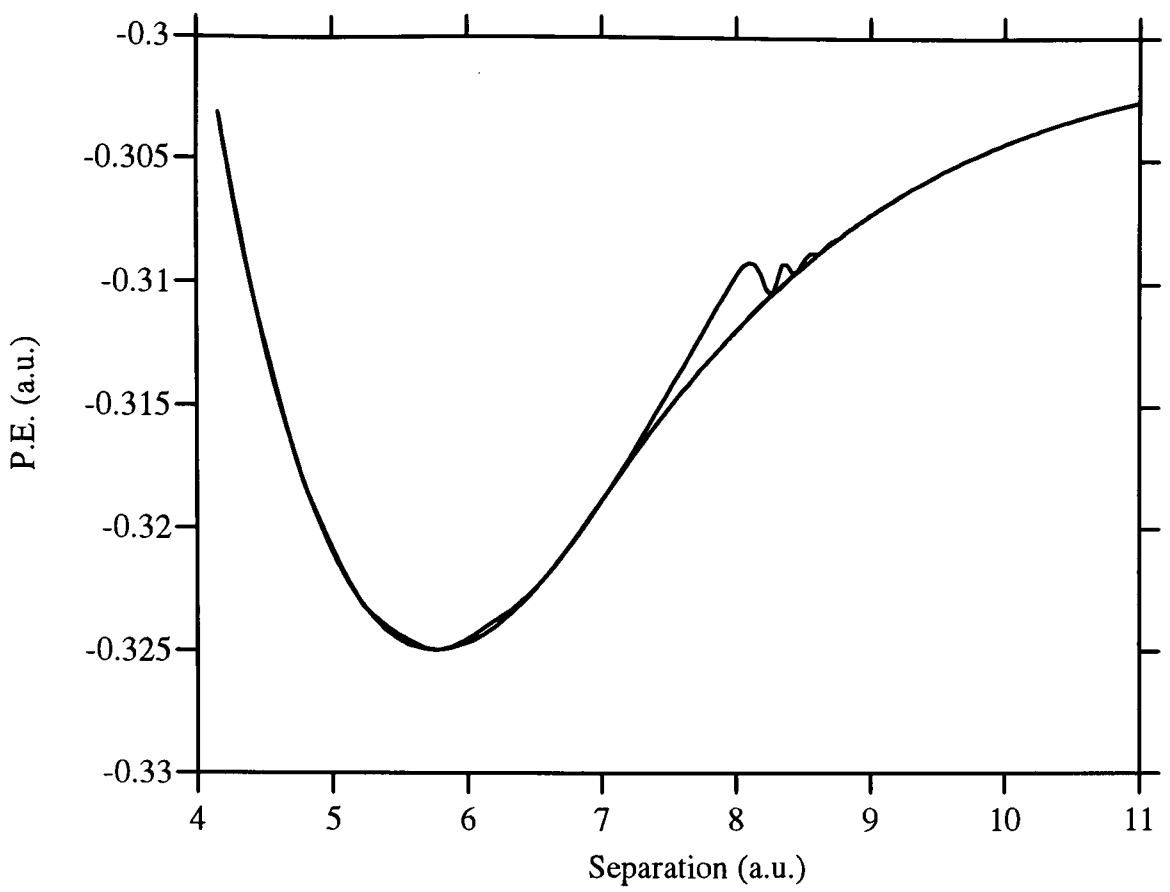


Figure 5.7: The ion potential energy for a dynamics run for Na_2, using a single Nosé-Hoover thermostat.

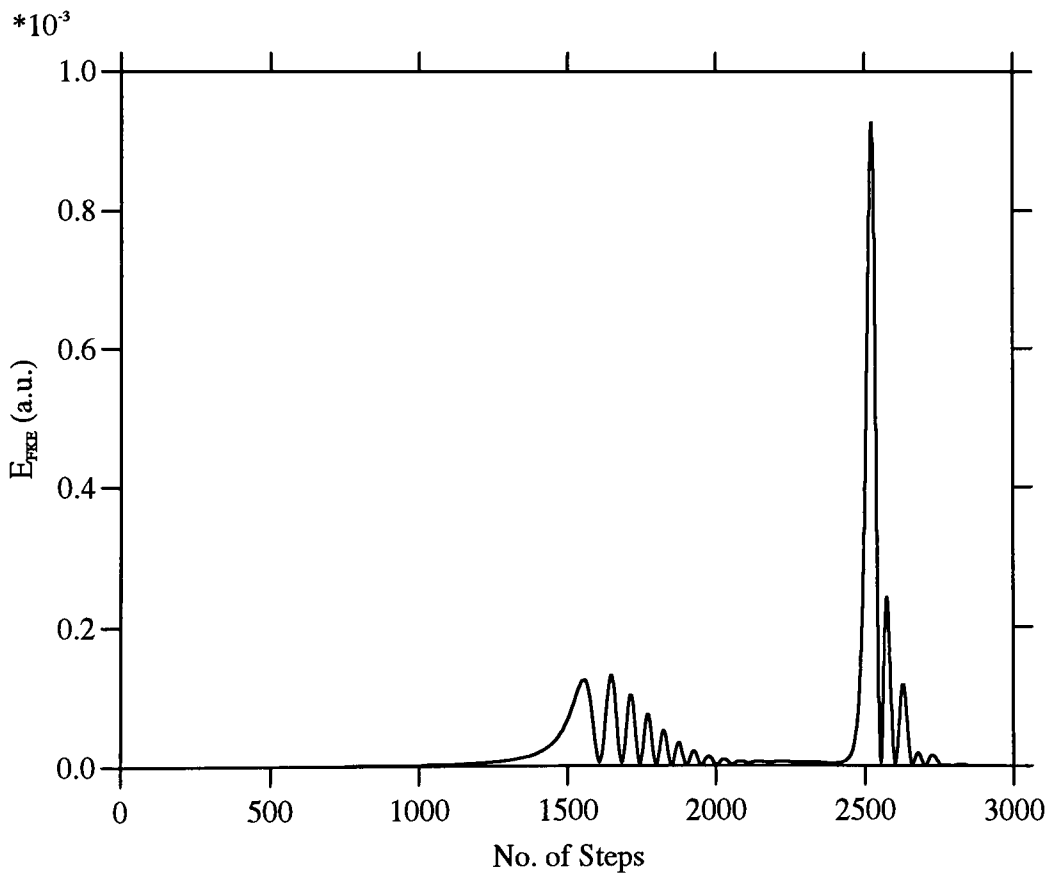


Figure 5.8: The fake kinetic energy for a dynamics run for Na_2, using a single Nosé-Hoover thermostat.

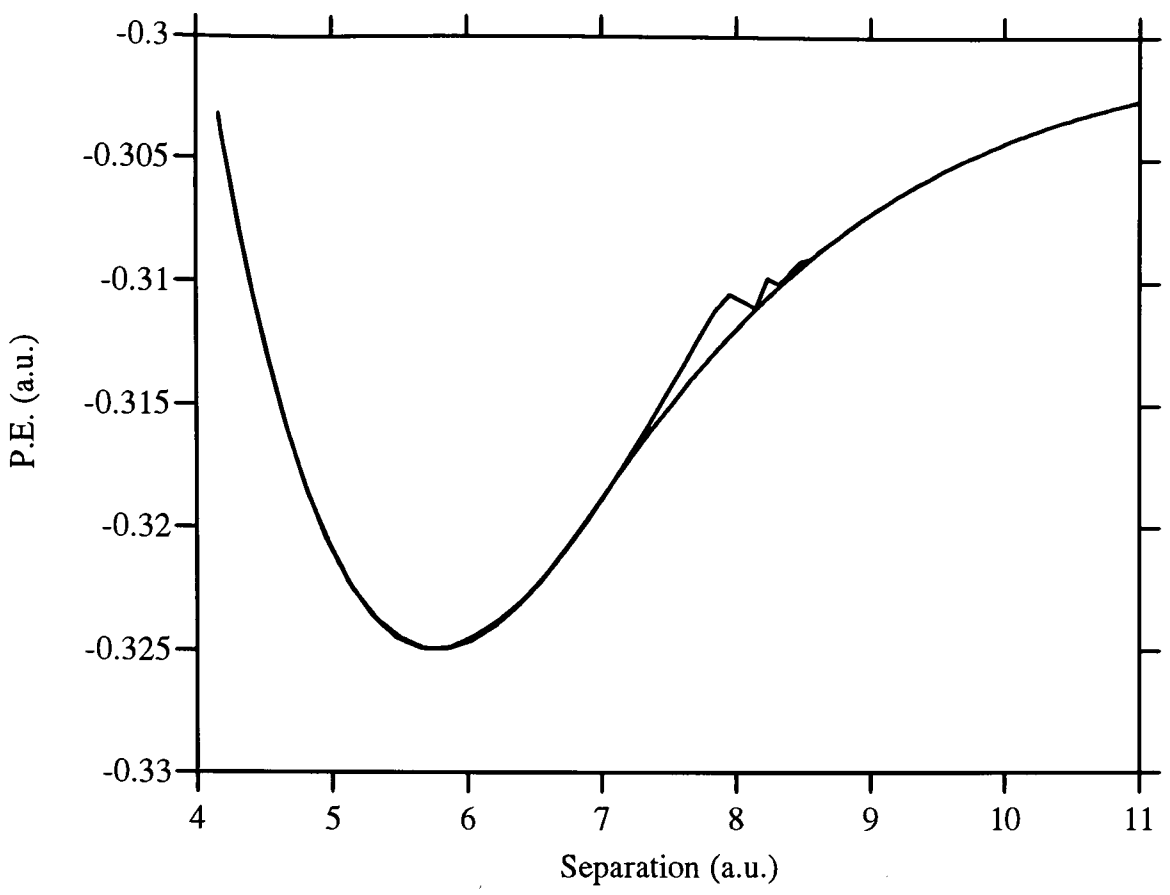


Figure 5.9: The ion potential energy for a dynamics run for Na_2, using two Nosé-Hoover thermostats.

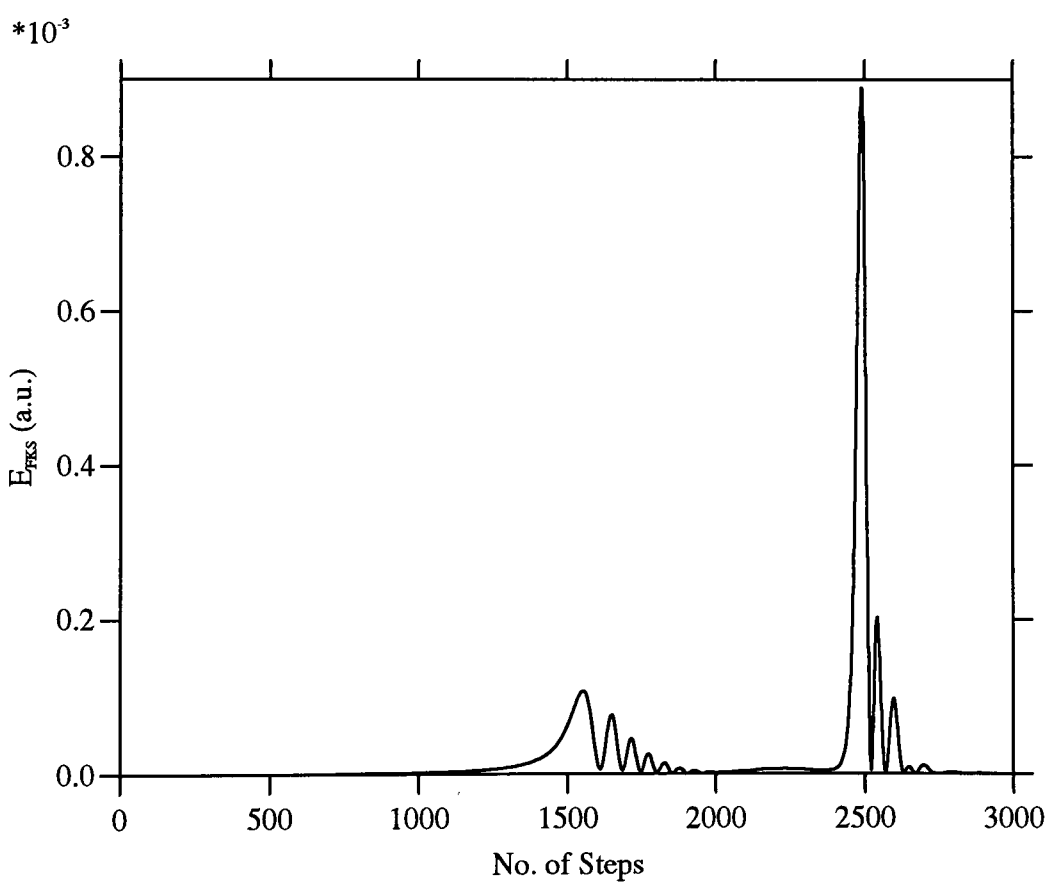


Figure 5.10: The fake kinetic energy for a dynamics run for Na_2, using two Nosé-Hoover thermostats.

describe this state with the CP method using the ideal floating basis, which consists of a set of such orbitals whose positions are the dynamic variables of the fake system. Then the adiabatic motion of those dynamical variables is exactly the same as the rate of change of the ionic positions. In this case the adiabatic fake kinetic energy is equal to the ionic kinetic energy multiplied by μ/M. If we use instead a large set of plane waves, rather than the floating functions, many more degrees of freedom would be involved but only the same wavefunction motion would be described. That is, the motion of the individual degrees of freedom would be highly correlated in order to replicate the atomic motion, the number of *independent* degrees of freedom would be highly constrained by adiabaticity. Adding more plane waves might improve the representation of the individual atomic orbitals but it would not add more *independent* degrees of freedom.

These arguments then lead us to choose a target fake kinetic energy (equivalent to a target temperature) of,

$$E_{\mathrm{FKE}}^{\mathrm{target}} = f\frac{\mu}{M}E_{\mathrm{IKE}}, \tag{5.29}$$

where f is a parameter, characteristic of the physical system which may be expected to be of order one. That f is a property of the system, and not of artefacts of the calculation such as the basis set size, means that appropriate values can be found in small test calculations and used reliably for larger calculations. Some support for this suggestion comes from an examination of figures which have appeared in the literature to illustrate the relationship between fake and ion kinetic energy in systems which show good adiabatic dynamics. In germanium (fig 1 in ref.[92]), and silicon (fig 1 in ref. [73]) values for f of 0.1 and 0.35 are found. In the calculation in figure 5.2, by considering the ratio of the fake to ion kinetic energy in the early part of the run, we find f equal to 0.05.

A related point is the rate of change of the damping parameter ξ, which is determined by the difference in the instantaneous values of E_{FKE}, and $E_{\mathrm{FKE}}^{\mathrm{target}}$. When the ions enter a non-adiabatic region, this parameter, ξ, will rise very quickly. As the ions emerge from the non-adiabatic region, E_{FKE} is damped back to its adiabatic value by the thermostat. At this point we require ξ to return quickly to zero, so that normal CP dynamics is resumed in the adiabatic region. However even with suitable $E_{\mathrm{FKE}}^{\mathrm{target}}$, $(E_{\mathrm{FKE}} - E_{\mathrm{FKE}}^{\mathrm{target}})$ does not become large enough negative to facilitate this. Thus ξ remains large. The resulting damped orbital equations of motion result in poor orbital propagation in the adiabatic region, and also help "stick" the system to the spin paired state when it should be spin unpairing. This asymmetry in the rise and fall of ξ has arisen because $E_{\mathrm{FKE}}^{\mathrm{target}}$ is much smaller than the E_{FKE} that would be achieved if the fake and ion motion were in equilibrium. Our solution to this is simply to reset ξ equal to zero whenever E_{FKE} is less than

$1.2E_{\mathbf{FKE}}^{\mathbf{target}}$.

The final scheme employed then is as follows:

$$E_{\mathbf{FKE}}^{\mathbf{target}} = f\frac{\mu}{M}E_{IKE}, \tag{5.30}$$

$$\xi_\sigma(t+\delta t) = \begin{cases} \xi_\sigma(t) + \frac{\delta t}{\zeta}(E_{\mathbf{FKE}} - E_{\mathbf{FKE}}^{\mathbf{target}}) & , \quad E_{\mathbf{FKE}} > 1.2E_{\mathbf{FKE}}^{\mathbf{target}}, \\ 0 & , \quad E_{\mathbf{FKE}} \leq 1.2E_{\mathbf{FKE}}^{\mathbf{target}}, \end{cases} \tag{5.31}$$

$$\begin{aligned} \psi_{i\sigma}(t+\delta t) &= \psi_{i\sigma}(t) + (\psi_{i\sigma}(t) - \psi_{i\sigma}(t-\delta t))(1-\chi) \\ &+ \frac{(\delta t)^2}{\mu}\left(-\frac{\delta E}{\delta \psi_{i\sigma}^*} + \sum_j \lambda_{ij}^{\sigma^*}\psi_{j\sigma}(t)\right), \end{aligned} \tag{5.32}$$

where $\chi = \xi(t)\delta t$; λ_{ij}^{σ} are calculated using the iterative scheme defined by equations 5.26-5.28, and the ion equations of motion are integrated using the leap-frog algorithm,

$$\mathbf{R}_{\mathbf{I}}(t+\delta t) = \mathbf{R}_{\mathbf{I}}(t) + \delta t \mathbf{v}_{\mathbf{I}}(t+\frac{1}{2}\delta t), \tag{5.33}$$

$$\mathbf{v}_{\mathbf{I}}(t+\frac{1}{2}\delta t) = \mathbf{v}_{\mathbf{I}}(t-\frac{1}{2}\delta t) + \frac{\delta t}{M_{\mathbf{I}}}\frac{\partial E}{\partial \mathbf{R}_{\mathbf{I}}(t)}. \tag{5.34}$$

5.3 Optimisation of the Nosé-Hoover Thermostat Parameters

Figures 5.11-5.16 show a sequence of P.E. curves Na_2 generated using the above scheme. All of these use a fake mass of 400 a.u., and a time step of 6.4 a.u. From the first two plots we can see that too high an inertia parameter causes $E_{\mathbf{FKE}}$ to be damped too slowly, allowing oscillations in the P.E. and a slow return to adiabatic dynamics. Figures 5.13 and 5.15 though show that ζ can be too low, causing $E_{\mathbf{FKE}}$ to be quenched too rapidly to allow the fake motion to be rapid enough to maintain adiabaticity. The best figure is the last where f has a value of 0.025 as predicted (NB. half $E_{\mathbf{FKE}}$ in each spin), and $\zeta = 1$. Even for this run there is a small "blister" where the P.E. departs briefly from the ground state. Figures 5.18-5.22 show the variation in $E_{\mathbf{FKE}}$, $\xi(=\frac{1}{2}(\xi_\alpha + \xi_\beta))$ and the net force on the ions for this run. The $E_{\mathbf{FKE}}$ and ξ figures show how resetting ξ to zero allows $E_{\mathbf{FKE}}$ to rise when large rearrangements of the orbitals are required. The forces figure shows that throughout the run the forces do remain reasonably reliable. The main departure is in the region of the blister, and although the forces on the inward and outward trajectories do not agree after this point it is clear that the forces do not depart seriously enough to prevent proper dynamics.

The best results for this system were obtained by further varying μ. The figures 5.23-5.29 show the results for a run with μ=200, ζ=0.5, f=0.025, δt=6.4, which gave the best results of all the calculations.

5.4 Examples of Nosé-Hoover Thermostated CP MD

5.4.1 The Pseudorotation of Na_3

In a series of papers [56, 109, 57, 26, 110] Lindsay *et al.* have studied the e.s.r. spectra of alkali metal clusters in inert argon and nitrogen matrices. Of particular interest is their work on sodium clusters in argon matrix. These show spectra assigned to Na_3, and Na_7 clusters. The Na_3 spectra [57] show that below T$\sim$20K two atoms are equivalent and the third distinct., while above this temperature all three atoms become equivalent on the e.s.r. time scale ($t \sim 10^{-8}$s). They have ascribed this behaviour to the pseudorotation of the cluster. Martins *et al.* [60] have derived a fitted BO surface for Na_3 and from this deduce that the transition state for this process is the isosceles and not the equilateral geometry. In this study then we wish to perform a dynamics simulation of Na_3 to see if we can reproduce the pseudorotation of the cluster, and to deduce the pathway and something of the kinetics of the process.

The first problem encountered is the length of run needed for there to be a high probability of a pseudorotation event. Clearly at T$\sim$20K where we would like to carry out the calculations this is going to be of $\sim 10^{-8}$s, which is obviously impossible. We are thus forced to run the simulation at a higher temperature, and 150K was chosen. The initial ion velocities were set up at this temperature in such a way that all the energy was in vibration, ie. linear and angular momentum was zero. This was done in the following way:

1. Set up velocities with random distribution (using NAG library routine G05CAF) in x and y directions. All velocities in the z (out of plane) direction set to zero.

2. Find centre of mass (c of m), and distance of each ion from it.

3. **(a)** Subtract net angular momentum from ions.
   (b) Calculate angular momentum, ω_z, about c of m.
   (c) If rx_i and ry_i are distances of i^{th} ion from c of m, we need to subtract the velocities $vxsub_i$, $vysub_i$, to give zero angular momentum, where,

$$vysub_i = \frac{\omega_z rx_i}{3\left(rx_i^2 + ry_i^2\right)}, \tag{5.35}$$

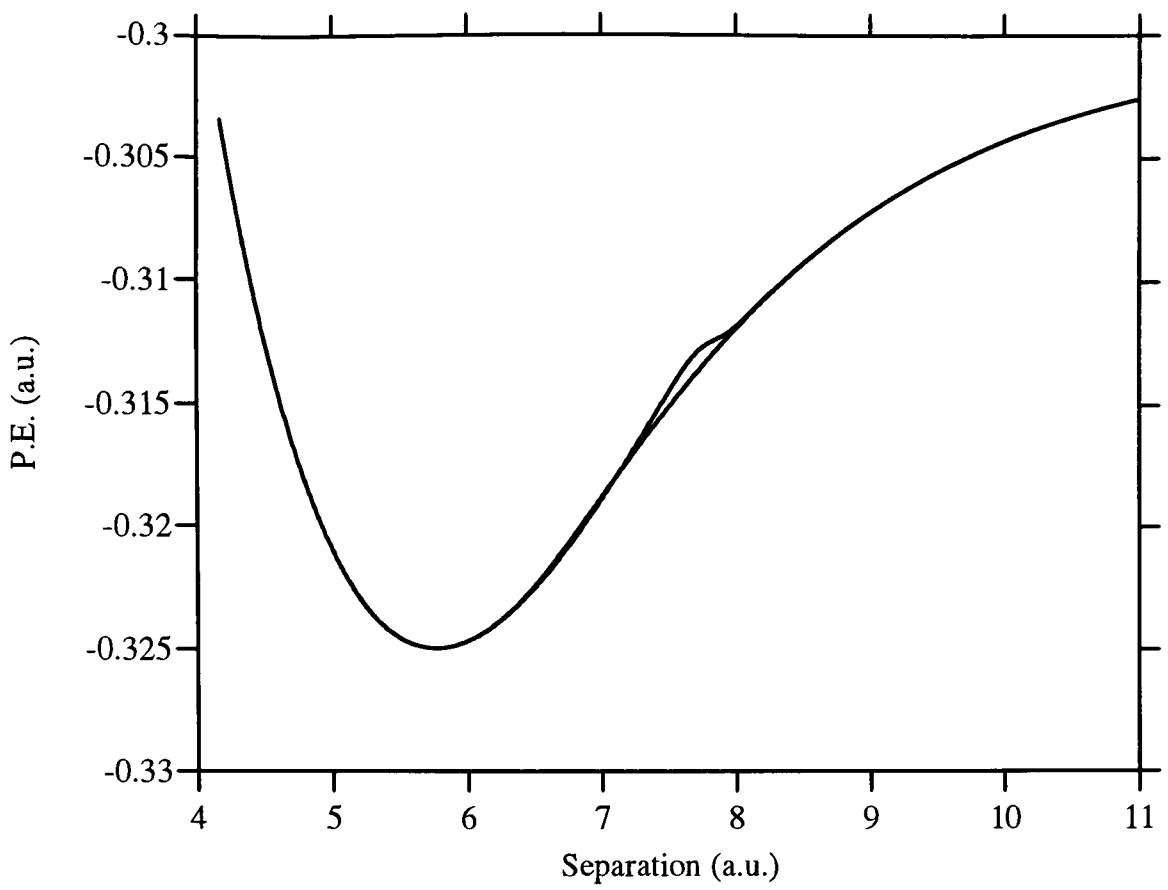


Figure 5.11: The ion potential energy for a dynamics run for Na_2, using the Nosé-Hoover thermostat using the parameters: μ=400, ζ=0.5, f=0.025, δt=6.4.

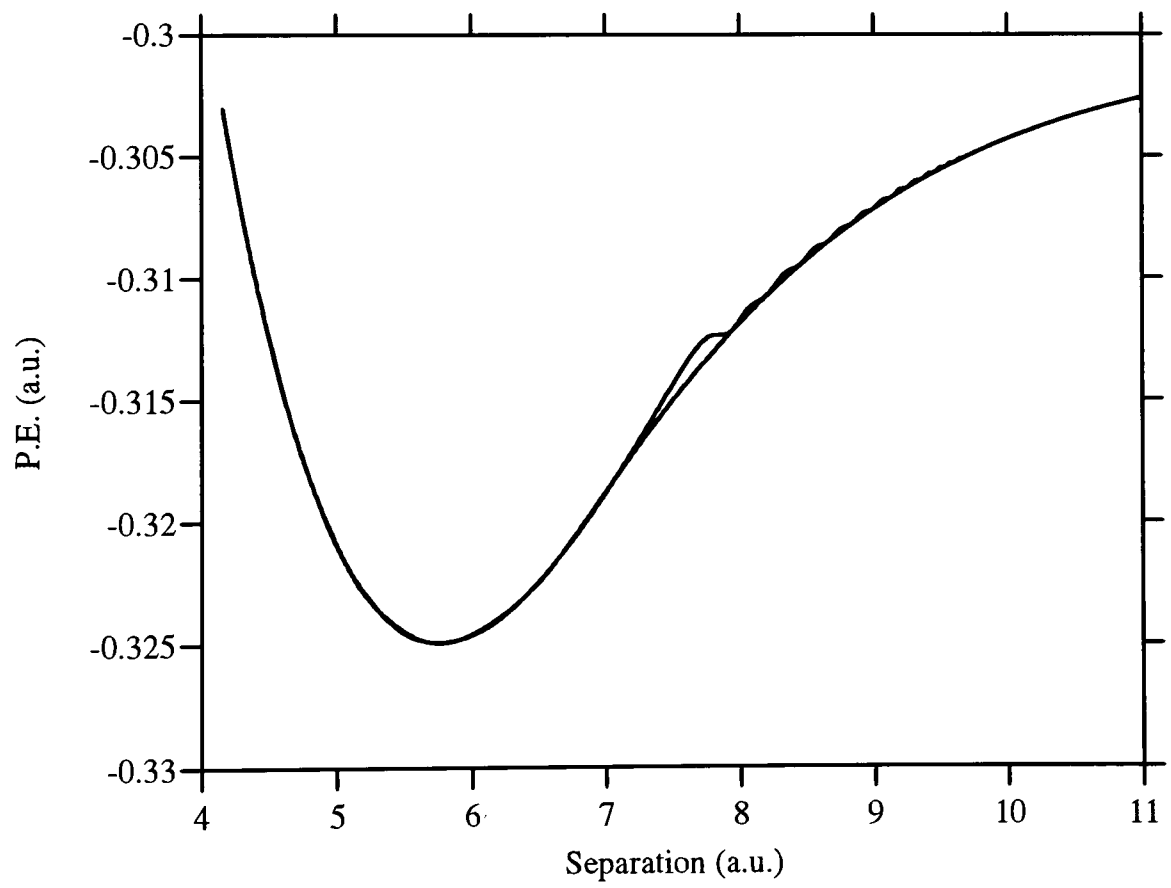


Figure 5.12: The ion potential energy for a dynamics run for Na_2, using the Nosé-Hoover thermostat using the parameters: μ=400, ζ=2.0, f=0.025, δt=6.4.

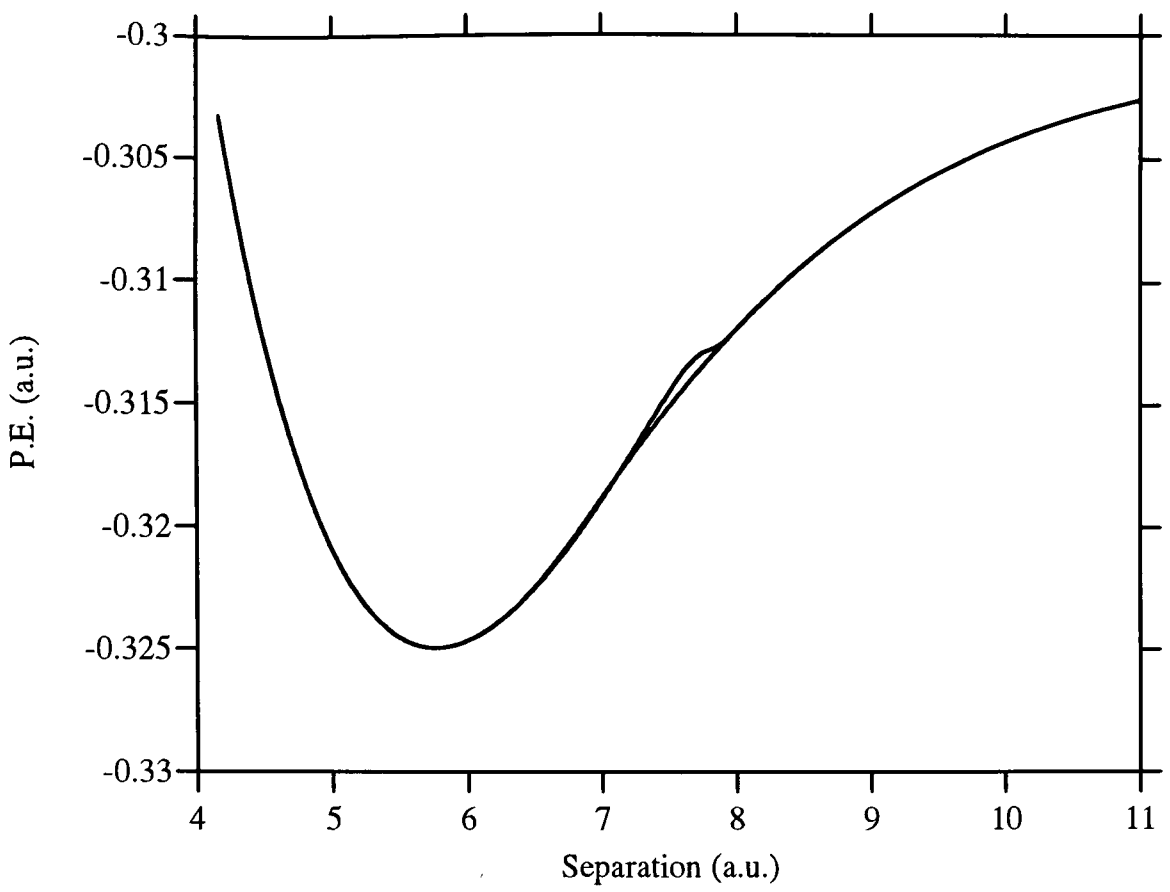


Figure 5.13: The ion potential energy for a dynamics run for Na_2, using the Nosé-Hoover thermostat using the parameters: μ=400, ζ=1.0, f=0.0125, δt=6.4.

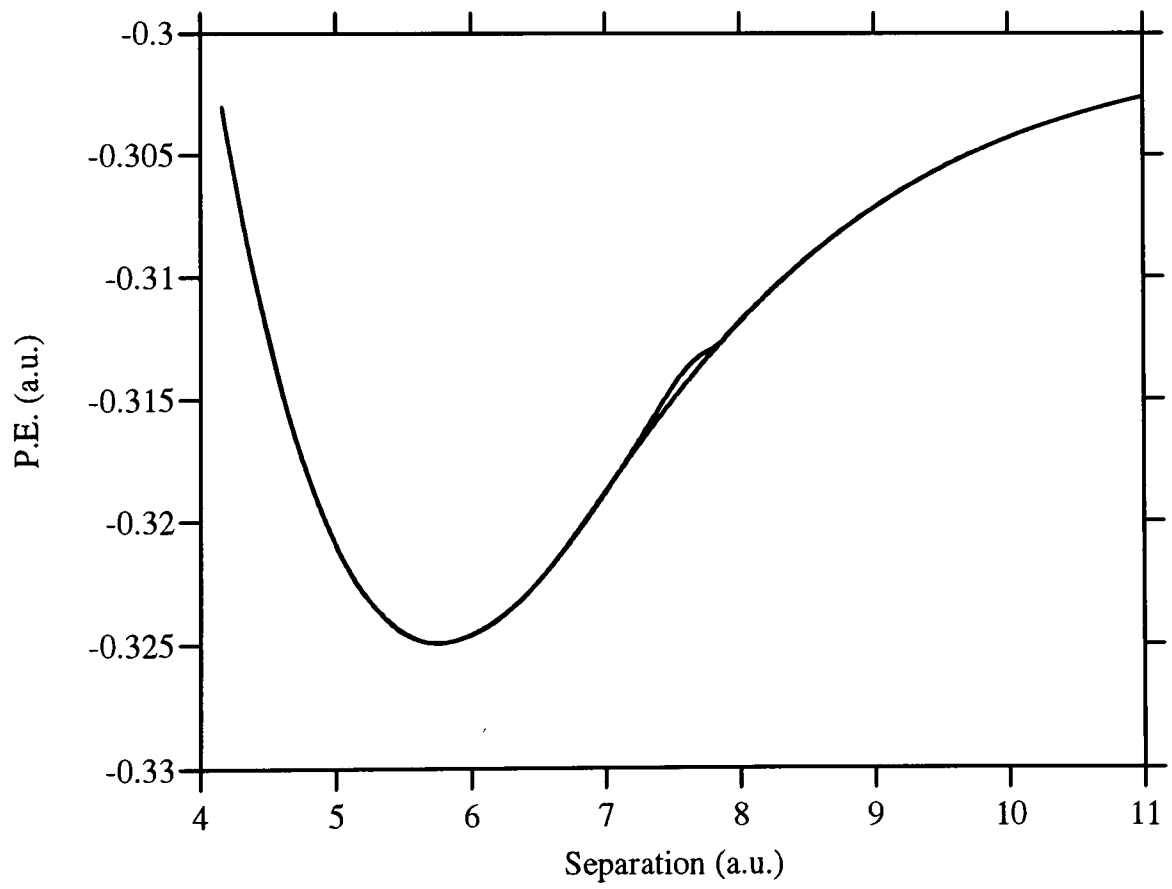


Figure 5.14: The ion potential energy for a dynamics run for Na_2, using the Nosé-Hoover thermostat using the parameters: μ=400, ζ=1.0, f=0.05, δt=6.4.

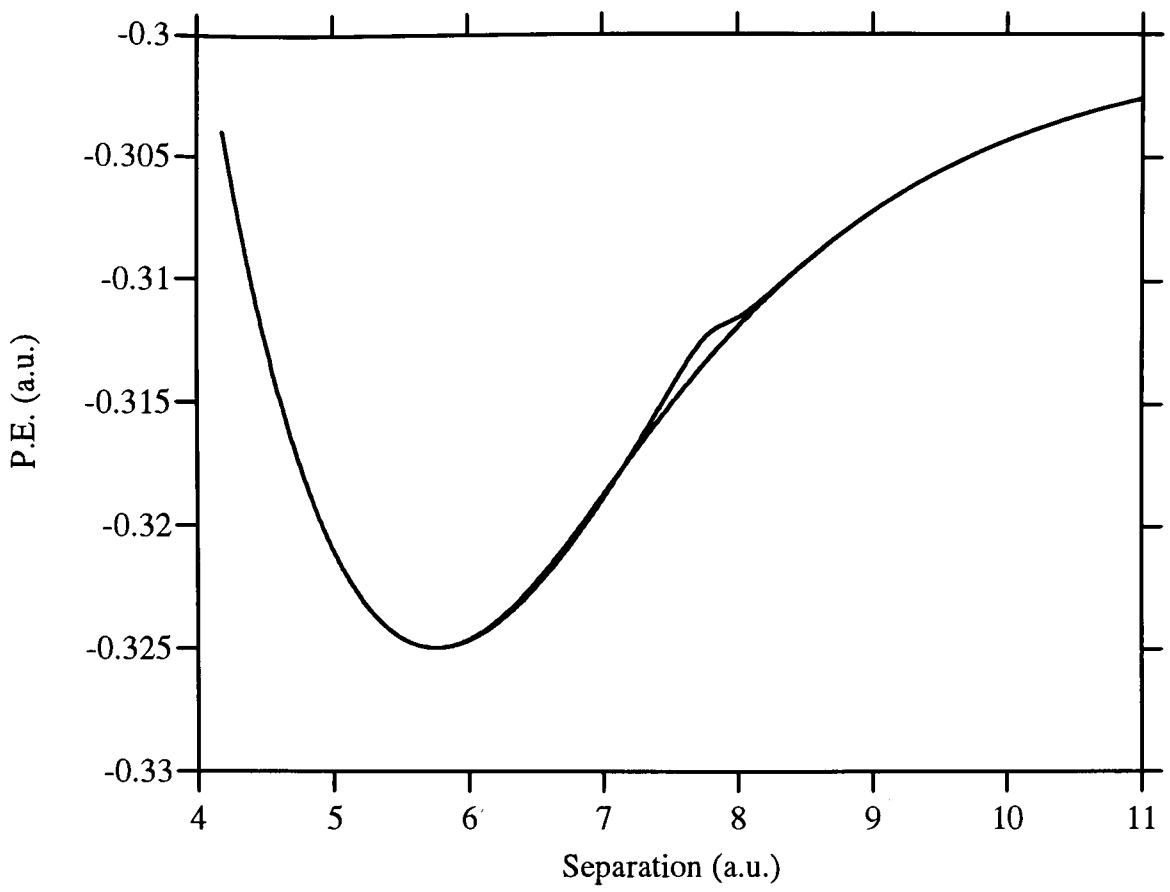


Figure 5.15: The ion potential energy for a dynamics run for Na_2, using the Nosé-Hoover thermostat using the parameters: μ=400, ζ=0.333, f=0.0125, δt=6.4.

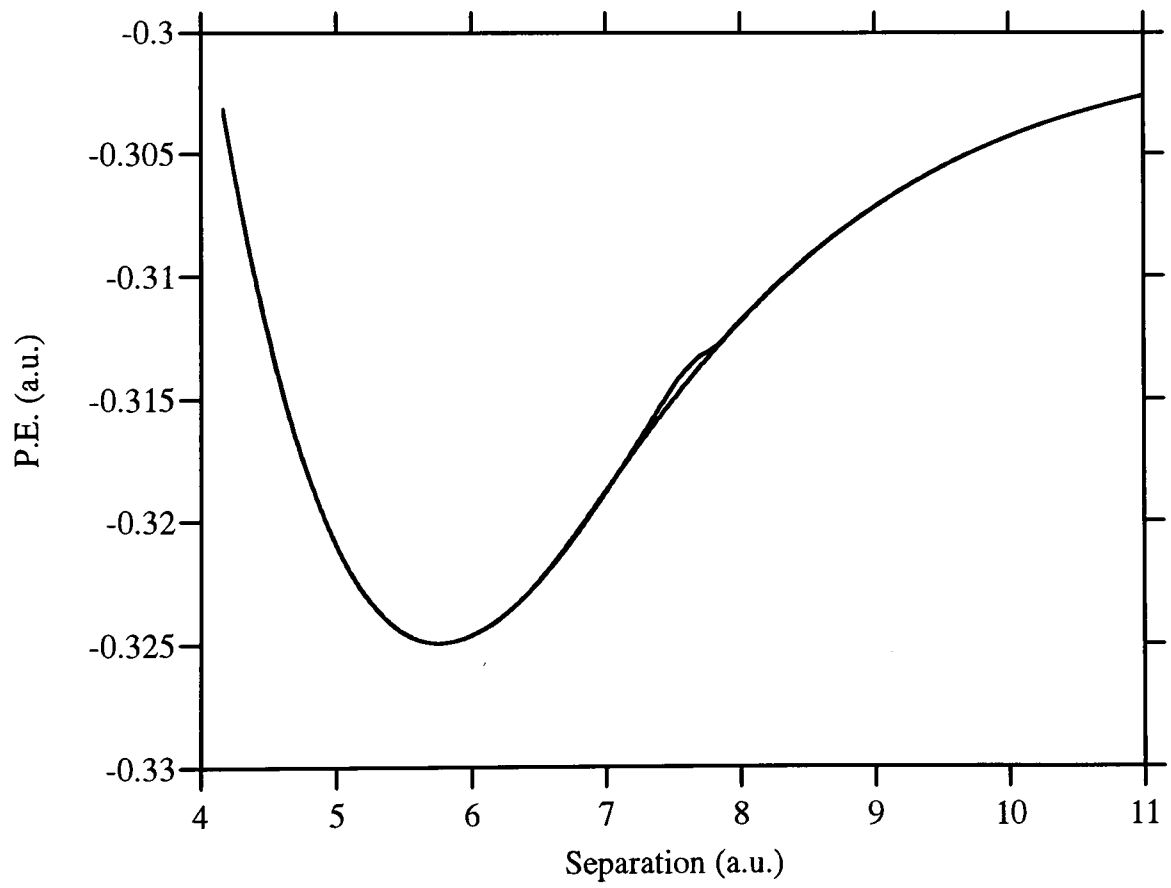


Figure 5.16: The ion potential energy for a dynamics run for Na_2, using the Nosé-Hoover thermostat using the parameters: μ=400, ζ=1.0, f=0.025, δt=6.4.

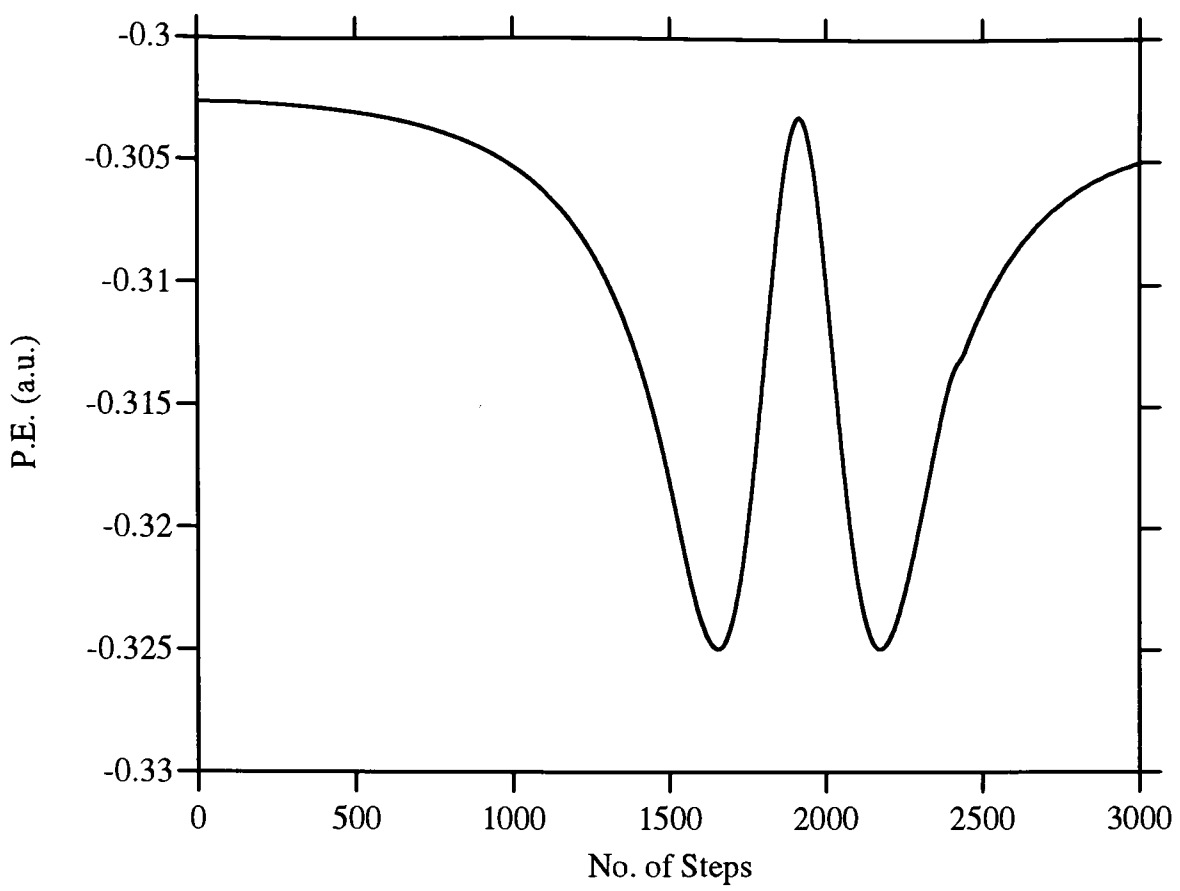


Figure 5.17: The ion potential energy versus step for a dynamics run for Na_2, using the Nosé-Hoover thermostat using the parameters: μ=400, ζ=1.0, f=0.025, δt=6.4.

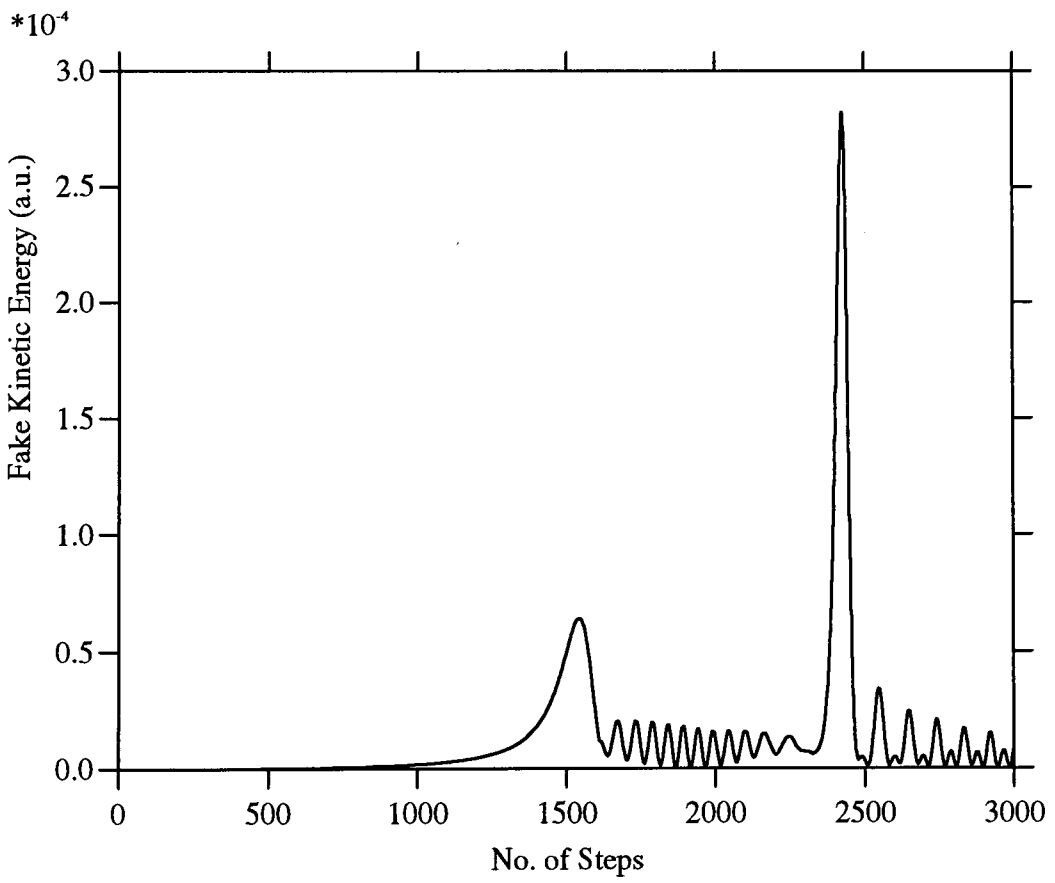


Figure 5.18: The fake kinetic energy for a dynamics run for Na_2, using the Nosé-Hoover thermostat using the parameters: μ=400, ζ=1.0, f=0.025, δt=6.4.

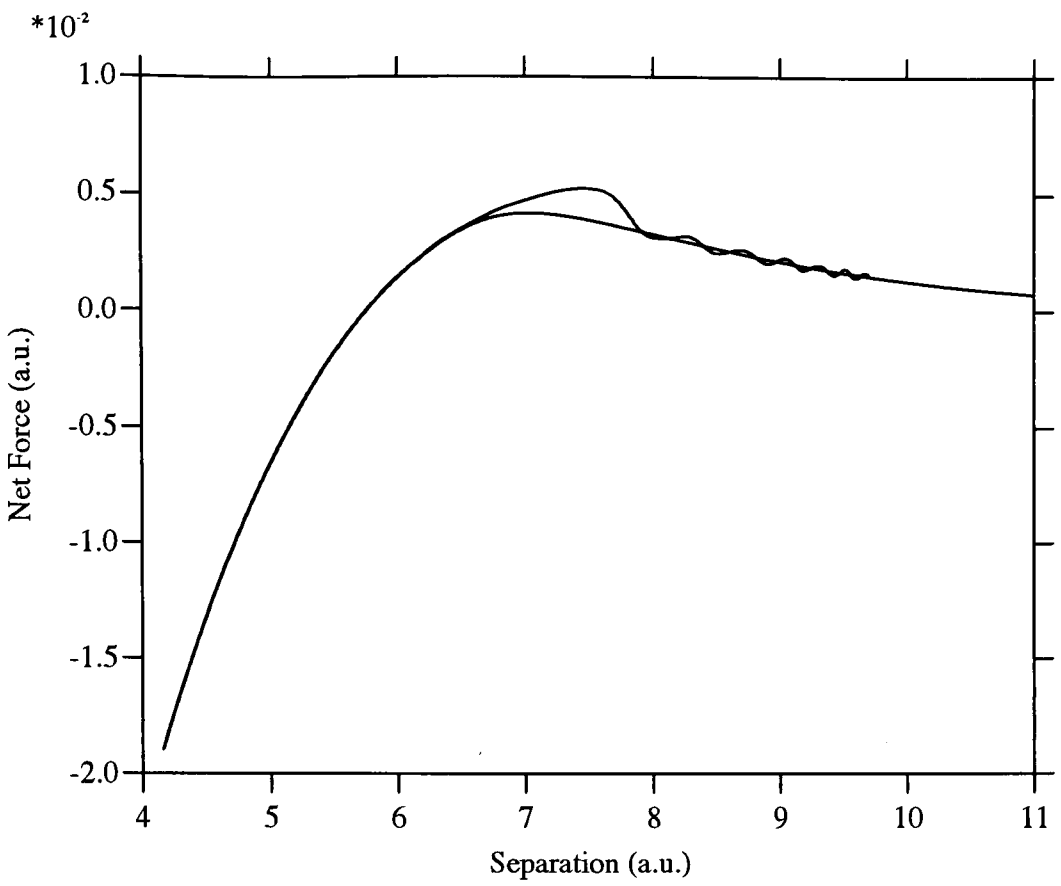


Figure 5.19: The net forces for a dynamics run for Na_2, using the Nosé-Hoover thermostat using the parameters: μ=400, ζ=1.0, f=0.025, δt=6.4.

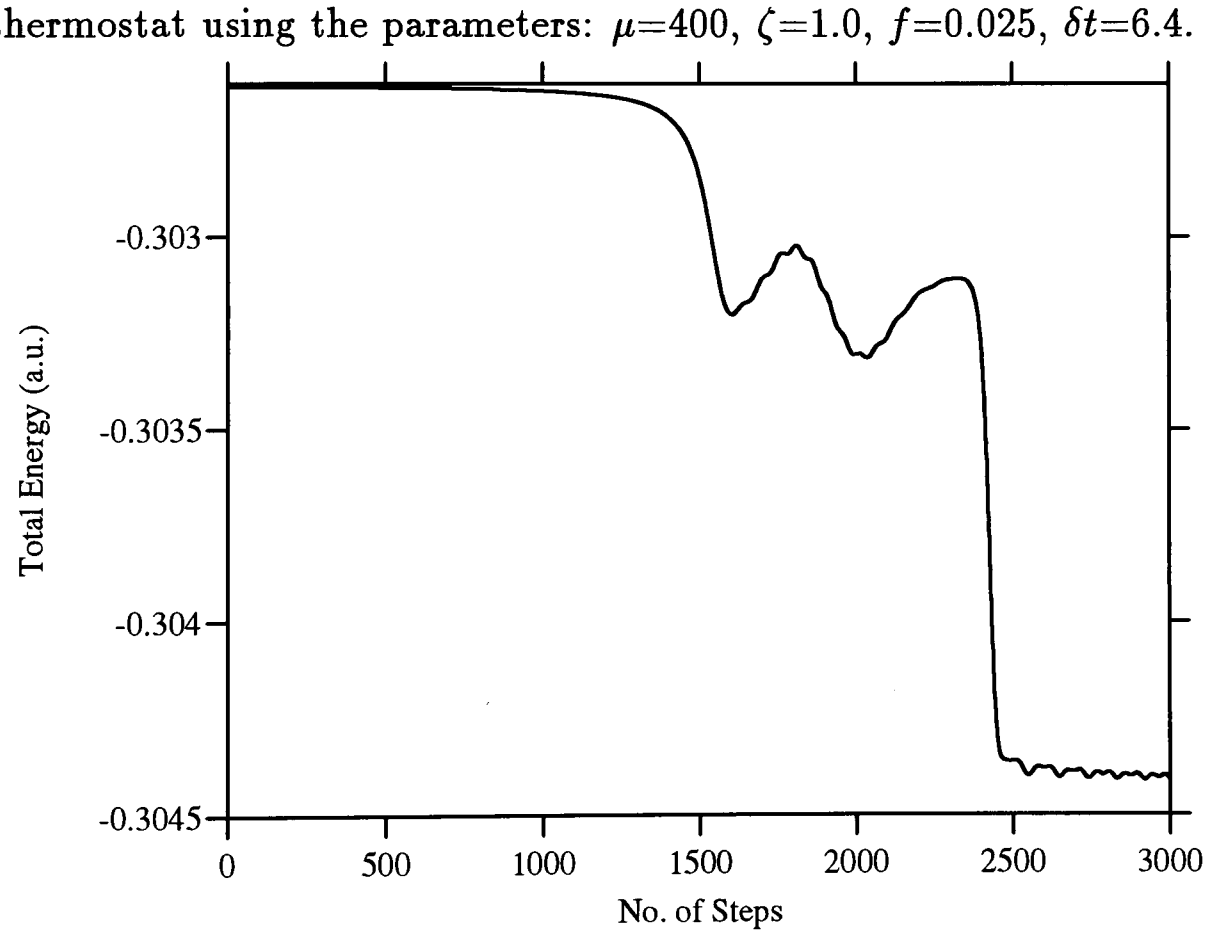


Figure 5.20: The total energy for a dynamics run for Na_2, using the Nosé-Hoover thermostat using the parameters: μ=400, ζ=1.0, f=0.025, δt=6.4.

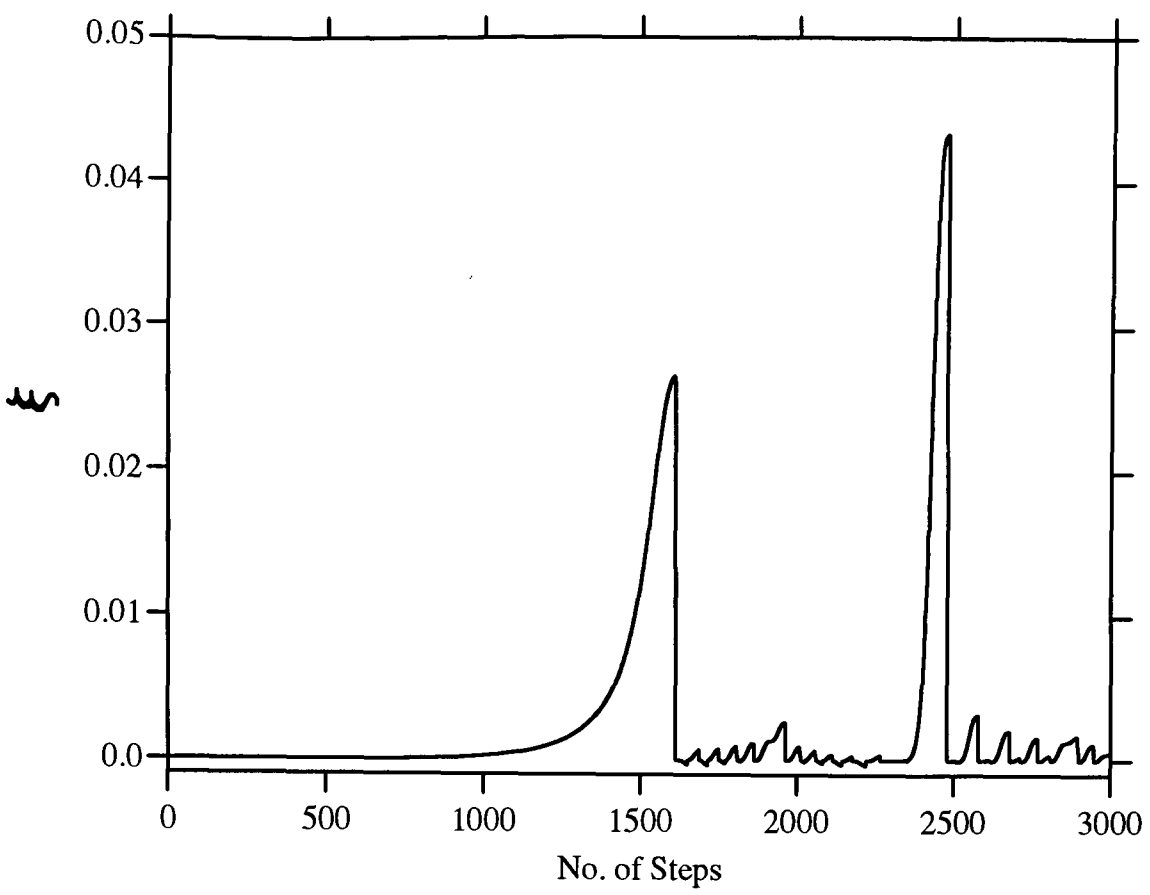


Figure 5.21: The thermostat parameter ξ for a dynamics run for Na_2, using the Nosé-Hoover thermostat using the parameters: μ=400, ζ=1.0, f=0.025, δt=6.4.

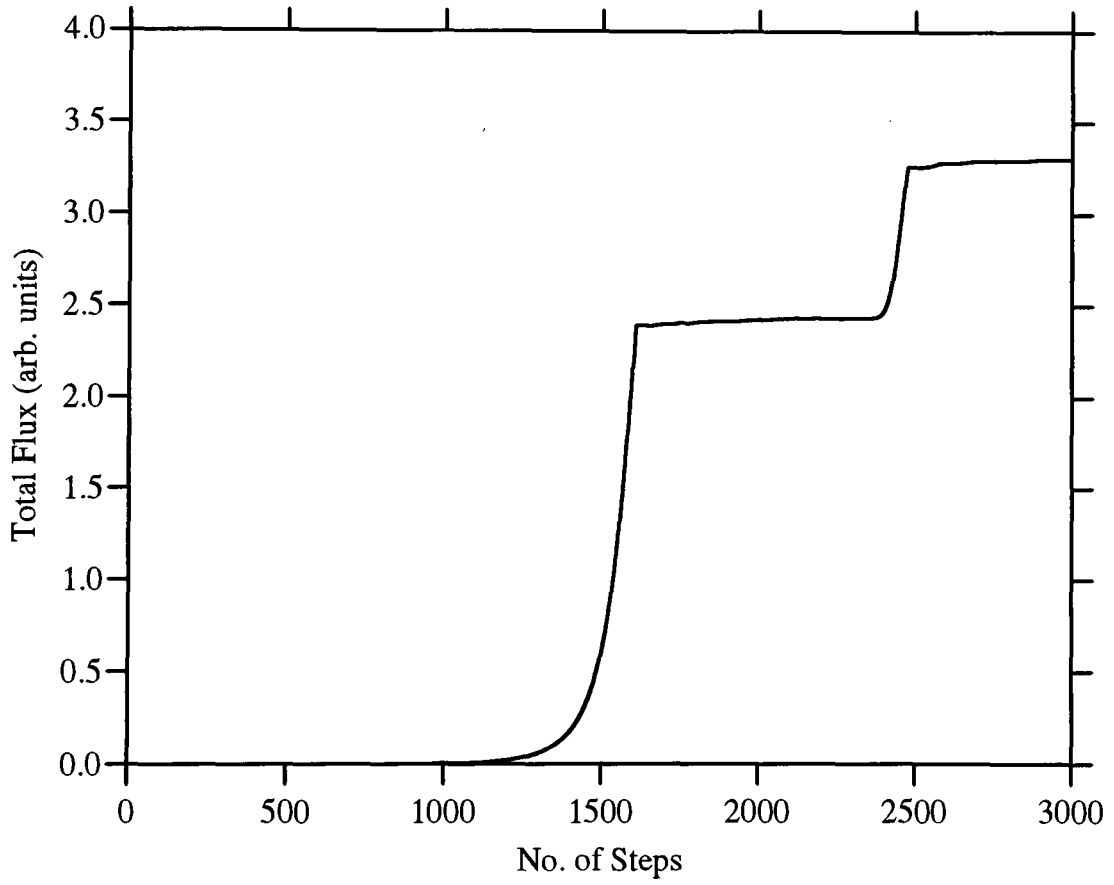


Figure 5.22: The energy flux through the thermostat for a dynamics run for Na_2, using the Nosé-Hoover thermostat using the parameters: μ=400, ζ=1.0, f=0.025, δt=6.4.

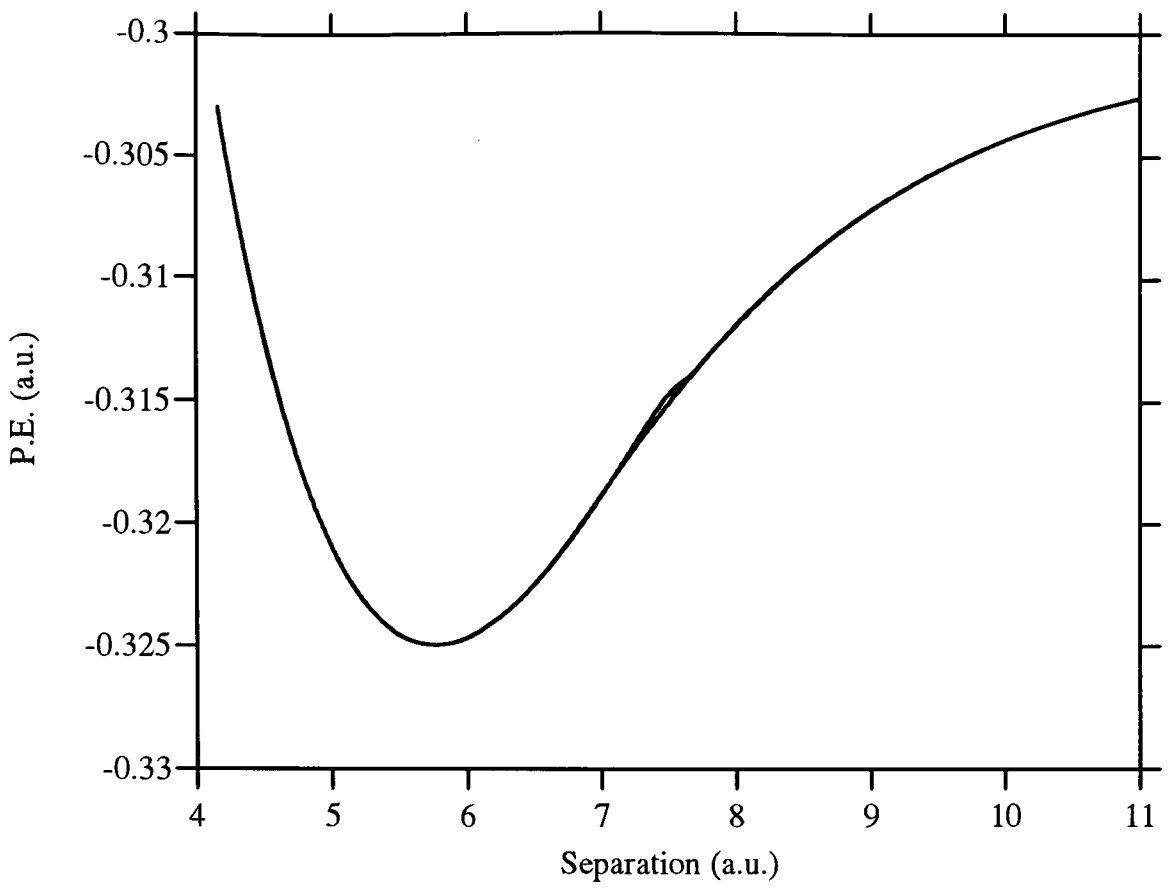


Figure 5.23: The ion potential energy for a dynamics run for Na_2, using the Nosé-Hoover thermostat using the optimum parameters: μ=200, ζ=0.5, f=0.025, δt=6.4.

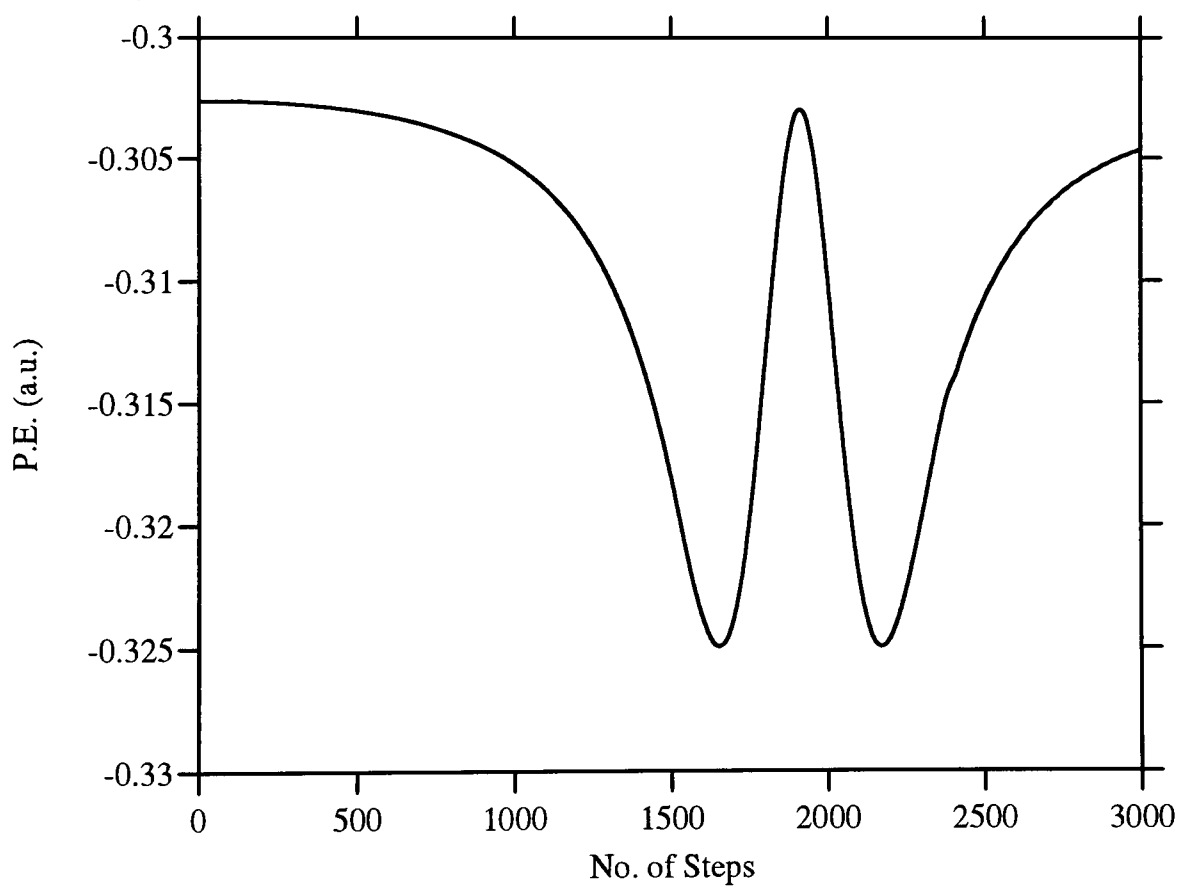


Figure 5.24: The ion potential energy versus step for a dynamics run for Na_2, using the Nosé-Hoover thermostat using the parameters: μ=200, ζ=0.5, f=0.025, δt=6.4.

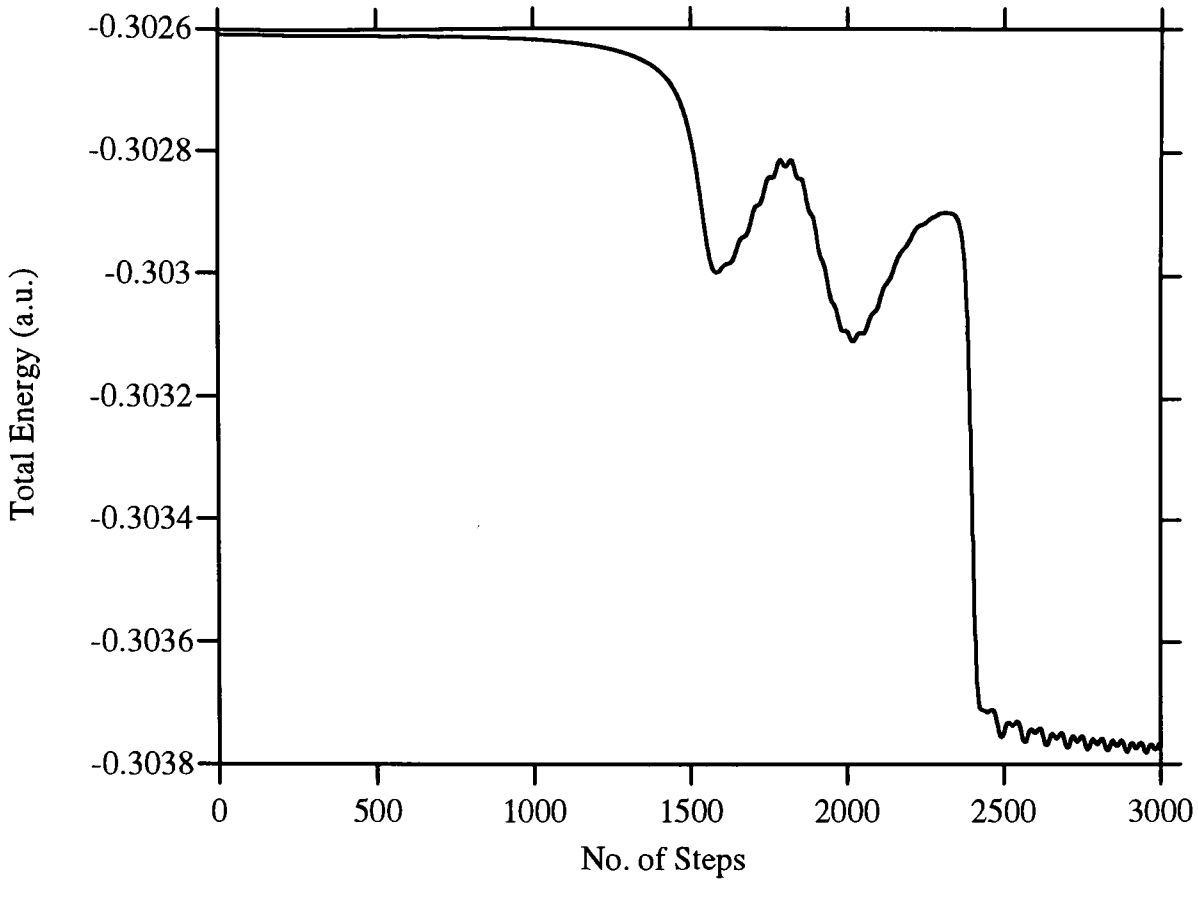


Figure 5.25: The total energy for a dynamics run for Na_2, using the Nosé-Hoover thermostat using the parameters: μ=200, ζ=0.5, f=0.025, δt=6.4.

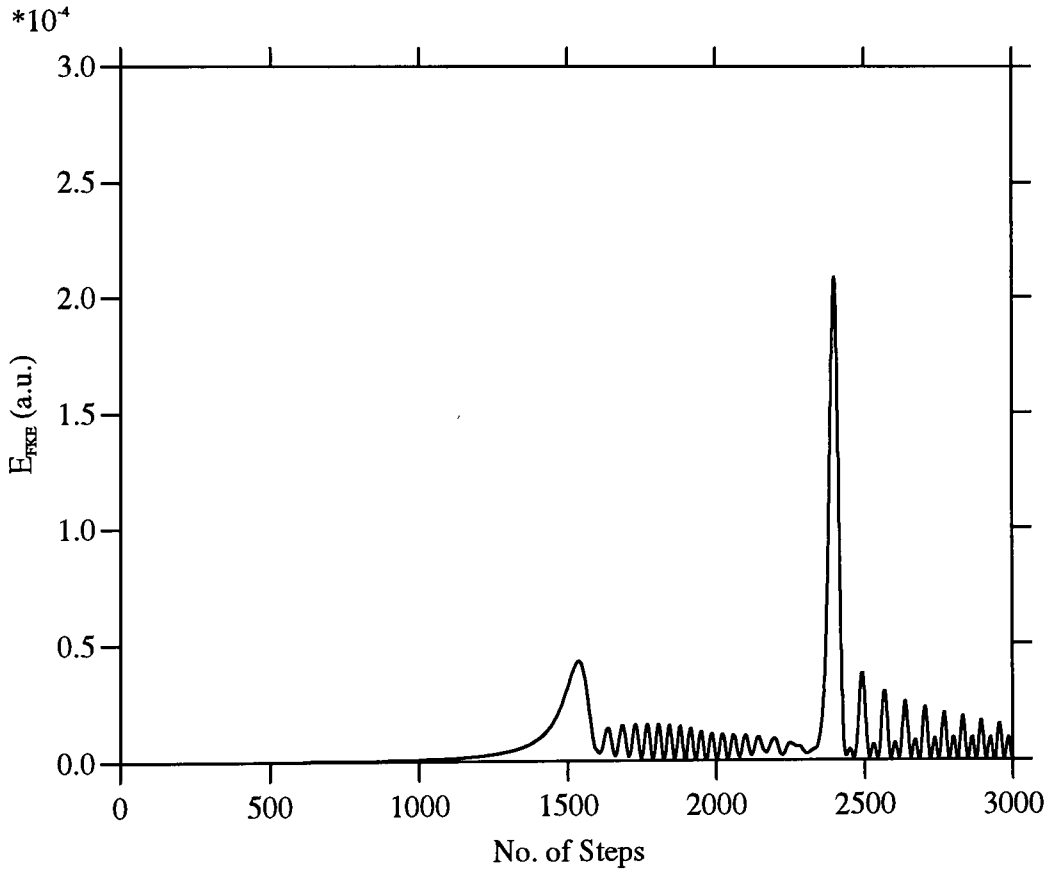


Figure 5.26: The fake kinetic energy for a dynamics run for Na_2, using the Nosé-Hoover thermostat using the parameters: μ=200, ζ=0.5, f=0.025, δt=6.4.

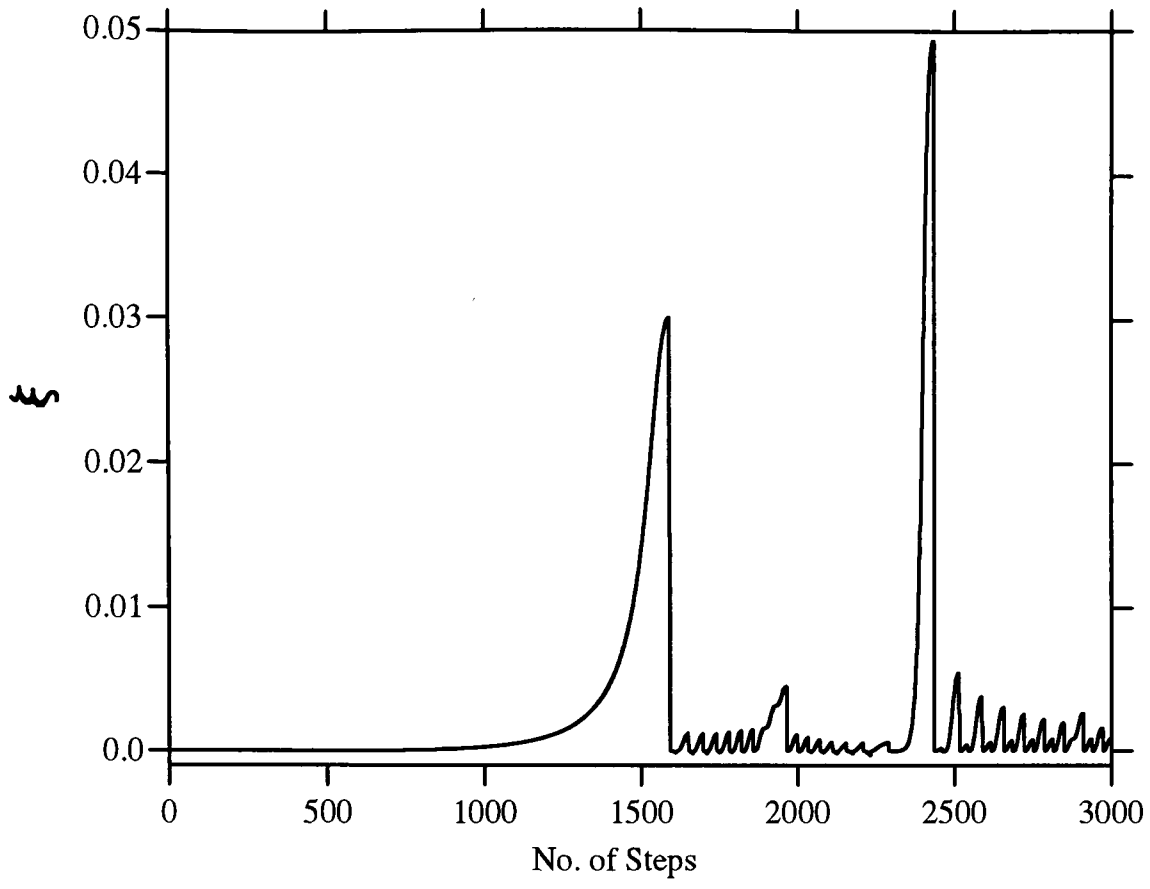


Figure 5.27: The thermostat parameter ξ for a dynamics run for Na_2, using the Nosé-Hoover thermostat using the parameters: μ=200, ζ=0.5, f=0.025, δt=6.4.

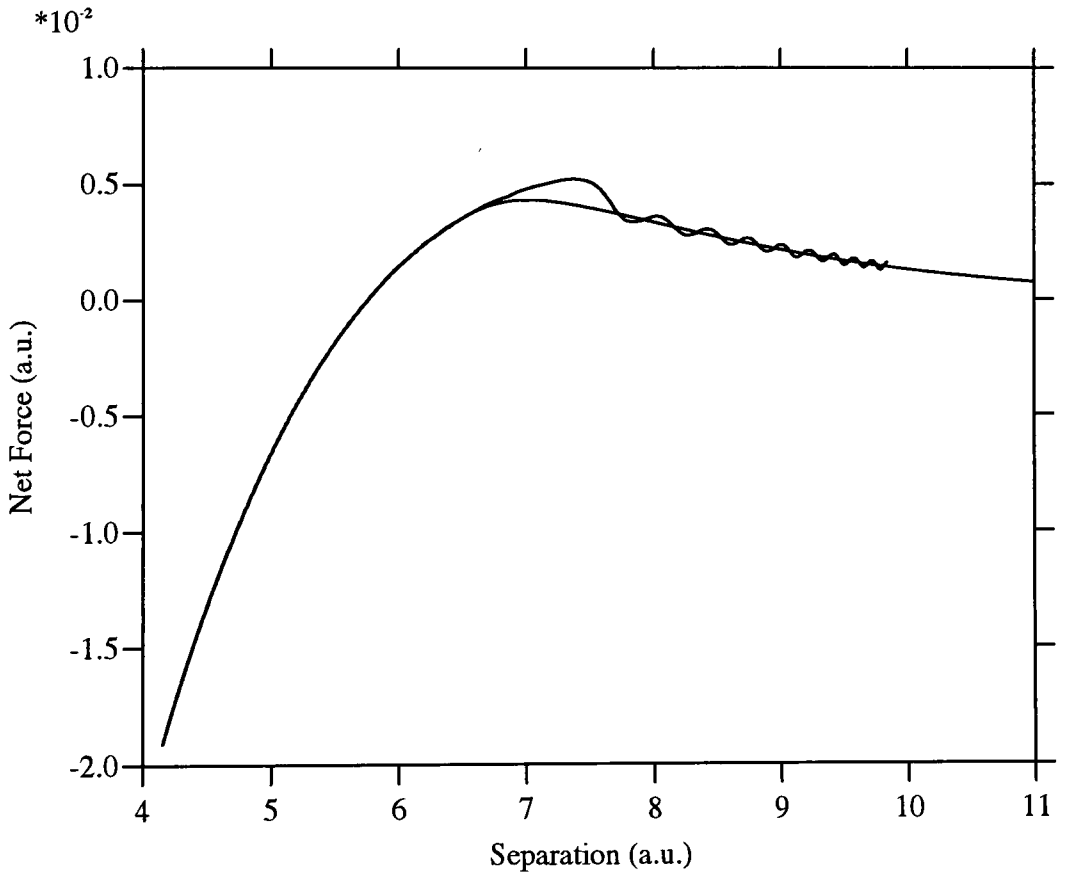


Figure 5.28: The net forces for a dynamics run for Na_2, using the Nosé-Hoover thermostat using the parameters: μ=200, ζ=0.5, f=0.025, δt=6.4.

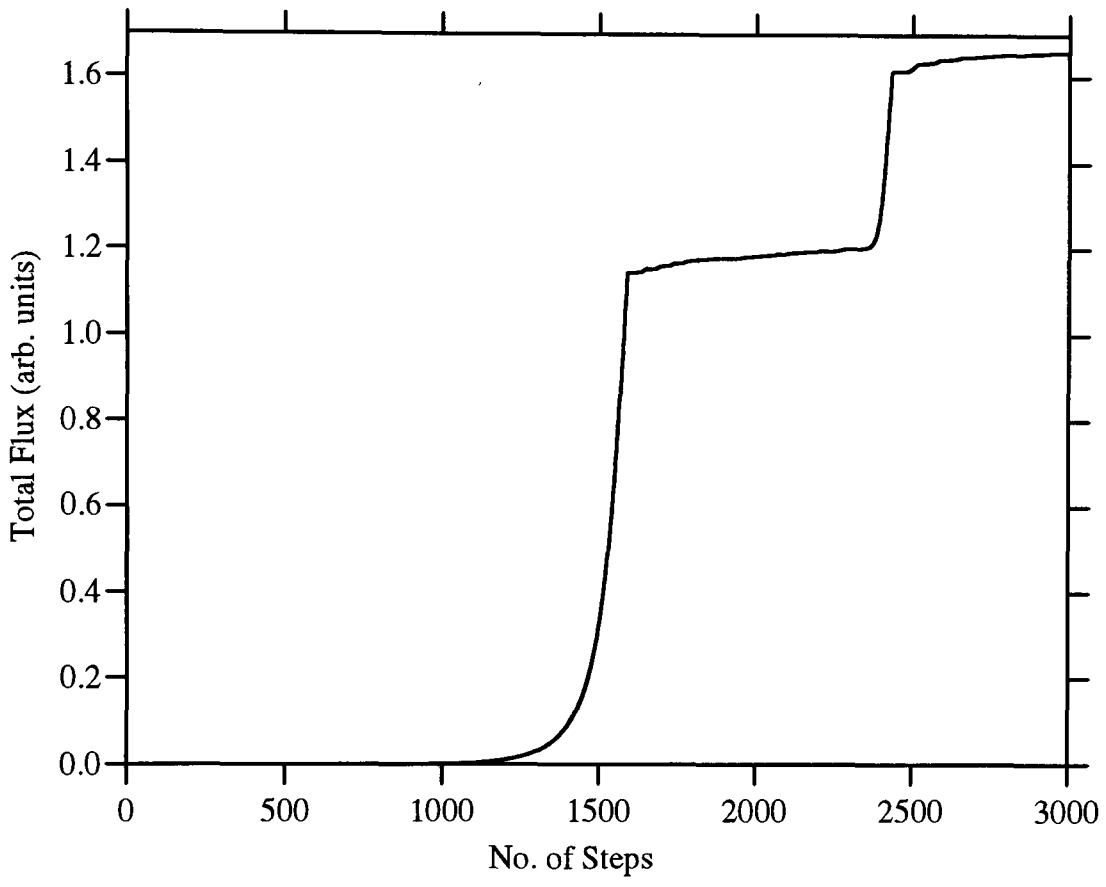


Figure 5.29: The energy flux through the thermostat for a dynamics run for Na_2, using the Nosé-Hoover thermostat using the parameters: μ=200, ζ=0.5, f=0.025, δt=6.4.

$$vxsub_i = -\frac{\omega_z ry_i}{3\left(rx_i^2 + ry_i^2\right)}. \tag{5.36}$$

(d) Rescale velocities to correct temperature, check tolerance in linear and angular momentum. Go to (a) if not reached.

To obtain the correct initial fake kinetic energy the ions are moved back one step and using a CG minimisation the correct coefficients for $\psi_{i\sigma}(-\delta t)$ were generated [92]. The other parameters used were those giving the best Na_2 dynamics, ie. $\mu = 200$, $\delta t = 6.4$, $\zeta = 0.5$, $f = 0.025$. The length of the runs was between 10000, and 20000 steps, and all runs were started from the ground state geometry.

Figures 5.30, 5.31, 5.32, 5.34 shows typical ion kinetic energy, fake kinetic energy, total energy flux, and potential energy plots for a 20000 step run. Figure 5.33 shows the corresponding variation in the bond lengths. The variation of the bond lengths show that the system remains in the obtuse isosceles triangle geometry for almost the entire run, with the longest bond opening and closing. Towards the end of the run though the bond suddenly migrates round the triangle. It can be clearly seen that the transition state does indeed have an acute isosceles geometry. Analysis of the other runs shows a similar pattern, ie. that the cluster maintains it geometry with sudden pseudorotation events.

The dynamics of runs which show a pseudorotation event rather than just vibrating in one configuration have been analysed using a molecular graphics package (MOLDYN) on a Silicon Graphics workstation. From this the mechanism shown in figure 5.35 was elucidated. The mechanism involves the cluster initially undergoing an asymmetric stretch. Towards the extremity of the stretch the two atoms in the shortest bond "rotate" about their midpoint. This then leaves the longest bond pseudorotated one place round the cluster.

An examination of the total energy flux along the run shows that the thermostat had to control the fake kinetic energy whenever the long bond length became close to the length of the two shorter bonds. The most noticeable case is just after 15000 steps when the actual pseudorotation event occurs. Although for reasons of available cpu time, no runs were carried out using normal CP dynamics, it seems reasonable to conclude that if this were done then the algorithm would breakdown at precisely the type of transition we would like to see. With the Nosè-Hoover thermostat applied though, the fake kinetic energy remains small and the system, throughout the run, shows no sign of departing from the BO surface.

We now wish to examine the kinetics of the peudorotation. This is a unimolecular reaction which may be described by the following scheme [52],

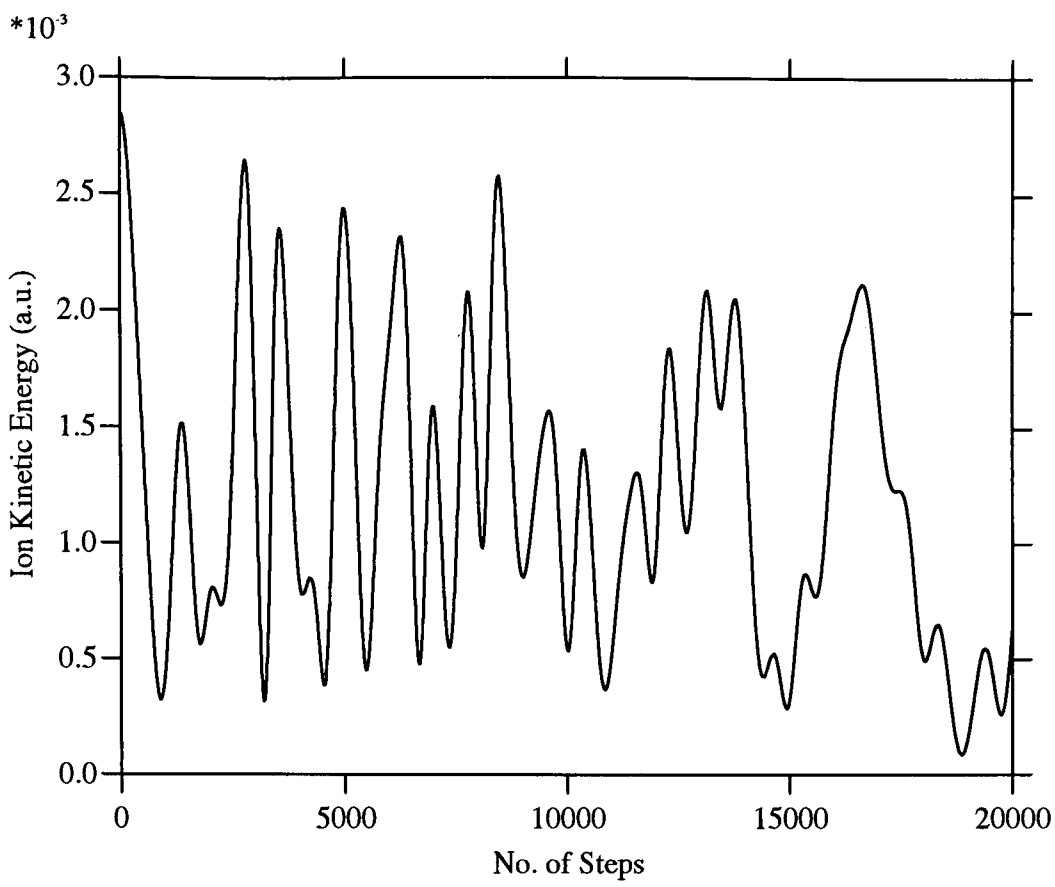


Figure 5.30: The ion kinetic energy for a typical 20000 step dynamics run for Na_3, using the Nosé-Hoover thermostat.

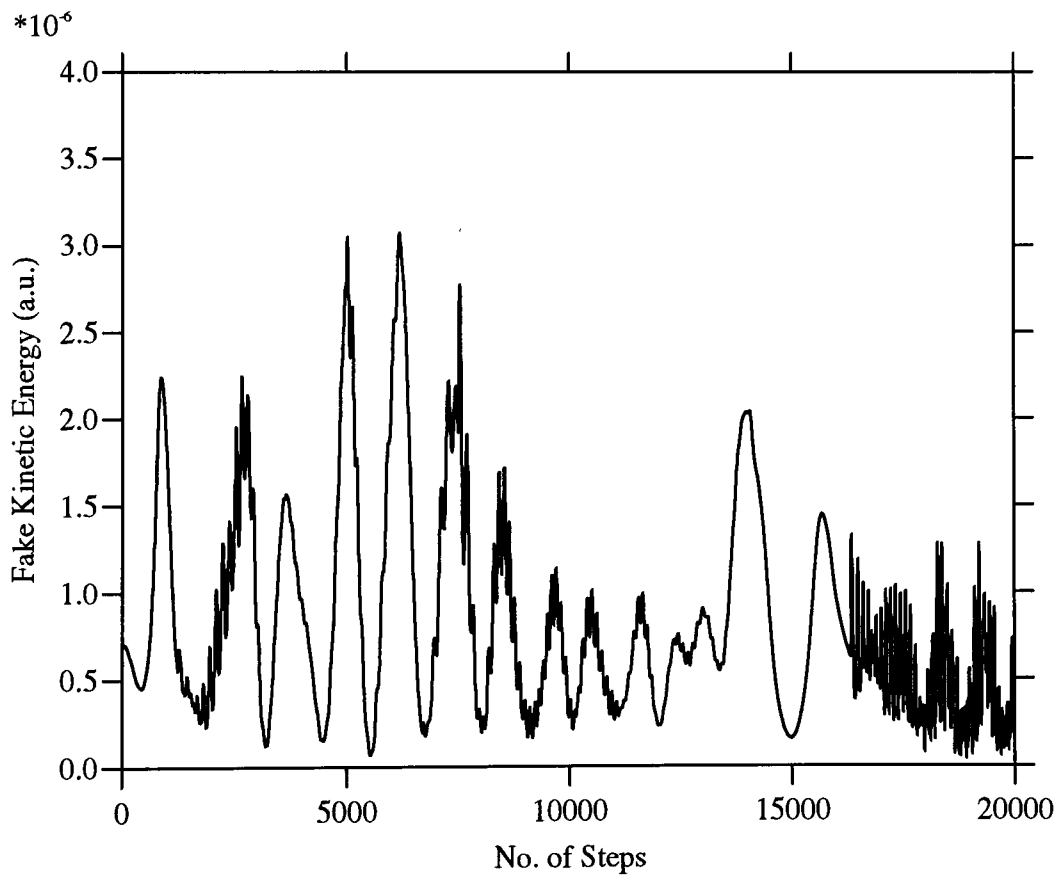


Figure 5.31: The fake kinetic energy for a typical 20000 step dynamics run for Na_3, using the Nosé-Hoover thermostat.

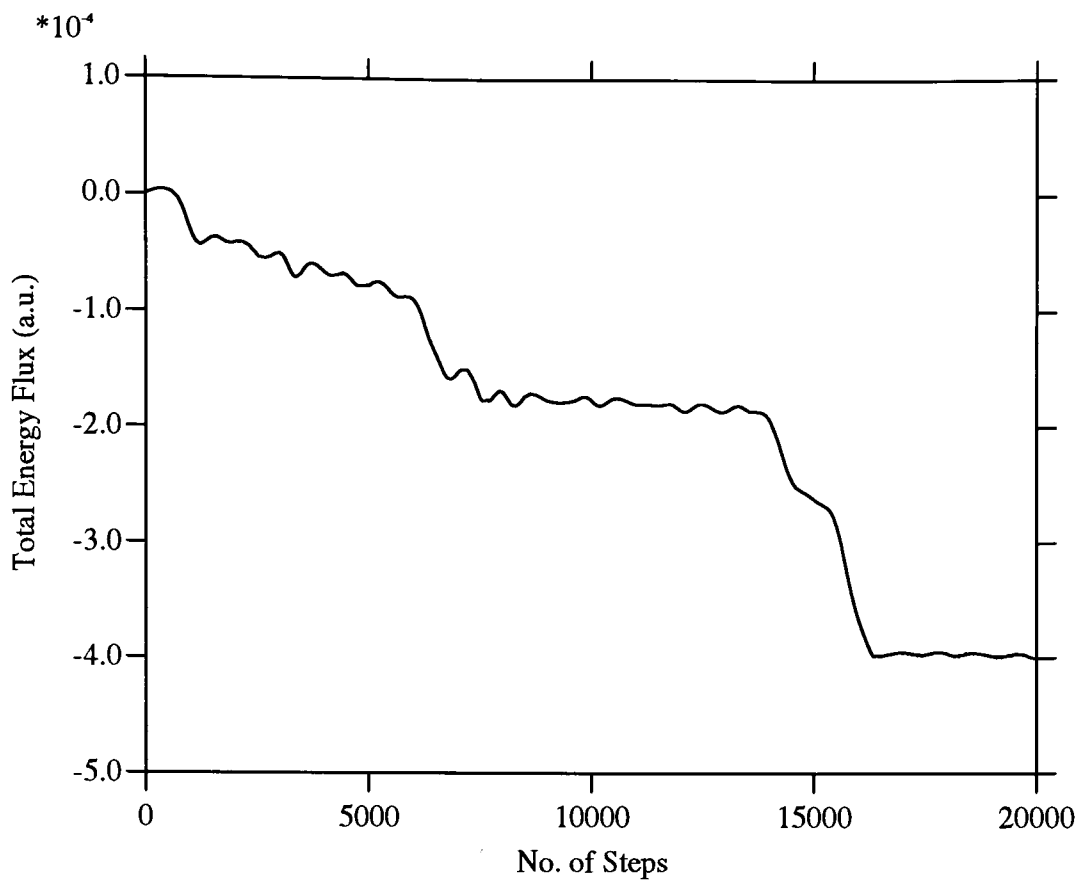


Figure 5.32: The total energy flux for a typical 20000 step dynamics run for Na_3, using the Nosé-Hoover thermostat.

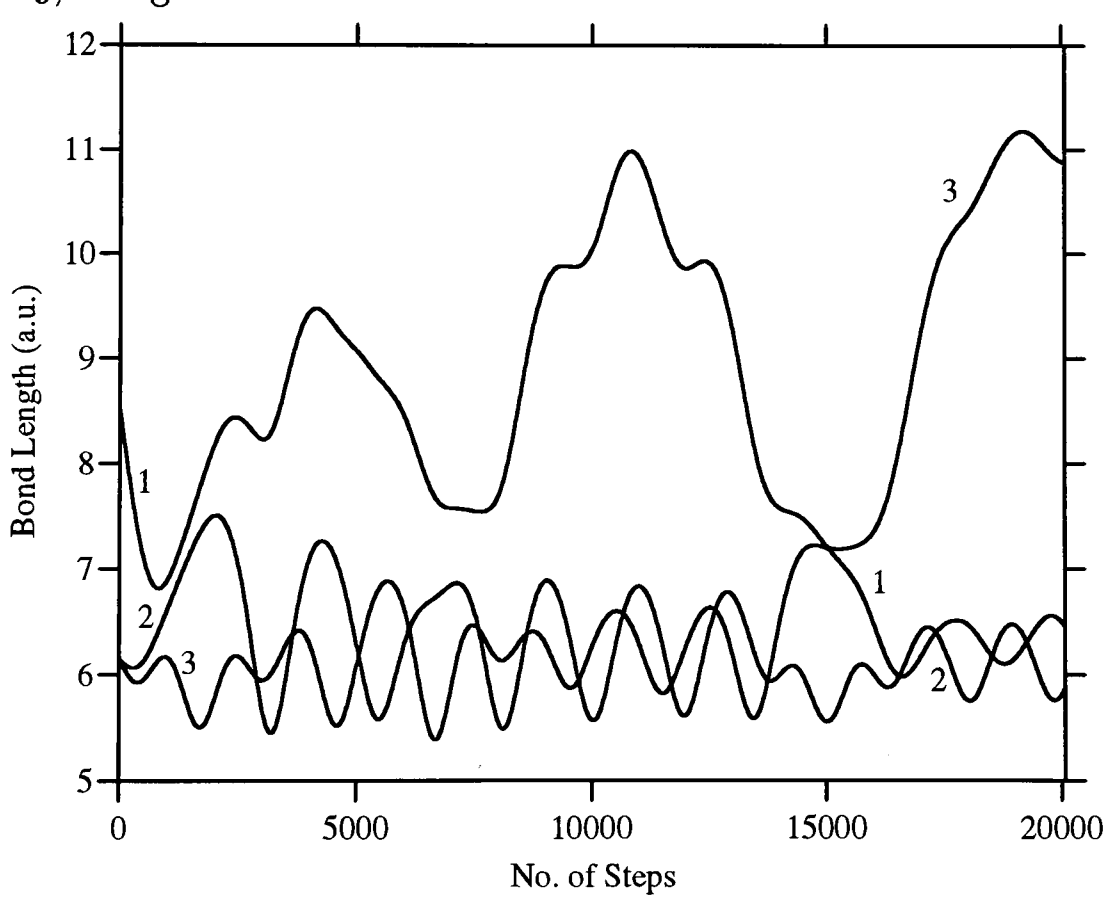


Figure 5.33: The variation in the bond lengths for a typical 20000 step dynamics run for Na_3, using the Nosé-Hoover thermostat.

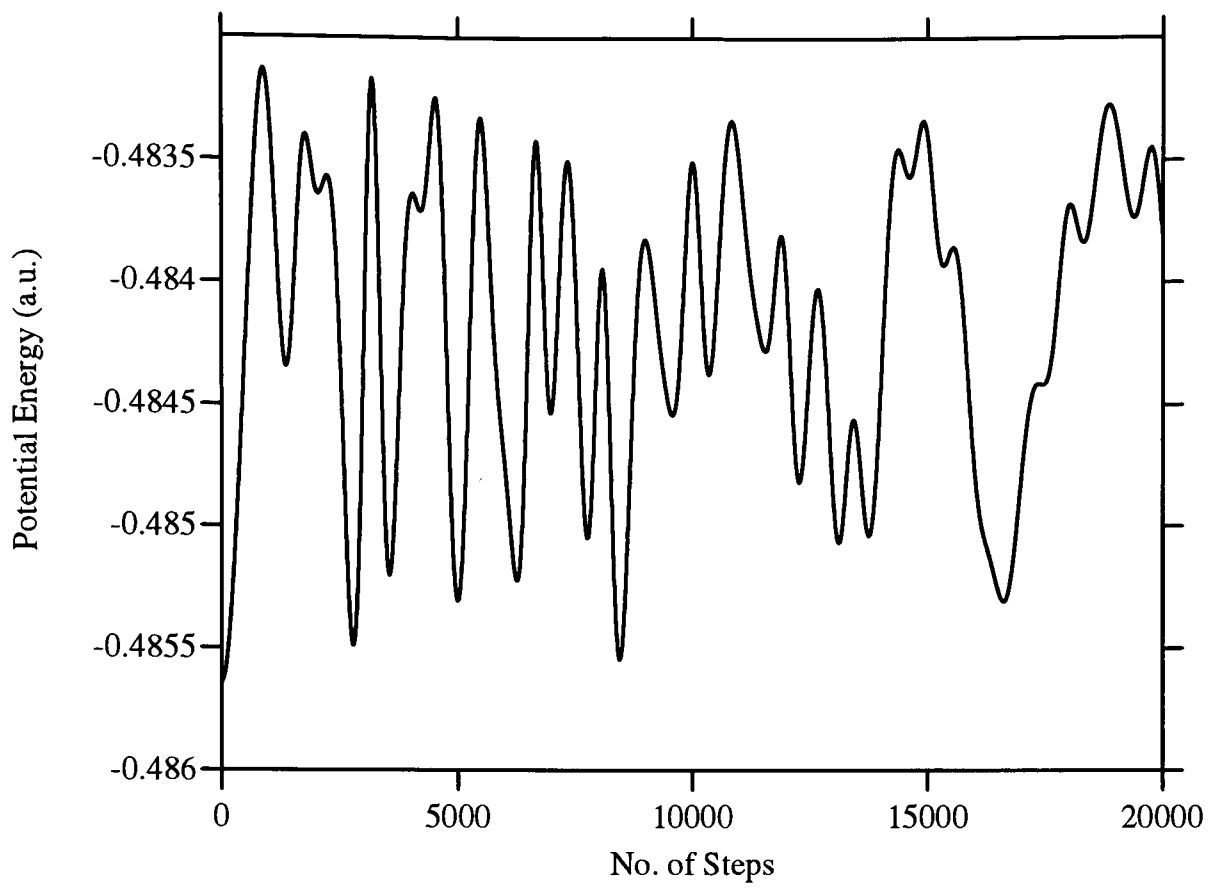


Figure 5.34: The ion potential energy for a typical 20000 step dynamics run for Na_3, using the Nosé-Hoover thermostat.

$$A + M \underset{k_{-1}}{\overset{k_1}{\rightleftharpoons}} A^* + M \tag{5.37}$$

$$A^* \xrightarrow{k_2} A^\ddagger \rightarrow \text{products} \tag{5.38}$$

Here M is any molecule that can transfer energy to A when a collision occurs. A^* is the energised molecule whilst $A^\ddagger$ is the activated molecule. The distinction between A^*, and $A^\ddagger$ is that whilst both have sufficient energy to undergo the reaction, $A^\ddagger$ has the energy in the correct degrees of freedom for reaction, $A^\ddagger$ is by definition an activated molecule passing through the dividing surface between reactants and products on the potential energy surface. Clearly what this step is modelling then is the second step of this scheme.

To follow the kinetics we need some method of deciding which of the three equivalent conformations the cluster is in. This was done in the following way. Firstly a vector $\mathbf{u}$ consisting of three components was assigned to the molecule. Each component represents one of the bonds; the component for the longest bond being set to 1, and to 0 for the rest. This was done for each step and the dot product,

$$d(t) = \mathbf{u}(t) \cdot \mathbf{u}(0) \tag{5.39}$$

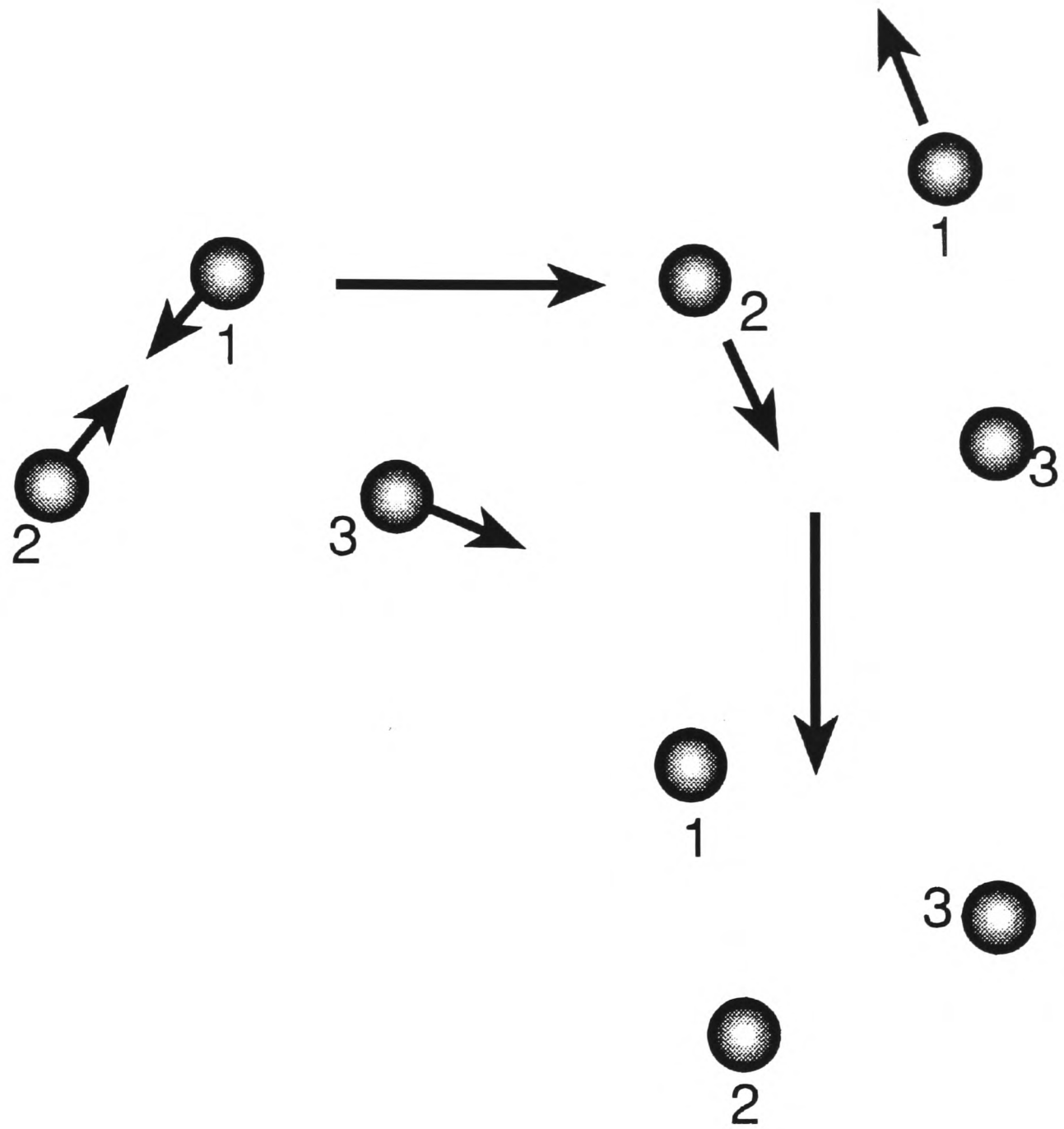


Figure 5.35: The mechanism for pseudorotation of Na_3.

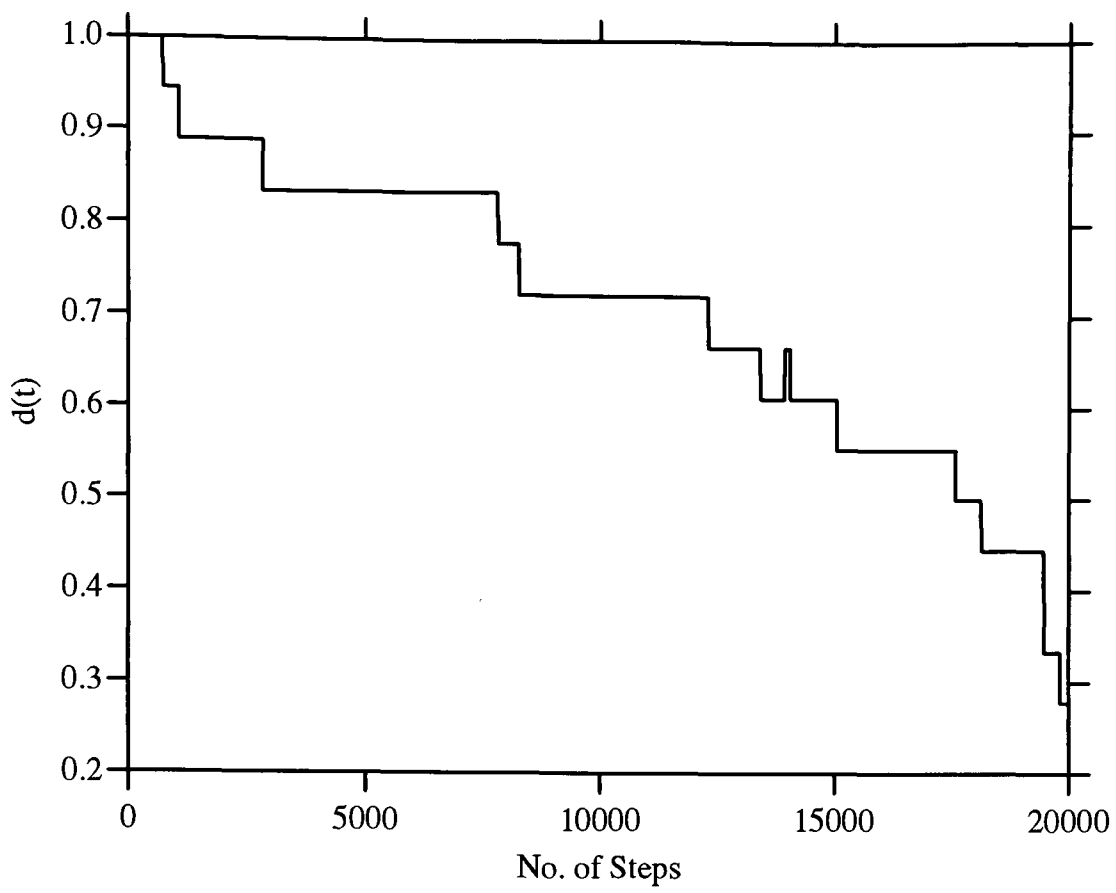


Figure 5.36: The isomerisation parameter, d(t), versus number of steps for Na_3 dynamics.

was taken. Clearly $d(t)$ will be 1 if the cluster is in the same configuration as initially and zero otherwise. $d(t)$ was then averaged over all the runs of 20000 steps. When the cluster conformation has completely randomised we expect $d(t)$ to be equal to $\frac{1}{3}$. Thus we take the time at which $d(t)$ first drops to $\frac{1}{3}$ to be the relaxation time of the system $t_2(= 1/k_2)$. $d(t)$ versus number of steps calculated in this way is shown in figure 5.36. From this we get $t_2 \sim 3.01 \times 10^{-12}$s.

We are also interested in the activation energy E_a for the reaction. This is simply th energy of the transition state minus the energy of the ground state geometries. If we define the transition state as the point at which $d(t)$ changes from 1 to 0 for a given run this is readily obtained from the potential energy plot for that run. In this way we obtain $\bar{E}_a = 486\text{cm}^{-1}$, and $E_a(\text{min}) = 327\text{cm}^{-1}$

5.4.2 The Pseudorotation of Na_4

Naively the pseudorotation of Na_4 via a square planar transition state (see figure 5.37) might seem a straightforward process. However on considering the electronic rearrangement necessary it is clear that this is not the case. To find out the actual electronic rearrangement for this process then we carried out the simulations described below.

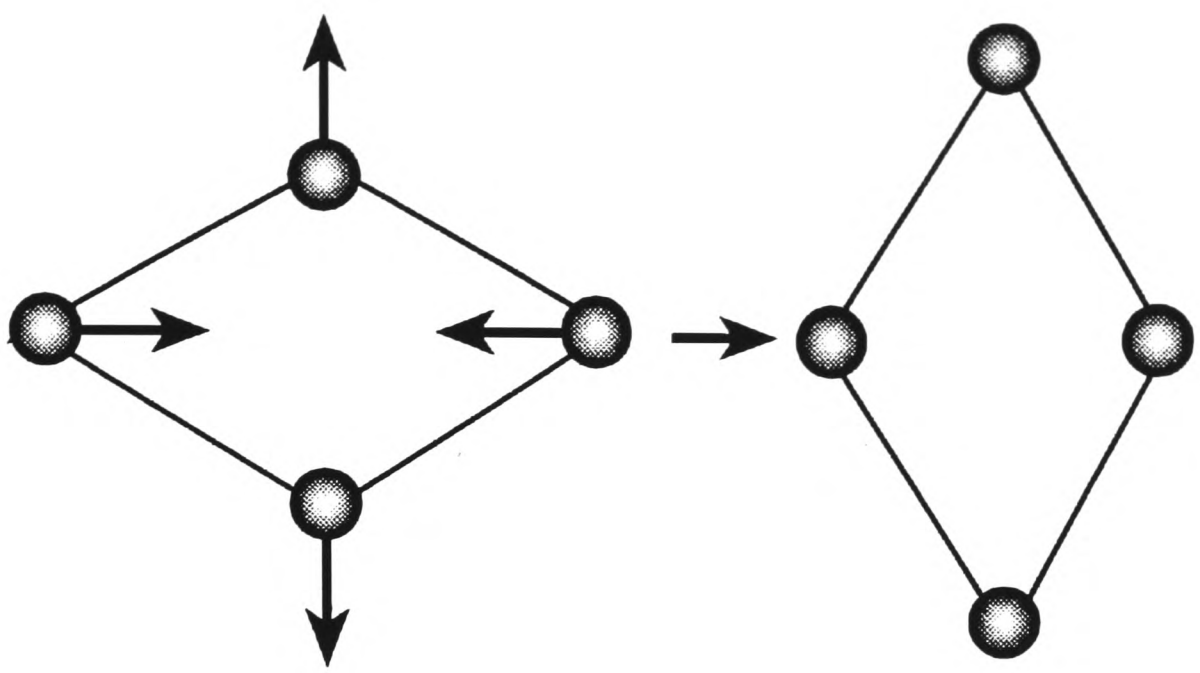


Figure 5.37: Initial velocities given toNa_4 cluster to attempt to "fire" it into the equivalent pseudorotated geometry.

The first study was to try and "fire" the cluster through to the other geometry. This was done by giving the atoms equal velocities in the directions indicated in figure 5.37. The parameters for the run were the same as for the Na_3 calculations. Again the "backstep" procedure for obtaining the correct initial fake kinetic energy was used. It was found that an initial kinetic energy of the order of 4.25×10^{-3}a.u. (equivalent to roughly 3000K) was required to overcome the energy barrier. Figures 5.38, and 5.39 shows the potential energy and fake kinetic energy plots for such a run. The potential energy is unexpectedly asymmetric. From the fake kinetic energy plot we can see that there is a very rapid rearrangement of the electrons when the potential energy is a maximum. Inspection of the average local moment parameter explains this; the system is going from fully spin paired to fully spin unpaired. We can now see that the asymmetry in the potential energy curve is due to the problem encountered in Na_2 of following the spin paired curve when it is no longer the ground state. It is clear from this that the thermostat has not been able to resolve the problem of spin unpairing, although the simultaneous unpairing of four electrons is rather a severe test. Note though that it does prevent breakdown of the algorithm as already observed for Na_2, we simply cannot guarantee that it will keep the system on the ground state surface when a spin unpairing process should occur. A separate method for inducing spin unpairing is still required, and this presumably requires some external perturbation to help break the symmetry. In fact we should expect this sort of problem for this system as in terms of Woodward-Hofmann rules for frontier molecular orbitals we have an avoided crossing [67].

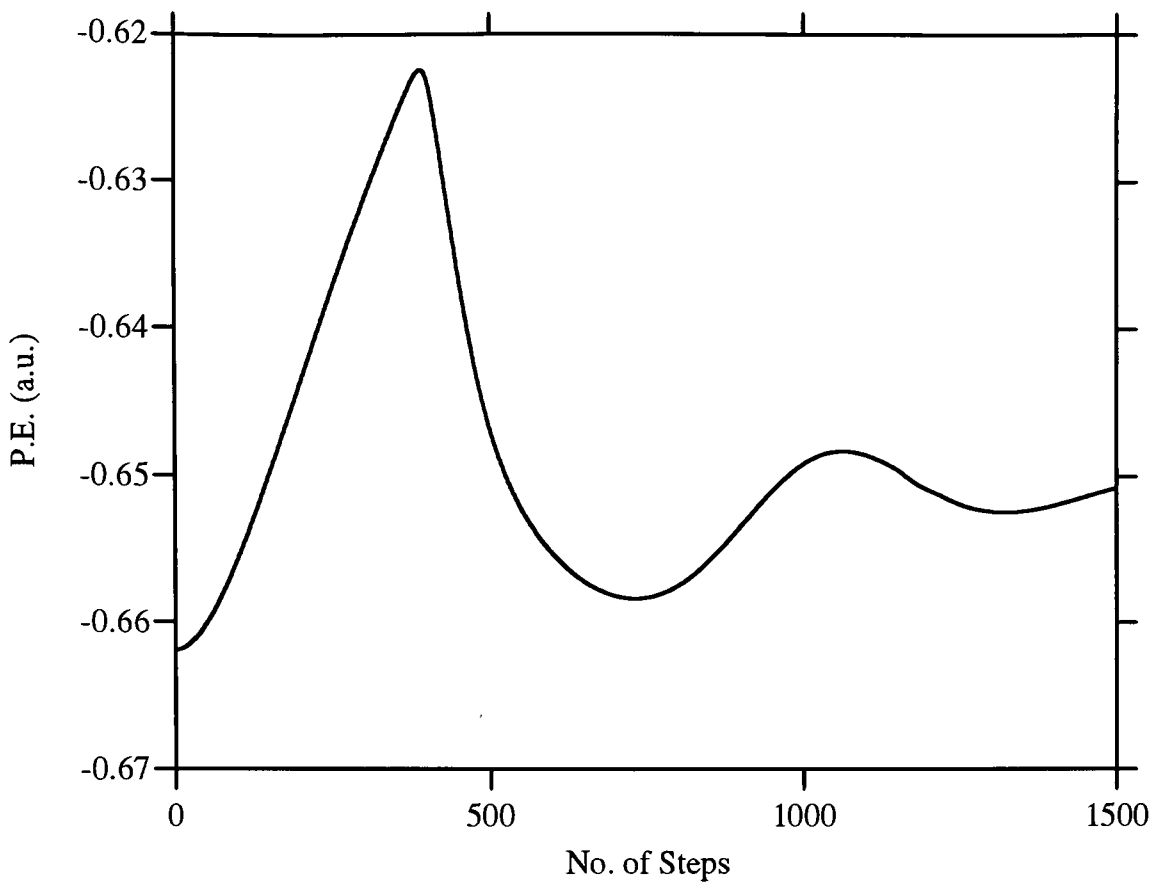


Figure 5.38: The potential energy for dynamics on Na_4 using SIC and starting from the rhombic geometry.

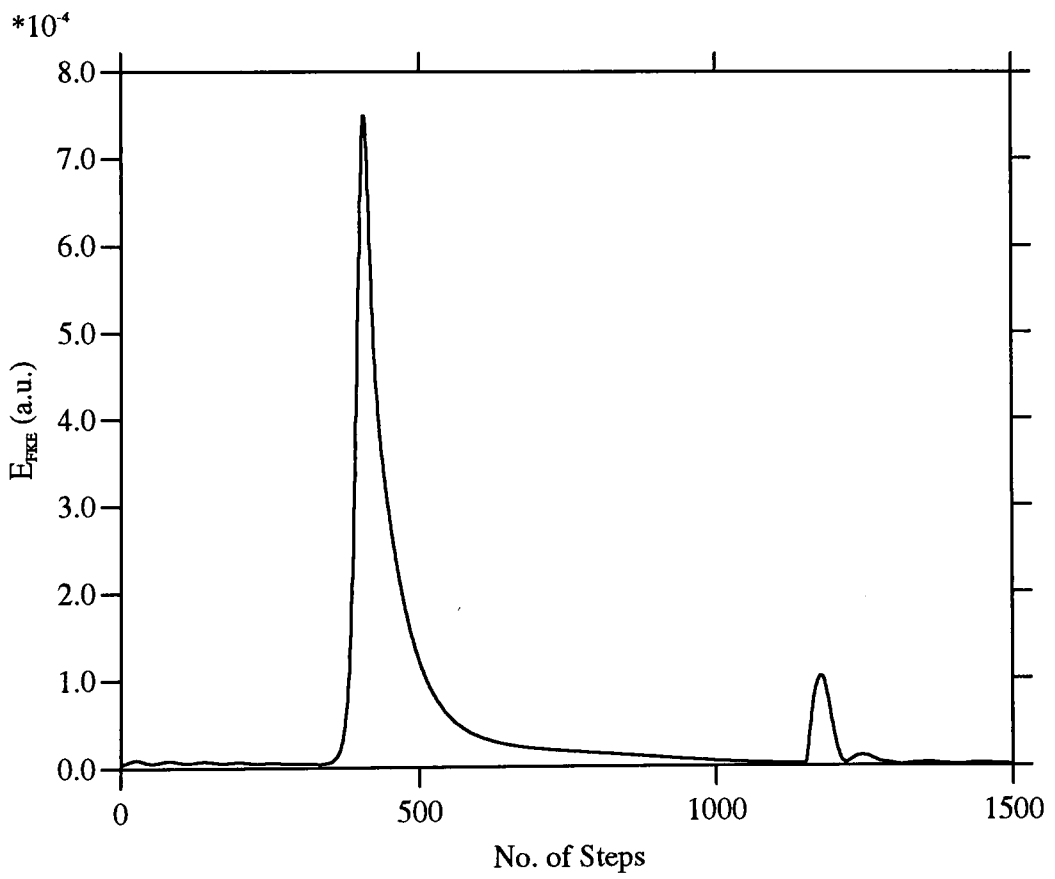


Figure 5.39: The fake kinetic energy for dynamics on Na_4 using SIC and starting from the rhombic geometry.

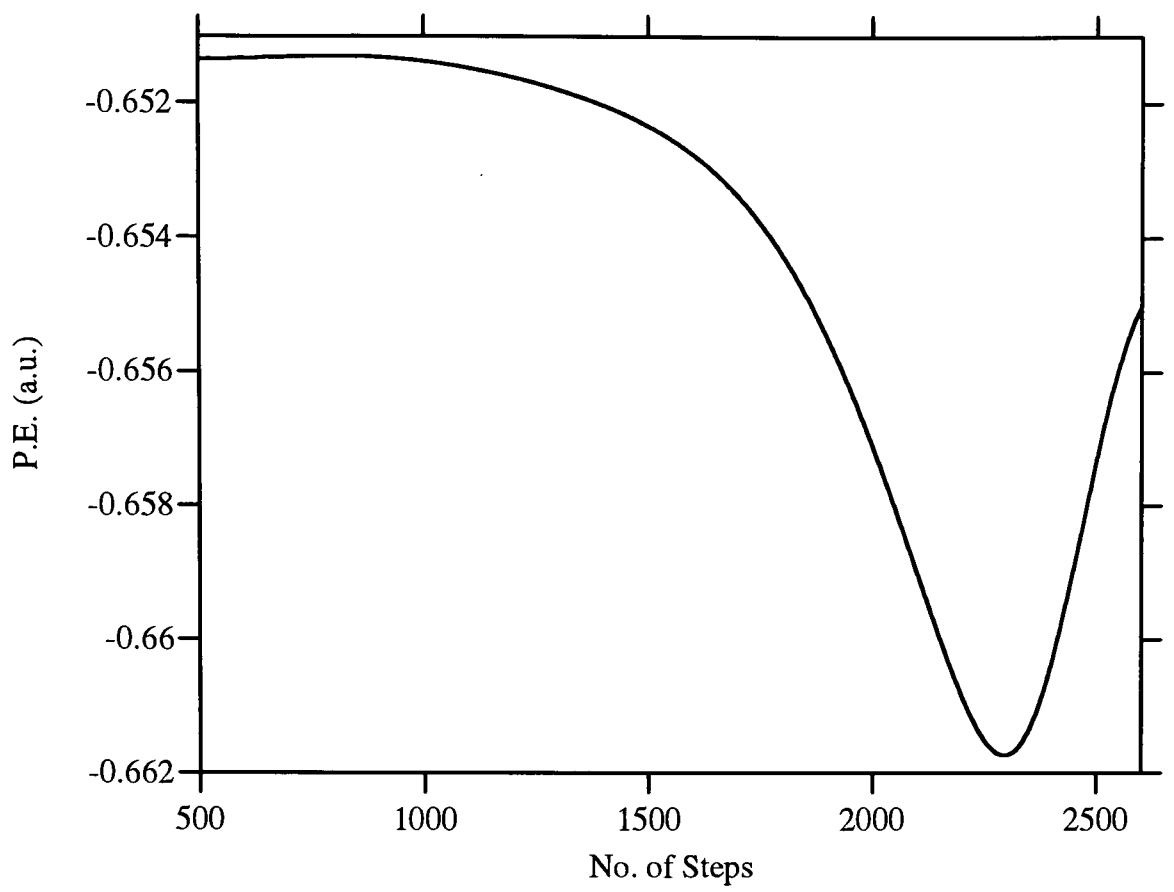


Figure 5.40: The potential energy for dynamics on Na_4 using SIC and starting from rest in the square planar geometry.

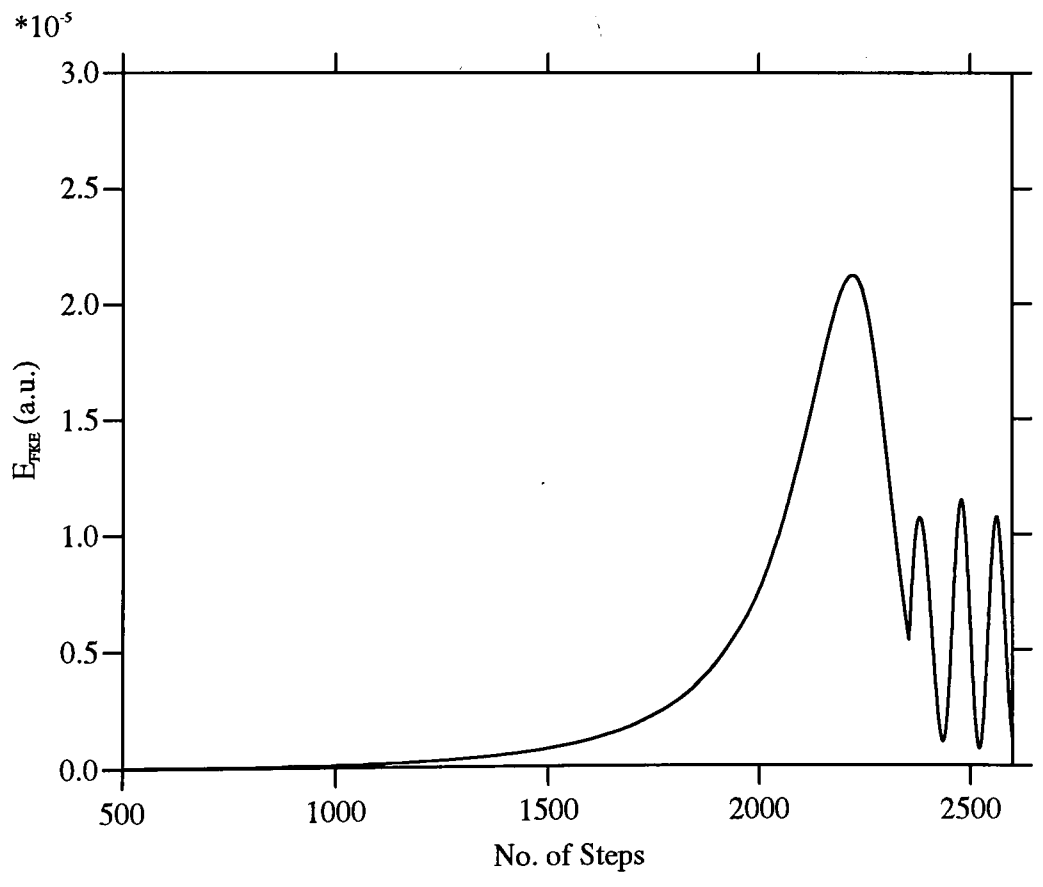


Figure 5.41: The fake kinetic energy for dynamics on Na_4 using SIC and starting from rest in the square planar geometry.

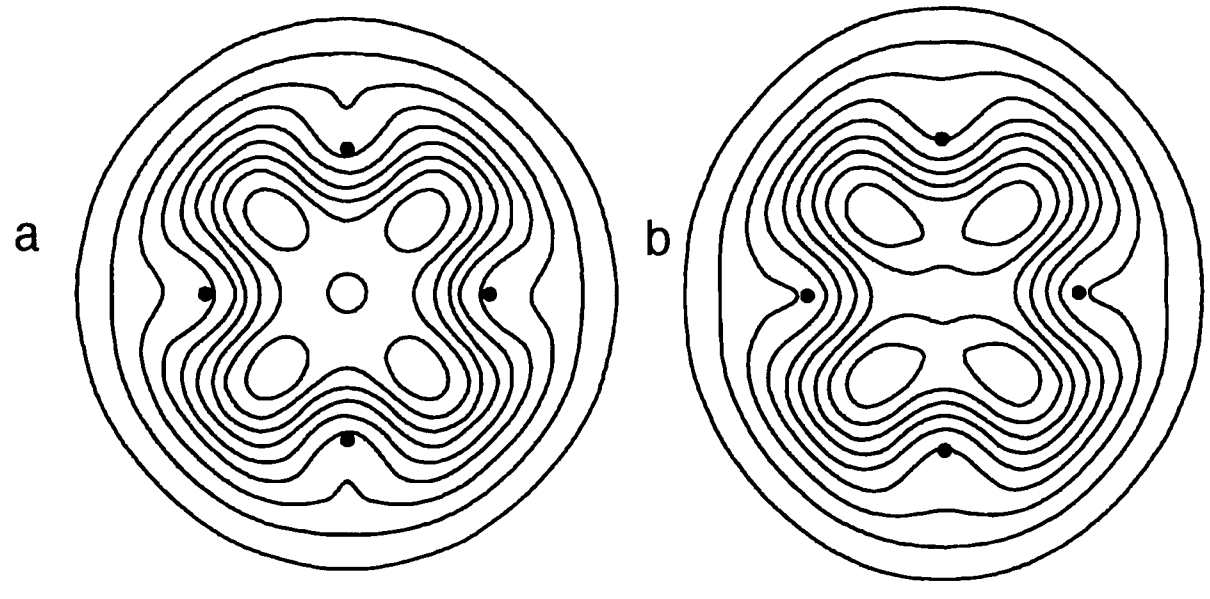


Figure 5.42: Na_4. valence electron densities after (a) 0, (b) 1400, (c) 2000, and (d) 2300 steps.

To proceed then it was decided to observe the transition from square planar to rhombic. This involves only spin pairing and thus we should have none of the difficulties encountered above. The square planar geometry passed through in the previous run was use as the initial geometry. The ground state was found by the usual CG method. The energy of this geometry was found to be 0.011 a.u. above that of the rhombus. The ions are allowed to move freely from rest. The potential energy and fake kinetic energy for this run are show in figures 5.40, and 5.41. Again there is the diagnostic rise in the fake kinetic energy as the system spin pairs, and it is reasonably clear that this time the system adheres to the ground state surface. The electron density was monitored throughout the run, and the electron densities in the plane of the cluster after 0, 1400, 2000, and 2300 steps are shown in figure 5.42. The square planar configuration has the rather unusual electron density described in chapter 4, which can be described as two centre one electron bonding. Electrons of the same spin are located on opposite edges of the square, so that the spin round the square has an alternating, "antiferromagnetic", arrangement. As the geometry distorts, this smoothly moves into the three centre two electron bonding of the ground state. A full discussion of the relative stabilities and electronic structures of these geometries in terms of the jellium model [66], and the generalised valence bond (GVB) model [62, 63] has all ready been given in section 4.2. The reliability of these density maps for each configuration have been checked by explicit CG minimisation at these positions. The results were indistinguishable from those shown in figure 5.42.

It is clear then that this method can not only be used to study the molecular dynamics of a system, but can also be used to investigate changes in the electronic structure "on the fly". This method is a lot cheaper in terms of cpu time than generating configurations using classical MD, then performing electronic structure calculations for each geometry of interest. Here the desired properties can be calculated as frequently as desired essentially without additional computational expense.

5.4.3 Inversion of the Na_6 Pentagonal Pyramid

Röthslisberger and Andreoni [93, 94] have carried out a series of *ab-initio* MD studies of sodium clusters using CP dynamics and LDA. In this work they have carried out calculations on Na_6 at different temperatures. They find that up to a temperature of 200K the pentagonal pyramid is quite "rigid". However at 350K the cluster oscillates between the two mirror $C_{5\nu}$ structures.

The purpose of our calculation is to find the barrier height for this structure inversion, using SIC and find if this is consistent with the above mentioned LDA calculations. To do this the apical atom was "fired" at the pentagonal plane of atoms with a kinetic energy of 1.7×10^{-3}a.u. The parameters

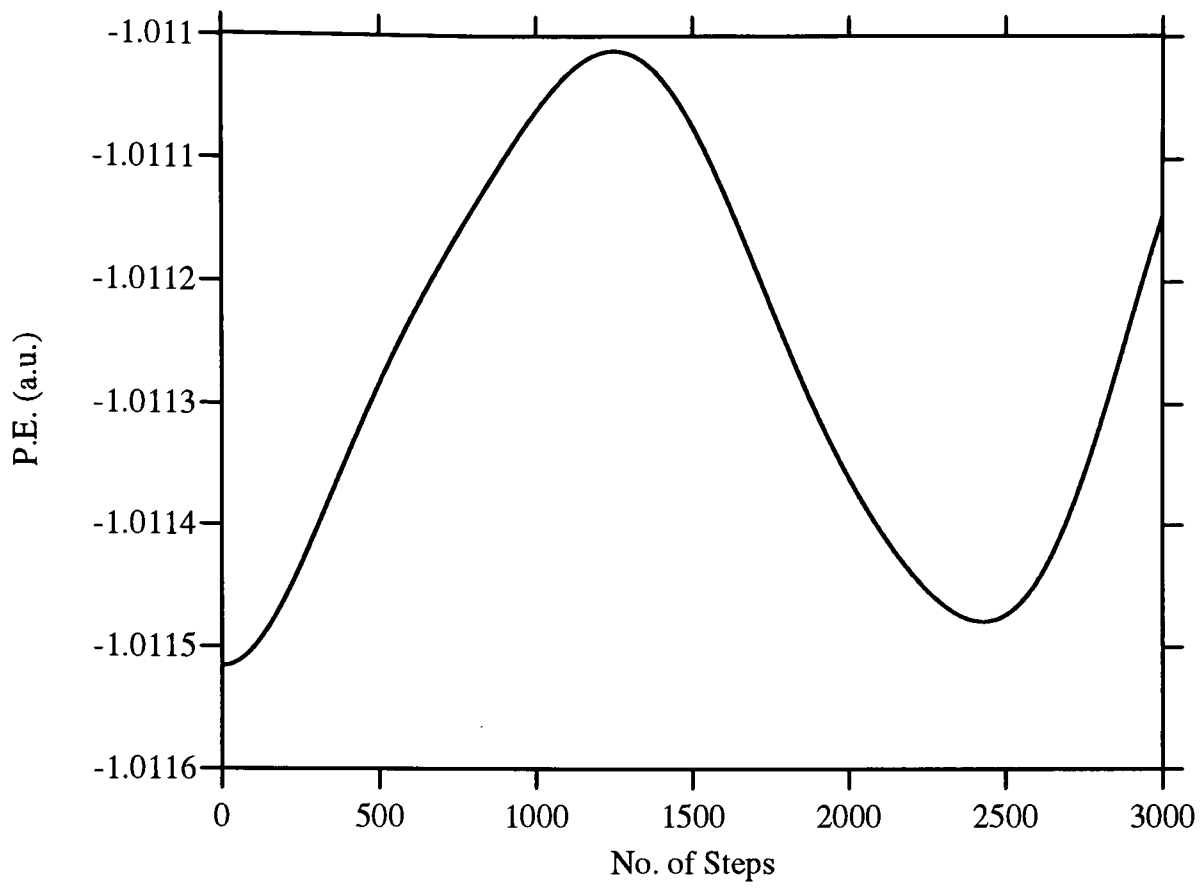


Figure 5.43: The potential energy for dynamics run on pentagonal pyramidal Na_6 using SIC and firing the apical atom through the pentagon.

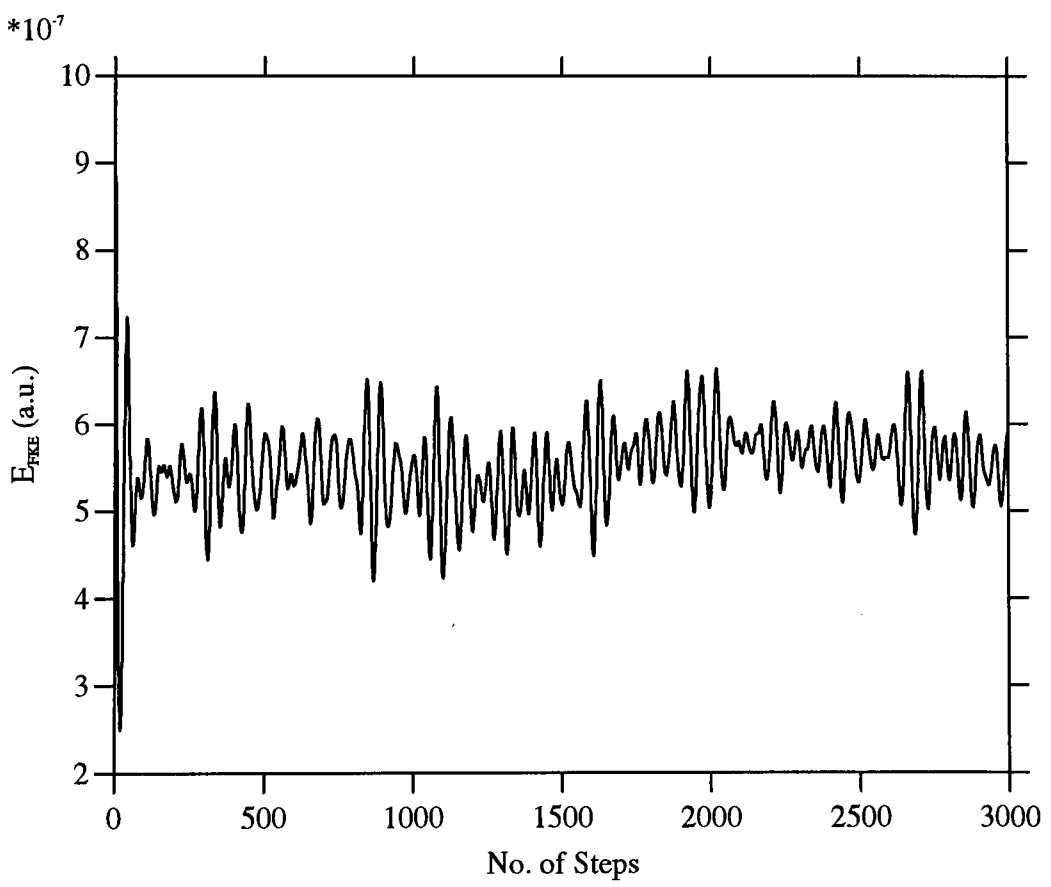


Figure 5.44: The fake kinetic energy for dynamics run on pentagonal pyramidal Na_6 using SIC and firing the apical atom through the pentagon.

used in the run were the same as for the Na_3 calculations and the "backstep" procedure used. The potential energy and fake kinetic energy plots for this run are shown in figures 5.43 and 5.44. It is clear that the atom readily passes through the plane and then rebounds. This is qualitatively in accord with the Röthslisberger and Andreoni result, however inspection of the barrier height from the potential energy curve yields a value of only 0.0005 a.u. This is equivalent to only ~16K. It is clear then that the SIC structure is far less rigid than the LDA, and hence LSD, as the system is fully spin paired. This is probably not surprising though in view of the arguments given in chapter 4 as to why the $C_{5\nu}$ geometry is not the ground state in the SIC calculations.

Chapter 6

Beyond the Local Density Approximation

So far most of this thesis has been concerned with the effect of removing the spurious self term in the LSD approximation, ie. the self-interaction correction. However in the last few years serious attempts have been made to find density gradient corrections to the local approximation of both the exchange energy and the correlation energy, with considerable success. Also there is now largely agreement on the conditions which any exact model of the exchange and correlation energies should meet. In this chapter then I will outline some of these advances and consider the implementation of some of the resulting functionals within the plane wave implementation of the CP and CG methods described in the preceding chapters.

6.1 The Stoll, Pavlidou, and Preuß Correction to the Correlation Energy

Most of this chapter will consider improvements to the local density exchange energy. However a functional form has to be given to the correlation energy. The LSD correlation functional can be used, but as pointed out already, it over estimates the correlation energy by as much as a factor of two. Stoll *et al.* [99] argued that this error was largely due to erroneously including correlation between electrons of the same spin. They thus proposed a correction that explicitly subtracted these terms,

$$E_c^{SPP}[\rho^\alpha, \rho^\beta] = E_c^{LSD}[\rho^\alpha, \rho^\beta] - E_c^{LSD}[\rho^\alpha, 0] - E_c^{LSD}[\rho^\alpha, 0] \quad (6.1)$$

$$= \int \rho \varepsilon_c(\rho, \zeta) d\mathbf{r} - \int \rho^\alpha \varepsilon_c(\rho^\alpha, 1) d\mathbf{r} - \int \rho^\beta \varepsilon_c(\rho^\beta, 1) d\mathbf{r}. \quad (6.2)$$

This corrected functional will be referred to as the SPP correlation energy.

This correction can be thought of as a form of self-interaction correction. For one electron systems it correctly gives zero for correlation energy,

$$E_{\mathrm{c}}^{\mathrm{SPP}}[|\phi_{i\sigma}(\mathbf{r})|^2, 0] = 0. \tag{6.3}$$

For atomic correlation energies SPP gives errors of only about 10%, which is a considerable improvement on LSD.

6.2 The Generalised Gradient Approximation for the Exchange Energy

For densities $\rho(\mathbf{r})$ which are slowly varying over space, a gradient expansion of the energy can be constructed [36, 46]. This gives the gradient expansion approximation (GEA),

$$E_{\mathrm{x}}[\rho] = A_{\mathrm{x}} \int d\mathbf{r} \rho^{\frac{4}{3}} + C_{\mathrm{x}} \int d\mathbf{r} \frac{|\nabla\rho|^2}{\rho^{\frac{4}{3}}}, \tag{6.4}$$

where $A_{\mathrm{x}} = -\frac{3}{4}\left(\frac{3}{\pi}\right)^{\frac{1}{3}}$, and $C_{\mathrm{x}} = -7/[432\pi\,(3\pi^2)^{\frac{1}{3}}]$a.u. The first term is simply the local density expression, so the method is a first order gradient correction to the local density approximation. However this does not lead to a systematic improvement.

To understand the cause of the problem note that the exchange-correlation energy can be described as the electrostatic interaction between each electron, and the fluctuation "hole" it digs around itself. Partitioning into separate exchange and correlation terms in the usual way leads to,

$$E_{\mathrm{x}}[\rho] = \frac{1}{2} \int d\mathbf{r} \rho(\mathbf{r}) \int d\mathbf{R} \frac{\rho_{\mathrm{x}}(\mathbf{r}, \mathbf{r}+\mathbf{R})}{R}, \tag{6.5}$$

where $\rho_{\mathrm{x}}(\mathbf{r}, \mathbf{r}+\mathbf{R})$ is the density at the position $\mathbf{r}+\mathbf{R}$ of the exchange hole about position $\mathbf{r}$. In fact E_{x} only depends on the spherically averaged exchange hole $\rho_{\mathrm{x}}^{\mathrm{SA}}(\mathbf{r}, R)$ as,

$$E_{\mathrm{x}}[\rho] = \frac{1}{2} \int d\mathbf{r} \rho(\mathbf{r}) \int_0^\infty dR\; 4\pi R^2 \left(\frac{1}{R}\right) \rho_{\mathrm{x}}^{\mathrm{SA}}(\mathbf{r}, R). \tag{6.6}$$

The exact exchange hole satisfies the conditions,

$$\rho_{\mathrm{x}}(\mathbf{r}, \mathbf{r}) = -\rho(\mathbf{r})/2, \tag{6.7}$$

$$\rho_{\mathrm{x}}(\mathbf{r}, \mathbf{r}+\mathbf{R}) \leq 0, \tag{6.8}$$

$$\int d\mathbf{R} \rho_{\mathrm{x}}(\mathbf{r}, \mathbf{r}+\mathbf{R}) = -1. \tag{6.9}$$

As is well known, the local density approximation satisfies all these conditions [30]. However, Perdew showed [78] that GEA violates both conditions 6.8, and 6.9. This observation explains the failure of GEA to systematically correct LDA.

It is clear then that conditions 6.7-6.9 are a non-trivial requirement of any density functional theory. To overcome the problems of GEA, Perdew [78] imposed cutoffs, chosen to satisfy conditions 6.8, and 6.9, on the GEA exchange hole. Subsequently Perdew and Wang [83] gave a simpler form of the result. In these papers it was shown that the GEA exchange hole, $\rho_{\mathrm{x}}^{\mathrm{GEA}}(\mathbf{r}, \mathbf{r}+\mathbf{R})$ could be written as,

$$\rho_{\mathrm{x}}^{\mathrm{GEA}}(\mathbf{r}, \mathbf{r}+\mathbf{R}) = -\frac{1}{2}\rho(\mathbf{r})\tilde{y}(\mathbf{r}, \mathbf{R}), \tag{6.10}$$

where,

$$\tilde{y} = J + \frac{4}{3}L\hat{\mathbf{R}}\cdot\mathbf{s} - \frac{16}{27}M\left(\hat{\mathbf{R}}\cdot\mathbf{s}\right)^2 - \frac{16}{3}Ns^2, \tag{6.11}$$

and,

$$\begin{aligned}
\hat{\mathbf{R}} &= \mathbf{R}/R, && (6.12)\\
k_F &= [3\pi^2\rho(\mathbf{r})]^{\frac{1}{3}}, && (6.13)\\
z &= 2k_F R, && (6.14)\\
J &= 72[4 + z^2 - (4 - z^2)\cos z - 4z\sin z]/z^6, && (6.15)\\
L &= 9(2 - 2\cos z - z\sin z)/z^3, && (6.16)\\
M &= 9(-z\cos z + \sin z)/(16z), && (6.17)\\
N &= 3[8 - (8 - 4z^2)\cos z - (8z - z^3)\sin z]/(16z^4), && (6.18)\\
\mathbf{s} &= \frac{\nabla\rho}{2k_F\rho}. && (6.19)
\end{aligned}$$

The generalised gradient approximation (GGA) to the exchange hole, $\rho_{\mathrm{x}}^{\mathrm{GGA}}(\mathbf{r}, \mathbf{r}+\mathbf{R})$, is then given by [83, 81],

$$\rho_{\mathrm{x}}^{\mathrm{GGA}}(\mathbf{r}, \mathbf{r}+\mathbf{R}) = -\frac{1}{2}\rho(\mathbf{r})\tilde{y}\Theta(\tilde{y})\Theta(R_c(\mathbf{r}) - R), \tag{6.20}$$

where $\Theta(x)$ is a step function equal to 1 for $x > 0$, and 0 for $x < 0$. The first step function imposes condition 6.8, ie. ensuring that the exchange hole is everywhere negative. The second step function imposes the sum rule of equation 6.9 by suitable choice of cutoff.

Equation 6.5 can now be written in the form,

$$E_{\mathrm{x}}^{\mathrm{GGA}}[\rho] = A_{\mathrm{x}}\int d\mathbf{r}\rho^{\frac{4}{3}}F^{\mathrm{GGA}}(s), \tag{6.21}$$

where,

$$F^{\mathrm{GGA}}(s) = -\frac{(3\pi^2)^{\frac{1}{3}}}{12\pi A_{\mathrm{x}}} \int_0^{z_c} dz \int \frac{d\hat{\mathbf{R}}}{4\pi} \tilde{y}\Theta(\tilde{y}). \tag{6.22}$$

The parameter $z_c = 2k_F R_c$ is determined by the condition,

$$-\frac{1}{12\pi} \int_0^{z_c} dz\ z^2 \int \frac{d\hat{\mathbf{R}}}{4\pi} \tilde{y}\Theta(\tilde{y}) = -1. \tag{6.23}$$

Carrying out the angular integration analytically and the z-integration numerically, Perdew and Wang [83] obtained the analytic fit to these numerical results,

$$F^{\mathrm{GGA}}(s) = (1 + 0.0864s^2/m + bs^4 + cs^6)^m, \tag{6.24}$$

where, $m = \frac{1}{15}$, $b = 14$, and $c = 0.2$. Note, the local density approximation is equivalent to $F^{\mathrm{LDA}} = 1$, whilst the Langreth and Mehl [53] approximation for exchange, based on a cutoff of the GEA hole in wave-vector space is,

$$F^{\mathrm{LM}}(s) = 1 + 1.521(0.0864s^2). \tag{6.25}$$

Other forms of gradient correction have been proposed, most notably by Becke [6, 7, 8]. However it is the Perdew functional defined by equations 6.21, and 6.24 that will be studied in this section.

The exchange potential, as shown in appendix C, is given by the functional derivative,

$$\frac{\delta E_{\mathrm{x}}}{\delta\rho(\mathbf{r})} = A_{\mathrm{x}}\rho^{\frac{1}{3}} \left[\frac{4}{3}F - ts^{-1}\frac{dF}{ds} - \left(u - \frac{4}{3}s^3\right)\frac{d}{ds}\left(s^{-1}\frac{dF}{ds}\right)\right], \tag{6.26}$$

where,

$$t = (2k_F)^{-2}\,\rho^{-1}\nabla^2\rho, \tag{6.27}$$

and,

$$u = (2k_F)^{-3}\,\rho^{-2}\,\nabla\rho\cdot\nabla\left|\nabla\rho\right|. \tag{6.28}$$

The spin density functionals used in this work are easily constructed from these density functionals using the relations,

$$E_{\mathrm{x}}[\rho_\alpha, \rho_\beta] = \frac{1}{2}E_{\mathrm{x}}[2\rho_\alpha] + \frac{1}{2}E_{\mathrm{x}}[2\rho_\beta], \tag{6.29}$$

$$\frac{\delta E_{\mathrm{x}}[\rho_\alpha, \rho_\beta]}{\delta\rho_\sigma(\mathbf{r})} = \left.\frac{\delta E_{\mathrm{x}}[\rho]}{\delta\rho(\mathbf{r})}\right|_{\rho(\mathbf{r})=2\rho_\sigma(\mathbf{r})}. \tag{6.30}$$

The functional defined by these equations, when used in conjunction with the LSD functional for correlation will be referred to as GGA, while when the SPP correlation functional is used it will be referred to as GGA-SPP.

Note that gradient corrections to the correlation energy can be treated in an analogous way. This has been done by, among others, Perdew [79]

6.3 Implementation of the Perdew and Wang GGA Exchange Functional in Self Consistent Calculations

In principle the implementation of the Perdew functional within a program such as that discussed and used in the preceding chapters should be straightforward. For the energy functional, the only extra parameter to be calculated is $|\nabla\rho_\sigma|$, needed to find s. This is simply calculated either by a finite difference method or more cheaply via FFT methods. Having checked that both gave identical results, the latter was used. This schematically involves,

$$\rho_\sigma(\mathbf{r}) \quad \stackrel{\text{FFT}}{\Longrightarrow} \quad \rho_\sigma(\mathbf{g}), \tag{6.31}$$

$$\frac{2\pi i}{L}\mathbf{g}\rho_\sigma(\mathbf{g}) \quad \stackrel{\text{inverse FFT}}{\Longrightarrow} \quad \nabla\rho_\sigma(\mathbf{r}). \tag{6.32}$$

Finding the modulus is then a trivial step, and the exchange energy then follows by direct substitution into the spin dependent version of the functional,

$$E_{\mathrm{x}}^{\mathrm{GGA}}[\rho_\alpha,\rho_\beta] = A_{\mathrm{x}}\int d\mathbf{r}\left((2\rho_\alpha)^{\frac{4}{3}}F^{\mathrm{GGA}}(s_\alpha)+(2\rho_\beta)^{\frac{4}{3}}F^{\mathrm{GGA}}(s_\beta)\right). \tag{6.33}$$

For the exchange potential the term,

$$\frac{d}{ds}\left(s^{-1}\frac{dF}{ds}\right) = s^{-1}\frac{d^2F}{ds^2} - s^{-2}\frac{dF}{ds}, \tag{6.34}$$

is required. Note, from now on the density functional equations will be used for clarity, even though the implementation was of the spin density functional.

The derivatives of F with respect to s can be found analytically and written in the form,

$$F = A^{\frac{1}{15}}, \tag{6.35}$$

$$\frac{dF}{ds} = \frac{B}{15L}, \tag{6.36}$$

$$\frac{d^2F}{ds^2} = \frac{1}{15}\left(\frac{C}{L}-\frac{14}{15}\frac{B^2}{L^2F}\right), \tag{6.37}$$

where,

$$A = 1+s^2\left(a+s^2\left(b+cs^2\right)\right), \tag{6.38}$$

$$B = s\left(2a+s^2\left(4b+6cs^2\right)\right), \tag{6.39}$$

$$C = 2a+s^2\left(12b+30cs^2\right), \tag{6.40}$$

$$L = A^{\frac{14}{15}}. \tag{6.41}$$

	LSD Density	HF Density [83]
LSD	-0.249	-0.268
GGA	-0.298	-0.311

Table 6.1: Hydrogen atom exchange energies using LSD and HF densities in the LSD and GGA exchange functionals. Results are in a.u.

The parameters are $a = 15(0.0864)$, $b = 14$, and $c = 0.2$.

The Laplacian of the density can also be found by FFT methods as,

$$-\left(\frac{2\pi}{L}\right)^2 \mathbf{g}\cdot\mathbf{g}\,\rho(\mathbf{g}) \stackrel{\text{inverse FFT}}{\Longrightarrow} \nabla^2\rho(\mathbf{r}), \tag{6.42}$$

and having found $|\nabla\rho|$, $\nabla|\nabla\rho|$ is found in exactly the same way as $\nabla\rho$.

Equation 6.33 was found by Perdew and Wang [83] to give a significant improvement over LSD for atomic exchange energies. The results of using LSD densities for the hydrogen atom in this functional, and in the LSD functional, using $q_{\max} = 16$ and a box length of 20 a.u., are compared in table 6.1 with the exchange energies found by Perdew and Wang [83] using the same functional, but with a Hartree-Fock density. The exact exchange energy is -0.3125 a.u.

GGA is found, in agreement with Perdew and Wang to significantly improve over LSD. However both the LSD and GGA exchange are significantly smaller than those found by Perdew and Wang. This is probably due to the incompleteness of the basis set in the calculations rather than differences in the LSD and HF densities. Certainly for the sodium clusters the various approximations tested in this thesis for exchange and correlation gave visually identical electron density maps for a given set of ion coordinates.

It is important to note though that the results in table 6.1 are *not* from self consistent calculations. It is in the self consistent implementation of GGA that problems arise. As already pointed out, the coding of equation 6.26 is quite straightforward, but implementation in the CG procedure described in chapter 2 fails to give convergence in the total energy to better than two decimal places for the hydrogen atom, using a $q_{\max} = 16$, and a box length of 20 a.u., which corresponds to a cutoff of about 28 Ry. Increasing $q_{\max}$ to 31,corresponding to 68350 coefficients, and decreasing the box length to 15, still does not solve the problem. It was clear that the whole algorithm was breaking down as soon as the density departed sufficiently from uniformity. Typically this was when the density in parts of the simulation was less than of the order of $10^{-6}/V$a.u. , where V is the cell volume. A major indicator of breakdown was that $\gamma^{(n+1)}$, given by equation 2.94, became significantly greater than unity. Starting from a random setup, or the converged LSD

wavefunction, or using real space calculations of derivatives all yielded a similar outcome. As the hydrogen atom is particularly demanding of the basis set required for a full description of the density, compared to sodium, using the Topp and Hopfield pseudopotential, the same trials were run using a sodium atom, with the same outcome.

At this point it was noted that for very low values of the spin density s_σ was frequently very large, often of the order of 10^5. This in turn lead to large values of $F(s_\sigma)$. The cause of this problem was quite simply numerical, the division of one small, essentially zero, number by another small, essentially zero, number. As $F(s_\sigma)$ is multiplied by $(2\rho_\sigma)^{\frac{4}{3}}$ in the exchange energy functional this does not cause a significant error in $E_{\mathbf{x}}^{\mathrm{GGA}}$. However the function of s_σ in the exchange potential is only multiplied by $(2\rho_\sigma)^{\frac{1}{3}}$. Thus even for very low densities where the exchange potential would be expected to be zero then there will be a significant contribution. Numerically as the numbers in the calculation are often less than of the order of 10^{-10}, the algorithm in these low density regions is likely to be unstable.

To deal with this low (essentially zero) density problem, the following strategy was employed. The parameter s_σ^2 in $F(s_\sigma)$ was replaced by,

$$\beta_\sigma = \left(\frac{s_\sigma^2}{1+\mu s_\sigma^2}\right), \tag{6.43}$$

.

ie.,

$$s_\sigma^2 \longrightarrow \frac{s_\sigma^2}{1+\mu s_\sigma^2}. \tag{6.44}$$

Thus $F(s_\sigma)$ and its derivatives, required for the exchange potential are, once more dropping the spin indices for convenience,

$$\begin{aligned} F(\beta) &= A^{\frac{1}{15}}, & (6.45)\\ \frac{dF}{ds} &= \frac{D}{15L}, & (6.46)\\ \frac{d^2F}{ds^2} &= \frac{1}{15}\left(\frac{E}{L} - \frac{14}{15}\frac{D^2}{L^2F}\right), & (6.47) \end{aligned}$$

where,

$$\begin{aligned} A &= (1+a\beta+b\beta^2+c\beta^3), & (6.48)\\ B &= a+2b\beta+3c\beta^2, & (6.49)\\ C &= 2b+6c\beta, & (6.50)\\ D &= \frac{2Bs}{1+\mu s^2}, & (6.51)\\ E &= \frac{4Cs^2}{(1+\mu s^2)^4} + \frac{2B}{(1+\mu s^2)^3}(1-3\mu s^2), & (6.52)\\ L &= A^{\frac{14}{15}}. & (6.53) \end{aligned}$$

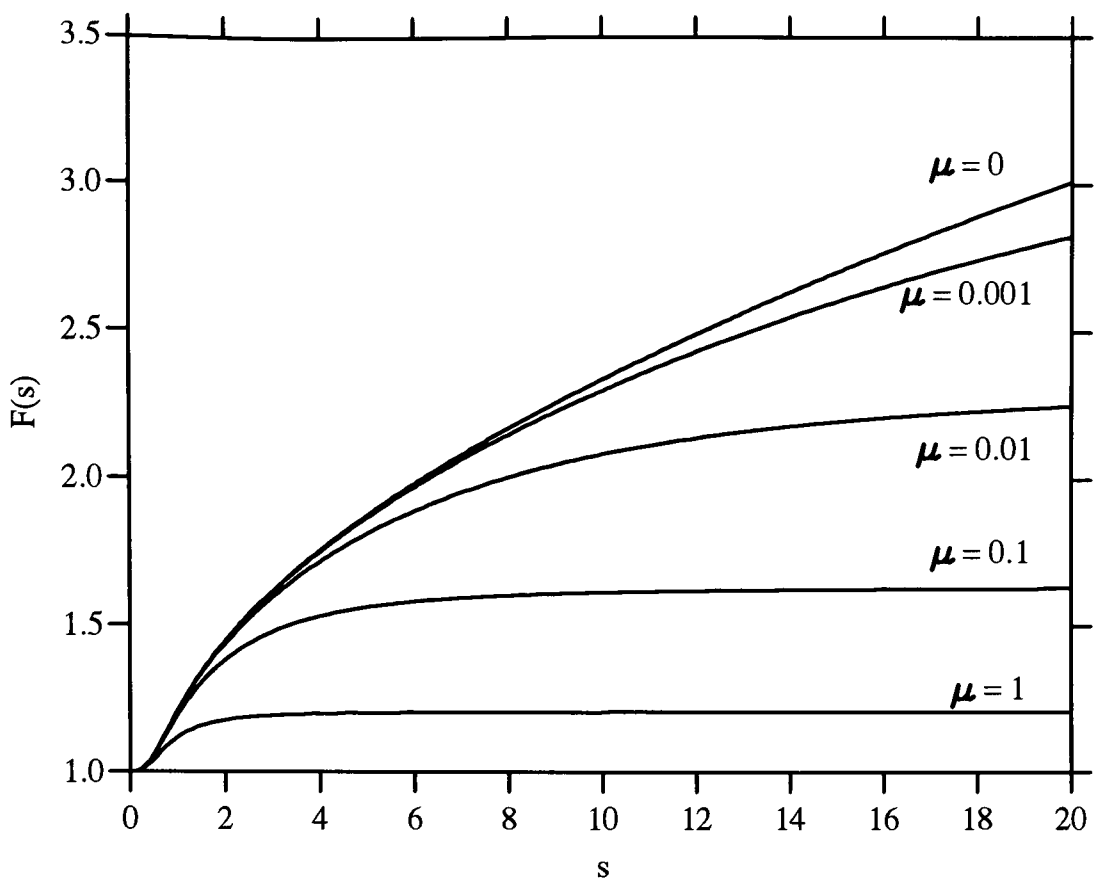


Figure 6.1: The modified functional $F(s)$ versus s for various values of the parameter μ.

How then does this modification help and how should μ be chosen? As μ tends to infinity then $F(\beta)$ will tend to 1, ie. the LSD result. When $\mu = 0$ it is clear the the modified functional reduces to the Perdew GGA formula. Thus varying μ switches us between the two limits. Figure 6.1 shows $F(\beta)$ versus s for different values of μ. It can be seen that for almost all values of μ good agreement is obtained for this modified functional and GGA, $\mu = 0$ functional. For higher values divergence occurs and the modified functional tends towards $F(1/\mu)$. In other words, modifying $F(s)$ in this fashion acts as a cutoff for large s values. μ should be chosen so that this function gives good agreement for small s values, that correspond to areas of significant density, but reduce the weighting given to large s values that occur as result of numerical errors, rather than having real physical significance. Note that for regions where the density is greater than of the order of $10^{-6}/V$, then values of s do not exceed 4. Thus μ was chosen to give a reasonable fit to the GGA functional of Perdew for s less than this value. As a result $\mu = 0.01$ was used.

By construction then the numerical problems in calculating s for very low densities is essentially removed. However this did not solve the problem of breakdown of the CG algorithm for hydrogen and sodium atoms. To study the problem further a single electron was placed in a simulation cell with a box length of 15 a.u. and with $q_{\mathbf{max}} = 16$. The *only* external potential applied

was a variable amplitude sinusoid, in the x-direction, whose wavelength was the same as the box length. *No* ionic pseudopotential was applied, ie. the system was an electron in a periodic cell with a variable strength sinusoidal potential applied parallel to one side of the cell. With no applied potential the calculation readily converged. However it was noticed that as the amplitude was increased, whether or not convergence was reached depended on the startup. Startup then was from the previously converged calculation which used an amplitude one order of magnitude less, as this gave convergence to the largest potentials. These calculations were carried out both with and without the modification to $F(s)$. The results are shown in table 6.2 and 6.3. note LSD correlation was used.

These calculations were carried out using, as with all calculations in this thesis, except when specified otherwise, the dual space formalism, $g_{\max} = q_{\max}$. To see what effect this had on the results the calculations were repeated undualled, ie $g_{\max} = 2q_{\max}$. The results are shown in table 6.4 and 6.5.

Undualling the calculation makes the biggest difference for the higher amplitudes as might be expected. Unexpectedly though, the undualled calculation using the unmodified functional leads to breakdown at less strong external fields. This breakdown is relatively less severe as convergence is to six decimal places, and is probably due to the problems at low density as the modified functional breaks down at the same amplitude whether dualled or undualled. It would appear that increasing the number of points describing the density by undualling does not appreciably help.

Figure 6.2-6.9 show the density, $|\nabla\rho|$, s, $F(\beta)$, $\nabla^2\rho$,$s^{-1}\frac{dF}{ds}$, and $s^{-1}\frac{d}{ds}\left(s^{-1}\frac{dF}{ds}\right)$, for the undualled calculation, for fixed y,z, values in the cell, ie. for a line in the direction in which the amplitude of the applied sinusoidal potential varies, for the different values of maximum amplitude. No smoothing or curve fitting is used for these plots. The lines are simply those joining the particular values of the function on given grid points in the x-direction. Thus any problems due to the number of grid points in real space is emphasised. As $q_{\max} = 16$, then there 64 grid points across the cell, ie. grid points are separated by $\sim \frac{1}{4}$a.u.

Figure 6.2 shows that as the amplitude of the potential is increased from zero initially the density takes on a sinusoidal variation, superimposed on the uniform density. At higher potentials this sinusoidal variation is perturbed by the restriction that the density cannot become negative, until the point is reached where all the electron density is excluded from one half of the cell.

Figure 6.3 shows $|\nabla\rho|$ for increasing amplitudes. These are consistent with the corresponding densities. Note though that for the largest amplitude even with a grid point every $\frac{1}{4}$a.u. this function is only just defined. It is chance that a grid point is situated at $|\nabla\rho| = 0$, a slight shift in the grid relative to the density would significantly alter the appearance of $|\nabla\rho|$. In other words the basis set is too small to sufficiently describe the discon-

Amplitude	Total E	E_x	$\rho_{\min} \times V$	Fully Converged
0	-0.167567	-6.20×10^{-2}	1.0000	Yes
10^{-3}	-0.167577	-6.20×10^{-2}	0.9645	Yes
10^{-2}	-0.168814	-6.55×10^{-2}	0.4907	Yes
10^{-1}	-0.217018	-7.79×10^{-2}	8.24×10^{-2}	Yes
10^{-0}	-0.993492	-1.09×10^{-1}	4.72×10^{-10}	No

Table 6.2: Convergence tests using GGA exchange with unmodified F. All data is in a.u.

Amplitude	Total E	E_x	$\rho_{\min} \times V$	Fully Converged
0	-0.167567	-6.20×10^{-2}	1.0000	Yes
10^{-2}	-0.168810	-6.54×10^{-2}	0.4918	Yes
10^{-1}	-0.216890	-7.77×10^{-2}	8.41×10^{-2}	Yes
10^{-0}	-0.993107	-1.08×10^{-1}	4.80×10^{-9}	No

Table 6.3: Convergence tests using GGA exchange with modified F. All data is in a.u.

Amplitude	Total E	E_x	$\rho_{\min} \times V$	Fully Converged
10^{-3}	-0.167577	-6.20×10^{-2}	0.9645	Yes
10^{-2}	-0.168815	-6.55×10^{-2}	0.4853	Yes
10^{-1}	-0.217057	-7.79×10^{-2}	8.10×10^{-2}	No

Table 6.4: Undualled convergence tests using GGA exchange with unmodified F. All data is in a.u.

Amplitude	Total E	E_x	$\rho_{\min} \times V$	Fully Converged
10^{-3}	-0.167577	-6.20×10^{-2}	0.9645	Yes
10^{-2}	-0.168811	-6.55×10^{-2}	0.4867	Yes
10^{-1}	-0.216935	-7.78×10^{-2}	8.24×10^{-2}	Yes
10^{-0}	-0.992633	-1.08×10^{-1}	5.74×10^{-10}	No

Table 6.5: Undualled convergence tests using GGA exchange with modified F. All data is in a.u.

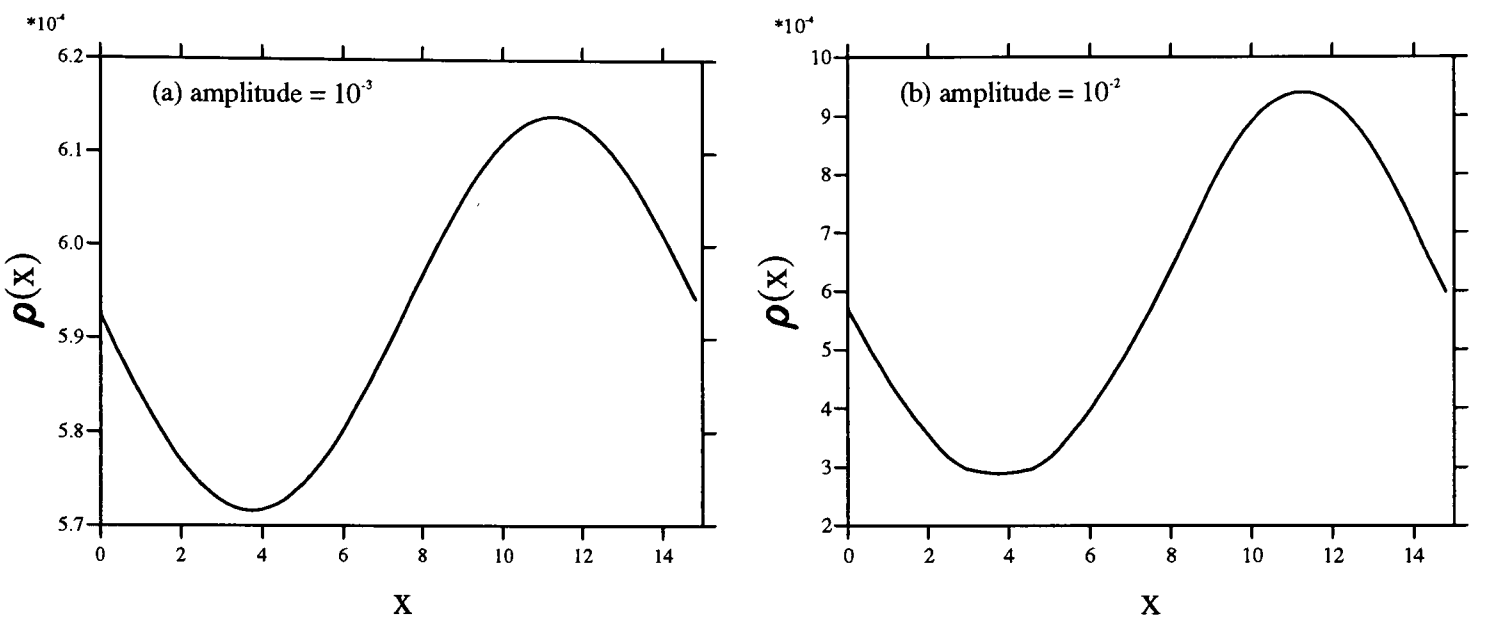


Figure 6.2: $\rho(x)$ (a.u.) for varying amplitudes of applied sinusoidal potential.

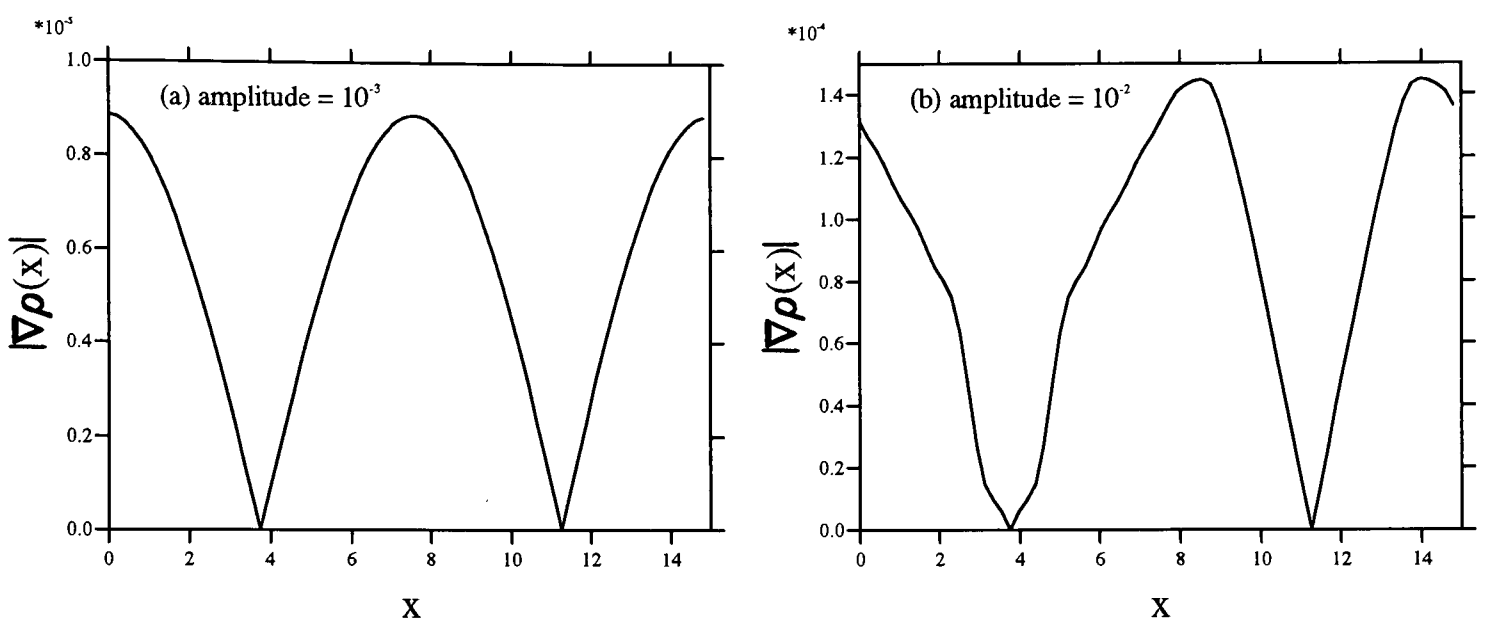
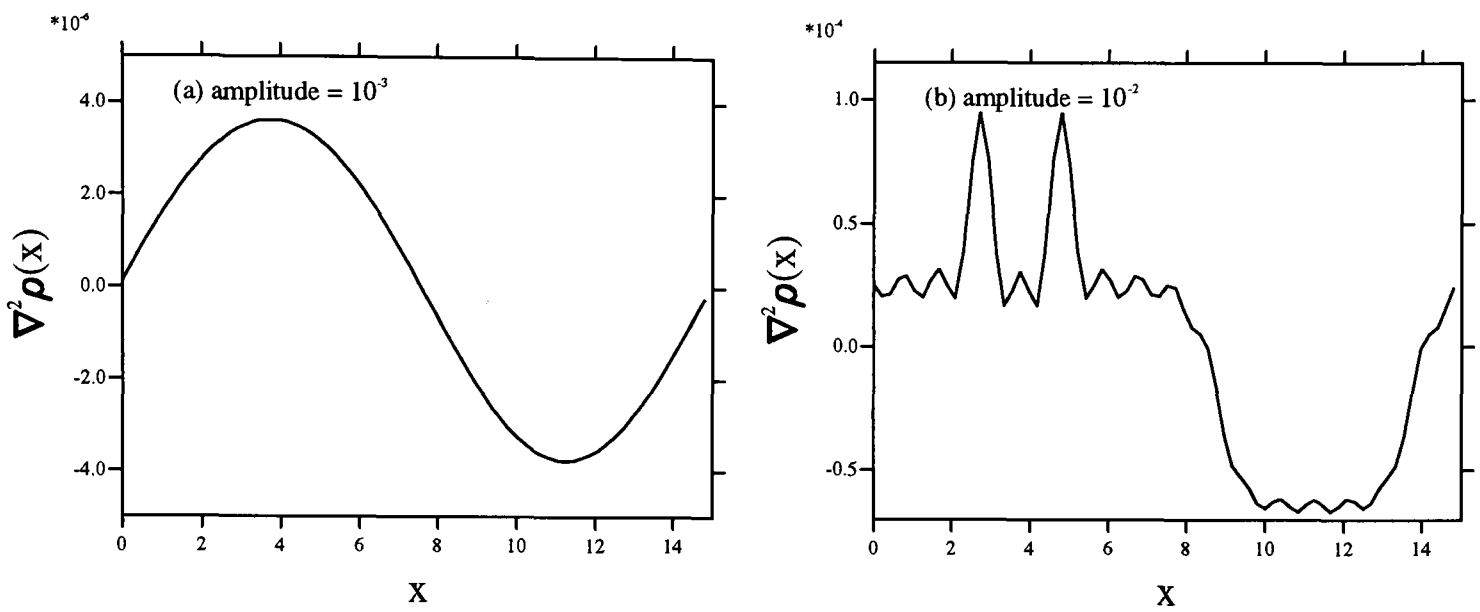


Figure 6.3: $|\nabla\rho(x)|$ (a.u.) for varying amplitudes of applied sinusoidal potential.



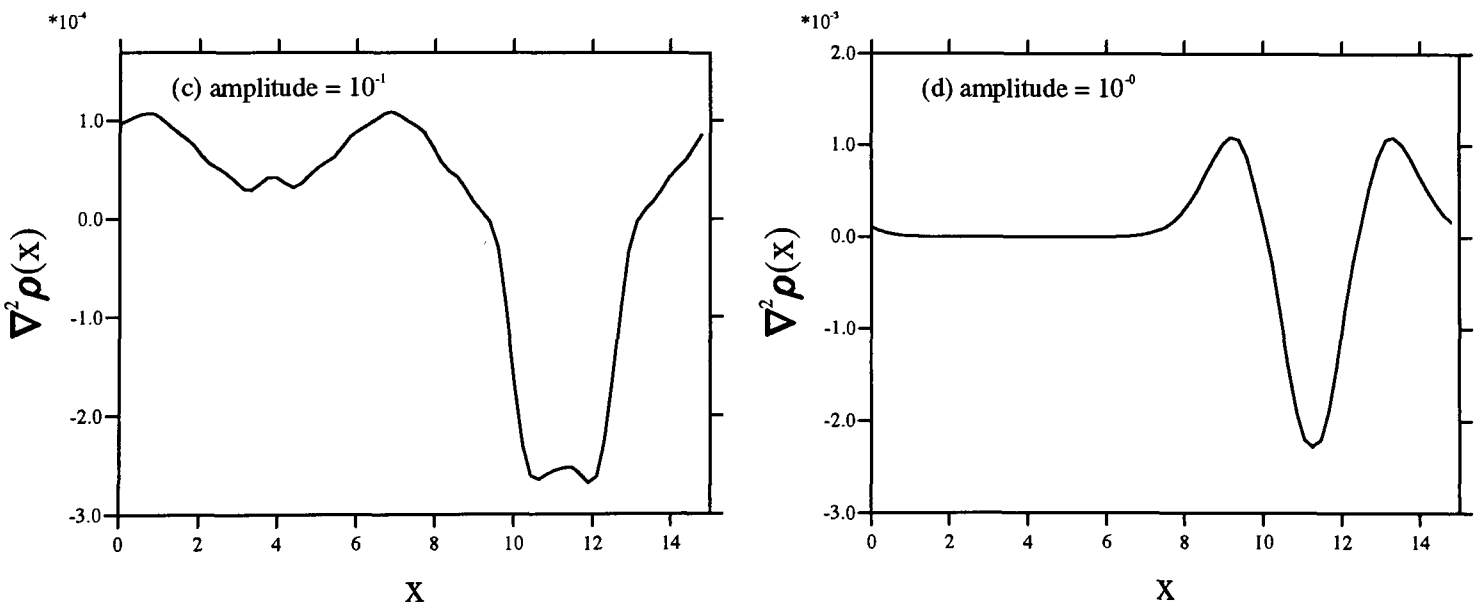
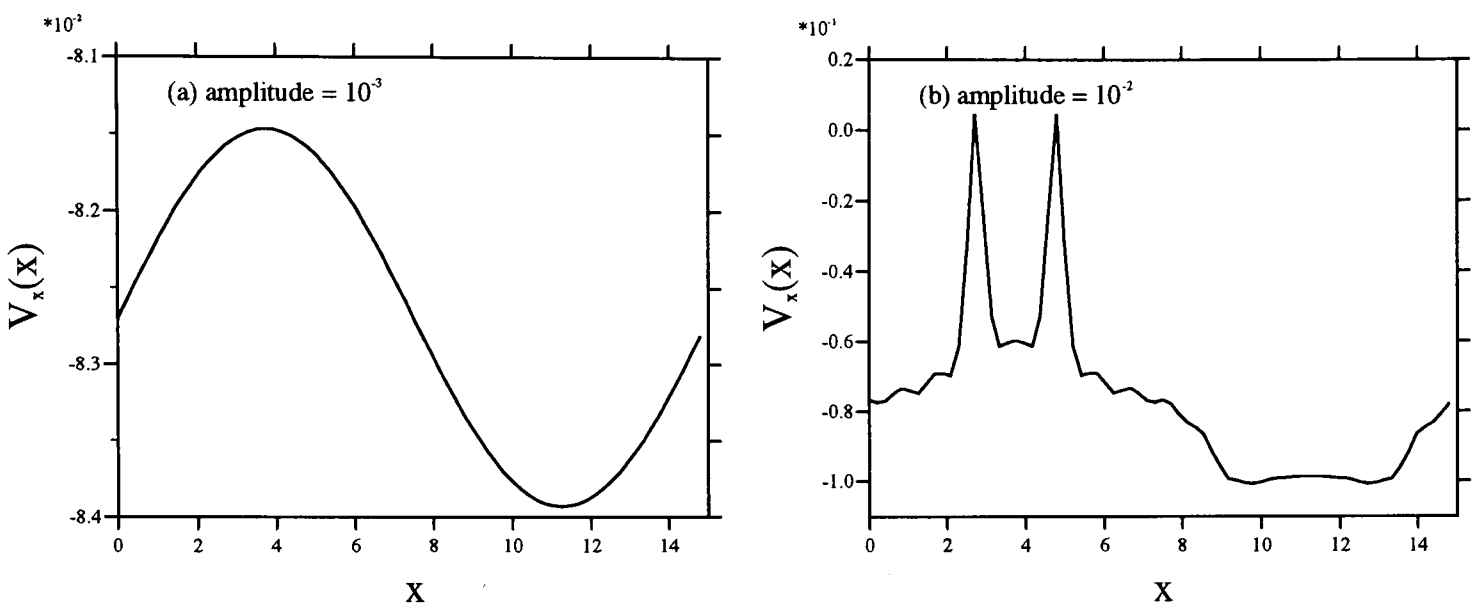


Figure 6.4: $\nabla^2\rho(x)$ (a.u.) for varying amplitudes of applied sinusoidal potential.



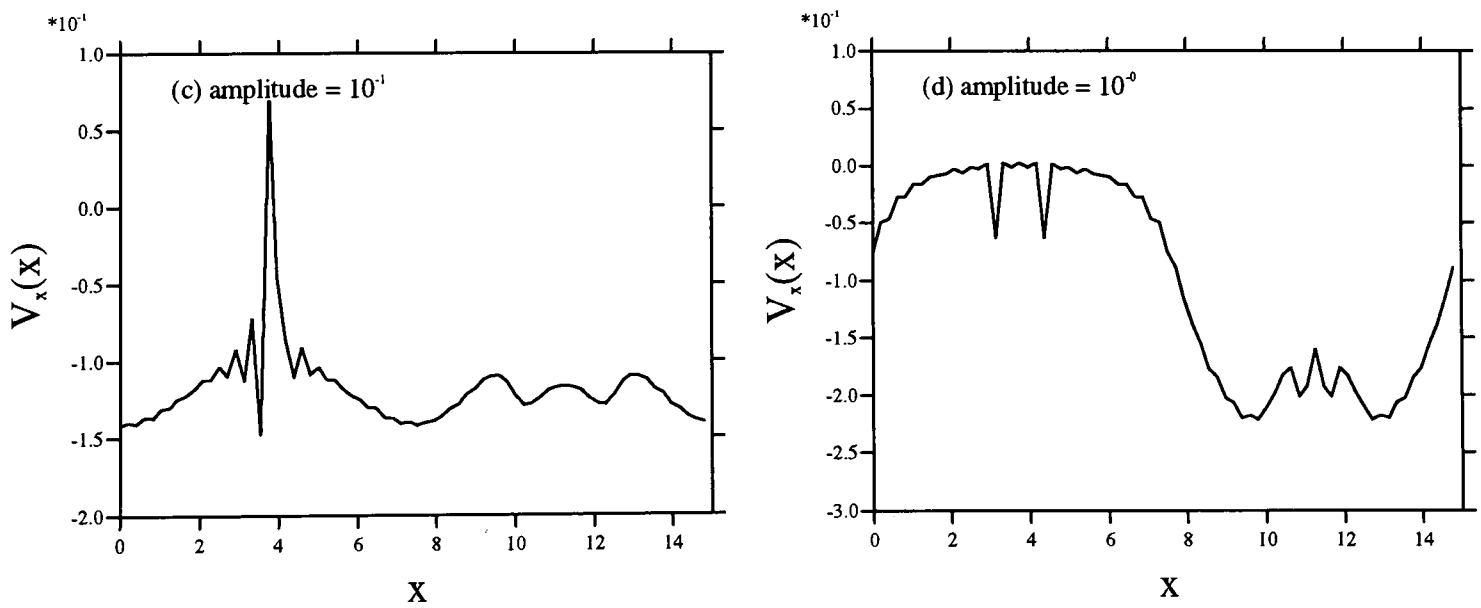


Figure 6.5: $V_x(x)$ (a.u.) for varying amplitudes of applied sinusoidal potential.

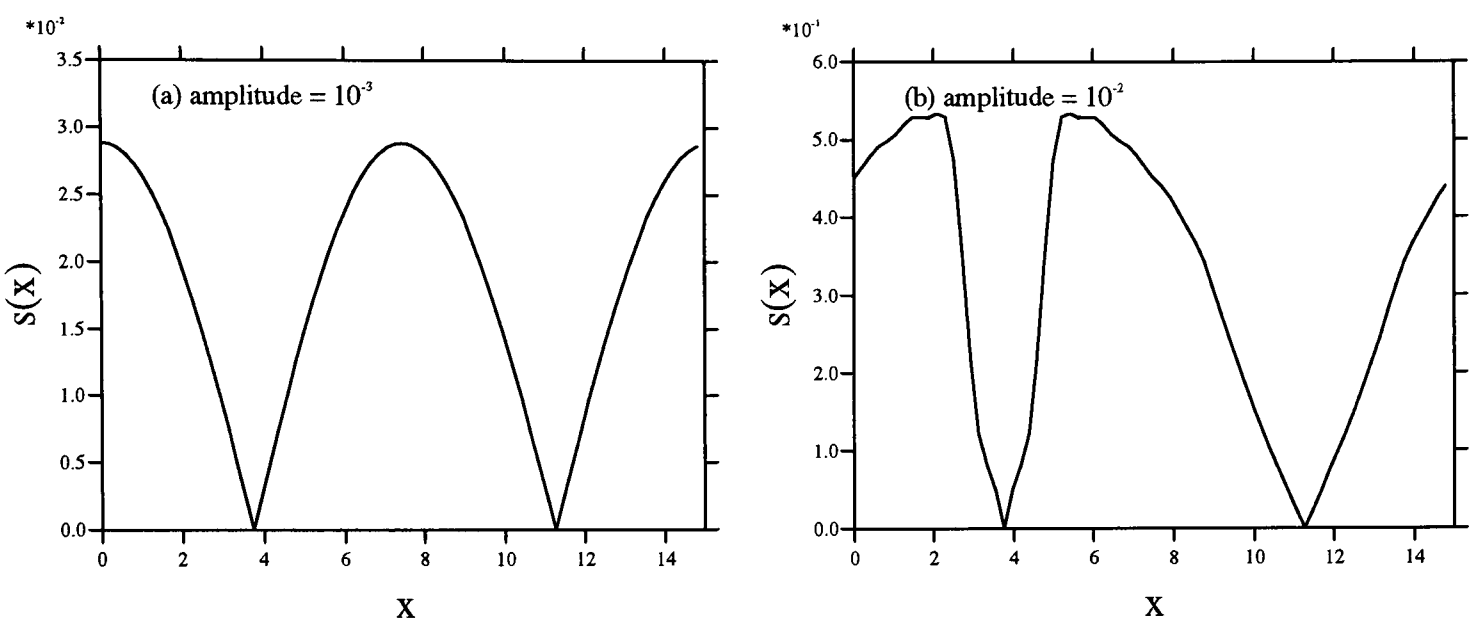


Figure 6.6: $s(x)$ (a.u.) for varying amplitudes of applied sinusoidal potential.

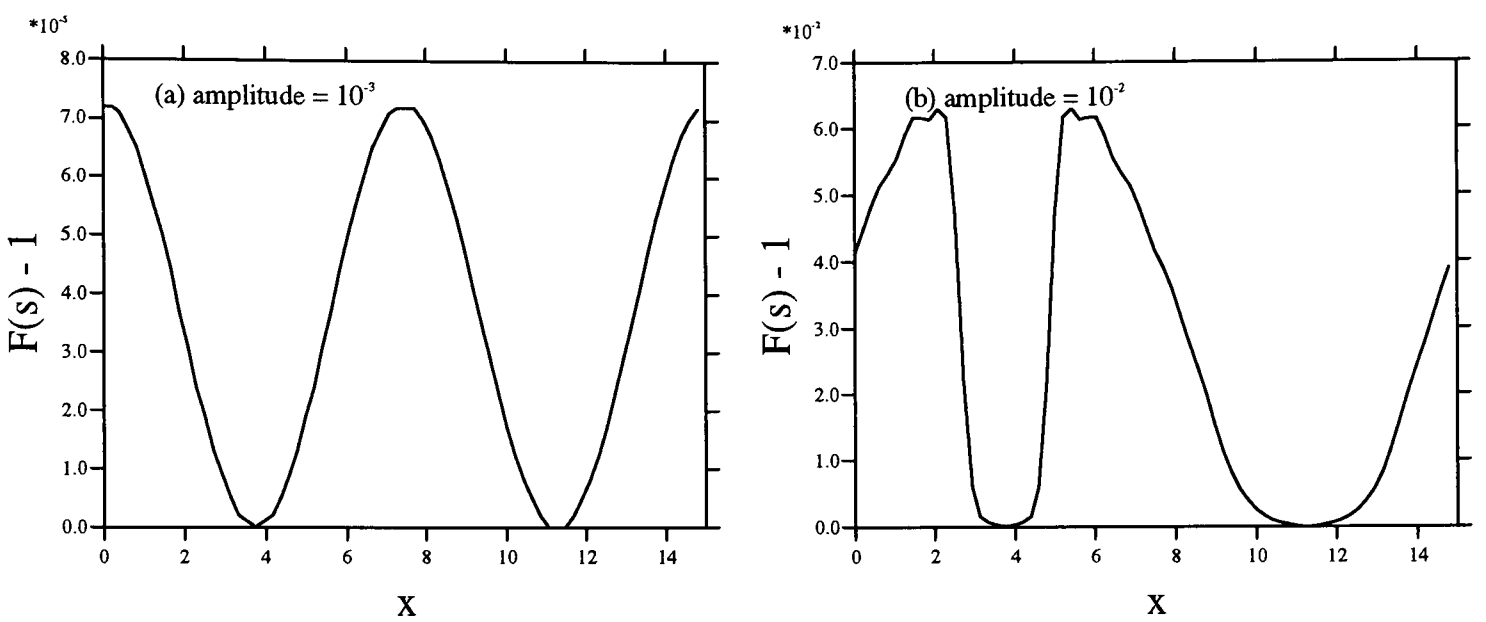
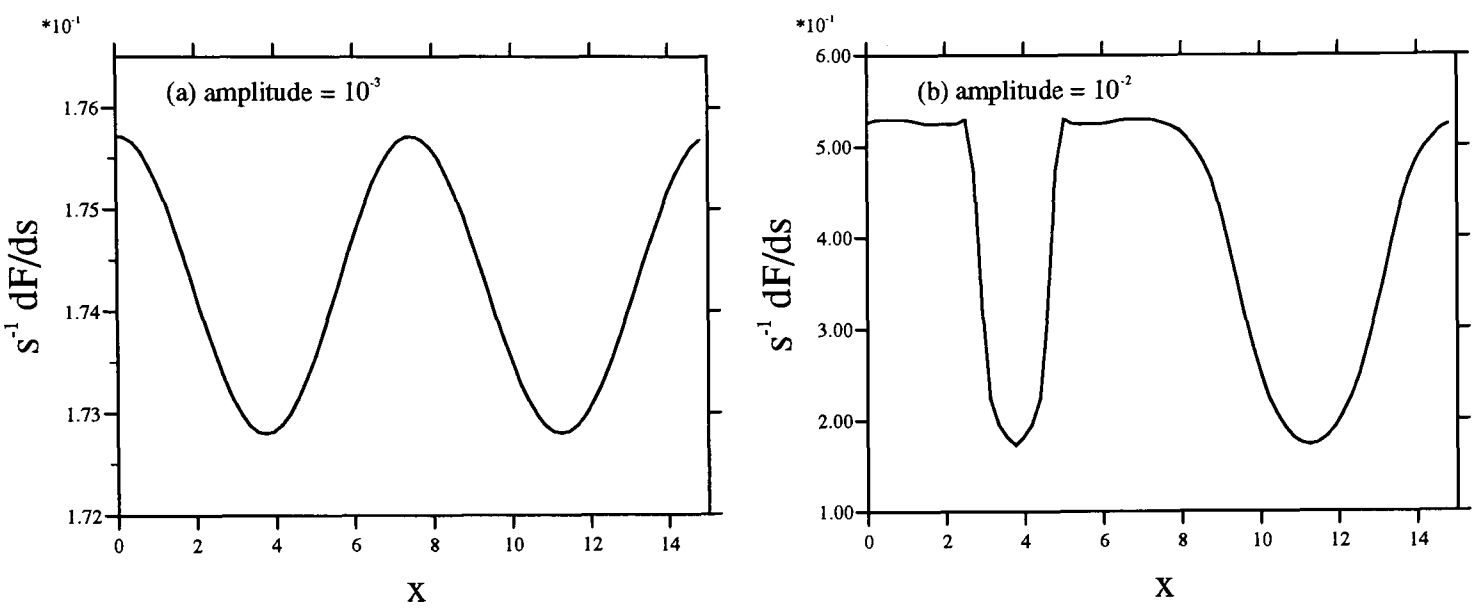


Figure 6.7: $F(s) - 1$ for varying amplitudes of applied sinusoidal potential.



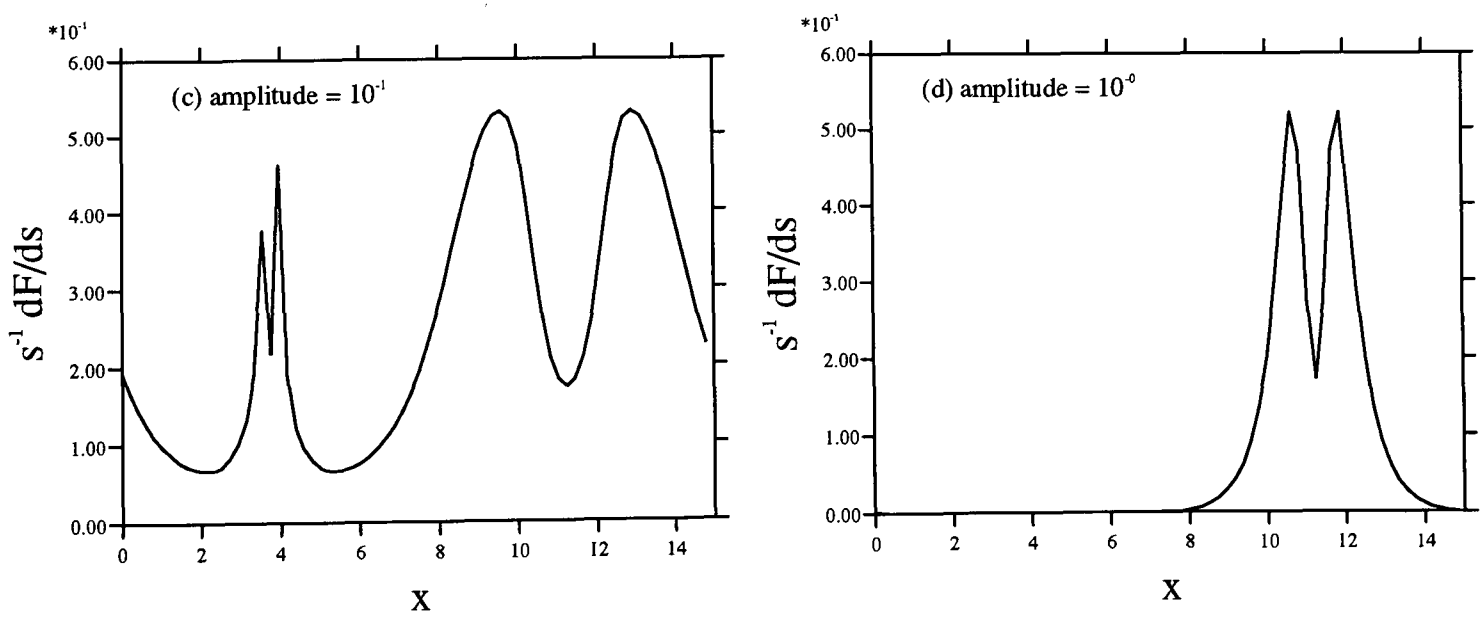


Figure 6.8: $s^{-1}\frac{dF}{ds}$ for varying amplitudes of applied sinusoidal potential.

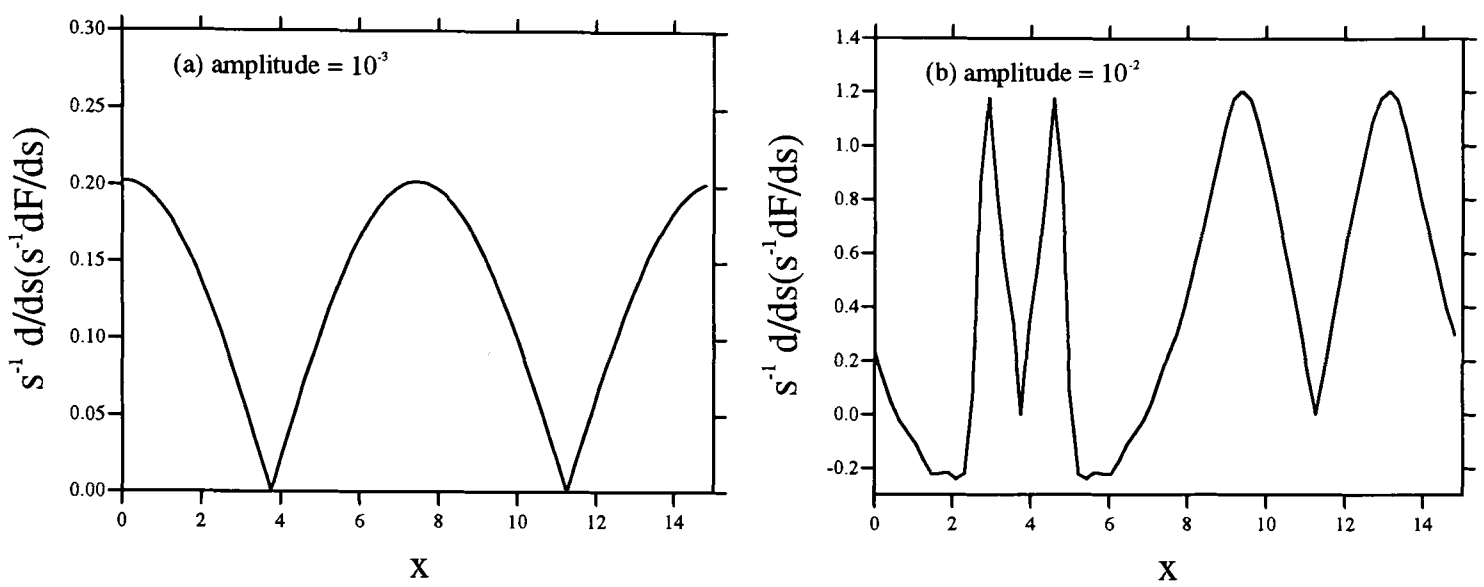


Figure 6.9: $s^{-1}\frac{d}{ds}\left(s^{-1}\frac{dF}{ds}\right)$ for varying amplitudes of applied sinusoidal potential.

tinuity that necessarily occurs in $|\nabla\rho|$. The problem is even more acute in the terms $s^{-1}\frac{dF}{ds}$ (figure 6.8), and $s^{-1}\frac{d}{ds}\left(s^{-1}\frac{dF}{ds}\right)$ (figure 6.9), which occur in the potential. Examination of figure 6.4 which show $\nabla^2\rho$ leads to a similar conclusion. In short then the basis set is inadequate to describe these functions. It is also clear that at least halving the grid spacing, ie a *minimum* of an eight fold increase in the number of grid points in real-space, and a corresponding increase in the cutoff in k-space is required for the largest amplitude calculation to converge.

Figure 6.6 shows $s(x)$. Comparing these to the appropriate $|\nabla\rho|$ figures the problem of over emphasis of very low density points is clear. Note though how the modification to $F(s)$ has smoothed this out, leading to a plateau in F, at just over 2.25. As a caution though it should be remembered that s still appears in the modified exchange potential functional and may still cause some problems.

The conclusion then is that using a plane wave basis set two major difficulties occur. The first is in accurately describing very low density regions. It has been shown that modifying the functional F to give smaller weight to large s values largely solves this problem. The second is that quite simply an extremely large basis set is required to describe $|\nabla\rho|$, especially at the maximum point in density, due to the discontinuity, and $\nabla^2\rho$. The problem for the hydrogen atom is far more severe than in this test, as the density varies much more rapidly. Even for sodium the atomic radius is less than the width of the density peak of these tests with an amplitude of 1, and note that that calculation only partially converged.

In further tests, using $q_{\max}$, and varying the box length for two sodium atoms in the bcc position, convergence was checked as the density decreased from solid densities. It was found that for box lengths of 7.5, 10.0, and 12.5 a.u. convergence was obtained, while for a box length of 15 a.u. breakdown occurred. Similarly checks were made with 64-66 sodium atoms in liquid like configurations. Configurations of 66 sodium atoms corresponding to temperatures of 420 and 1270 K, with box lengths respectively of 26.1034 a.u., and 28.1932 a.u., with $q_{\max} = 16$ (giving a cutoff in the latter of 14.3 Ry) readily converged. A 64-atom configuration corresponding to 2200 K, with a box length of 34.1500 a.u., which is more gas-like, failed to converge, even when $q_{\max}$ was increased to 30 ($q_{\max} = 20$ roughly corresponds to the cut off in the 1270 K simulation).

Thus the position is that for relatively dense fluids and solids the electron density is sufficiently uniform for convergence to be obtained. However in this region LSD is expected to be a good approximation anyway, and the GGA correction relatively small. For low density systems, molecules and atoms, where the density is far from uniform, sufficient convergence in the basis set requires, with the current facilities available, a prohibitively large

cut off. Unfortunately this is the very region in which GGA is expected to significantly improve over LSD. These problems, as their origin is in $|\nabla\rho|$ and $\nabla^2\rho$, are expected to be common to all gradient corrections in a plane wave basis set, and not just to the Perdew and Wang GGA.

Are these conclusions consistent with published implementations of gradient corrections? These can be divided into four categories. The first is where the calculation is not self consistent. For example Perdew *et al.* [82] use Hartree-Fock densities with the Perdew and Wang (PW) exchange functional for first row diatomics. As the problems are in the exchange potential then they will have avoided them. The second category is where solids are studied. These will have relatively uniform densities and so readily converge as seen in the low temperature liquid sodium calculations. Leung *et al.* [55] have used the PW functional to study the magnetic properties of iron, cobalt and nickel monoxides, whilst Barbiellini *et al.* [5] have used it to study transition metals. The third category, that partly overlaps with the previous one, is calculations using a Gaussian basis set. These are far better at describing a localised function, for which convergence is reached with far fewer terms than a plane wave basis set. Kutzler and Painter [50] used an augmented Gaussian basis set to study B_2, C_2, O_2, and F_2, using both the Langreth and Mehl [53], and PW functionals. Mlynarski and Saluhab [68] have also studied small molecules with a Gaussian basis set. Other local basis sets have also been used. Fan and Ziegler [18, 19] have tested non-local corrections in self-consistent calculations using an uncontracted Slater type orbital basis augmented by other atomic like functions. None of these categories present any problems in any terms of the arguments given for breakdown. However recently a paper has been published in the fourth category. Laasonen *et al.* [51] have studied the H_2O dimer using the Becke exchange functional [7], and the Perdew correlation functional [79] using a plane wave basis set. Clearly this should have a highly non-uniform density and would be expected to experience the difficulties discussed above. However there are two points to note. Firstly they use a very high cut off (80 Ry). Also they use a surprisingly small box length (16 a.u.). This has two effects. The first is that it reduces $q_{\max}$ and hence the number of plane waves needed for an 80 Ry cut off. The second is that the clusters in the cell can be expected to interact with its images in the periodic boundary conditions they use. The electron density then is not expected to drop completely to zero anywhere in the box, and is likely to be far more uniform than if the dimer was *truly* isolated.

6.3.1 Partially Converged Na_2 Calculations

In order to obtain an idea of the effect that GGA would have on calculations, calculations were carried out on H_2 and Na_2. Unfortunately the degree of convergence for the H_2 calculation was insufficient to deduce anything mean-

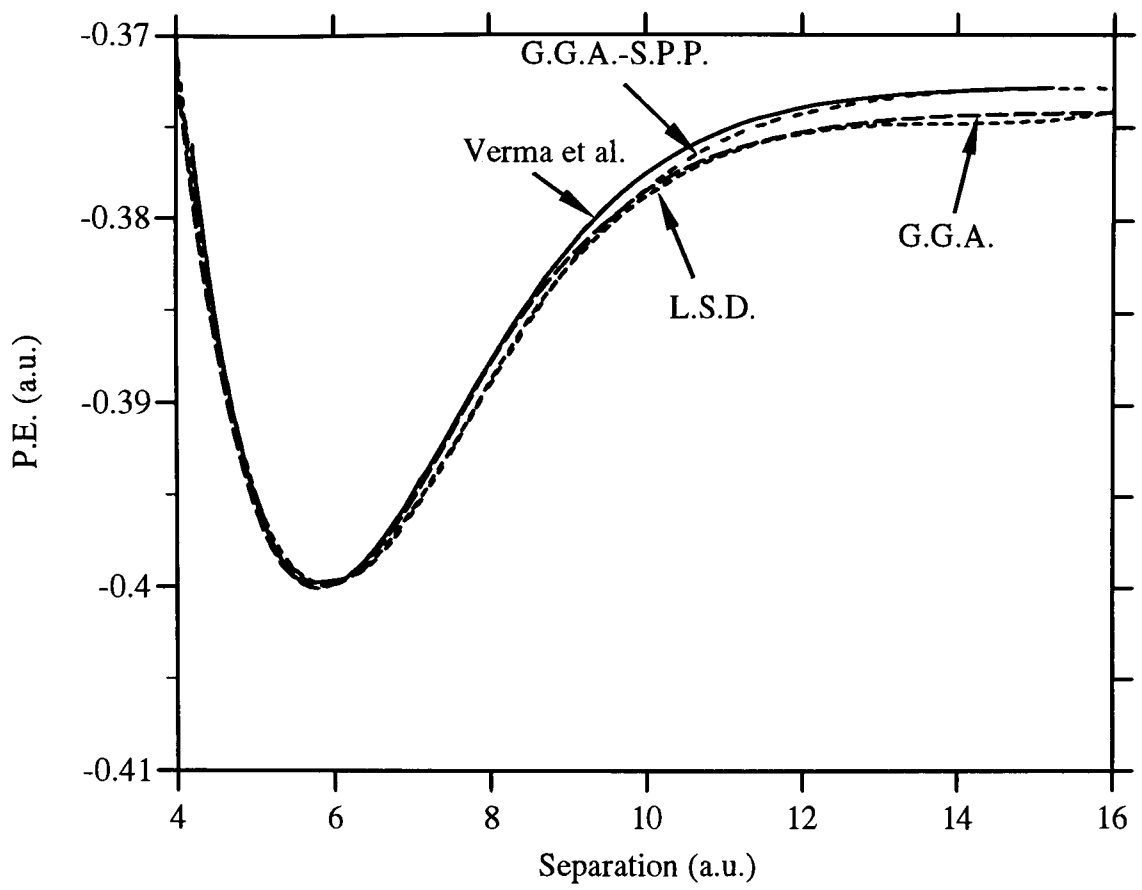


Figure 6.10: The potential energy curves for Na_2. The experimental potential energy curve is due to Verma *et al.* [116] .

ingful. With Na_2 convergence to three decimal places in the total energy, using $q_{\max} = 16$ and a box length of 36 a.u. was achieved. The average local moment data was too unreliable for useful analysis, but the ionic potential energy data was moderately reliable, also being converged to three decimal places. Figure 6.10 shows a comparison of LSD, GGA, and GGA-SPP with experiment. The minima were matched to allow shape comparison. The curves were produced in the same way as described in chapter 3. Despite the fact that the pseudopotential was optimised for LSD, GGA produces a remarkably good fit with experiment for separations less than 9 a.u. and gives a dissociation limit close to the LSD value. GGA-SPP in the vicinity of the minimum fits very closely to the LSD curve, but then departs to give a dissociation limit extremely close to experiment.

Certainly GGA and GGA-SPP look promising. However probably too much should not be read into these results. Firstly there is uncertainty as to the validity of direct comparison with experiment because the pseudopotential was not optimised for these functionals. Secondly it should still be remembered that only partial convergence had been achieved.

6.4 The Hartree-Fock-Kohn-Sham Method

One advantage of the LSD exchange energy is that only the spin densities and not the orbitals need be considered. However with the Kohn-Sham method spin orbitals have already been reintroduced into density functional theory. With these orbitals we can construct the exact exchange functional,

$$E_{\mathrm{x}}[\rho^{\alpha},\rho^{\beta}] = -\frac{1}{2}\int\int \frac{1}{r_{12}}\left[|\rho_1^{\alpha\alpha}(\mathbf{r}_1,\mathbf{r}_2)|^2 + |\rho_1^{\beta\beta}(\mathbf{r}_1,\mathbf{r}_2)|^2\right] d\mathbf{r}_1 d\mathbf{r}_2, \tag{6.54}$$

with,

$$\rho_1^{\sigma\sigma}(\mathbf{r}_1,\mathbf{r}_2) = \sum_i n_{i\sigma}\phi_{i\sigma}(\mathbf{r}_1)\phi_{i\sigma}^*(\mathbf{r}_2). \tag{6.55}$$

This is exactly the same functional as used in Hartree-Fock theory. Inserting this into the total energy functional yields,

$$\begin{aligned} E[\rho^{\alpha},\rho^{\beta}] &= \sum_{i\sigma} n_{i\sigma}\int d\mathbf{r}\ \phi_{i\sigma}^*(\mathbf{r})\left(-\frac{1}{2}\nabla^2\right)\phi_{i\sigma}(\mathbf{r}) + J[\rho] \\ &- \frac{1}{2}\int\int \frac{1}{r_{12}}\left[|\rho_1^{\alpha\alpha}(\mathbf{r}_1,\mathbf{r}_2)|^2 + |\rho_1^{\beta\beta}(\mathbf{r}_1,\mathbf{r}_2)|^2\right] d\mathbf{r}_1 d\mathbf{r}_2 \\ &+ E_{\mathrm{c}}[\rho^{\alpha},\rho^{\beta}] + \int V_{\mathrm{ext}}(\mathbf{r})\rho(\mathbf{r})d\mathbf{r}. \end{aligned} \tag{6.56}$$

Minimising $E[\rho^{\alpha},\rho^{\beta}]$ with the usual orthonormality constraints,

$$\int \phi_{i\sigma}^*(\mathbf{r})\phi_{j\sigma}(\mathbf{r})d\mathbf{r} = \delta_{ij}, \tag{6.57}$$

gives the Euler-Lagrange equations,

$$-\frac{1}{2}\nabla^2\phi_{i\sigma}(\mathbf{r}) + \int v_{\mathrm{eff}}^{\sigma}(\mathbf{r},\mathbf{r}')\phi_{i\sigma}(\mathbf{r}')d\mathbf{r}' = \varepsilon_{i\sigma}\phi_{i\sigma}, \tag{6.58}$$

where,

$$v_{\mathrm{eff}}^{\sigma}(\mathbf{r},\mathbf{r}') = \left[V_{\mathrm{ext}}(\mathbf{r}) + \int \frac{\rho(\mathbf{r}'')}{|\mathbf{r}-\mathbf{r}''|}d\mathbf{r}'' + \frac{\delta E_{\mathrm{c}}}{\delta\rho^{\sigma}(\mathbf{r})}\right]\delta(\mathbf{r}-\mathbf{r}') - \frac{\rho_1^{\sigma\sigma}(\mathbf{r},\mathbf{r}')}{|\mathbf{r}-\mathbf{r}'|} \tag{6.59}$$

This approach was initially suggested by Kohn and Sham [46], but has not been used very much. As it uses the Hartree-Fock exchange, in this thesis it will be referred to as the Hartree-Fock-Kohn-Sham (HFKS) method. It is exact apart from the correlation term. As noted above LSD correlation can be improved on by using SPP. When SPP is used in conjunction with the exact exchange functional, it will be referred to as the HFKS-SPP method. It is worth pointing out though that if correlation is ignored, ie. $E_{\mathrm{c}}[\rho^{\alpha},\rho^{\beta}] = 0$ then this method is identical to the Hartree-Fock method. Thus HFKS can be thought of either as density functional theory with exact exchange, or as Hartree-Fock theory with a correction for the correlation.

6.4.1 Implementation

Implementation of HFKS is relatively simple and rests on the relation,

$$h(\mathbf{r}) = \int \frac{f(\mathbf{r}')}{|\mathbf{r}-\mathbf{r}'|} d\mathbf{r}' \overset{\text{FFT}}{\Longrightarrow} f(\mathbf{g}) \frac{4\pi}{g^2}, \tag{6.60}$$

where,

$$f(\mathbf{r}) \overset{\text{FFT}}{\Longrightarrow} f(\mathbf{g}). \tag{6.61}$$

This is already employed for the Coulomb term where $f(\mathbf{r})$ is simply $\rho(\mathbf{r})$. Thus to implement the energy functional in equation 6.54 note that,

$$|\rho_1^{\sigma\sigma}(\mathbf{r},\mathbf{r}')|^2 = \sum_i \sum_j \phi_{i\sigma}(\mathbf{r}) \phi_{j\sigma}^*(\mathbf{r})\ \phi_{i\sigma}^*(\mathbf{r}') \phi_{j\sigma}(\mathbf{r}'). \tag{6.62}$$

For each i, j then $\phi_{i\sigma}^*(\mathbf{r}')\phi_{j\sigma}(\mathbf{r}')$ is taken as $f(\mathbf{r}')$ in equation 6.60 and Fourier transformed to give $f(\mathbf{g})$. Substituting in $f(\mathbf{g})\frac{4\pi}{g^2}$, and carrying out the inverse FFT yields $h_{ij}(\mathbf{r})$, the subscripts denoting that this is $h(\mathbf{r})$ for the ij^{th} term in the sum in equation 6.62. The final integral,

$$E_{\mathbf{x}}[\rho^\alpha, \rho^\beta] = -\frac{1}{2} \sum_i \sum_j \int h_{ij}(\mathbf{r})\ \phi_{i\sigma}(\mathbf{r}) \phi_{j\sigma}^*(\mathbf{r}) d\mathbf{r}, \tag{6.63}$$

is then carried out in real space.

The integral,

$$\int \frac{\rho^{\sigma\sigma}(\mathbf{r},\mathbf{r}')}{|\mathbf{r}-\mathbf{r}'|} \phi_{i\sigma}(\mathbf{r}') d\mathbf{r}' = \sum_j \phi_{j\sigma}(\mathbf{r}) \int \frac{\phi_{j\sigma}^*(\mathbf{r}')\phi_{i\sigma}(\mathbf{r}')}{|\mathbf{r}-\mathbf{r}'|} d\mathbf{r}', \tag{6.64}$$

which is required for the gradients in the CG method is calculated in an entirely analogous manner.

6.5 Comparison of LSD, SIC, SPP, HFKS, and HFKS-SPP for Simple Diatomic Systems

In section 3.3 LSD and SIC were compared for simple diatomic systems. In this section the same systems will be used to compare these functionals with those introduced in this chapter. The methods by which this data was obtained are identical to those used in section 3.3.

Method	Binding Energy/Atom (a.u.)	Bond Length (a.u.)
Expt. [103]	0.08309	1.40
LSD	0.08533	1.54
SIC	0.08602	1.45
HFKS	0.08673	1.43
HFKS-SPP	0.08598	1.45
SPP	0.08458	1.55

Table 6.6: Comparison of the H_2 binding energies and bond lengths from various calculations with experiment.

6.5.1 H_2

Figure 6.11 shows the potential energy curves for H_2 using LSD, SIC, SPP, HFKS, HFKS-SPP, and Hartree Fock (HF), along with the "exact" curve due to Kolos and Wolniewicz [45]. The HF data was generated simply by setting the correlation terms to zero in the HFKS scheme. The zero of the ionic potential energy was taken to be that of two isolated hydrogen atoms, as found within the appropriate approximation, ie. twice the ionic potential energy of the hydrogen atom within the appropriate approximation was subtracted from each curve. Table 6.6 shows the bond lengths and binding energies for these approximations. For all these calculations $q_{\max} = 16$ and a box length of 20 a.u. was used.

All methods overestimate the bond length, but there is a noticeable pattern. SIC, HFKS, HFKS-SPP all have similar bond lengths, as do LSD, and SPP, the latter being longer. Note that the SPP correction to LSD correlation lengthens the bond, while using HFKS, or SIC which correct for the self term in the exchange terms, shorten the bond. It is particularly noticeable that SIC and HFKS-SPP give the same bond length.

Regarding the binding energies a similar pattern emerges. All methods overestimate the binding energy, but the methods have the same grouping as in the bond length; SPP and LSD giving the smaller binding energy. The SPP correction with both LSD and HFKS exchange reduces the binding energy, while correcting for the self exchange and coulomb terms increases the binding energy. Thus HFKS has the largest binding energy, whilst SIC and HFKS-SPP are in remarkable agreement.

Examining the potential energy curves, again the grouping of LSD with SPP, and HFKS, SIC, and HFKS-SPP is seen. Indeed SIC and HFKS-SPP are almost completely indistinguishable even when the figure is enlarged. These are also in good agreement with the exact curve, except in the spin pairing/unpairing region. Note that the HF curve is hopelessly inadequate by

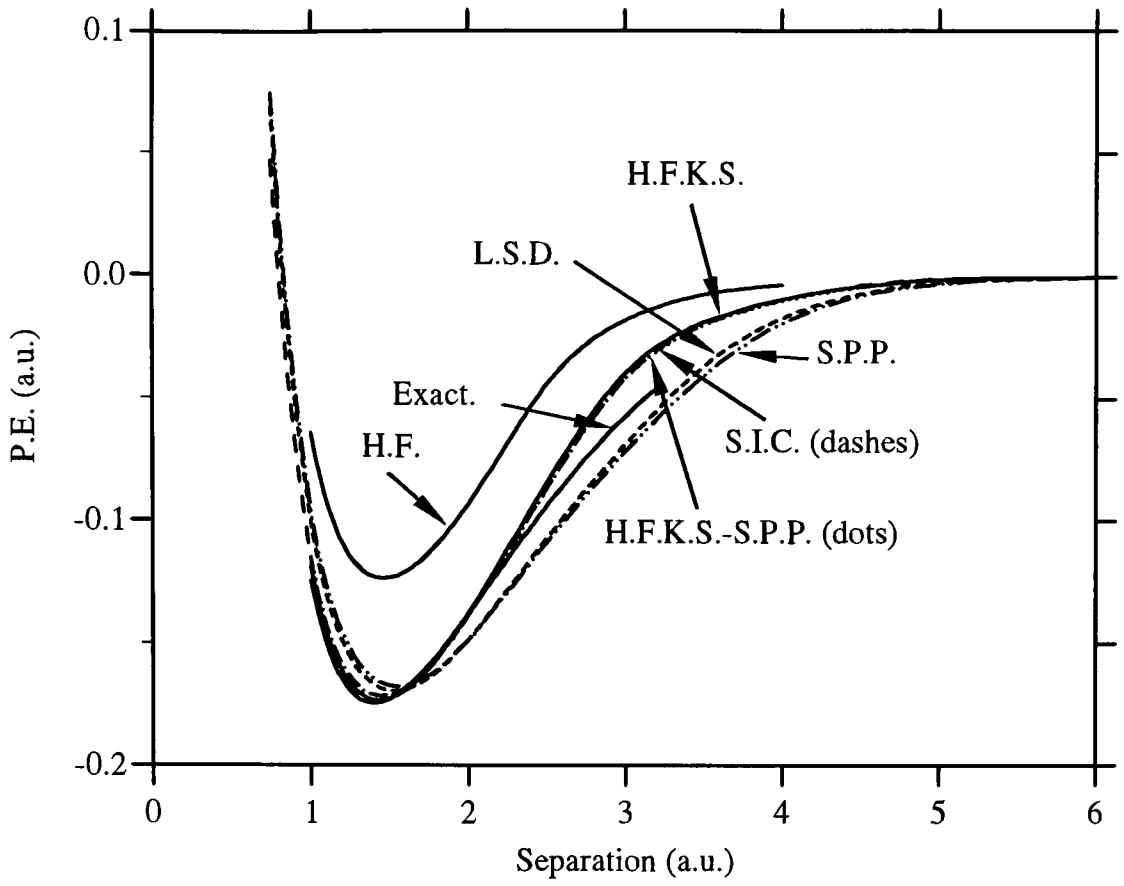


Figure 6.11: The potential energy curves for H_2 using HFKS, HFKS-SPP, SPP, LSD and SIC. The "exact" potential energy curve due to Kolos and Wolniewicz [45] is also shown.

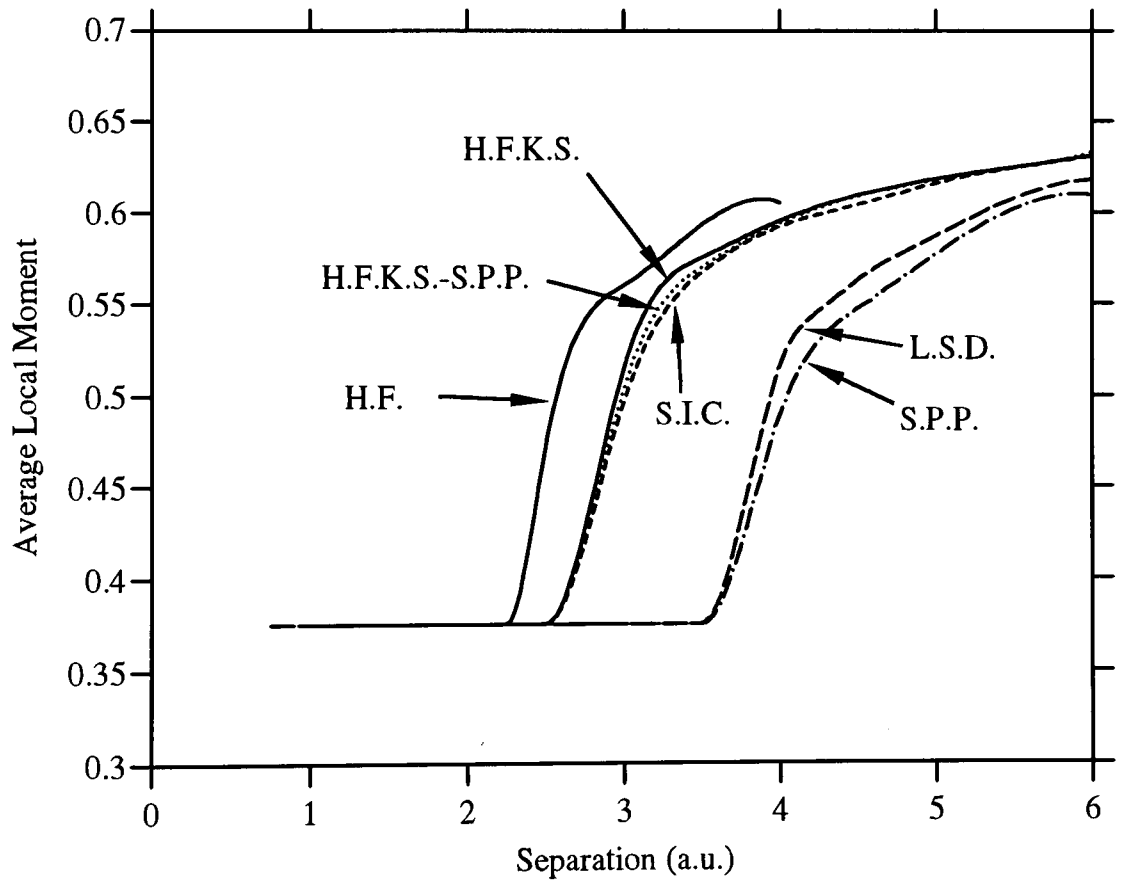


Figure 6.12: The local moment curves for H_2 using HFKS, HFKS-SPP, SPP, LSD and SIC.

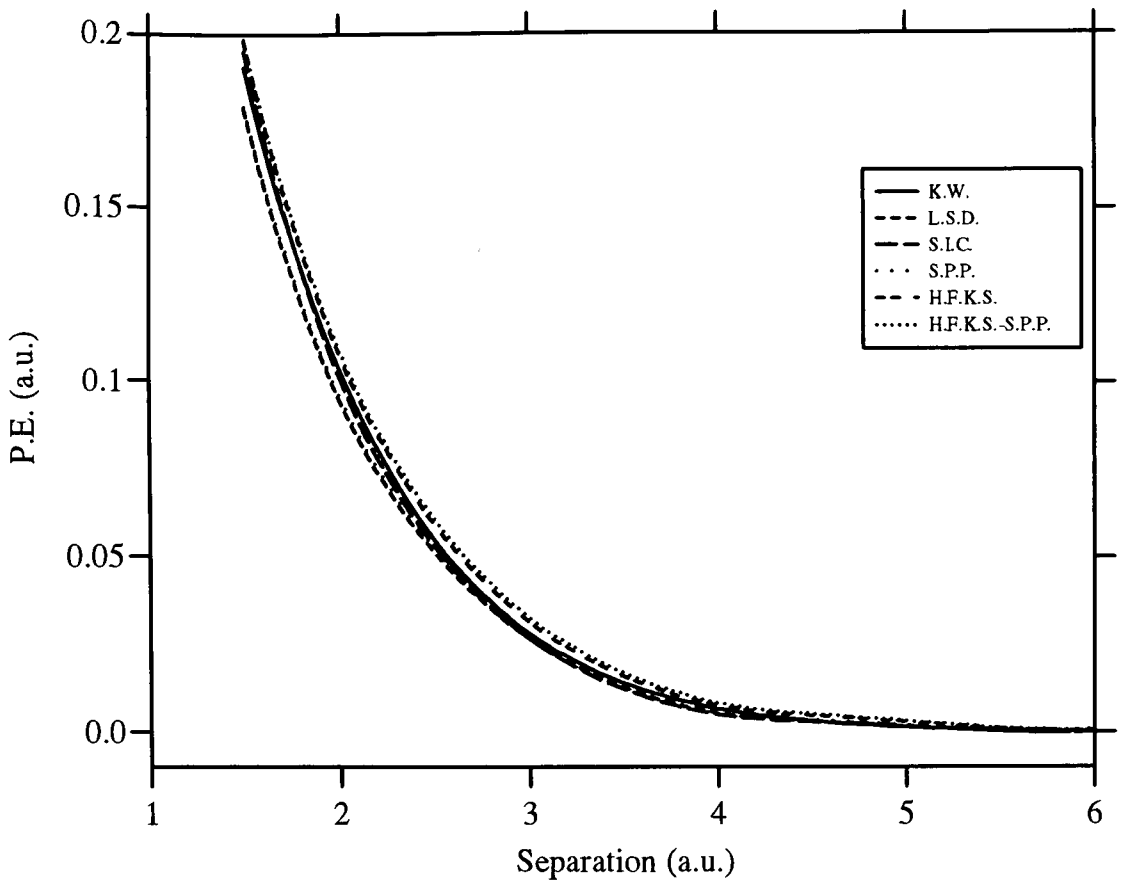


Figure 6.13: The potential energy curves for triplet H_2 using HFKS, HFKS-SPP, SPP, LSD and SIC. The potential energy curve due to Kolos and Wolniewicz [44] is also shown.

comparison. It is clear then that using LSD or SPP as an approximate correlation energy greatly improves the HF method, and is considerably cheaper than carrying out CI calculations. Indeed Savin *et al.* [95] and Kemister and Nordholm [40, 41] have already proposed such schemes.

Figure 6.12 shows the local moment curves for the same approximations. It can be seen that in HF the system spin unpairs earlier than all the other approximations, whilst LSD and SPP do not spin unpair until relatively large separations. The SPP correction appears to delay the onset of spin unpairing, whilst correcting the self exchange/coulomb term greatly encourages spin unpairing. Again HFKS, HFKS-SPP, and SIC all give very similar curves with SIC being slightly slower in spin unpairing.

In order to compare the various methods in a calculation with more than one electron of a given spin, the potential energy curve for the triplet state of H_2 was calculated. This was simply done by setting the number of electrons in the H_2 calculation to be two of one spin and none of the other. The results are shown in figure 6.13 for LSD, SIC, SPP, HFKS, and HFKS-SPP, as well as the curve due to Kolos and Wolniewicz (KW) [44] which is accurate to at least ± 0.1 cm^{-1}. The zero of energy is taken again as two isolated hydrogen atoms. From this figure it can be seen that LSD, and SPP give almost identical results, falling somewhat below the KW data, whilst HFKS, and

Method	Binding Energy/Atom (a.u.)	Bond Length (a.u.)
Expt.	0.0137	5.818
LSD	0.0130	5.89
SIC	0.0122	5.76
HFKS	0.0116	5.70
HFKS-SPP	0.0122	5.83
SPP	0.0134	6.06

Table 6.7: Comparison of the Na_2 binding energies and bond lengths from various calculations with experiment.

HFKS-SPP give very similar results, this time giving higher repulsive energies than KW. The SIC curve is in very good agreement though throughout the region studied, with a minor discrepancy between 2, and 4 a.u. From this simulation it would seem then that SIC gives the best results of any of the methods for many electron calculations.

Finally note that the calculation was only carried out to a separation of 6 a.u. At larger separations the difference between the calculated potential energy and the energy of the two isolated hydrogen atoms is smaller than the reliable accuracy of the calculation. Thus no attempt was made to study the weakly bound Van der Waals dimer.

6.5.2 Na_2

Figure 6.14 shows the PE curves for Na_2. In contrast to the figure in section 3.3 the zero is taken to be the energy of two isolated sodium atoms. Table 6.7 shows the binding energies and bond lengths for the various approximations. For these calculations $q_{\max} = 14$ and a box length of 36 a.u. were used.

Similar patterns to those for H_2 in the agreement of the various methods are apparent. LSD and SPP give similar bond lengths and binding energies, as do the other three approximations. All the methods underestimate the binding energy, with LSD, and SPP giving the better agreement with experiment. LSD and SPP overestimate the bond length, as does HFKS-SPP, which is the closest to the experimental energy. Notice SPP again increases bond lengths, and this time slightly increases binding energies.

From figure 6.14 it can be seen that HFKS-SPP, and SIC are once more in excellent agreement. It is noticeable that in this case the SPP correction has a far greater impact than was the case for H_2. LSD gives the best fit to the experimental data due to Verma *et al.* [116], but this is not surprising, because, as has been stated earlier, the pseudopotential was optimised for LSD. (Note that the deviation of the LSD curve around a separation of 14

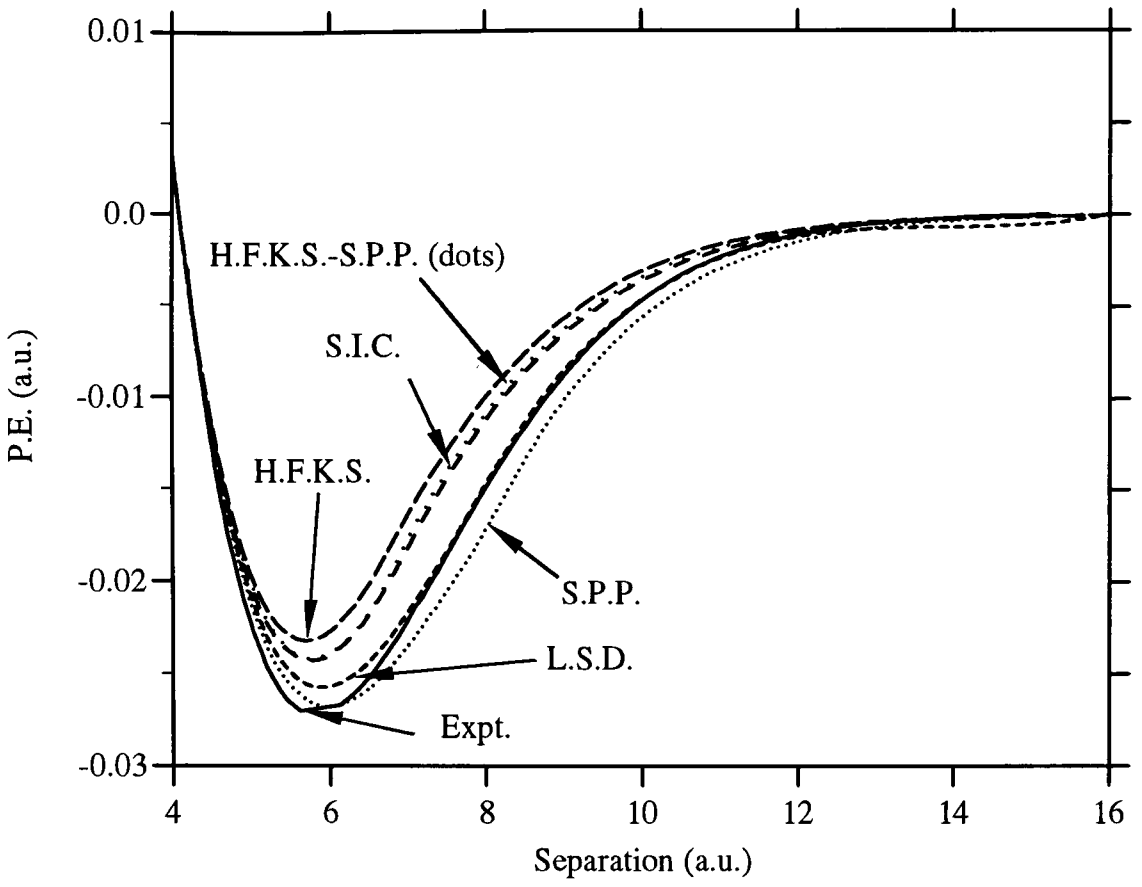


Figure 6.14: The potential energy curves for Na_2 using HFKS, HFKS-SPP, SPP, LSD and SIC. The experimental potential energy curve due to Verma *et al.* [116] is also shown.

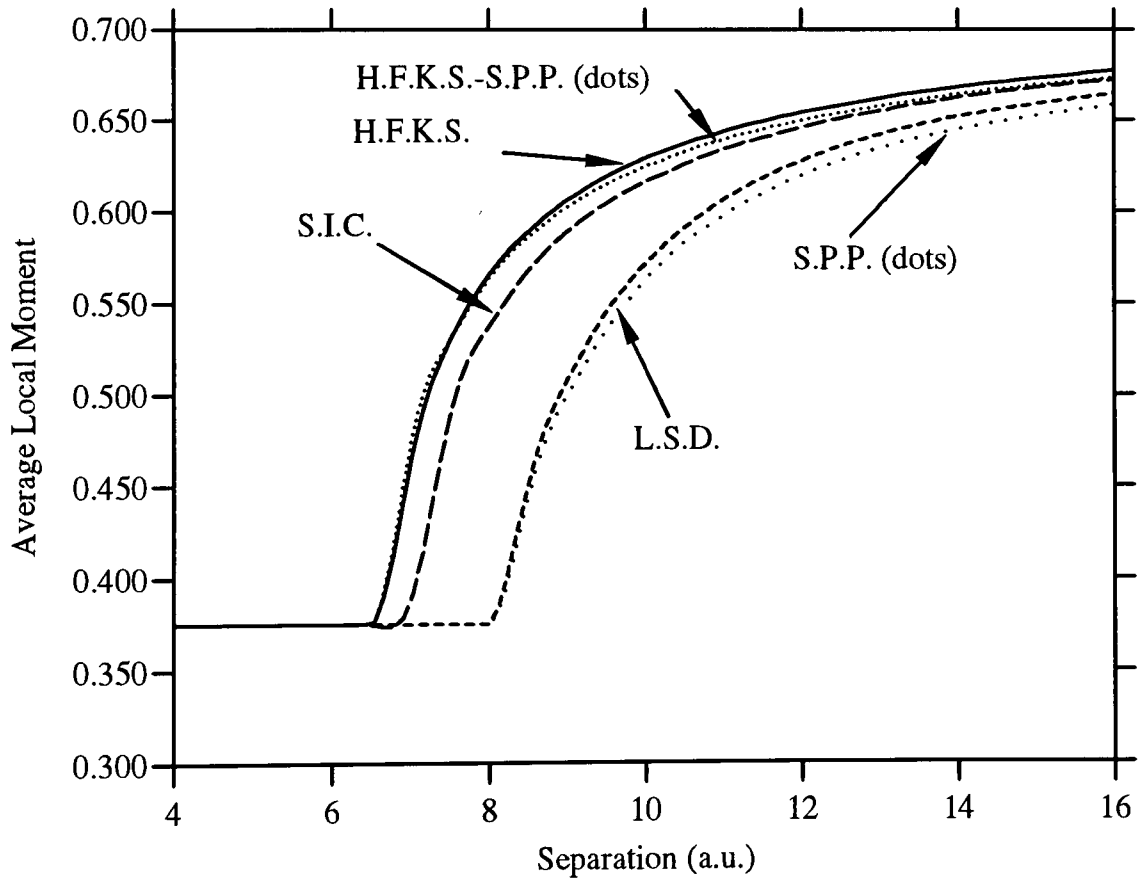


Figure 6.15: The local moment curves for Na_2 using HFKS, HFKS-SPP, SPP, LSD and SIC.

Method	Binding Energy/Atom (a.u.)	Bond Length (a.u.)
Expt.	0.00831	8.79
LSD	0.00753	8.35
SIC	0.00790	8.30
HFKS	0.00984	8.20
HFKS-SPP	0.01018	8.42
SPP	0.01036	8.61

Table 6.8: Comparison of the Cs_2 binding energies and bond lengths from various calculations with experiment.

a.u. is purely and artefact of the fitting procedure.)

Figure 6.15 shows the average local moment curves for Na_2. Again the grouping of LSD and SPP, and HFKS, HFKS-SPP, and SIC is apparent. Interestingly the local moment curve for HFKS-SPP is closer to that for HFKS than that for SIC. This is probably due to the curve fitting procedure though rather than any physical difference.

6.5.3 Cs_2

Table 6.8 shows the binding energies and bond lengths for Cs_2, while figure 6.16 shows the PE curves. As for Na_2, $q_{\max} = 14$ and a box length of 36 a.u. was used.

In these calculations the grouping of the results that occurred for H_2 and Na_2 is not really apparent. As commented in section 3.3 the results are in relatively poor agreement with experiment, probably due to polarizability and relativistic effects, even though these will partly be implicitly included in the pseudopotential. SPP again increases the bond length while correcting the exchange term shortens it. LSD gives the smallest binding energy and SPP the biggest, with SIC closest to the experimental value. Figure 6.16 reinforces these points.

Figure 6.17 compares the local moment curves. The conclusions are identical to those for Na_2.

6.5.4 NaH

Table 6.9 compares the binding energies and bond lengths for NaH. Figure 6.18, and figure 6.19 show the potential energy and local moment curves respectively. $q_{\max} = 16$, and a box length of 20 a.u. was used. Once more it can be seen that correcting for the self-correlation increases the bond length, though only slightly, whilst using exact or corrected exchange shortens the

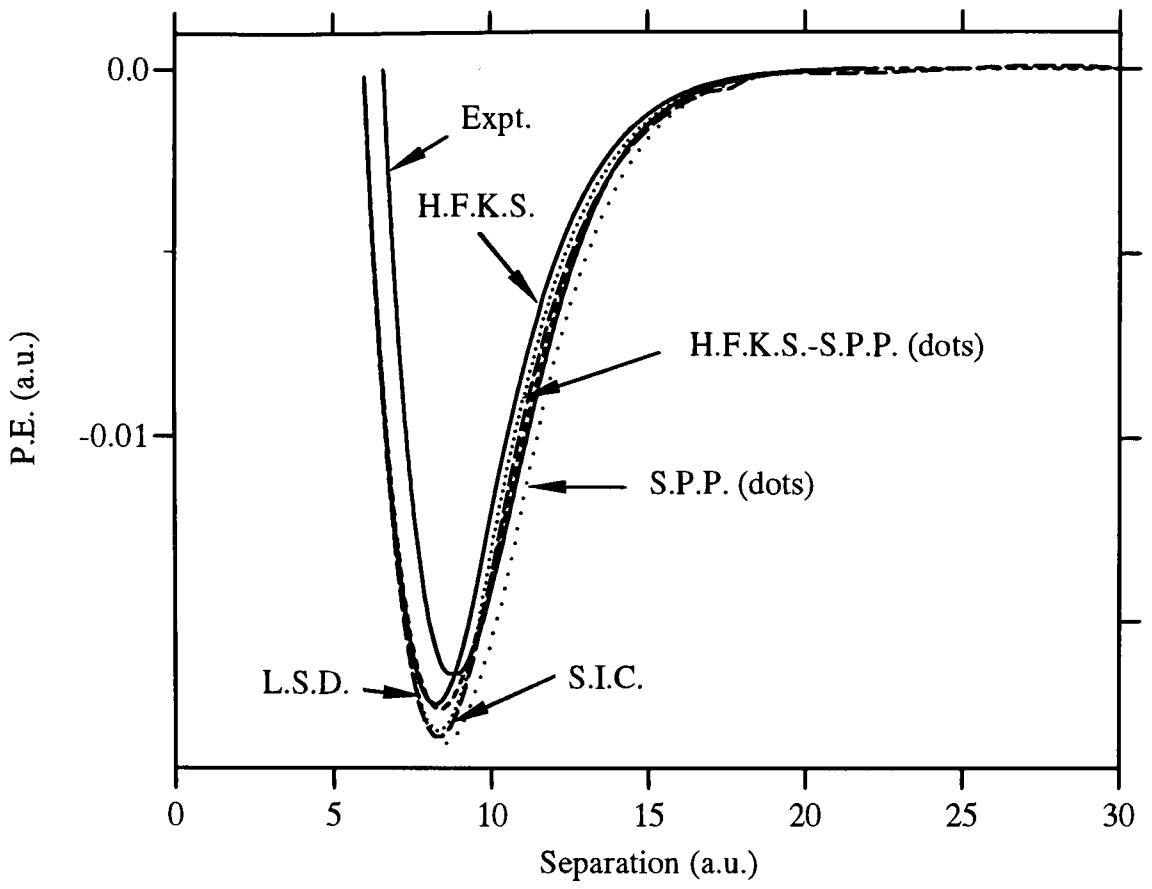


Figure 6.16: The potential energy curves for Cs_2 using HFKS, HFKS-SPP, SPP, LSD and SIC. The experimental potential energy curve due to Weickenmeier *et al.* [121] is also shown.

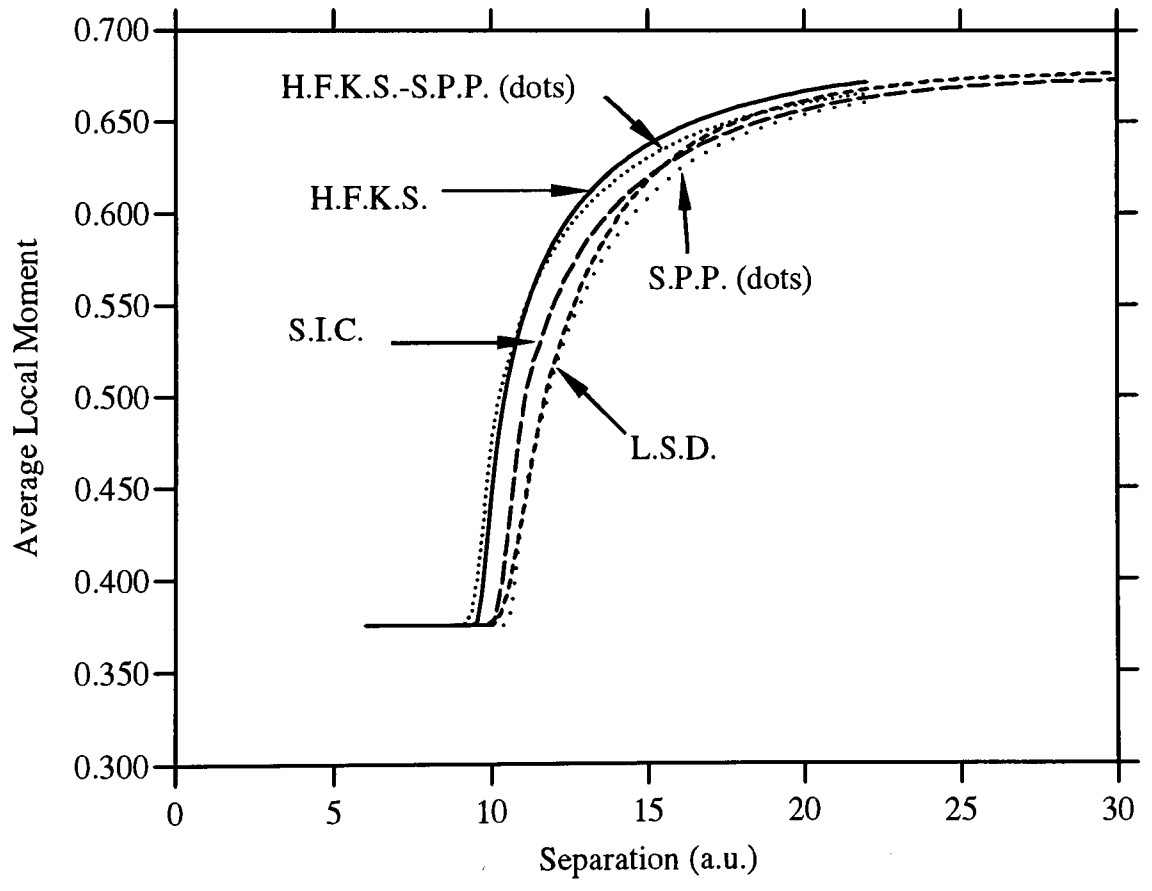


Figure 6.17: The local moment curves for Cs_2 using HFKS, HFKS-SPP, SPP, LSD and SIC.

Method	Binding Energy/Atom (a.u.)	Bond Length (a.u.)
LSD	0.346	3.09
SIC	0.343	3.05
HFKS	0.348	3.05
HFKS-SPP	0.342	3.06
SPP	0.342	3.09

Table 6.9: Comparison of the NaH binding energies and bond lengths from various calculations.

bond length. The binding energy data indicates that the self correlation is the dominant effect, as SIC, HFKS-SPP, and SPP, all of which correct for this have very similar binding energies, whilst LSD and HFKS are noticeably larger.

The potential energy curves have the same grouping as for the homonuclear diatomics with LSD and SPP being virtually indistinguishable, as are HFKS, HFKS-SPP, and SIC. Note the zero of energy is the PE at a separation of 10 a.u. The local moment curves show the same grouping.

Figure 6.20 shows the dipole moment curves. Note no fitting has been carried out here. The usual grouping is still apparent but is less distinct than for the PE and local moment curves. Using the SPP correction appears to reduce electron transfer and enhance spin unpairing. Thus SPP, and HFKS-SPP have lower dipole moments than LSD, and HFKS.

6.5.5 Conclusions

The most obvious conclusion is that HFKS-SPP, HFKS, and SIC all produce very similar results. As SPP in a two electron scheme is identical to SIC for correlation, and knowing that HFKS uses the exact exchange energy, this would infer that SIC is a good approximation, significantly improving on LSD. Conversely comparing HFKS, and HFKS-SPP to HF for H_2 it is clear that an LSD based correlation energy provides a computationally cheap and simple improvement of the HF model, which gives accurate results.

The effect of various approximations on the bond length is also clear. Correcting the LSD correlation increases the bond length, correcting the LSD exchange reduces it. Although these effects do not exactly cancel, it is precisely these opposing effects of the errors in LSD that lead to its well known reliability. For binding energies matters are confused by the problem with the pseudopotentials, and no pattern for all the dimers emerges. However if the trend for H_2 is taken, where the potential used is known to be correct, correcting the LSD correlation decreases the binding energy, while correcting

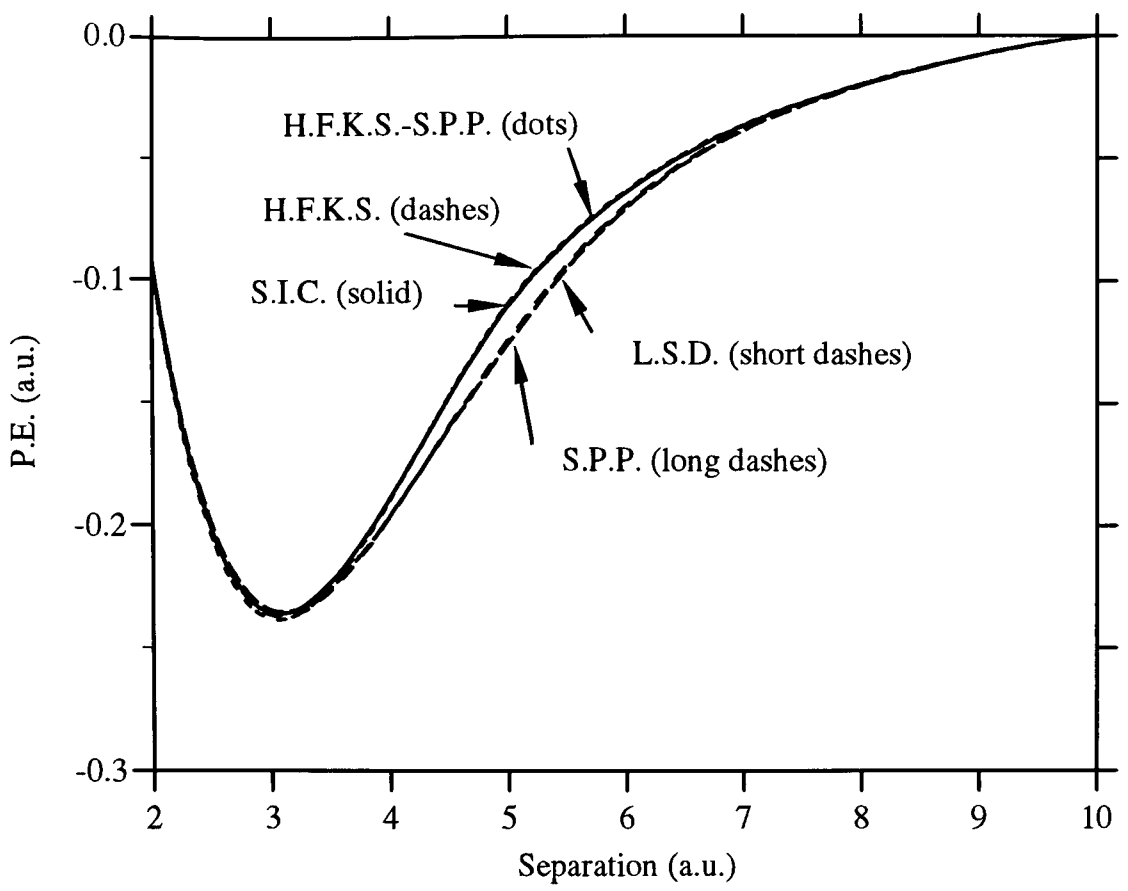


Figure 6.18: The potential energy curves for NaH using HFKS, HFKS-SPP, SPP, LSD and SIC.

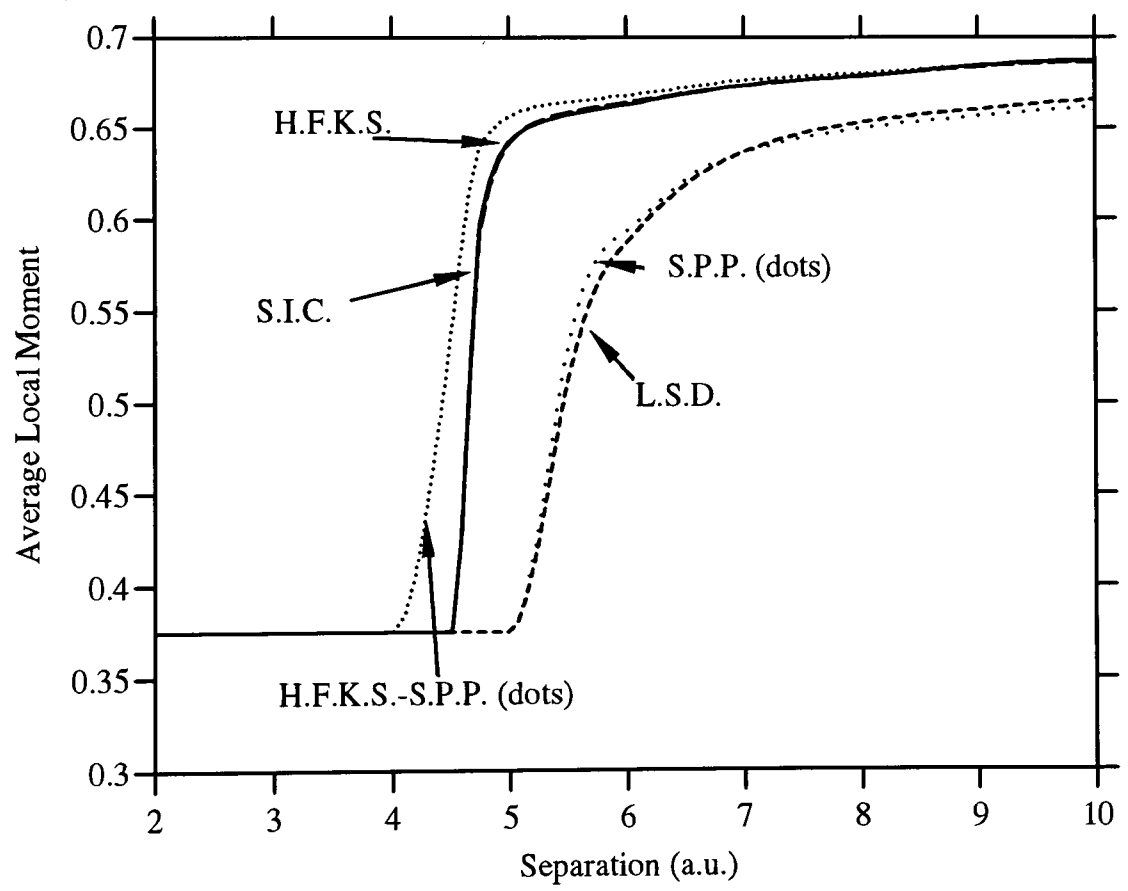


Figure 6.19: The local moment curves for NaH using HFKS, HFKS-SPP, SPP, LSD and SIC.

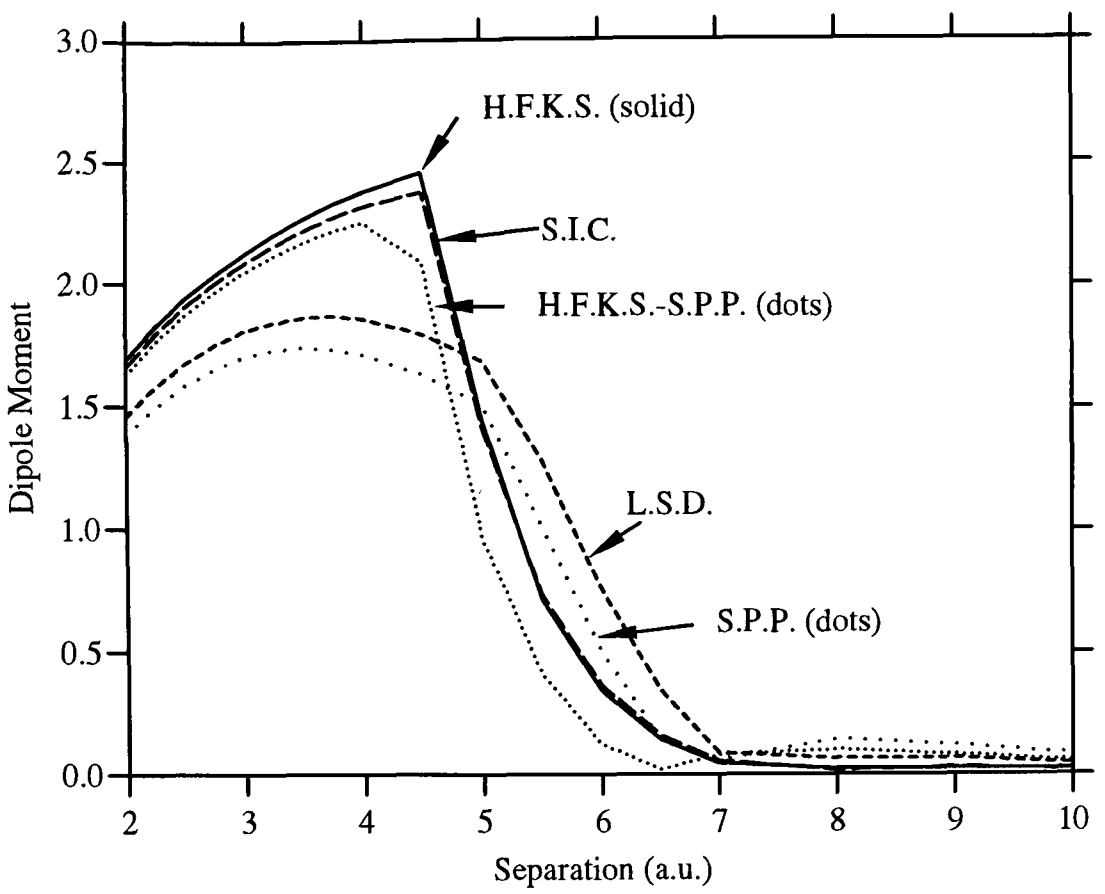


Figure 6.20: The dipole moment curves for NaH using HFKS, HFKS-SPP, SPP, LSD and SIC.

the LSD exchange increases the binding energy.

For H_2, where there is no dispute over the pseudopotential, HFKS, HFKS-SPP, and SIC are in remarkable agreement with each other and accurately reproduce the "exact" curve. The major discrepancy is in the spin pairing/unpairing region, which clearly requires further improvements to the model if it is to be accurately described.

6.6 The Use of HFKS and HFKS-SPP To Study Small Sodium Clusters

In this section preliminary calculations on Na_3, and Na_4 will be briefly discussed. The methods used are identical to those outlined in chapter 4 for LSD, and SIC. These calculations are intended to be illustrative and certainly not exhaustive.

6.6.1 Geometries and Binding Energies

Only three clusters were tested, Na_3 in both the acute and obtuse isosceles geometries, and Na_4 in the rhombic geometry. Each calculation was started from the SIC optimised geometry. For Na_4, and Na_3 in the obtuse geometry

Method	a	b	Binding Energy/Atom (eV)
HFKS	6.11	9.04	0.278
HFKS-SPP	6.45	12.89	0.274

Table 6.10: Binding energies and bond lengths for Na_3 using HFKS, and HFKS-SPP.

Method	a	b	Binding Energy/Atom (eV)
HFKS	5.80	6.66	0.358
HFKS-SPP	5.98	6.82	0.357

Table 6.11: Binding energies and bond lengths for Na_4 using HFKS, and HFKS-SPP.

no qualitative change in geometry was observed. However the Na_3 calculation started from the acute geometry resulted in exactly the same geometry as the calculation started from the obtuse isomer. This tends to support the assertion in chapter 4 that the acute Na_3 is not a true minimum, but the transition state for the pseudorotation of Na_3.

The bond lengths and binding energies found for these clusters are shown in tables 6.10, and 6.11. The short bond lengths for Na_3 are shorter for HFKS than for LSD and only slightly shorter than for SIC. The long bond length is somewhat longer then both the LSD and SIC calculations. HFKS-SPP gives both bond lengths to be substantially longer than for LSD and SIC, with a larger obtuse angle as well. For Na_4 the HFKS bond lengths are very similar to those for SIC, while the HFKS-SPP values are close to those from LSD.

The binding energies for both Na_3, and Na_4 are closer to the CI values than to the LSD and SIC values. The value found by Fantucci *et al.* [20] for Na_3 is smaller and their value for Na_4 is larger. Both HFKS, and HFKS-SPP give very similar binding energies. In the absence further calculations on other clusters it is not possible to meaningfully comment on any trends in the binding energies.

6.6.2 Polarizabilities

Table 6.12 gives the polarizabilities for Na_4 using HFKS, and HFKS-SPP using the same method as described in chapter 4. The values for $\bar{\alpha}$ straddle the experimental value of $81.9\mathring{A}^3$. Both methods give larger values for the components of $\boldsymbol{\alpha}$ than the results of Moullet *et al.* [69]. However the HFKS-SPP results are very close to the results found using LSD. HFKS has a similar value of $\bar{\alpha}$ to SIC (74.7 vs 75.2 $\mathring{A}^3$), but the components are quite different;

	α_{xx}	α_{yy}	α_{zz}	$\bar{\alpha}$
HFKS	130.0	48.6	45.6	74.7
HFKS-SPP	146.0	65.7	50.9	87.5

Table 6.12: Diagonal components of the polarizability tensor and the spherically averaged polarizability $\bar{\alpha}$ in $\mathring{A}^3$ for Na_4 using HFKS, and HFKS-SPP.

the former method giving a larger value of α_{xx} but smaller values of the other two components.

6.6.3 Conclusions

Too few calculations have been carried out to properly compare these results with those from other methods. However they do show that the HF exchange functional can be successfully incorporated into the CP algorithm, and steepest descent dynamics (and thus normal dynamics) carried out. As pointed out for the dimers this provides a far cheaper alternative to CI to give results that, from this limited sample, seem to be of comparable accuracy. One advantage this may have over a true density functional approach is that the calculation of excited states in both static and dynamic runs should be implementable, and have a firmer theoretical foundation than the "excited states" generated in density functional theory. Indeed a variation of the CG method has been used to calculate excited states within LSD; clearly its adaptation to HFKS, and HFKS-SPP present interesting future lines of investigation.

Appendix A

The Derivation of the Orthonormality Constraint Algorithms for CP Dynamics

We wish to determine the values of Lagrange multipliers for the CP equations of motion. In this appendix I will derive the result for the Nosé-Hoover thermostat. The result for normal CP dynamics can be obtained merely by setting ξ to zero. Note in this appendix spin indices are omitted for clarity.

The equation of motion for the Nosé-Hoover thermostat is,

$$\begin{aligned}\psi_i(t+\delta t) &= \psi_i(t) + (\psi_i(t) - \psi_i(t-\delta t))(1-\chi) \\ &+ \frac{(\delta t)^2}{\mu}\left(-\frac{\delta E}{\delta \psi_i^*} + \sum_j \lambda_{ij}^* \psi_j(t)\right). \qquad \text{(A.1)}\end{aligned}$$

Where $\chi = \xi(t)\delta t$. We now wish to find λ_{ij} such that,

$$\langle \psi_i(t+\delta t) | \psi_j(t+\delta t)\rangle = \delta_{ij}. \qquad \text{(A.2)}$$

Letting $D = \frac{(\delta t)^2}{\mu}$, and $\mathbf{F}_i = \frac{\delta E}{\delta \psi_i^*(t)}$ by substituting equation A.1 into equation A.2 we get after expanding,

$$\begin{aligned}\delta_{ij} &= (4 - 4\chi + \chi^2)\langle \psi_i(t)|\psi_j(t)\rangle + (-2 + 3\chi - \chi^2)\langle \psi_i(t)|\psi_j(t-\delta t)\rangle \\ &+ (-2+\chi)D\langle \psi_i(t)|\mathbf{F}_j\rangle + (2-\chi)D\sum_l \lambda_{jl}^* \langle \psi_i(t)|\psi_l(t)\rangle \\ &+ (-2 + 3\chi - \chi^2)\langle \psi_i(t-\delta t)|\psi_j(t)\rangle + (1 - 2\chi + \chi^2)\langle \psi_i(t-\delta t)|\psi_j(t-\delta t)\rangle \\ &+ (1-\chi)D\langle \psi_i(t-\delta t)|\mathbf{F}_i\rangle + (-1+\chi)D\sum_l \lambda_{jl}\langle \psi_i(t-\delta t)|\psi_l(t)\rangle \\ &+ (-2+\chi)D\langle \mathbf{F}_i|\psi_j(t)\rangle + (1-\chi)D\langle \mathbf{F}_i|\psi_j(t-\delta t)\rangle \\ &+ D^2\langle \mathbf{F}_i|\mathbf{F}_j\rangle - D^2\sum_l \lambda_{jl}^*\langle \mathbf{F}_i|\psi_l(t)\rangle\end{aligned}$$

$$
\begin{aligned}
&+ \quad (2-\chi)D\sum_k \lambda_{ik}\left\langle\psi_k(t)|\psi_j(t)\right\rangle + (-1+\chi)D\sum_k \lambda_{ik}\left\langle\psi_k(t)|\psi_j(t-\delta t)\right\rangle \\
&- \quad D^2\sum_k \lambda_{ik}\left\langle\psi_k(t)|\mathbf{F}_j(t)\right\rangle + D^2\sum_k\sum_l \lambda_{ik}\lambda^*_{jl}\left\langle\psi_k(t)|\psi_l(t)\right\rangle . \qquad \text{(A.3)}
\end{aligned}
$$

Now if we define,

$$
\begin{aligned}
H_{ij} &= \left\langle\psi_i(t)|\mathbf{F}_j\right\rangle , \\
HO_{ij} &= \left\langle\psi_i(t-\delta t)|\mathbf{F}_j\right\rangle , \\
L_{ij} &= \left\langle\mathbf{F}_i|\psi_j(t)\right\rangle , \\
LO_{ij} &= \left\langle\mathbf{F}_i|\psi_j(t-\delta t)\right\rangle , \\
R1_{ij} &= \left\langle\psi_i(t-\delta t)|\psi_j(t)\right\rangle , \\
R2_{ij} &= \left\langle\psi_i(t)|\psi_j(t-\delta t)\right\rangle , \\
G_{ij} &= \left\langle\mathbf{F}_i|\mathbf{F}_j\right\rangle , \\
S_{ij} &= \left\langle\psi_i(t)|\psi_j(t)\right\rangle , \\
SO_{ij} &= \left\langle\psi_i(t-\delta t)|\psi_j(t-\delta t)\right\rangle , \\
D_{ij} &= (4-4\chi+\chi^2)\delta_{ij} + (-2+3\chi-\chi^2)R2_{ij}, \\
&+ \quad (-2+3\chi-\chi^2)R1_{ij} + (1-2\chi+\chi^2)SO_{ij}, \\
&+ \quad (-2+\chi)DH_{ij} + (1-\chi)DHO_{ij}, \\
&+ \quad (-2+\chi)DL_{ij} + (1-\chi)DLO_{ij} + D^2G_{ij}, \qquad \text{(A.4)}
\end{aligned}
$$

and with a little more rearrangement we get,

$$
\begin{aligned}
0 &= D_{ij} - \delta_{ij} \\
&+ \quad \sum_l \lambda^*_{jl}\left((2-\chi)DS_{il} + (-1+\chi)DR1_{il} - D^2L_{il}\right) \\
&+ \quad \sum_k \lambda_{ik}\left((2-\chi)DS_{kj} + (-1+\chi)DR2_{kj} - D^2H_{kj}\right) \\
&+ \quad D^2\sum_k\sum_l \lambda_{ik}\lambda^*_{jl}S_{kl}. \qquad \text{(A.5)}
\end{aligned}
$$

Now define,

$$
\begin{aligned}
\Delta S_{ij} &= S_{ij} - \delta_{ij}, \qquad \text{(A.6)} \\
\Delta RN_{ij} &= RN_{ij} - \delta_{ij}. \qquad \text{(A.7)}
\end{aligned}
$$

Substituting for S_{ij},RN_{ij} we get after some more straight forward a algebra,

$$
\begin{aligned}
\lambda_{ij} &= -\frac{1}{D}\left(D_{ij} - \delta_{ij}\right) \\
&- \quad \sum_l \lambda^*_{jl}\left((2-\chi)\Delta S_{il} + (\chi-1)\Delta R1_{il} - DL_{il}\right) \\
&- \quad \sum_k \lambda_{ik}\left((2-\chi)\Delta S_{kj} + (\chi-1)\Delta R2_{kj} - DH_{kj}\right) \\
&- \quad D\left(\sum_k\sum_l \lambda_{ik}\lambda^*_{jl}\delta_{kl}\right) - \lambda^*_{ji}. \qquad \text{(A.8)}
\end{aligned}
$$

This then is the basis of the iterative scheme for the Lagrange multipliers. If we start with an initial guess of,

$$\lambda_{ij} = H_{ij} - DG_{ij}, \tag{A.9}$$

then we can generate the next guess by substitution into the right hand side of equation A.8.

As already noted the Lagrange multipliers for the straight CP method can be obtained simply by setting $\xi = 0$ in the above expression.

Appendix B

Pseudopotentials

It is a well established principle in chemistry that the electrons in an atom can be divided into two categories; valence, and core. The valence electrons are relatively weakly bound to the nucleus and are thus capable of being involved chemically with other atoms, while the core electrons are so tightly bound that they only have a minor, perturbative, effect on most properties of materials. It would thus be convenient if only the valence electrons had to be described in a model. This is doubly important as not only are the core electrons of little interest, they are very expensive to describe in terms of a plane wave expansion. Pseudopotentials then are a way of formalising the distinction between core and valence electrons and allowing the latter to be treated in a computationally tractable manner.

A thorough review of the subject is given by Heine [35], and other authors in the same volume of *Solid State Physics*. Here I will briefly outline the method as presented by Harrison [32].

Essentially we wish to solve the Schrödinger equation for the valence states,

$$-\frac{1}{2}\nabla^2\psi + V(\mathbf{r})\psi = E\psi. \tag{B.1}$$

As the core states also satisfy this equation we can write,

$$-\frac{1}{2}\nabla^2\psi_{c,j} + V(\mathbf{r})\psi_{c,j} = E_{c,j}\psi_{c,j}, \tag{B.2}$$

where the index c represents the core quantum numbers, and j the ion position. To proceed the valence electrons are expanded in terms of orthogonal plane waves,

$$OPW_k = |\mathbf{k}> - \sum_{c,j} |c,j><c,j|\mathbf{k}>, \tag{B.3}$$

where $|c,j>= \psi_c(\mathbf{r}-\mathbf{r}')$, and $|\mathbf{k}>= e^{i\mathbf{k}\cdot\mathbf{r}}$. Noting that we can write a projection operator, P, in the form,

$$P = \sum_{c,j} |c,j><c,j|, \tag{B.4}$$

then the orthogonalised plane wave can be rewritten as,

$$OPW_k = (1 - P)|\mathbf{k} > . \tag{B.5}$$

The advantage of orthogonalised plane waves is that by construction they are orthogonal to the core states. This should mean that the expansion is far more rapidly convergent than if just plane waves were used. Thus we have,

$$\psi_v = (1 - P) \sum_k a_k |\mathbf{k} >, \tag{B.6}$$

where v indicates that these are valence states. However note that knowledge of the core states is still required. The sum over $\mathbf{k}$ is rapidly convergent and $\phi = \sum_k a_k|\mathbf{k} >$ will be a smooth function, referred to as the pseudowavefunction. Note that this function is equal to the true wavefunction outside the core since P is zero there, and hopefully it remains smooth in the core region. In this case, as most of the properties of interest are concerned with the wavefunction outside the core, we may profitably rewrite the Schrödinger equation for the valence states in terms of ψ. This leads to,

$$-\frac{1}{2}\nabla^2\phi + V(\mathbf{r})\phi - \left(-\frac{1}{2}\nabla^2\phi + V(\mathbf{r})\phi\right) P\phi + EP\phi = E\phi, \tag{B.7}$$

or,

$$-\frac{1}{2}\nabla^2\phi + W\phi = E\phi, \tag{B.8}$$

where,

$$W = V(\mathbf{r}) + \sum_{c,j}(E - E_{c,j})|c,j >< c,j|. \tag{B.9}$$

Equation B.8 is called the pseudopotential equation, and W the pseudopotential. Thus the true Schrödinger equation is replaced by one in which the eigenvalues are the same, and the wavefunction outside the core region is the same. All that remains is to determine a convenient form of W which describes the effects of the core electrons. It should be noted that this is not necessarily a trivial problem.

In general the pseudopotential for a given atom will have to be non-local in order to give reliable results. However this is not the case for sodium and caesium. For sodium the Topp and Hopfield pseudopotential [111] has been used in this thesis. This has the form,

$$V(\mathbf{r}) \;=\; \begin{cases} V_0 \cos kr + C & , \quad r < r_c; \\ -\frac{1}{r} & , \quad r > r_c, \end{cases} \tag{B.10}$$

where,

$$r_c \;=\; 3.00,$$

$$
\begin{aligned}
V_0 &= 0.1790, \\
k &= 1.224, \\
C &= -0.179.
\end{aligned}
\tag{B.11}
$$

For caesium a "home grown" pseudopotential due to Ettore Fois was used. This has the form,

$$
V(\mathbf{r}) = -\frac{1}{r}\mathrm{erf}\left(\frac{r}{r_c}\right) + a_0 \exp(-b_0 r^2), \tag{B.12}
$$

where,

$$
\begin{aligned}
r_c &= 1.30, \\
a_0 &= 1.70, \\
b_0 &= 0.33.
\end{aligned}
\tag{B.13}
$$

Appendix C

Derivation of the Exchange Potential for Perdew's Exchange Energy Functional

This appendix will outline the method of taking the functional derivative of the exchange functional due to Perdew,

$$E_{\mathbf{x}}[\rho] = A_{\mathbf{x}} \int d\mathbf{r} \rho^{\frac{4}{3}} F(s), \tag{C.1}$$

where,

$$A_{\mathbf{x}} = -\frac{3}{4}\left(\frac{3}{\pi}\right)^{\frac{1}{3}}, \tag{C.2}$$

$$s = \frac{|\nabla\rho|}{2k_F\rho}$$

$$= \frac{|\nabla\rho|}{\alpha\rho^{\frac{4}{3}}}, \tag{C.3}$$

$$k_F = (3\pi^2\rho)^{\frac{1}{3}}, \tag{C.4}$$

$$\alpha = 2(3\pi^2)\frac{1}{3}. \tag{C.5}$$

Equation C.1 can be written in the form,

$$E_{\mathbf{x}}[\rho] = \int d\mathbf{r} K(\rho, \nabla\rho) \; ; \; K(\rho, \nabla\rho) = A_{\mathbf{x}}\rho^{\frac{4}{3}} F(s). \tag{C.6}$$

This allows the use of the standard form for the functional derivative (see appendix A of [72]) to give,

$$\frac{\delta E_{\mathbf{x}}}{\delta\rho} = \frac{\partial K}{\partial\rho} - \nabla\left(\frac{\partial K}{\partial\nabla\rho}\right). \tag{C.7}$$

Now the first term is simply,

$$\frac{\partial K}{\partial \rho} = A_x \rho^{\frac{1}{3}} \left(\frac{4}{3} F(s) + \rho \frac{dF}{ds} \frac{\delta s}{\delta \rho} \right). \tag{C.8}$$

But,

$$\frac{\delta s}{\delta \rho} = \frac{\delta}{\delta \rho} \left(\frac{|\nabla \rho|}{\alpha \rho^{\frac{4}{3}}} \right) = -\frac{4}{3} \frac{|\nabla \rho|}{\alpha \rho^{\frac{7}{3}}}, \tag{C.9}$$

thus,

$$\frac{\partial K}{\partial \rho} = A_x \rho^{\frac{1}{3}} \left(\frac{4}{3} F(s) - \frac{4}{3} s \frac{dF}{ds} \right). \tag{C.10}$$

The second term in equation C.7 requires,

$$\frac{\partial K}{\partial \nabla \rho} = A_x \rho^{\frac{4}{3}} \frac{dF}{ds} \frac{\delta s}{\delta \nabla \rho}, \tag{C.11}$$

where,

$$\begin{aligned} \frac{\delta s}{\delta \nabla \rho} &= \frac{\delta}{\delta \nabla \rho} \left(\frac{|\nabla \rho|}{\alpha \rho^{\frac{4}{3}}} \right) \\ &= \frac{1}{\alpha \rho^{\frac{4}{3}}} \frac{\nabla \rho}{|\nabla \rho|}. \end{aligned} \tag{C.12}$$

Thus we have,

$$\frac{\partial K}{\partial \nabla \rho} = \frac{A_x}{\alpha} \frac{dF}{ds} \frac{\nabla \rho}{|\nabla \rho|}. \tag{C.13}$$

The second term in equation C.7 then is,

$$\begin{aligned} \nabla \cdot \left(\frac{\partial K}{\partial \nabla \rho} \right) &= \frac{A_x}{\alpha} \nabla \cdot \left(\frac{dF}{ds} \frac{\nabla \rho}{|\nabla \rho|} \right) \\ &= \nabla \rho \cdot \nabla \left(\frac{dF}{ds} \frac{1}{|\nabla \rho|} \right) + \frac{dF}{ds} \frac{1}{|\nabla \rho|} \nabla^2 \rho, \end{aligned} \tag{C.14}$$

using the fact that,

$$\nabla \cdot (\phi \mathbf{a}) = \mathbf{a} \cdot \nabla \phi + \phi (\nabla \cdot \mathbf{a}). \tag{C.15}$$

After a little algebra it is found that,

$$\begin{aligned} \nabla \left(\frac{dF}{ds} \frac{1}{|\nabla \rho|} \right) &= \frac{d^2 F}{ds^2} \left(\frac{\nabla (|\nabla \rho|)}{|\nabla \rho| \alpha \rho^{\frac{4}{3}}} - \frac{4}{3} \frac{\nabla \rho}{\alpha \rho^{\frac{7}{3}}} \right) \\ &- \frac{dF}{ds} \frac{\nabla (|\nabla \rho|)}{|\nabla \rho|^2}. \end{aligned} \tag{C.16}$$

Substituting back into equation C.14 gives,

$$\nabla \cdot \frac{dF}{ds}\frac{\nabla\rho}{|\nabla\rho|} = \frac{d^2F}{ds^2}\left(\frac{\nabla\rho\cdot\nabla(|\nabla\rho|)}{\alpha\rho^{\frac{4}{3}}|\nabla\rho|} - \frac{4}{3}\frac{\nabla\rho\cdot\nabla\rho}{\alpha\rho^{\frac{4}{3}}}\right) - \frac{dF}{ds}\left(\frac{\nabla\rho\cdot\nabla(|\nabla\rho|)}{|\nabla\rho|^2} - \frac{\nabla^2\rho}{|\nabla\rho|}\right). \tag{C.17}$$

So we then have from equation C.14,

$$\nabla\left(\frac{\partial K}{\partial\nabla\rho}\right) = \frac{A_x}{\alpha}\left\{-\frac{dF}{ds}\left(\frac{\nabla\rho\cdot\nabla(|\nabla\rho|)}{|\nabla\rho|^2} - \frac{\nabla^2\rho}{|\nabla\rho|}\right) - \frac{d^2F}{ds^2}\left(\frac{s\nabla\rho\cdot\nabla(|\nabla\rho|)}{|\nabla\rho|^2} - \frac{4}{3}s^2\rho^{\frac{1}{3}}\alpha\right)\right\}. \tag{C.18}$$

Finally substituting back into equation C.7 gives,

$$\frac{\delta E_x}{\delta\rho} = A_x\rho^{\frac{1}{3}}\left\{\frac{4}{3}F(s) - \frac{dF}{ds}\left(\frac{4}{3}s - \frac{\rho^{\frac{-1}{3}}}{\alpha}\frac{\nabla\rho\cdot\nabla(|\nabla\rho|)}{|\nabla\rho|^2} + \frac{\rho^{\frac{-1}{3}}}{\alpha}\frac{\nabla^2\rho}{|\nabla\rho|}\right) + \frac{d^2F}{ds^2}\left(-\frac{\rho^{\frac{-1}{3}}}{\alpha}\frac{s\nabla\rho\cdot\nabla(|\nabla\rho|)}{|\nabla\rho|^2} + \frac{4}{3}s^2\right)\right\}. \tag{C.19}$$

It is then a matter of algebra to put this in the form given by Perdew and Wang,

$$\frac{\delta E_x}{\delta\rho(\mathbf{r})} = A_x\rho^{\frac{1}{3}}\left[\frac{4}{3}F - ts^{-1}\frac{dF}{ds} - \left(u - \frac{4}{3}s^3\right)\frac{d}{ds}\left(s^{-1}\frac{dF}{ds}\right)\right], \tag{C.20}$$

where,

$$t = (2k_F)^{-2}\rho^{-1}\nabla^2\rho, \tag{C.21}$$

and,

$$u = (2k_F)^{-3}\rho^{-2}\,\nabla\rho\cdot\nabla|\nabla\rho|. \tag{C.22}$$

Appendix D

Useful Conversion Factors

The babel of languages at times appears to be matched by the babel of units used by various workers. Most of this thesis has been presented in atomic units, which were used for the calculations. Here however are some of the conversion factors to the other most commonly used units.

- 1a.u. (time) $= 2.4188 \times 10^{-17}$s
- 1a.u. (length) $= 0.529177$Å
- 1a.u. (energy) $= 27.2116$eV $= 1$ Hartree
- 1a.u. (energy) $= 4.3597482 \times 10^{-18}$J
- 1a.u. (mass) $= m_e = 9.109534 \times 10^{-31}$kg
- 1eV $= 11604.5$K
- 1eV $= 8065.48$cm^{-1}
- 1eV $= 1.60219 \times 10^{12}$erg
- 1K $= 0.695039$cm^{-1}
- 1K $= 1.98722 \times 10^{-3}$ kcal/mol
- 1kcal/mol $= 4.34 \times 10^{-2}$ eV
- 1cal $= 4.184$J
- m_p = proton mass $= 1836 m_e$

Bibliography

[1] Allen, M.P., and Tildesley, D.J., *Computer Simulation of Liquids*, O.U.P., (1987).

[2] Arias, T.A., Payne, M.C., and Joannopoulos, J.P. *Phys. Rev. B* **45**, 1538, (1992).

[3] Ashcroft, N.W., and Mermin, N.D., *Solid State Physics*, Holt-Saunders, (1976).

[4] Bader, R.F.W., Nygen-Dang, T.T., and Tol, Y., *Rep. Prog. Phys.* **44**, 893, (1981).

[5] Barbiellini, B., Maroni, E.G., and Jarlborg, T., *J. Phys. Condensed Matter* **2**, 7597, (1990).

[6] Becke, A.D., *J. Chem. Phys.* **84**, 4524, (1986).

[7] Becke, A.D., *Phys. Rev. A* **38**, 3098, (1988).

[8] Becke, A.D., *J. Chem. Phys.* **96**, 2155, (1992).

[9] Bonačić-Koutecký, V., Fantucci, P., and Koutecký, J., *Chem. Phys. Lett.* **166**, 32, (1990).

[10] Bonačić-Koutecký, V., Pittner, J., Scheuch, C., Guest, M.F., and Koutecký, J., *J. Chem. Phys.* **96**, 7938, (1992).

[11] Bréchignac, C., Cahuzac, Ph., Carlier, F., and Leygnier, J., *Chem. Phys. Lett.* **164**, 433, (1989).

[12] Broyer, M., Delacrétaz, G., Ni, G.Q., Whetton, R.L., Wolf, J.P., and Wöste, L., *Phys. Rev. Lett.* **62**, 2100, (1989).

[13] Car, R., and Parrinello, M., *Phys. Rev. Lett.* **55**, 2471, (1985).

[14] Car, R., and Parrinello, M., referenced in [92] but never actually published.

[15] Car, R., and Parrinello, M., in *Simple Molecular Systems at Very High Densities*, ed. Polian, A., Plenum, (1989).

[16] Ceperley, D.M., and Alder, B.J., *Phys. Rev. Lett.* **45**, 566, (1980).

[17] Demtröder, W., and Stoch, M., *J. Molec. Spectrosc.* **55**, 476, (1975).

[18] Fan, L., and Ziegler, T., *J. Chem. Phys.* **94**, 6057, (1991).

[19] Fan, L., and Ziegler, T., *J. Chem. Phys.* **95**, 7401, (1991).

[20] Fantucci, J., Bonačić-Koutecký, V., and Koutecký, J., *Z. Phys. D* **12**, 307, (1989).

[21] Fantucci, P., and Koutecký, J., *Chem. Rev.* **86**, 539, (1986).

[22] Fermi, E., *Rend. Accad. Linui* **6**, 602, (1927).

[23] Feuston, B., Lee, C., and Clementi, E., *MOTECC-91* ed. Clementi, E., ESCOM, (1991).

[24] Foucrault, M., Millie, Ph., and Daudey, J.P., *J. Chem. Phys.* **96**, 1257, (1992).

[25] Galli, G., Martin, R., Car, R., and Parrinello, M., *Phys. Rev. Lett.* **62**, 555, (1989).

[26] Garland, D.A., and Lindsay, D.M., *J. Chem. Phys.* **78**, 2813, (1983).

[27] Glaser, R., Waldron, R.F., and Wiberg, K.B., *J. Chem. Phys.* **94**, 7357, (1990).

[28] Goldstein, H., *Classical Mechanics*, Addison-Wesley, (1980).

[29] Gomes Dacosta, P., Nielson, O.H., and Kunc, C., *J. Phys. C* **19**, 3163, (1986).

[30] Gunarsson, O., and Lundqvist, B.I., *Phys. Rev. B* **13**, 4274, (1976).

[31] Hall,R.W., *J. Chem. Phys.* **93**, 8211, (1990).

[32] Harrison, W.A., *Solid State Theory*, Dover, (1980).

[33] Hartke, B., and Carter, E.A., *Chem. Phys. Lett.* **189**, 358, (1992).

[34] de Heer, W.A., Knight W.D., and Chou, M.C., *Solid State Physics* **40**, 93, (1989).

[35] Heine, V., *Solid State Physics* **24**, 1, (1970).

[36] Hohenberg,P., and Kohn, W., *Phys. Rev.* **136**, B864, (1964).

[37] Höning, G., Cazjkowski, M., Stock, M., and Demtröder, W., *J. Chem. Phys.* **71**, 2138, (1979).

[38] Hoover, W.G., *Phys. Rev. A* **31**, 1695, (1986).

[39] Jones, R.O., and Gunarsson, O., *Rev. Mod. Phys.* **61**, 689, (1989).

[40] Kemister, G., and Nordholm, S., *J. Chem. Phys.* **83**, 5163, (1985).

[41] Kemister, G., and Nordholm, S., *Chem. Phys. Lett.* **133**, 121, (1987).

[42] Knight, W.D., Clemenger, K., de Heer, W.A., and Saunders,W.A., *Phys. Rev. B* **31**, 2539, (1985).

[43] Knight, W.D., Clemenger, K., de Heer, W.A., Saunders, W.A., Chou, M.Y., and Cohen, M.L., *Phys. Rev. Lett.* **52**, 2141, (1984).

[44] Kolos, W., and Wolniewicz, L., *J. Chem. Phys.* **43**, 2429, (1965).

[45] Kolos, W., and Wolniewicz, L., *J. Chem. Phys.* **49**, 404, (1968).

[46] Kohn, W., and Sham, L.J., *Phys. Rev.* **140**, A1133, (1965).

[47] Kohn, W., and Vashita, P., in *Theory of the Inhomogenous Electron Gas*, eds., Lundqvist, S., and March, N.H., Plenum, (1983).

[48] Kresin, V., *Phys. Rev.* **39**, 3042, (1989).

[49] Kusch, P., and Hessel, M.M., *J. Chem. Phys.* **68**, 2591, (1978).

[50] Kutzler, F.W., and Painter, G.S., *Phys. Rev. Lett.* **59**, 1285, (1987).

[51] Laasonen, K., Csajka, F., and Parinello, M., *Chem. Phys. Lett.* **194**, 179, (1992).

[52] Laidler, K.J., *Chemical Kinetics*, 3rd ed., Harper and Row, (1987).

[53] Langreth, D.C., and Mehl, M.J., *Phys. Rev. B* **28**, 1809, (1983).

[54] Laskowski, B.C., and Langhoff, S.R., *Chem. Phys. Lett.* **92**, 49, (1992).

[55] Leung, T.C., Chan, C.T., and Harman, B.N., *Phys. Rev. B* **44**, 2932, (1991).

[56] Lindsay, D.M., Herschbach, D.R., and Kwiram, A.L., *Molec. Phys.* **32**, 1199, (1976).

[57] Lindsay, D.M., and Thompson, G.A., *J. Chem. Phys.* **77**, 1114, (1982).

[58] Löwen, H., Madden,P.A., and Hansen, J-P., *Phys. Rev. Lett.* **68**, 1081, (1992).

[59] Magaud, L., Khanna, S.N., and Jenna, P., *Chem. Phys. Lett.* **183**, 333, (1991).

[60] Martins, J.L., Car, R., and Buttet, J., *J. Chem. Phys.* **78**, 5646, (1983).

[61] Martins, J.L., Car, R., and Buttet, J., *Phys. Rev. B* **31**, 1804, (1985).

[62] McAdon, M.H., and Goddard, W.A., *Phys. Rev. Lett.* **55**, 2563, (1985).

[63] McAdon, M.H. and Goddard, W.A., *J. Chem. Phys.* **88**,277, (1988).

[64] McWeeny, R., *Coulson's Valence*, O.U.P., (1979).

[65] Meroni, A., Hansen, J-P., and Madden, P.A., *J. Non-Cryst. Solids* to be published.

[66] Mingos, D.M.P., and Lin, Z., *Chem. Phys.* **137**, 15, (1989).

[67] Mingos, D.M.P., and Wales, D.J., *Introduction to Cluster Chemistry*, Prentice Hall, (1990).

[68] Mlynarski, P., and Salahub, D.R., *Phys. Rev. B* **43**, 1399, (1991).

[69] Moullet, I., Martins, J.L., Reuse, F., and Buttet, J., *Phys. Rev. B* **42**, 11598, (1990).

[70] Nosé, S., *Molec. Phys.* **52**, 255, (1984).

[71] Ortitz, G., and Ballone, P., *Phys. Rev. B* **43**, 6376, (1991).

[72] Parr, R.G., and Yang, W., *Density Functional Theory of Atoms and Molecules*, O.U.P., (1989).

[73] Pastore, G., Smargiassi, E., and Buda F., *Phys. Rev. A* **44**, 6334, (1991).

[74] Payne, M.C., *J. Phys. Condensed Matter* **1**, 2199, (1989).

[75] Payne, M.C., Bristowe, P.D., and Joannopolous, J.D., *Molec. Simul.* **4**, 79, (1989).

[76] Pederson, M.R., and Lin, C.C., *J. Chem. Phys.* **88**, 1807, (1987).

[77] Pederson, M.R., Heaton, R.A., and Lin, C.C., *J. Chem. Phys.* **80**, 1972, (1984).

[78] Perdew, J.P., *Phys. Rev. Lett.* **55**, 1665, (1985).

[79] Perdew, J.P., *Phys. Rev. B* **33**, 8822, (1986).

[80] Perdew, J.P., *Adv. Quantum Chem.* **21**, 113, (1990).

[81] Perdew, J.P., *Physica B* **172**, 1, (1991).

[82] Perdew, J.P., Levy, M., Painter, G.S., Wei, S., and Lagowski, J.B., *Phys. Rev. B* **37**, 838, (1988).

[83] Perdew, J.P., and Wang, Y., *Phys. Rev. B* **33**, 8800, (1986).

[84] Perdew, J.P., and Zunger, A., *Phys. Rev. B* **23**, 5048, (1981).

[85] Press, W.H., Flannery B.P., Teukolsky, S.A., and Vetterling, W.T., *Numerical Recipes - The Art of Scientific Computing*, C.U.P., (1986).

[86] Pulay, P., *Molec. Phys.* **17**, 197, (1969).

[87] Pulay, P., *Adv. Chem. Phys.* **69**, 241, (1987).

[88] Raab, M., Weickenmeier, H., and Demtröder, W., *Chem. Phys. Lett.* **88**, 377, (1982).

[89] Raimondi, M., private communication.

[90] Ray, A.K., *Sol. State Commun.* **71**, 311, (1989).

[91] Remler D.K., *D.Phil. Thesis*, unpublished, (1988).

[92] Remler, D.K., and Madden, P.A., *Molec. Phys* **70**, 921, (1990).

[93] Röthlisberger, U., and Andreoni, W., *J. Chem. Phys.* **94**, 8129, (1991).

[94] Röthlisberger, U., and Andreoni, W., *Z. Phys. D* **20**, 243, (1991).

[95] Savin, A., Stoll, H., and Preuß, H., *Theor. Chim. Acta.* **70**, 407, (1986).

[96] Seeley, G., and Keyes, T., *J. Chem. Phys.* **91**, 5581, (1989).

[97] Selby, K., Kresin, V., Masui, J., Vollmer, W., de Heer, W.A., Scheidemann, A., and Knight, W.D., *Phys. Rev.* **43**, 4565, (1991).

[98] Selby, K., Vollmer, M., Masui, J., Kresin, V., de Heer, W.A., and Knight, W.D., *Phys. Rev. B* **40**, 5417, (1989).

[99] Stoll, H., Pavlidou, C.M.E., and Preuß, H., *Theor. Chim. Acta.* **49**, 143, (1978).

[100] Space, B., and Coker, D.F., *J. Chem. Phys.* **96**, 652, (1992).

[101] Sprik, M., *J. Phys. Chem.* **95**, 2283, (1991).

[102] Sprik, M., and Klein, M.L., *J. Chem. Phys.* **89**, 7556, (1988).

[103] Stark, J.G., and Wallace, H.G., *Chemistry Data Book*, John Murray, (1982).

[104] Štich, I., Car, R., Parrinello, M., and Baroni, S., *Phys. Rev. B* **39**, 4997, (1989).

[105] Svane, A., and Gunarsson, O., *Phys. Rev. B* **37**, 9919, (1988).

[106] Szabo, A., and Ostlund, N.S., *Modern Quantum Chemistry*, Macmillan, (1982).

[107] Thomas, L.H., *Proc. Camb. Phil. Soc.* **23**, 542, (1927).

[108] Thompson, T.C., Izmertan, G., Lemon, S.J., Trechlar, D.G., and Mead, C.A., *J. Chem. Phys.* **82**, 5597, (1985).

[109] Thompson, G.A., and Lindsay, D.M., *J. Chem. Phys.* **74**, 959, (1981).

[110] Thompson, G.A., Tischler, F., and Lindsay, D.M., *J. Chem. Phys.* **78**, 5946, (1983).

[111] Topp, W.C., and Hopfield, J.J., *Phys Rev B* **7**, 1295, (1973).

[112] Tornaghi, E., Cooper, D.L., Gerratt, J., and Raimondi, M., *Croatica Chemica Acta* **64**, 429, (1991).

[113] Tornaghi, E., Cooper, D.L., Gerratt, J., Raimondi, M., and Sironi, M., *J. Molec. Struc. (Theochem.)* **259**, 383, (1992).

[114] Tosi, M., *Solid State Physics* **16**, 110, (1964).

[115] Toxvaerd, S., *Molec. Phys.* **72**, 159, (1991).

[116] Verma, K.K., Bahns, J.T., Rajae-Rizi, A.R., Stwalley, W.C., *J. Chem. Phys.* **55**, 476, (1975).

[117] Walch, S.P., Bauschlicher, C.W., Siegbahn, P.E.M., and Partridge, H., *Chem. Phys. Lett.* **92**, 54, (1982).

[118] Wales, D.J., Mingos, D.M.P., Slee, T., and Lin, Z., *Acc. Chem. Res.* **23**, 17, (1990).

[119] Wang, C.R.C., Pollack, S., Dahlseid, T.A., Kerretsky, G.M., and Kappes, M.M., *J.Chem. Phys.* **96**, 7931, (1992).

[120] Wang, C.R.C., Pollack, S., and Kappes, M.M., *Chem. Phys. Lett.* **165**, 26, (1990).

[121] Weickenmeier, H., Dremer, U., Wahl, M., Raab, M., Demtröder, W., and Müller, W., *J. Chem. Phys.* **82**, 5354, (1985).

[122] Zérah, G., Clérouin, J., and Pollock, E.L., *Phys. Rev. Lett.* **69**, 446, (1992).